catalysts

Special Issue Reprint

Zeolites as Catalysts

Applications in Chemical Engineering, Energy Sources and Environmental Protection, 2nd Edition

Edited by
De Fang

mdpi.com/journal/catalysts

MDPI

Zeolites as Catalysts: Applications in Chemical Engineering, Energy Sources and Environmental Protection, 2nd Edition

Zeolites as Catalysts: Applications in Chemical Engineering, Energy Sources and Environmental Protection, 2nd Edition

Guest Editor

De Fang

MDPI

Basel • Beijing • Wuhan • Barcelona • Belgrade • Novi Sad • Cluj • Manchester

Guest Editor
De Fang
School of Materials Science
and Engineering
Wuhan University of
Technology
Wuhan
China

Editorial Office
MDPI AG
Grosspeteranlage 5
4052 Basel, Switzerland

This is a reprint of the Special Issue, published open access by the journal *Catalysts* (ISSN 2073-4344), freely accessible at: https://www.mdpi.com/journal/catalysts/special_issues/25837A8UNJ.

For citation purposes, cite each article independently as indicated on the article page online and as indicated below:

Lastname, A.A.; Lastname, B.B. Article Title. *Journal Name* **Year**, *Volume Number*, Page Range.

ISBN 978-3-7258-5591-9 (Hbk)
ISBN 978-3-7258-5592-6 (PDF)
https://doi.org/10.3390/books978-3-7258-5592-6

Contents

catalysts

MDPI

Article

Cu/MOF-808 Catalyst for Transfer Hydrogenation of 5-Hydroxymethylfurfural to 2, 5-Furandimethanol with Formic Acid Mediation

Jingxin Tan †, Mengqi Li †, Lingtao Liu, Lijian Wang, Haocun Wang, Junjie Bian * and Chunhu Li

Key Laboratory of Marine Chemistry Theory and Technology of Ministry of Education, Ocean University of China, Qingdao 266100, China

* Correspondence: junjiebian@ouc.edu.cn; Tel.: +86-(532)-66782502

† These authors contributed equally to this work.

Abstract: Biomass platform compound 5-Hydroxymethylfurfural (HMF), with its low price and abundant source, can be used as a renewable resource to replace traditional petrochemicals. MOF-808(Zr) has tunable active sites and excellent stability under high temperatures and acidic as well as basic environments, and the unsaturated coordination of metal ions within its framework structure can exhibit Lewis acidity, facilitating catalytic transfer hydrogenation from HMF to 2, 5-Furandimethanol (BHMF). The hydrothermal–impregnation–reduction method was used to prepare Cu/MOF-808 catalysts with high catalytic performance. Formic acid was chosen as the hydrogen donor solvent. The selectivity and yield of BHMF were 75.65% and 71%, respectively, at 150 °C for 4 h. A reaction pathway for the catalytic hydrogen transfer of HMF to BHMF was proposed. The high activity and stability of the Cu/MOF-808 catalyst with dual active sites provide a viable method for feasible hydrogenation of HMF to high value-added compounds.

Keywords: 5-hydroxymethylfurfural; 5-(hydroxymethyl)-furfuryl alcohol; hydrogen transfer; acid catalyst; MOF-808

1. Introduction

Biomass is recognized as a crucial carbon-neutral energy source, and research is increasingly focused on utilizing renewable biomass to produce high-value chemicals and fuels [1–3]. This strategy is a significant part of the global effort to ensure an abundant supply of renewable biomass energy [4]. By 2018, biomass energy, a leading component of renewable energy, accounted for 18% of global energy consumption, with biomass alone contributing 72.3% to this share [5]. Predictions for 2030 indicate that biomass could provide 20% of the world's transportation fuels and 25% of its chemicals [6,7]. Among the various biomass platform molecules, lignocellulose is particularly promising as a feedstock, yielding chemicals such as 5-hydroxymethylfurfural (HMF) [8] and furfural (FUR) [9] through both chemical and biological processes. HMF, in particular, is a prevalent and crucial furan derivative known for its exceptional chemical activity. It serves as a pivotal intermediate in the production of a wide array of fine chemicals, polymers, and other value-added compounds, playing a vital role in the synthesis of numerous fine chemicals, polymers, and high-value chemicals [10–12]. Moreover, the hydrogenation of HMF results in the production of various high-value chemicals, including 2, 5-furandimethanol (BHMF) [13,14], 2, 5-dimethylfuran (2, 5-DMF) [15,16], and 2, 5-dimethyltetrahydrofuran (2,.5-DMTHF), which further underscores the importance of biomass conversion in advanced biological feedstock processing [17].

2, 5-Furandimethanol (BHMF) is a high-value-added product from the selective hydrogenation of HMF, an alcohol compound with a wide range of applications and a great market potential [18,19]. It can be used in the synthesis of value-added chemicals for

molecular recognition studies and as a monomer in polymers for more promising applications [20], such as furanamides and polyurethanes [11,21]. The main pathways that will be used to generate BHMF from HMF as a feedstock are chemical catalysis and the role of basic sites [22]. However, biocatalytic upgrading of HMF remains a major challenge [23]. The use of chemical catalysis is the most widely studied pathway. The use of hydrogen as a hydrogen source for HMF hydrogenation to produce BHMF is the most common research system in current studies, but there are some disadvantages of using hydrogen as a hydrogen source, such as high reaction pressure and high cost of transportation and storage, which limit its further application as a hydrogen source in industry. In recent years, there has been an increasing number of reports on HMF catalytic transfer hydrogenation (CTH) [24]. The common sources of liquid hydrogen studied are formic acid [25,26], silanes [27], and small molecule alcohols [28,29]. Among them, formic acid is a byproduct of the catalytic decomposition of biomass sugars, which in turn are used to produce high-value-added biomass products, which greatly improves utilization and economy [30]. However, the use of metal catalysts in liquid hydrogen source systems is often accompanied by lower BHMF selectivity, higher reaction temperatures, and excess hydrogen donors [15,31], making it particularly important to design and develop efficient catalysts for the production of BHMF from HMF [27].

Two key steps are crucial for hydrogen transfer, the first of which, hydrogen dissociation from the donor, is catalyzed by metals including copper and/or cobalt. Metal organic frameworks (MOFs) are a class of crystalline organic–inorganic hybrid compounds formed by bonding metal clusters or ions to organic ligands [32]. MOFs are typically highly porous, formed by uniformly sized pores whose intrinsic properties are determined by organic ligands and metal ions. Researchers have investigated various metal catalysts for the catalytic transfer hydrogenation of HMF to BHMF. Zheng et al. [33] successfully prepared Cu–Co bimetallic catalysts containing carbon and nitrogen, showing good selectivity, catalytic activity, and cyclic stability in the conversion of HMF to BHMF. Kasanneni et al. [33] successfully prepared Cu–Al_2O_3 catalysts having a maximum BHMF yield of 93% under optimized reaction conditions (3 MPa H_2, 130 °C, 1 h).

In this paper, we have successfully prepared a series of Cu/MOF-808(Zr) catalysts with large specific surface area, large porosity, good stability under acidic reaction conditions, and good thermal stability. The Lewis acidic site of the catalysts facilitates the conversion of HMF to BHMF. To investigate the optimum conditions for the catalytic transfer hydrogenation of HMF, the effects of reaction conditions such as time, temperature, reaction solvent, formic acid dosing, and catalyst dosing on the reaction were considered separately. In addition, the catalysts were characterized to investigate the catalytic mechanism of the reaction.

2. Result and Discussion

2.1. Catalyst Characterization

Figure 1 shows the XRD simulation profile of the MOF-808(Zr) catalyst and the XRD diffraction spectrum of the actually prepared MOF-808(Zr) catalyst and the Cu/MOF-808(Zr) catalyst. The prepared MOF-808(Zr) has characteristic peaks at 2θ = 8.37°, 8.70°, 10°, and 11°, thus indicating the successful preparation of MOF-808(Zr). The peaks corresponding to the diffraction peaks of Cu should be 2θ = 43.4°, 50.5°, and 74.1° [34], and the intensity of the peaks increases with the increase of Cu loading, but it does not form the more obvious crystal diffraction peaks, probably due to the fact that the Cu particles are not large enough to form Cu clusters instead of forming crystals [35]. During Cu/MOF-808(Zr) synthesis, the fully dispersed Cu^{2+} in solution was reduced by using an excess of $NaBH_4$ reducing agent. The pore structure of MOF-808(Zr) was damaged to a certain extent, so the intensity of the diffraction characteristic peak of the synthesized crystal was decreased [36,37]. As the loading of Cu increased, the dosage of reducing agent $NaBH_4$ increased. At low loading, the crystallinity of the crystal is good, and as the loading increases, the intensity of the characteristic peaks gradually decreases and the characteristic

peaks gradually broaden, but the diffraction characteristic peaks of MOF-808(Zr) are still maintained in the XRD spectra [34].

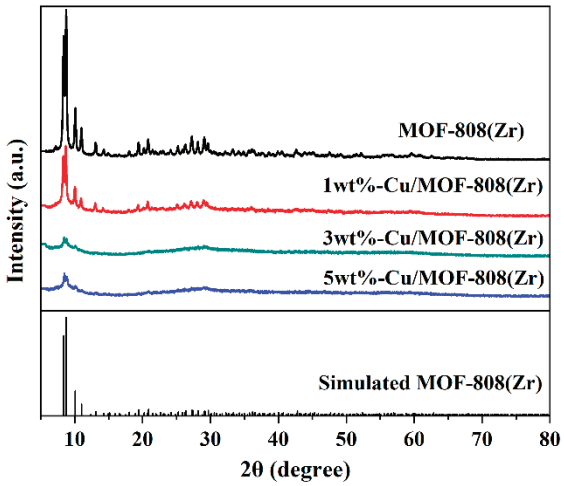

Figure 1. XRD patterns of samples MOF-808, 1wt%–Cu/MOF-808(Zr), 3 wt%-Cu/MOF-808(Zr), and 5wt%-Cu/MOF-808(Zr).

Figure S2a–c shows that the MOF-808(Zr) crystals resemble regular ortho-octahedra with crystal sizes in the range of 200–250 nm, which is approximately the same as the morphology reported in the literature [38]. Figure S2d–f shows the morphology of the MOF-808(Zr) crystals after loading with Cu nanoparticles, and it can be seen that the morphology and structure remain almost unchanged after loading, and the size of the crystal particles also remains almost unchanged. According to Figure S2g, it can be seen that the Cu nanoparticles are uniformly distributed on the surface of the MOF-808(Zr).

As shown by the TEM characterization in Figure 2, Cu nanoparticles were successfully loaded on the surface of MOF-808(Zr). Furthermore, MOF-808(Zr) still retains its original octahedral structure and has not been destroyed by $NaBH_4$ reduction.

As shown in Figure 3, the isotherms of both MOF-808(Zr) and 3 wt%-Cu/MOF-808(Zr) belong to the H3 hysteresis return line in the Type IV isotherm. This indicates that the two catalysts, MOF-808(Zr) and 3 wt%-Cu/MOF-808(Zr), have similar mesoporous and microporous structures. As shown in Figure 3b, the BET specific surface areas of MOF-808(Zr) and 3 wt%-Cu/MOF-808(Zr) were 1148.05 $m^2\ g^{-1}$ and 579.89 $m^2\ g^{-1}$, respectively; the pore volumes were 1.40 $cm^3\ g^{-1}$ and 0.89 $cm^3\ g^{-1}$, respectively; and the average pore sizes calculated by the HK model were 1.84 nm and 1.85 nm, respectively. Both the BET specific surface area and pore volume of 3 wt%-Cu/MOF-808(Zr) were significantly reduced compared to MOF-808(Zr), and the decrease of the specific surface area and porosity of the 3 wt%-Cu/MOF-808(Zr) sample is a dramatic degradation of its crystalline structure. This is consistent with the results shown by XRD.

The XPS spectra of the catalyst 3 wt%-Cu/MOF-808(Zr) sample was able to obtain the elemental composition of the catalyst and the valence state of the elements The XPS spectra of the 3 wt%-Cu/MOF-808 (Zr) catalyst are shown in Figure 4, and the energy spectral information of each element is listed in Table 1 in order to investigate the effect of the introduction of Cu nanoparticles on the surface of MOF-808 (Zr) crystals. The characteristic peaks of element C in the catalyst are shown in Figure 4a. The binding energies of the two characteristic peaks are 286.43 eV and 283.26 eV, respectively, and the two characteristic peaks were determined to belong to O–C=O and C=C, respectively [39]. As shown in Figure 4b, the O 1s characteristic peak with an analyzed catalyst binding energy of 529.62 eV is the characteristic peak in the Zr–O bond [40]. As shown in Figure 4c, the two characteristic peaks with binding energies of 184.64 eV and 181.71 eV belong to Zr 3d, corresponding to Zr $3d_{3/2}$ and Zr $3d_{5/2}$, respectively, which are approximately the same as those reported in the literature [41]. As shown in Figure 4d, the XPS spectrum of

the Cu element in the catalyst 3 wt%-Cu/MOF-808(Zr) is shown. The five characteristic peaks of the Cu element with binding energies at 950.26 eV and 925.58 eV, respectively, correspond to the Cu^0 $2p_{1/2}$ orbital and the $2p_{3/2}$ orbital of Cu^0, which are approximately the same as those reported in the literature [42].

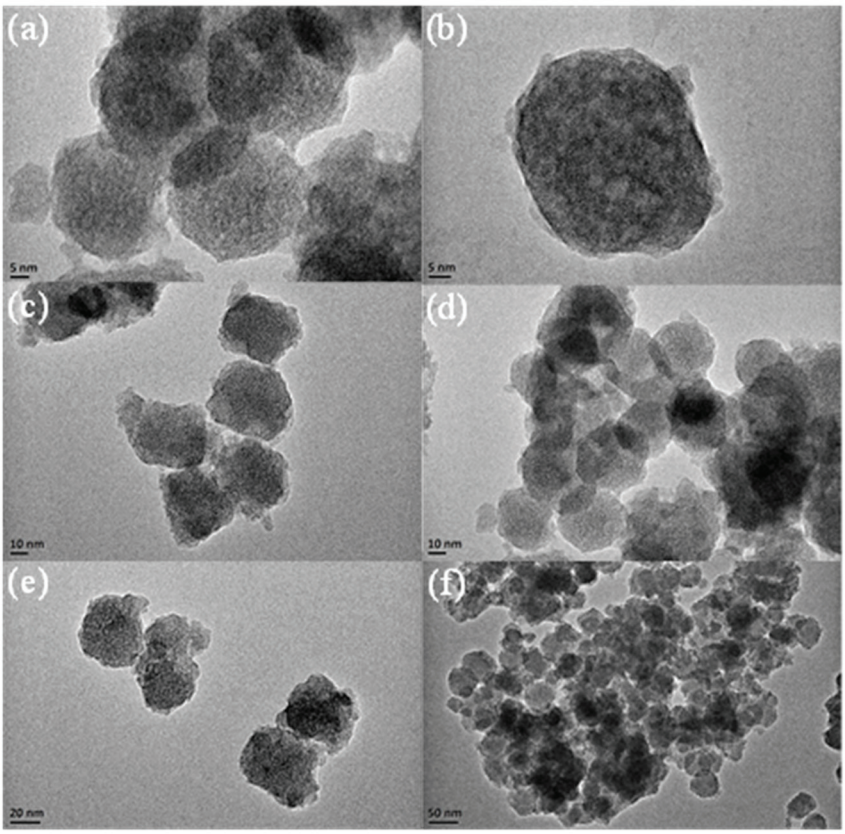

Figure 2. (**a**–**f**) TEM images of 3 wt%-Cu/MOF-808(Zr).

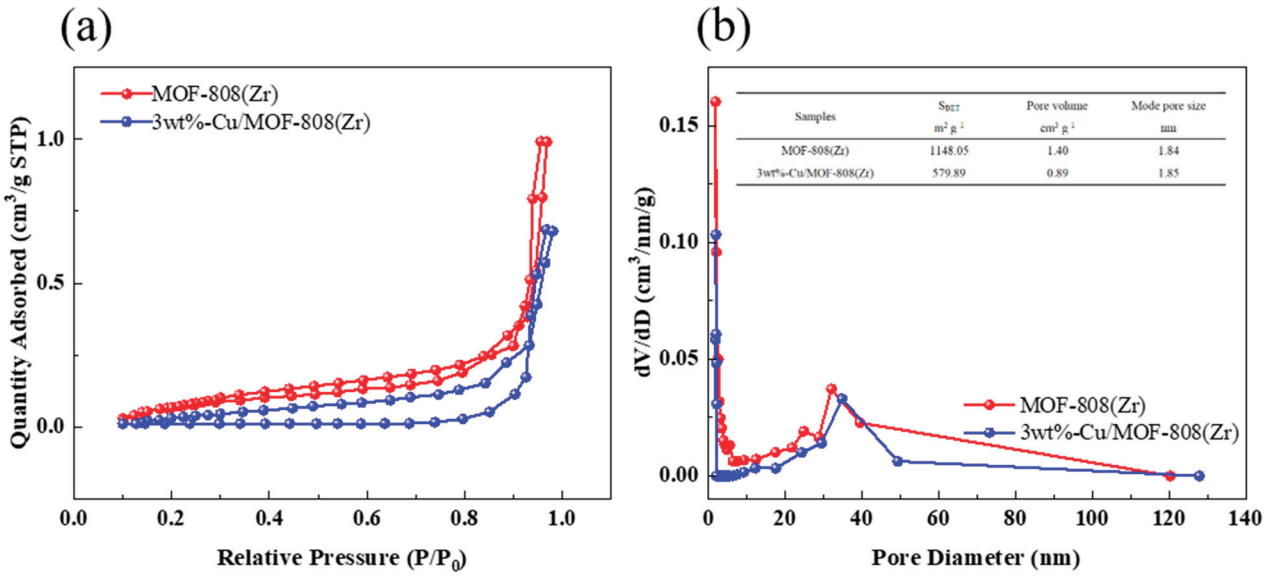

Figure 3. (**a**) N_2 adsorption–desorption isotherms of MOF-808(Zr) and 3 wt%-Cu/MOF-808(Zr); (**b**) corresponding pore size distribution curve crystal. This indicates that the low concentration of Cu nanoparticles was uniformly loaded on the MOF-808(Zr) carrier and BET specific surface area, mode pore size, and pore volume of catalysts MOF-808(Zr) and 3 wt%-Cu/MOF-808(Zr).

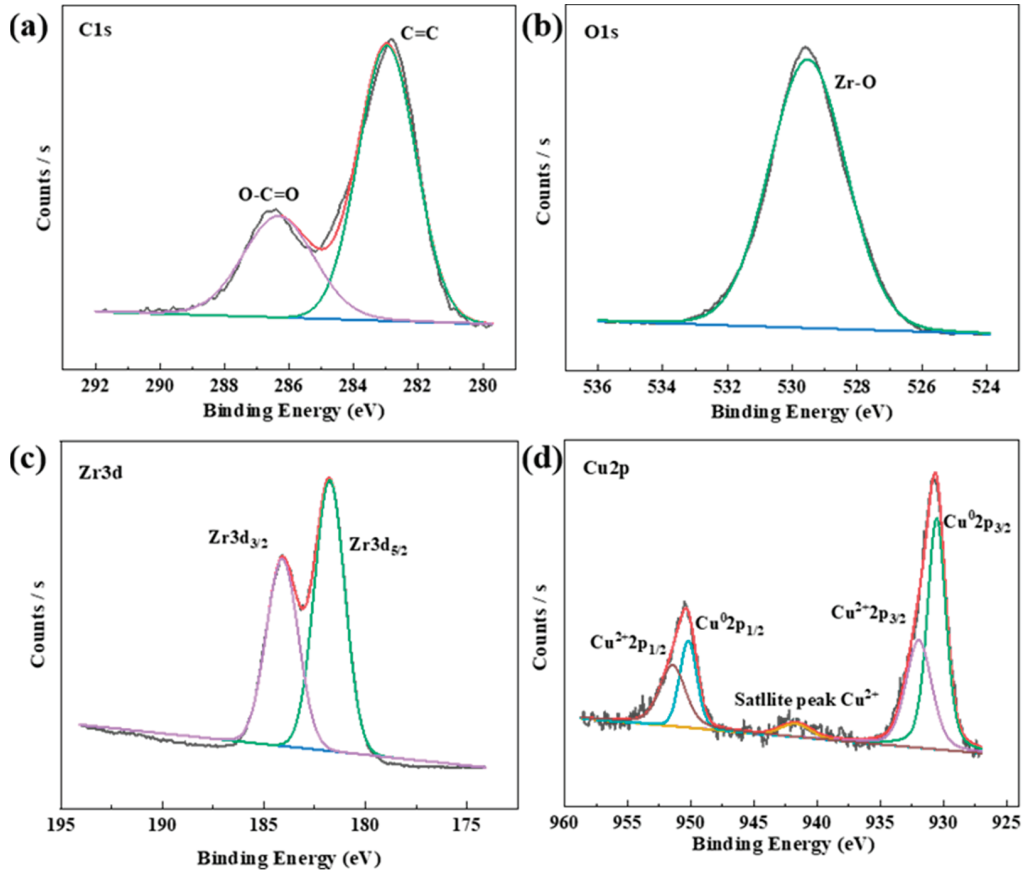

Figure 4. (**a**) C 1s (**b**) O 1s, (**c**) Zr 3d, (**d**) Cu 2p XPS spectra of sample 3 wt%-Cu/MOF-808(Zr).

Table 1. Energy spectrum information of 3 wt%-Cu/MOF-808(Zr) catalyst.

Main Elements	Analysis of XPS Spectra		
	Binding Energy (eV)	FWHM (eV)	Atomic (%)
C 1s	284.82	2.21	50.35
O 1s	529.62	2.62	40.34
Zr 3d	182.27	2.16	8.53
Cu 2p	932.69	2.30	0.77

The FT-IR spectra of the catalyst samples MOF-808(Zr) and Cu/MOF-808(Zr) are shown in Figure 5. The positions of the characteristic peaks of the samples are the same as those reported in the literature. The characteristic peaks of the samples appeared at 1623 nm^{-1}, 1448 nm^{-1}, 1383 nm^{-1}, and 650 nm^{-1}, respectively [32]. The three vibrational absorption peaks at 1623 nm^{-1} and 1448 nm^{-1} are characteristic peaks of the aromatic ring in the compound. At 1623 nm^{-1} is an asymmetric stretching vibrational peak of –COOH attached to the central metal Zr, and at 1383 nm^{-1} is a symmetric stretching peak of –COOH. The presence of the vibrational peak of Zr–O at approximately 650 nm^{-1} indicates a coordination reaction between the carboxyl group in H_3BTC and Zr^{4+}, suggesting that MOF-808(Zr) was successfully prepared and that the structure of the Cu nanoparticles was not destroyed during preparation [43].

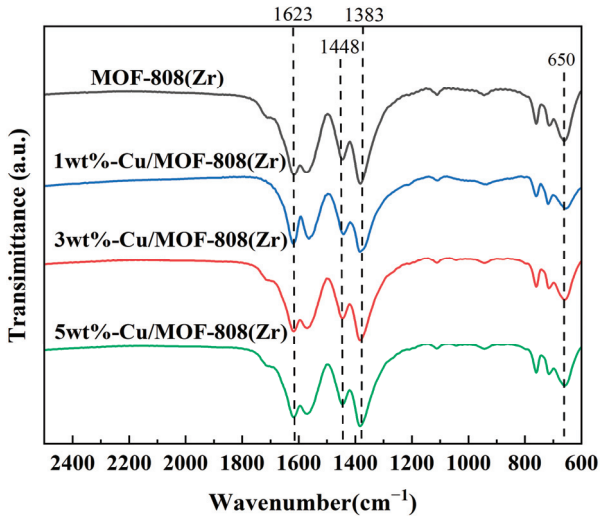

Figure 5. FT-IR spectra of MOF-808(Zr) and Cu/MOF-808(Zr) samples.

Thermogravimetric analysis was used to characterize the mass loss and stability of the prepared catalyst materials with increasing temperature. As can be seen in Figure 6a, the introduction of Cu nanoparticles increases the stability of the catalyst. The mass loss of the MOF-808(Zr) sample alone was 52.5% at 700 °C, while the mass loss of the catalyst sample after the introduction of Cu nanoparticles was 29.1% at 700 °C. The mass loss of the catalyst sample at 200 °C is due to the volatilization of solvents (water, methanol, and DMF) adsorbed in the catalyst pores and on the catalyst surface and the removal of –OH with the coordination with the Zr central atom. At a temperature of 300–500 °C, the mass loss of the catalyst is caused by the removal of –COOH from H_3BTC coordinated with the central atom of Zr, and the H_3BTC is completely burned and the mass drops dramatically. When the temperature is above 500 °C, the skeleton structure of the catalyst collapses ZrO_2 and is left as the only residue [44,45].

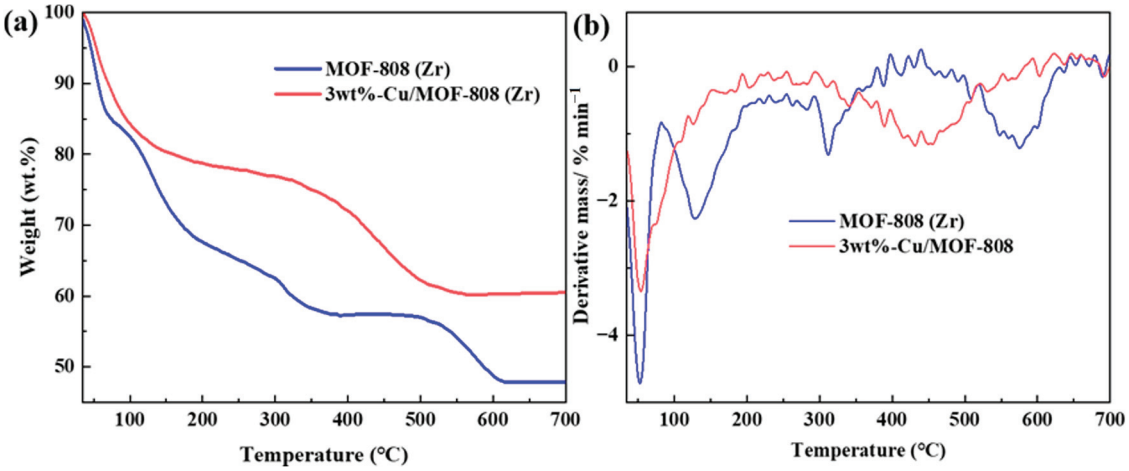

Figure 6. (**a**) TG curves for catalysts MOF-808(Zr) and 3 wt%-Cu/MOF-808(Zr) and (**b**) corresponding DTG curves.

Lewis acid catalysts typically exhibit high catalytic activity for the reduction of aldehyde groups and the oxidation of hydroxyl groups [46]. The acidity of the catalyst surface can be analyzed through infrared spectra of pyridine adsorbed and is shown in Table S1. MOF-808(Zr) has a total acid content of 7.785 mmol g^{-1} and a medium acid content of 0.347 mmol g^{-1}. After the introduction of 3 wt%-Cu nanoparticles, the total acid content was 7.750 mmol g^{-1} and the medium acid content was 0.566 mmol g^{-1}. In our experi-

ments, we observed a trend of decreasing total acidity with increasing Cu loading. The 3 wt%-Cu/MOF-808(Zr) sample had the highest strong acid content and surface acidity. Therefore, the introduction of 3 wt% of Cu enhanced the acidity, which was one of the main factors contributing to the superior performance of the catalyst in the intermolecular hydrogen transfer reaction of HMF.

Weak acid sites in catalysts can promote the transfer of hydrogen atoms while reducing the formation of carbon deposits [47]. The carboxyl groups from H_3BTC ionized in the solvent to release protons from relatively strong conjugate bases, thus belonging to weak Brønsted acids. Moreover, the Cu metal sites in the catalyst not only facilitate the transfer of hydrogen atoms but also, due to their reducibility, can help prevent carbon atoms from depositing on the catalyst surface and forming carbon deposits.

2.2. Optimization of HMF Hydrogenation Reaction Conditions

In this section, we investigate the optimum reaction conditions for the catalytic transfer hydrogenation of HMF at different reaction conditions at an initial N_2 pressure of 0.25 MPa and a speed of 600 rpm. Figure 7 shows the effect of these parameters on the conversion of the reaction substrate and the selectivity of the target product.

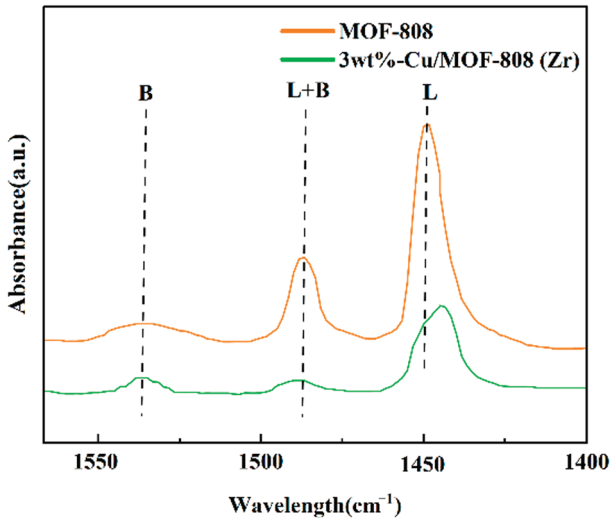

Figure 7. The IR spectra of pyridine adsorbed catalyst. At 1450 cm^{-1} and 1540 cm^{-1} wavelengths in the infrared spectrum, the characteristic peaks of the Lewis and Brønsted acid sites are respectively.

Firstly, we chose Cu/MOF-808(Zr) catalyst to explore the effect of solvent on the reaction process. Common solvents such as methanol, ethanol, isopropanol, formic acid, ethyl acetate, 1, 4-dioxane, DMF, and THF were used as reaction solvents. As shown in Figure 8a, under the condition of formic acid as the hydrogen donor solvent, Cu/MOF-808(Zr) has a low BHMF selectivity and yield in alcoholic solvents, while it has a relatively high HMF conversion and BHMF selectivity and yield in solvents such as 1, 4-dioxane, DMF, and THF. This suggests that when alcohol solvents are used as reaction solvents, the alcohols are not present in the system as hydrogen donor solvents.

In proton solvents such as alcohols, formic acid is more likely to produce H^+ and thus lead to the polymerization of HMF, to the detriment of BHMF production [26]. Therefore, 1, 4-dioxane is a more suitable reaction solvent to achieve high HMF conversion and BHMF selectivity and yield. Figure 8b demonstrates the effect of the addition of the hydrogen donor solvent on the reaction under the conditions of using 1, 4-dioxane as the reaction solvent. The addition of 0, 100, 200, 300, 400, 500, and 600 μL of formic acid was applied during the experiment. At a formic acid addition of 400 μL, BHMF reached a maximum selectivity and yield of 89% and 75.65%, respectively. Therefore, we chose 400 μL of formic acid as the optimum hydrogen donor solvent addition for the subsequent study.

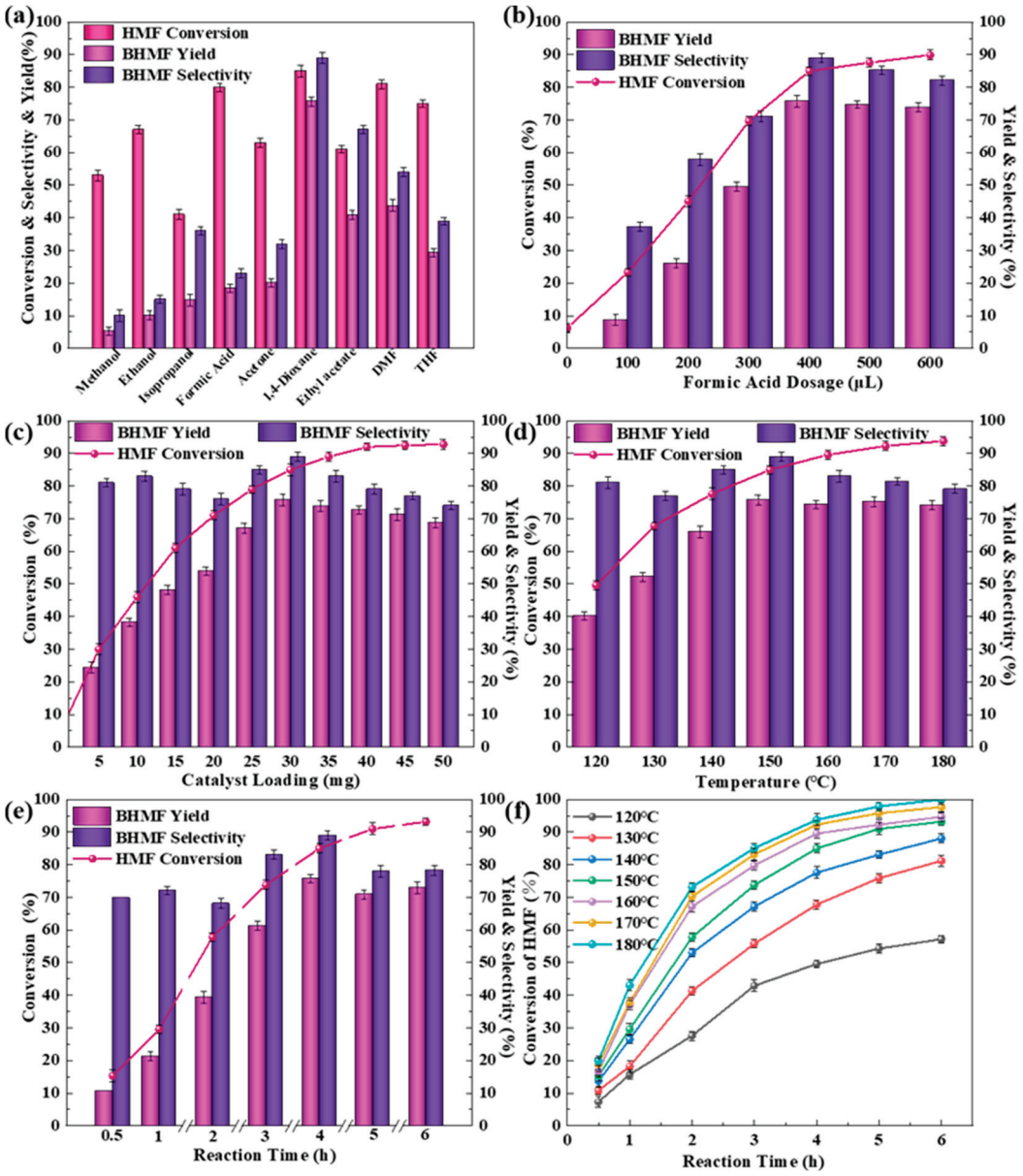

Figure 8. Optimization of reaction conditions for catalytic transfer hydrogenation of HMF to BHMF on Cu/MOF-808. (**a**) Reaction solvent. (**b**) Formic acid dosage. (**c**) Catalyst loading. (**d**) Reaction temperatures. (**e**) Reaction times. (**f**) Reaction temperatures and reaction times.

Figure 8c demonstrates the effect of different catalyst dosing levels on the reaction under the conditions of an optimum reaction solvent of 1, 4-dioxane and an optimum addition of 400 μL of hydrogen supply solvent. The active site and number of catalysts also play a very important role in the catalytic reaction process. The maximum selectivity and yield of BHMF were achieved at a catalyst dosage of 30 mg. As the catalyst dosage continued to increase, the selectivity and yield of BHMF gradually decreased, although the conversion of HMF continued to increase. This may be due to the overuse of catalyst, which leads to side reactions and by-products, or to over-hydrogenation of HMF due to excess catalyst. Therefore, 30 mg was chosen as the optimum catalyst dosage for subsequent investigation.

In addition, the optimum reaction temperature and reaction time were also explored. As shown in Figure 8d–f, the optimum reaction temperature was explored in the temperature range of 120–180 °C. Temperature also had an effect on the reaction. As the

temperature increased, the conversion of HMF increased from 49.6% to 93.8%. The highest selectivity and yield of BHMF was obtained at a reaction temperature of 150 °C and a reaction time of 4 h. This indicates that the temperature has a significant influence on the catalytic reaction as well as the conversion of HMF. The relevant findings of others are listed in Table 2, in addition, Upare et al. [48] used Amberlyst-15 combined with Cu(50)-SiO_2 catalyst to achieve a stepwise conversion of fructose for the preparation of BHMF, with 95% conversion of HMF and 97% yield of BHMF. In this study, formic acid was used as a liquid hydrogen source, which is safer and more economical. Based on the experimental results of the catalytic reactions, the reaction kinetics were further investigated to gain insight into the intrinsic catalytic reactivity of the catalysts.

Table 2. Catalytic system for the preparation of BHMF by catalytic conversion of HMF.

	Catalyst	Hydrogen Source	Reaction Condition	Selectivity (%)	Ref.
1	3 wt% Cu/MOF-808(Zr)	Formic acid	150 °C, 4 h	75.65	This work
2	MOF-808(Zr)	Formic acid	150 °C, 4 h	56.24	This work
3	MOF-808(Zr) (reduced by $NaBH_4$)	Formic acid	150 °C, 4 h	56.31	This work
4	Pt-Sn/Al_2O_3	13 bar H_2	60 °C, 5 h	82.00	[49]
5	Pt/MCM-41	8 bar H_2	35 °C, 2 h	98.90	[50]
6	Ru/CeO_2	H_2	130 °C, 2 h	81.00	[51]
7	Ir/C	60 bar H_2	50 °C, 3 h	69.70	[52]
8	Ni-Fe/CNTs	30 bar H_2	110 °C, 18 h	96.10	[53]
9	Ni/CNTs	30 bar H_2	110 °C, 18 h	76.40	[53]
10	Cu/Zn	H_2	120 °C, 3 h	95.00	[53]
11	Ru/Co_3O_4	Isopropanol	190 °C, 6 h	89.00	[52]
12	Pd/C	Formic acid	Temperature change, 4 h	86.00	[25]

The conversion of HMF over Cu/MOF-808(Zr) at different temperatures (130, 150, and 170 °C) was investigated. The apparent activation energy of a catalytic reaction is calculated by the Arrhenius equation.

As can be seen from Figure S4a, $\ln(C_{A,0}/C_A)$ shows a linear relationship with the reaction time during the conversion of HMF; Figure S4b calculates that the apparent activation energy E_a = 30.112 kJ mol^{-1} for the catalytic transfer hydrogenation reaction of HMF under the reaction conditions of formic acid as the hydrogen donor solvent and Cu/MOF-808(Zr) as the catalyst.

The first-order kinetic fit showed a good linear relationship, on which it was further fitted with the L–H kinetic model. As shown in Figure S4, the R^2 of the data were all greater than 0.95, indicating that the reaction process of HMF over Cu/MOF-808(Zr) catalyst followed the two-center adsorption model and that the rate-determining step of the whole catalytic process was the reaction of adsorbed molecules on the catalyst surface.

2.3. Catalyst Reusability Study

To investigate the stability of the catalyst, the 3 wt%-Cu/MOF-808(Zr) catalyst under optimal reaction conditions (150 °C, 4 h) was selected for stability cycling experiments after centrifugation, washing, drying, and grinding. As shown in Figure 9a, the conversion of HMF and the yield of BHMF over the 3%-Cu/MOF-808 catalyst after five cycles of the reaction is demonstrated. As can be seen from the figure, neither the conversion of HMF

nor the yield of BHMF produced significant changes as the number of times the catalyst was used increased. In addition, the FT-IR spectra of the cycled catalysts were carried out as shown in Figure 9b. The structure of the IR spectrum of the cycled 3 wt%-Cu/MOF-808(Zr) catalyst had the same band structure as the newly prepared 3 wt%-Cu/MOF-808(Zr) catalyst, which indicates that the catalyst has some stability.

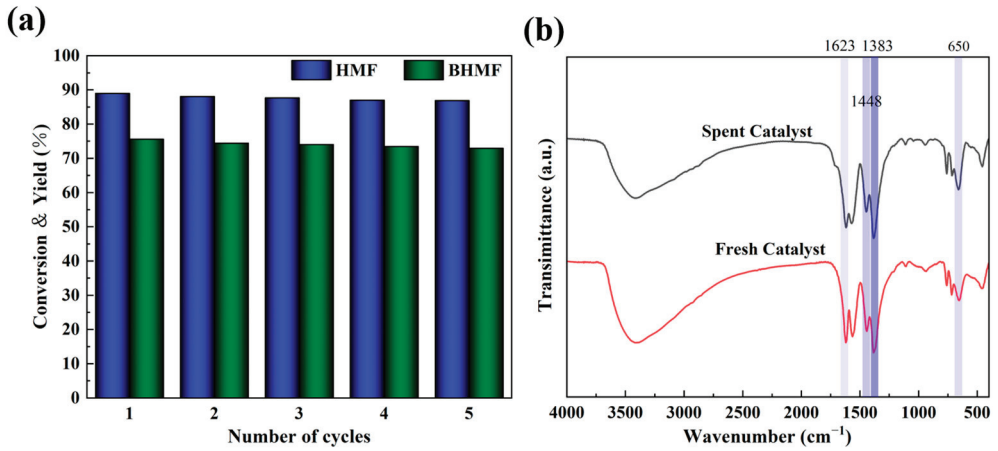

Figure 9. (**a**) Evaluation of the catalytic performance of catalyst in cycling runs and (**b**) FT-IR spectra before and after the reaction.

2.4. Mechanism of CTH of HMF with FA

A possible reaction mechanism for the preparation of BHMF by catalytic transfer hydrogenation of HMF over Cu/MOF-808 catalyst was proposed under the condition of formic acid as the hydrogen supply solvent [54], as shown in Figure 10. Firstly, the reduced metal Cu site adsorbs formic acid molecules to the surface of the catalyst and traps a hydrogen atom in formic acid to form a Cu–H^+ intermediate. Since the $HCOO^-$ species is electron-rich, the oxygen atoms in the $HCOO^-$ group are coordinated with the Lewis-acid-site metal zirconium to form the Zr–$HCOO^-$ species. The Zr–$HCOO^-$ species and HMF form a six-membered ring transition state, and we believe that the reduction step is mainly due to the hydrogen transfer in Cu–H^+ and Zr–$HCOO^-$. Subsequently, the two hydrogen atoms of Cu–H^+ and Zr–$HCOO^-$ intermediate were transferred to the carbonyl group to form the reduction product BHMF, and the Cu/MOF-808(Zr) after the release of CO_2 continued to the next cycle [55].

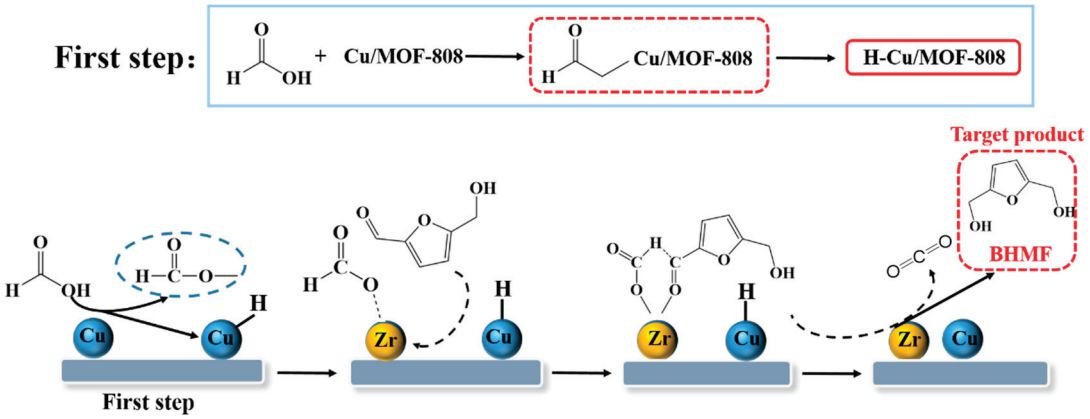

Figure 10. Possible reaction mechanism of catalytic transfer hydrogenation of HMF over Cu/MOF-808 catalyst.

The highest-occupancy molecular orbital (HOMO) of HMF is shown in Figure S5a. It has been observed that HOMO shows obvious localization on the furan ring and aldehyde

group, and the electron density of C1, C3, C4, C6, O2, and O7 atoms is relatively high, which makes these atoms susceptible to the attack of electrophiles, so they are easily adsorbed by Lewis acid and activated for the next hydrogenation reaction. Figure S5b shows that the lowest unoccupied molecular orbital (LUMO) exhibits a prominent localization on the carbonyl oxygen atom, making it susceptible to nucleophiles. This is consistent with our hypothetical reaction mechanism, in which HMF is easily activated by Zr^{4+} adsorption as Lewis acid to form a six-membered ring transition state. In addition, we calculated the local reactivity of the atoms on the HMF by the Fukui function, and obtained the f^-, f^+, and f^0 values for all atoms, showing higher positive potentials around the atoms C1, C6, and O7, indicating that their affinity for nucleophiles increases. The atoms C1, C6, and O7 exhibit higher negative potentials, indicating greater reactivity to electrophiles. Finally, Table S2 provides HMF's Hirshfeld-based electrophilic offensive index (f^-), nucleophilic offensive index (f^+), and in-person-based offensive index (f^0).

3. Chemicals and Methods

3.1. Chemicals

Zirconium chloride ($ZrCl_4$, 99%), 1, 3, 5-benzenetricarboxylic acid (H_3BTC, 99%), dimethyl sulfoxide (DMSO, 99%), 5-hydroxymethyl furfural (HMF, 98%), and 2, 5-furandimethanol (BHMF, 98%) were purchased from Aladdin Industries (Shanghai, China). N, N-dimethylformamide (DMF, AR), formic acid (HCOOH, AR), 1, 4-dioxane (AR), ethyl acetate (AR), methanol (AR), ethanol (AR), iso-propanol (AR), tetrahydrofuran (THF, AR), and $Cu(NO_3)_2 \cdot 9H_2O$ (AR), $NaBH_4$ (AR) were purchased from Sinopharm Chemical Regent (Shanghai, China).

3.2. Preparation of MOF-808(Zr) Catalysts

$ZrCl_4$ (489.4 mg, 2.1 mmol) and H_3BTC (440 mg, 2.1 mmol) were dissolved in 60 mL of a solvent mixture of HCOOH/DMF (*v*:*v* = 1:1), stirred at room temperature until dissolved and then transferred to a hydrothermal kettle with PTFE and heated in an oven at 100 °C for two days; the resulting white solid was extracted and washed three times with DMF, after which it was subjected to solvent exchange. Firstly, the solvent was exchanged in DMF for 3 days, changing 3 times a day; in deionized water for 3 days, changing 3 times a day; and in an-hydrous acetone for 3 days, changing 3 times a day. The white solid was extracted and dried overnight in an oven.

3.3. Preparation of Cu/MOF-808(Zr) Catalysts

We dissolved 0.25 g of MOF-808(Zr) in 100 mL of ethanol, sonicated for 30 min to disperse it well, added a certain amount of $Cu(NO_3)_2 \cdot 9H_2O$ at room temperature and stirred for 12 h, and then placed it in an oven to dry overnight. An aqueous solution of 0.2 M $NaBH_4$ was prepared and the dried sample was added to the solution and stirred for 2 h. The sample was extracted and dried overnight in an oven at 60 °C. The resulting samples were named 1wt%-Cu/MOF-808(Zr), 3 wt%-Cu/MOF-808(Zr), and 5wt%-Cu/MOF-808(Zr). The catalyst preparation procedure is shown in Figure S1.

3.4. Catalyst Activity Testing

The HMF catalytic transfer hydrogenation reaction to prepare BHMF was carried out in a triple parallel autoclave (Yanzheng Instrument Company, Shanghai, China, YZMR-325D). HCOOH was used as the hydrogen supply solvent in the reaction system. First, 30 mg of HMF, 7 mL of reaction solvent and 50 mg of catalyst were added sequentially to the Teflon-lined reactor, purged three times with N_2, and programmed to a set temperature, after which the reaction was stirred at 600 rpm for a specified time before the reactor was cooled to room temperature and separated by centrifugation. The liquid-phase product was filtered through a 0.22 μm organic-phase needle filter (Navigator Lab Instrument Co., Ltd., Tianjin, China) and transferred to the gas-phase feed sample, and the solid catalyst was washed and dried before being recovered for reusability experiments. The reaction

products were subjected to qualitative analysis by gas chromatography (GC) and qualitative analysis by gas chromatography–mass spectrometry (GC–MS).

3.5. Products Analysis

Production of BHMF was confirmed by various methods of qualitative and quantitative analysis, such as GC and GC–MS. The analytical procedure can be founded in the supporting information. Figure S3 shows the GC–MS chromatogram of BHMF prepared by catalytic conversion of HMF.

3.6. Catalyst Recycling

After each reaction, the remaining catalyst was separated and recovered by centrifugation, washed three times with methanol and DMF alternately, and then dried in a vacuum oven until being directly applied to the next experiment.

4. Conclusions

The hydrothermal–impregnation–reduction method was used to prepare Cu/MOF-808 catalysts for the catalytic conversion of HMF to BHMF with high catalytic performance. The best yield and selectivity of BHMF were 75.65% and 89%, respectively, with formic acid as the hydrogen donor and 1, 4-dioxane as the solvent at 150 °C for 4 h. This is more economical than using alcohols as hydrogen donor solvents and presents a possible reaction mechanism for the catalytic conversion of HMF to BHMF, developing a new approach for the catalytic conversion of biomass.

Supplementary Materials: The following supporting information can be downloaded at: https://www.mdpi.com/article/10.3390/catal14120929/s1, Figure S1: Schematic diagram of the synthesis of Cu/MOF-808 (Zr) catalysts; Figure S2: (a–c) SEM images of MOF-808, (d–f) SEM images of 3 wt%-Cu/MOF-808(Zr), and (g) corresponding EDS mapping of 3 wt%-Cu/MOF-808(Zr); Figure S3: GC-MS chromatogram of BHMF prepared by catalytic conversion of HMF; Figure S4: (a) $\ln(C_{A,0}/C_A)$ vs. reaction time plots of HMF hydrogenation over catalyst, (b) Relationship between lnk and 1/T in the conversion of HMF; Figure S5: (a) HOMO and (b) LUMO plots of HMF; Table S1: Acid amounts of MOF-808(Zr) and 3 wt%-Cu/MOF-808(Zr) catalysts; Table S2: calculated Fukui index of HMF.

Author Contributions: J.T.: conceptualization, investigation, data curation, writing—original draft. M.L.: writing—review and editing. L.L.: investigation, validation. L.W.: data curation, formal analysis. H.W.: data curation, methodology. J.B.: methodology, supervision, writing—review and editing. C.L.: writing—review and editing. All authors have read and agreed to the published version of the manuscript.

Funding: This research is funded by ZR2022MB049 and ZR2021MB104.

Data Availability Statement: Data will be made available on request.

Acknowledgments: The authors are grateful for the financial support from the Natural Science Foundation of Shandong Province (ZR2022MB049, ZR2021MB104), the National Natural Science Foundation of China (22078174), and the Key Technology Research and Development Program of Shandong (2017GSF217008).

Conflicts of Interest: The authors declare that they have no known competing financial interests or personal relationships that could have appeared to influence the work reported in this paper.

Abbreviations

HMF	5-hydroxymethylfurfural
FUR	furfural
BHMF	2, 5-furandimethanol
CTH	catalytic transfer hydrogenation
MOFs	metal organic frameworks
FA	formic acid

References

1. Corma, A.; Iborra, S.; Velty, A. Chemical Routes for the Transformation of Biomass into Chemicals. *Chem. Rev.* **2007**, *107*, 2411–2502. [CrossRef] [PubMed]
2. Rosillo-Calle, F. A Review of Biomass Energy–Shortcomings and Concerns. *J. Chem. Technol. Biotechnol.* **2016**, *91*, 1933–1945. [CrossRef]
3. Ruppert, A.M.; Weinberg, K.; Palkovits, R. Hydrogenolysis Goes Bio: From Carbohydrates and Sugar Alcohols to Platform Chemicals. *Angew. Chem. Int. Ed.* **2012**, *51*, 2564–2601. [CrossRef] [PubMed]
4. Sun, Y.; Xiong, C.; Liu, Q.; Zhang, J.; Tang, X.; Zeng, X.; Liu, S.; Lin, L. Catalytic Transfer Hydrogenolysis/Hydrogenation of Biomass-Derived 5-Formyloxymethylfurfural to 2, 5-Dimethylfuran Over Ni–Cu Bimetallic Catalyst with Formic Acid As a Hydrogen Donor. *Ind. Eng. Chem. Res.* **2019**, *58*, 5414–5422. [CrossRef]
5. Ji, Q.; Yu, X.; Yagoub, A.E.-G.A.; Li, M.; Fakayode, O.A.; Yan, D.; Zhou, C.; Chen, L. Ultrasound-Ionic Liquid Pretreatment Enhanced Conversion of the Sugary Food Waste to 5-Hydroxymethylfurfural in Ionic Liquid/Solid Acid Catalyst System. *Catal. Lett.* **2020**, *150*, 1373–1388. [CrossRef]
6. Gupta, D.; Kumar, R.; Pant, K.K. Hydrotalcite Supported Bimetallic (Ni-Cu) Catalyst: A Smart Choice for One-Pot Conversion of Biomass-Derived Platform Chemicals to Hydrogenated Biofuels. *Fuel* **2020**, *277*, 118111. [CrossRef]
7. Chheda, J.N.; Huber, G.W.; Dumesic, J.A. Liquid-Phase Catalytic Processing of Biomass-Derived Oxygenated Hydrocarbons to Fuels and Chemicals. *Angew. Chem. Int. Ed.* **2007**, *46*, 7164–7183. [CrossRef] [PubMed]
8. van Putten, R.-J.; van der Waal, J.C.; de Jong, E.; Rasrendra, C.B.; Heeres, H.J.; de Vries, J.G. Hydroxymethylfurfural, A Versatile Platform Chemical Made from Renewable Resources. *Chem. Rev.* **2013**, *113*, 1499–1597. [CrossRef]
9. Wang, T.; Xie, W.; Pang, Y.; Qiu, W.; Feng, Y.; Li, X.; Wei, J.; Tang, X.; Lin, L. Solvent-Free Hydrogenation of 5-Hydroxymethylfurfural and Furfural to Furanyl Alcohols and Their Self-Condensation Polymers. *ChemSusChem* **2022**, *15*, e202200186. [CrossRef] [PubMed]
10. Wan, Y.; Lee, J.-M. Recent Advances in Reductive Upgrading of 5-Hydroxymethylfurfural via Heterogeneous Thermocatalysis. *ChemSusChem* **2022**, *15*, e202102041. [CrossRef]
11. Hu, L.; Xu, J.; Zhou, S.; He, A.; Tang, X.; Lin, L.; Xu, J.; Zhao, Y. Catalytic Advances in the Production and Application of Biomass-Derived 2, 5-Dihydroxymethylfuran. *ACS Catal.* **2018**, *8*, 2959–2980. [CrossRef]
12. Wang, J.; Zhao, J.; Fu, J.; Miao, C.; Jia, S.; Yan, P.; Huang, J. Highly Selective Hydrogenation of 5-Hydroxymethylfurfural to 2, 5-Bis(Hydroxymethyl)Furan over Metal-Oxide Supported Pt Catalysts: The Role of Basic Sites. *Appl. Catal. Gen.* **2022**, *643*, 118762. [CrossRef]
13. Esen, M.; Akmaz, S.; Koç, S.N.; Gürkaynak, M.A. The Hydrogenation of 5-Hydroxymethylfurfural (HMF) to 2, 5-Dimethylfuran (DMF) with Sol–Gel Ru-Co/SiO_2 Catalyst. *J. Sol-Gel Sci. Technol.* **2019**, *91*, 664–672. [CrossRef]
14. Hu, L.; Tang, X.; Xu, J.; Wu, Z.; Lin, L.; Liu, S. Selective Transformation of 5-Hydroxymethylfurfural into the Liquid Fuel 2, 5-Dimethylfuran over Carbon-Supported Ruthenium. *Ind. Eng. Chem. Res.* **2014**, *53*, 3056–3064. [CrossRef]
15. Jae, J.; Zheng, W.; Lobo, R.F.; Vlachos, D.G. Production of Dimethylfuran from Hydroxymethylfurfural through Catalytic Transfer Hydrogenation with Ruthenium Supported on Carbon. *ChemSusChem* **2013**, *6*, 1158–1162. [CrossRef] [PubMed]
16. Gao, Z.; Li, C.; Fan, G.; Yang, L.; Li, F. Nitrogen-Doped Carbon-Decorated Copper Catalyst for Highly Efficient Transfer Hydrogenolysis of 5-Hydroxymethylfurfural to Convertibly Produce 2, 5-Dimethylfuran or 2, 5-Dimethyltetrahydrofuran. *Appl. Catal. B Environ.* **2018**, *226*, 523–533. [CrossRef]
17. Zeng, Z.; Tang, Q.; Wen, B.; Luo, L.; Liu, X.; Xu, Q.; Zhong, W. Zn-Modified Co/N-C Catalysts for Adjustable Conversion of 5-Hydroxymethylfurfural to Furan-Based Chemicals. *J. Environ. Chem. Eng.* **2024**, *12*, 112190. [CrossRef]
18. He, A.; Hu, L.; Zhang, Y.; Jiang, Y.; Wang, X.; Xu, J.; Wu, Z. High-Efficiency Catalytic Transfer Hydrogenation of Biomass-Based 5-Hydroxymethylfurfural to 2, 5-Bis(Hydroxymethyl)Furan over a Zirconium–Carbon Coordination Catalyst. *ACS Sustain. Chem. Eng.* **2021**, *9*, 15557–15570. [CrossRef]
19. Rao, K.T.V.; Hu, Y.; Yuan, Z.; Zhang, Y.; Xu, C.C. Green Synthesis of Heterogeneous Copper-Alumina Catalyst for Selective Hydrogenation of Pure and Biomass-Derived 5-Hydroxymethylfurfural to 2, 5-Bis(Hydroxymethyl)Furan. *Appl. Catal. Gen.* **2021**, *609*, 117892. [CrossRef]
20. Gelmini, A.; Albonetti, S.; Cavani, F.; Cesari, C.; Lolli, A.; Zanotti, V.; Mazzoni, R. Oxidant Free One-Pot Transformation of Bio-Based 2, 5-Bis-Hydroxymethylfuran into α-6-Hydroxy-6-Methyl-4-Enyl-2H-Pyran-3-One in Water. *Appl. Catal. B Environ.* **2016**, *180*, 38–43. [CrossRef]
21. Tang, X.; Wei, J.; Ding, N.; Sun, Y.; Zeng, X.; Hu, L.; Liu, S.; Lei, T.; Lin, L. Chemoselective Hydrogenation of Biomass Derived 5-Hydroxymethylfurfural to Diols: Key Intermediates for Sustainable Chemicals, Materials and Fuels. *Renew. Sustain. Energy Rev.* **2017**, *77*, 287–296. [CrossRef]
22. Bao, Y.; Pu, W.; Zhang, Y.; Xiao, Y.; Liu, Y. Ni-Co Nano-Alloys Confined by N-Doped Porous Carbon Overlayer to Boost Hydrodeoxygenation of 5-Hydroxymethylfurfural. *J. Environ. Chem. Eng.* **2024**, *12*, 114914. [CrossRef]
23. Palmqvist, E.; Hahn-Hägerdal, B. Fermentation of Lignocellulosic Hydrolysates. II: Inhibitors and Mechanisms of Inhibition. *Bioresour. Technol.* **2000**, *74*, 25–33. [CrossRef]
24. Liao, X.; Cui, H.; Luo, H.; Lv, Y.; Liu, P. Highly Efficient Selective Hydrodeoxygenation of 5-Hydroxymethylfurfural to 2, 5-Dimethylfuran over Co-Ni *in-Situ* Encapsulated in Biochar-Based Carbon Catalysts: The Crucial Role of CoNi Alloys and Co-Nx Species. *Chem. Eng. J.* **2025**, *503*, 158336. [CrossRef]

25. Thananatthanachon, T.; Rauchfuss, T.B. Efficient Production of the Liquid Fuel 2, 5-Dimethylfuran from Fructose Using Formic Acid as a Reagent. *Angew. Chem. Int. Ed.* **2010**, *49*, 6616–6618. [CrossRef] [PubMed]
26. Fu, Z.; Wang, Z.; Lin, W.; Song, W.; Li, S. High Efficient Conversion of Furfural to 2-Methylfuran over Ni-Cu/Al_2O_3 Catalyst with Formic Acid as a Hydrogen Donor. *Appl. Catal. Gen.* **2017**, *547*, 248–255. [CrossRef]
27. Zhao, W.; Wu, W.; Li, H.; Fang, C.; Yang, T.; Wang, Z.; Yang, S. Quantitative Synthesis of 2, 5-Bis(Hydroxymethyl)Furan from Biomass-Derived 5-Hydroxymethylfurfural and Sugars over Reusable Solid Catalysts at Low Temperatures. *Fuel* **2018**, *217*, 365–369. [CrossRef]
28. Li, H.; Fang, Z.; He, J.; Yang, S. Orderly Layered Zr-Benzylphosphonate Nanohybrids for Efficient Acid–Base-Mediated Bifunctional/Cascade Catalysis. *ChemSusChem* **2017**, *10*, 681–686. [CrossRef]
29. Wang, T.; Wei, J.; Liu, H.; Feng, Y.; Tang, X.; Zeng, X.; Sun, Y.; Lei, T.; Lin, L. Synthesis of Renewable Monomer 2, 5-Bishydroxymethylfuran from Highly Concentrated 5-Hydroxymethylfurfural in Deep Eutectic Solvents. *J. Ind. Eng. Chem.* **2020**, *81*, 93–98. [CrossRef]
30. Nie, R.; Tao, Y.; Nie, Y.; Lu, T.; Wang, J.; Zhang, Y.; Lu, X.; Xu, C.C. Recent Advances in Catalytic Transfer Hydrogenation with Formic Acid over Heterogeneous Transition Metal Catalysts. *ACS Catal.* **2021**, *11*, 1071–1095. [CrossRef]
31. Hao, W.; Li, W.; Tang, X.; Zeng, X.; Sun, Y.; Liu, S.; Lin, L. Catalytic Transfer Hydrogenation of Biomass-Derived 5-Hydroxymethyl Furfural to the Building Block 2, 5-Bishydroxymethyl Furan. *Green Chem.* **2016**, *18*, 1080–1088. [CrossRef]
32. Ullah, L.; Zhao, G.; Xu, Z.; He, H.; Usman, M.; Zhang, S. 12-Tungstophosphoric Acid Niched in Zr-Based Metal-Organic Framework: A Stable and Efficient Catalyst for Friedel-Crafts Acylation. *Sci. China Chem.* **2018**, *61*, 402–411. [CrossRef]
33. Zhao, W.; Zhu, X.; Zeng, Z.; Lei, J.; Huang, Z.; Xu, Q.; Liu, X.; Yang, Y. Cu-Co Nanoparticles Supported on Nitrogen-Doped Carbon: An Efficient Catalyst for Hydrogenation of 5-Hydroxymethylfurfural into 2, 5-Bis(Hydroxymethyl)Furan. *Mol. Catal.* **2022**, *524*, 112304. [CrossRef]
34. Bugday, N.; Deng, W.; Zou, G.; Hou, H.; Ji, X.; Yaşar, S. Cu@MOF Based Composite Materials: High Performance Anode Electrodes for Lithium-Ion and Sodium-Ion Batteries. *J. Energy Storage* **2024**, *104*, 114570. [CrossRef]
35. Li, Q.; Zhang, S.-W.; Zhang, Y.; Chen, C. Magnetic Properties in a Partially Oxidized Nanocomposite of Cu-CuCl. *Nanotechnology* **2005**, *17*, 4981. [CrossRef]
36. Feng, L.; Wang, K.-Y.; Day, G.S.; Ryder, M.R.; Zhou, H.-C. Destruction of Metal–Organic Frameworks: Positive and Negative Aspects of Stability and Lability. *Chem. Rev.* **2020**, *120*, 13087–13133. [CrossRef] [PubMed]
37. Fonseca, J.; Gong, T.; Jiao, L.; Jiang, H.-L. Metal–Organic Frameworks (MOFs) beyond Crystallinity: Amorphous MOFs, MOF Liquids and MOF Glasses. *J. Mater. Chem. A* **2021**, *9*, 10562–10611. [CrossRef]
38. Li, Z.-Q.; Yang, J.-C.; Sui, K.-W.; Yin, N. Facile Synthesis of Metal-Organic Framework MOF-808 for Arsenic Removal. *Mater. Lett.* **2015**, *160*, 412–414. [CrossRef]
39. Zhang, W.; Bu, A.; Ji, Q.; Min, L.; Zhao, S.; Wang, Y.; Chen, J. pK_a-Directed Incorporation of Phosphonates into MOF-808 via Ligand Exchange: Stability and Adsorption Properties for Uranium. *ACS Appl. Mater. Interfaces* **2019**, *11*, 33931–33940. [CrossRef] [PubMed]
40. Cure, J.; Mattson, E.; Cocq, K.; Assi, H.; Jensen, S.; Tan, K.; Catalano, M.; Yuan, S.; Wang, H.; Feng, L.; et al. High Stability of Ultra-Small and Isolated Gold Nanoparticles in Metal–Organic Framework Materials. *J. Mater. Chem. A* **2019**, *7*, 17536–17546. [CrossRef]
41. Ardila-Suárez, C.; Rodríguez-Pereira, J.; Baldovino-Medrano, V.G.; Ramírez-Caballero, G.E. An Analysis of the Effect of Zirconium Precursors of MOF-808 on Its Thermal Stability, and Structural and Surface Properties. *CrystEngComm* **2019**, *21*, 1407–1415. [CrossRef]
42. Huang, L.; Peng, F.; Ohuchi, F.S. "In Situ" XPS Study of Band Structures at Cu_2O/TiO_2Heterojunctions Interface. *Surf. Sci.* **2009**, *603*, 2825–2834. [CrossRef]
43. Chen, S.; Xiao, S.; Liu, J.; Li, Z. Synthesis and Hydrogen Storage Properties of Zirconium Metal-Organic Frameworks UiO-66(H_2ADC) with 9,10-Anthracenedicarboxylic Acid as Ligand. *J. Porous Mater.* **2018**, *25*, 1783–1788. [CrossRef]
44. Xuan, K.; Pu, Y.; Li, F.; Luo, J.; Xiao, F. Metal-Organic Frameworks MOF-808-X as Highly Efficient Catalysts for Direct Synthesis of Dimethyl Carbonate from CO_2 and Methanol. *Chin. J. Catal.* **2019**, *40*, 553–566. [CrossRef]
45. Khosroshahi, N.; Goudarzi, M.D.; Safarifard, V. Fabrication of a Novel Heteroepitaxial Structure from an MOF-on-MOF Architecture as a Photocatalyst for Highly Efficient Cr(VI) Reduction. *New J. Chem.* **2022**, *46*, 3106–3115. [CrossRef]
46. Liu, S.; Wang, J.; Wang, Y. Cu–Ce Bimetallic Oxide Catalyst Regulates the Intermolecular Hydrogen Transfer Reaction of 5-Hydroxymethylfurfural. *Ind. Eng. Chem. Res.* **2024**, *63*, 13514–13524. [CrossRef]
47. Su, J.; Ge, F.; Zhang, Y.; Zhou, M.; Zhao, X. Lignin-MOF Hybrid Polymetallic Composites for Selective Hydrogenolysis of Cellulose Derived 5-Hydroxymethylfurfural. *J. Anal. Appl. Pyrolysis* **2024**, *182*, 106706. [CrossRef]
48. Upare, P.P.; Hwang, Y.K.; Hwang, D.W. An Integrated Process for the Production of 2, 5-Dihydroxymethylfuran and Its Polymer from Fructose. *Green Chem.* **2018**, *20*, 879–885. [CrossRef]
49. Balakrishnan, M.; Sacia, E.R.; Bell, A.T. Etherification and Reductive Etherification of 5-(Hydroxymethyl)Furfural: 5-(Alkoxymethyl)Furfurals and 2, 5-Bis(Alkoxymethyl)Furans as Potential Bio-Diesel Candidates. *Green Chem.* **2012**, *14*, 1626–1634. [CrossRef]
50. Chatterjee, M.; Ishizaka, T.; Kawanami, H. Selective Hydrogenation of 5-Hydroxymethylfurfural to 2, 5-Bis-(Hydroxymethyl)Furan Using Pt/MCM-41 in an Aqueous Medium: A Simple Approach. *Green Chem.* **2014**, *16*, 4734–4739. [CrossRef]

51. Aellig, C.; Jenny, F.; Scholz, D.; Wolf, P.; Giovinazzo, I.; Kollhoff, F.; Hermans, I. Combined 1,4-Butanediol Lactonization and Transfer Hydrogenation/Hydrogenolysis of Furfural-Derivatives under Continuous Flow Conditions. *Catal. Sci. Technol.* **2014**, *4*, 2326–2331. [CrossRef]
52. Cai, H.; Li, C.; Wang, A.; Zhang, T. Biomass into Chemicals: One-Pot Production of Furan-Based Diols from Carbohydrates via Tandem Reactions. *Catal. Today* **2014**, *234*, 59–65. [CrossRef]
53. Bottari, G.; Kumalaputri, A.J.; Krawczyk, K.K.; Feringa, B.L.; Heeres, H.J.; Barta, K. Copper–Zinc Alloy Nanopowder: A Robust Precious-Metal-Free Catalyst for the Conversion of 5-Hydroxymethylfurfural. *ChemSusChem* **2015**, *8*, 1323–1327. [CrossRef]
54. Li, X.; Zhang, J.; Huang, C.; Chen, B.; Li, J.; Lei, Z. Stability, Deactivation, and Regeneration of Chloroaluminate Ionic Liquid as Catalyst for Industrial C4 Alkylation. *Catalysts* **2018**, *8*, 7. [CrossRef]
55. Xu, L.; Nie, R.; Chen, X.; Li, Y.; Jiang, Y.; Lu, X. Formic Acid Enabled Selectivity Boosting in Transfer Hydrogenation of 5-Hydroxymethylfurfural to 2, 5-Furandimethanol on Highly Dispersed Co–N_x Sites. *Catal. Sci. Technol.* **2021**, *11*, 1451–1457. [CrossRef]

catalysts

MDPI

Article

Synthesis of High-Quality TS-1 Zeolites Using Precursors of Diol-Based Polymer and Tetrapropylammonium Bromide for 1-Hexene Epoxidation

Yuting Sun, Xinyu Chang, Junling Zhan, Chongyao Bi, Zhehan Dong, Shuaishuai Sun and Mingjun Jia *

Key Laboratory of Surface and Interface Chemistry of Jilin Province, College of Chemistry, Jilin University, Changchun 130012, China; syt15354685582@163.com (Y.S.); cxy21@mails.jlu.edu.cn (X.C.); zhanjl_96@163.com (J.Z.); bicy22@mails.jlu.edu.cn (C.B.); dongzhehan2021@163.com (Z.D.); sunshuaishuai1997@163.com (S.S.)

* Correspondence: jiamj@jlu.edu.cn; Tel.: +86-431-85168420

Abstract: To synthesize high-quality TS-1 zeolites with enhanced catalytic performance for 1-hexene epoxidation is highly attractive for meeting the increased need for sustainable chemistry. Herein, we report that a series of framework Ti-enriched TS-1 zeolites with high crystallinity can be effectively synthesized by the hydrothermal crystallization of a composite precursor composed of diol-based polymer (containing titanium and silicon) and tetrapropylammonium bromide (TPABr). The pre-addition of a certain amount of TPABr into the polymer-based precursor plays a very positive role in maintaining the high crystallinity and framework Ti incorporation rate of TS-1 zeolites under the premise that a relatively low concentration of tetrapropylammonium hydroxide (TPAOH) template is adopted in the following hydrothermal crystallization process. The condition-optimized TS-1 zeolite with a smaller particle size (300–500 nm) shows excellent catalytic activity, selectivity, and recyclability for the epoxidation of 1-hexene with H_2O_2 as an oxidant, which can achieve a 75.4% conversion of 1-hexene and a 99% selectivity of epoxide at a reaction temperature of 60 °C, which is much better than the TS-1 zeolites reported in the previous literature. The relatively small particle size of the resultant TS-1 crystals may enhance the accessibility of the catalytically active framework Ti species to reagents, and the absence of non-framework Ti species, like anatase TiO_2, and low polymerized six-coordinated Ti species could effectively inhibit the ineffective decomposition of H_2O_2 and the occurrence of side reactions, leading to an improvement in the catalytic efficiency for the epoxidation of 1-hexente with H_2O_2.

Keywords: TS-1 zeolite; polymer precursor; hydrothermal crystallization; framework titanium; olefin epoxidation

1. Introduction

As a unique class of heteroatom-substituted zeolite, titanium silicalite-1 (TS-1) with an MFI topology has been widely used as active heterogeneous catalyst for several industrially important catalytic oxidation processes [1], including the hydroxylation of phenol [2,3], the ammoximation of cyclohexanone [4,5], the epoxidation of propene, and oxidative desulfurization [6–14]. It is well known that the catalytic performance of zeolite TS-1 could be modulated by adjusting the Si/Ti ratio [15], the coordination state of the Ti species, and the morphology, crystal size, and porosity of the zeolites [16–20]. The isolated tetra-coordinated framework Ti species (TiO_4) is generally considered as the main active site for various H_2O_2-mediated oxidation reactions [9,19,20], while other types of Ti species, such as isolated hexacoordinated Ti species (TiO_6) and dinuclear Ti species are also recognized as highly active centers for catalyzing selective oxidation reactions like the epoxidation of propene [21,22]. To achieve high catalytic oxidation efficiency, the non-framework Ti species like oligomeric six-coordinated Ti species and the anatase phase should be avoided

as far as possible, since they may result in the ineffective decomposition of the oxidant H_2O_2 thus decreasing the utilization rate of H_2O_2.

So far, different approaches have been adopted to synthesize framework Ti-enriched TS-1 zeolites, including optimizing the crystallization method and conditions (e.g., addition of alkali metal ions, dynamic crystallization), introducing complexing agents and zeolite growth modifiers, or changing the types of titanium and silicon sources [23]. The main concern is focused on how to match the hydrolysis rate of titanium and silicon sources and to inhibit the generation of non-framework Ti species during synthesis [24–27]. As a result, a number of anatase-free TS-1 zeolites with enhanced catalytic efficiency for various selective oxidation reactions have been synthesized successfully. For instance, Wang et al. reported that an anatase-free hierarchical TS-1 single crystal with high oxidative desulfurization property could be obtained by using Ti-NKM-5 (hierarchical Ti-containing silica) as a precursor through a steam-assisted strategy [28]. Zhang et al. reported that anatase-free TS-1 zeolite could be synthesized by a special combination of solid-phase and liquid-phase conversion mechanisms in the presence of 1,3,5-benzenetricarboxylic acid. The as-synthesized TS-1 zeolite demonstrated an enhanced catalytic performance in the epoxidation of 1-hexene [29]. Yu and coauthors reported that nanosized hierarchical TS-1 without non-framework titanium species could be synthesized by using polyethylene glycol tert-octylphenyl ether (Triton X-100) as an assisted template under rotational crystallization conditions [30]. The resulting TS-1 zeolite showed relatively high catalytic activity for the epoxidation of 1-hexene with hydrogen peroxide (H_2O_2) as an oxidant, with a conversion of up to 52.6% and selectivity above 97%.

Despite these progresses, the catalytic properties of these anatase-free TS-1 zeolites are still inadequate for the epoxidation of terminal olefins like 1-hexene, and relatively low 1-hexene conversion (usually lower 50%) would commonly be obtained under the test conditions, which are primarily due to the diffusion limitation of the microporous channels of the MFI-type zeolites and/or the poisoning of the active sites by the strong adsorption of epoxide products. Although a few recent examples have shown that the catalytic activity of TS-1 zeolites for 1-hexene epoxidation may be enhanced by constructing mesopores and/or decreasing the crystalline size to nanoscale, an obvious decrease in the epoxide selectivity is usually observed, which might be related to the presence of some defective sites (e.g., acidic Ti-OH in [TiO_6] species) in the hierarchical or the nanosized TS-1 zeolites. Therefore, it is still an attractive subject to develop high-quality TS-1 zeolites with improved catalytic performance for application in the epoxidation of terminal olefins.

Recently, Liu and colleagues reported that TS-1 zeolites without non-framework titanium species could be synthesized from a diol-based polymer precursor containing titanium and silicon (Ti-diol-Si polymer) in the presence of a TPAOH template [31]. The usage of the Ti-diol-Si polymer precursor facilitates the insertion of Ti into the silica framework during hydrothermal crystallization, leading to the formation of high-quality TS-1 zeolites. Under the test conditions, a relatively high 1-hexene conversion (45.6%) and epoxide selectivity (97.7%) could be achieved after a 2 h reaction. In addition, a variety of alky diols such as ethylene glycol, 1,4-butanediaol, and 1,3-propanediol could also be used for preparing the network-like diol-based polymers, demonstrating the great potential of this polymer precursor synthesis strategy in producing high-quality TS-1 zeolites.

To further optimize the synthesis method of the above polymer precursor route, as well as reduce the usage amount of the expensive template of TPAOH, we tried to introduce a portion of low-cost TPABr template into the Ti-diol-Si polymer and then use the resultant hybrid composites as precursors for the hydrothermal synthesis of TS-1 zeolites in the presence of a lower concentration of TPAOH template. By adjusting the addition amount of TPABr in the polymer-based composite, framework Ti-enriched TS-1 zeolite with relatively small particle size and high crystallinity could be synthesized within a short crystallization time, and the resultant sample showed enhanced catalytic efficiency for the epoxidation of 1-hexence with H_2O_2 as the oxidant.

2. Results and Discussion

A series of TS-1 zeolites (TS-1_xB) were synthesized by the hydrothermal crystallization of composite precursors containing diol-based polymer (Ti-diol-Si) and TPABr, which were obtained through the transesterification of the alkoxy groups of ethyl orthosilicate and butyl titanate with 1,4-butanediol in presence of a certain amount of TPABr. As shown in Figure S1, the powder XRD patterns of all the TS-1 samples present the characteristic diffraction peaks at 2θ of 7.8°, 8.8°, 23.0°, 23.9°, and 24.4° for the corresponding MFI structure [1,32], confirming the phase purity of these TS-1 zeolites [33]. Compared with the conventional sample of TS-1_con, the samples of TS-1_xB derived from the Ti-BDO-Si/TPABr composites exhibit a higher diffraction peak intensity, indicating higher crystallinity. Among them, TS-1_0.10B shows the highest relative crystallinity (Table S1), suggesting that the addition of a suitable amount of TPABr into the polymer precursor is beneficial for the growth of TS-1 crystals.

The FT-IR spectra of various TS-1 samples exhibit several strong bands at 450 cm^{-1}, 550 cm^{-1}, 800 cm^{-1}, 1100 cm^{-1}, and 1225 cm^{-1} (Figure S2). The band at 550 cm^{-1} could be ascribed to the vibration of the double five-membered rings of the zeolite framework [34,35], while the band at 800 cm^{-1} is a typical band of the MFI topologies [36]. The weak signal at 960 cm^{-1} is attributed to the stretching vibration of the Si-O-Ti bond or the adjacent Si–O bond disturbed by the presence of Ti atoms in the framework [37–39].

Figure 1 presents the corresponding SEM images of various TS-1 zeolites. It can be seen that all the samples exhibit similar elliptical morphology with different crystal particle sizes. Among them, the particle size of the conventional sample TS-1_con is the smallest, with an average particle size of around 200 nm (Figure 1e), suggesting that introducing a higher concentration of TPAOH is beneficial for the formation of nanosized TS-1 zeolite crystals under the conventional hydrothermal crystallization condition. The two samples of TS-1_0B and TS-1_ref, which are synthesized from the polymer precursor of Ti-BDO-Si (without the pre-addition of TPABr into the precursor), have larger crystal size of 700–900 nm (Figure 1a,f). As for the three TS-1_xB samples synthesized from the composite precursors of Ti-BDO-Si/TPABr, relatively small crystal sizes in the range of 300–500 nm (for TS-1_0.10B) or 200–300 nm (for TS-1_0.15B) could be detected (Figure 1b–d), lower than those of TS-1_0B and TS-1_ref. These results demonstrate that the introduction of a small amount of TPABr into the polymer precursor may play a positive role in accelerating the nucleation/growth of the TS-1 zeolites to a certain extent, finally leading to the formation of smaller zeolite particles with high crystallinity.

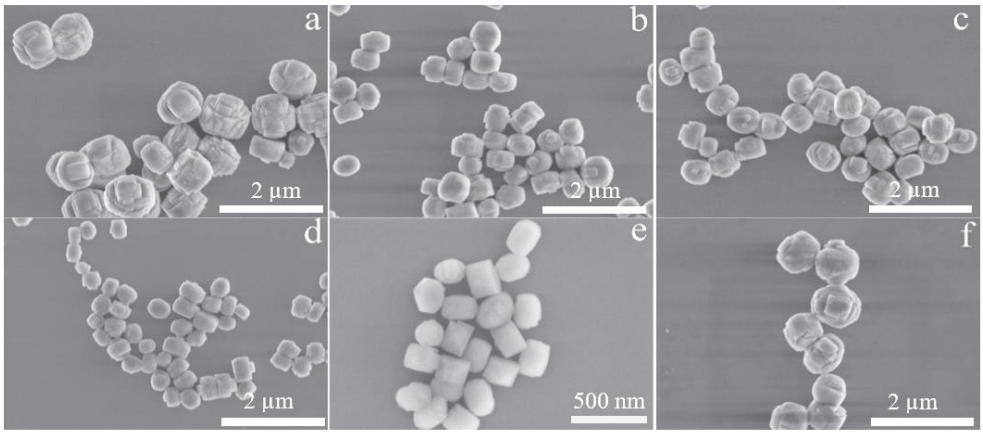

Figure 1. SEM images of (**a**) TS-1_0B, (**b**) TS-1_0.05B, (**c**) TS-1_0.10B, (**d**) TS-1_0.15B (**e**) TS-1_con, (**f**) TS-1_ref.

Figure 2 shows the N_2 adsorption−desorption isotherms of various TS-1 zeolites. All the samples have a significant increase in nitrogen adsorption capacity in the low relative pressure range ($P/P_0 < 0.1$), showing type-I sorption features which are characteristic of microporous

materials. The appearance of a weak absorption in the P/P_0 range of 0.9 to 1.0 usually indicates the presence of secondary particle-piled pores in these samples. As shown in Tables 1 and S2, the polymer precursor-derived TS-1 zeolites (TS-1_xB and TS-1_ref) exhibit higher micropore volume (V_{micro}) and micropore-specific surface area (S_{micro}) than the conventional TS-1_con sample. Among them, TS-1_0.10B possesses the highest S_{micro} of 376 m^2/g and V_{micro} of 0.20 cm^3/g. The elemental analysis results determined by ICP-OES show that the Si/Ti ratio of TS-1_0.10B is 48.5, which is the lowest among the tested samples. These results suggest that the addition of a certain amount of TPABr into the polymer precursor is favorable for the construction of TS-1 zeolites with abundant micropores and high incorporation rate of Ti species during the subsequent hydrothermal crystallization process.

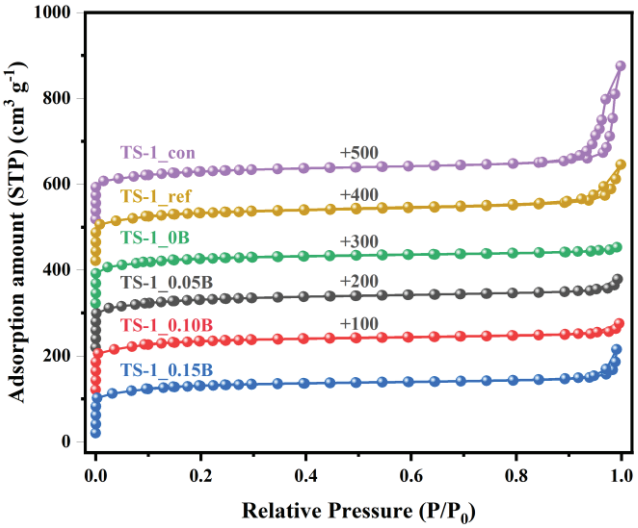

Figure 2. N_2 adsorption−desorption isotherms of various TS-1 samples.

Table 1. Textural properties of various TS-1 samples.

Sample	Si/Ti [a]	S_{BET} [b] ($m^2 \cdot g^{-1}$)	S_{mic} [c] ($m^2 \cdot g^{-1}$)	S_{ext} [c] ($m^2 \cdot g^{-1}$)	V_{micro} [c] ($cm^3 \cdot g^{-1}$)	V_{meso} [d] ($cm^3 \cdot g^{-1}$)
TS-1_con	57.7	409	185	225	0.10	0.43
TS-1_0B	54.6	395	358	36	0.18	0.06
TS-1_0.05B	61.6	413	370	42	0.19	0.08
TS-1_0.10B	48.5	420	376	36	0.20	0.06
TS-1_0.15B	51.6	409	367	34	0.19	0.04
TS-1_ref	50.5	418	360	50	0.19	0.16

[a] Measured by ICP; [b] S_{BET} calculated by BET method; [c] S_{mic}, S_{ext} and V_{micro} calculated by t-plot method. [d] V_{meso} calculated by BJH method.

The UV−Vis DRS measurements were carried out to investigate the coordination states of the Ti species in various TS-1 zeolites. As shown in Figure 3, all the samples show a strong absorption band in the region of 210–220 nm, indicating the existence of tetrahedral framework Ti species (TiO_4) [40]. This kind of TiO_4 species has been recognized as the catalytically active center for various selective oxidation reactions [41,42]. The broad band centered at around 330 nm, which is attributed to the characteristic absorption of anatase TiO_2, could only be detected in the conventional TS-1_con, indicating the presence of a certain amount of anatase TiO_2 in this sample. For the samples obtained from the polymer precursor, no obvious signal appeared in this region, suggesting that the formation of anatase TiO_2 could be effectively inhibited by adopting the modified synthesis method based on the polymer precursor route. Notably, no significant signal centered at 270 nm could be observed in the spectra of all the TS-1 samples, including the conventional one, implying that the concentration of the octahedrally coordinated Ti (VI) species should be very low or even negligible [43].

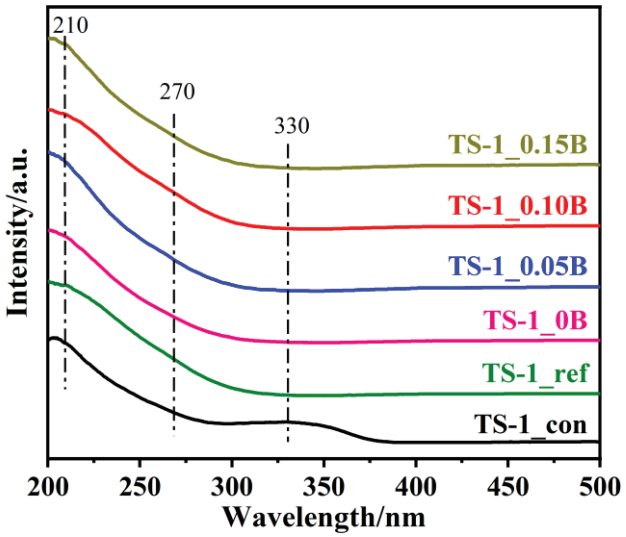

Figure 3. UV−Vis DRS spectra of various TS-1 zeolite samples.

UV resonance Raman spectroscopy with an excitation wavelength of 325 nm was used for the further characterization of the states of the Ti species in various TS-1 zeolites. The strong bands at 960 and 1125 cm^{-1} could be assigned to the characteristic signals of the framework Ti-O-Si species and the tetrahedral-coordinated Ti site in TS-1 zeolites, respectively. The two bands at 380 and 800 cm^{-1} are related to the siliceous zeolites with an MFI topology [44]. The Raman bands at 515 and 637 cm^{-1} could be correlated with the formation of anatase TiO_2 [21,45]. As shown in Figure 4, the tetrahedral framework Ti species is dominant in all the TS-1 samples. The appearance of weak signals at 515 and 637 cm^{-1} in the spectrum of the conventional TS-1_con sample confirms the presence of anatase TiO_2, as already revealed by the UV−Vis DRS spectra. In this region, no obvious anatase TiO_2 signals could be detected in the spectra of the TS-1 zeolites synthesized from Ti-BDO-Si polymer composites, which further illustrates the fact that the formation of extra-framework titanium species can be considerably inhibited by using the polymer composite precursor strategy.

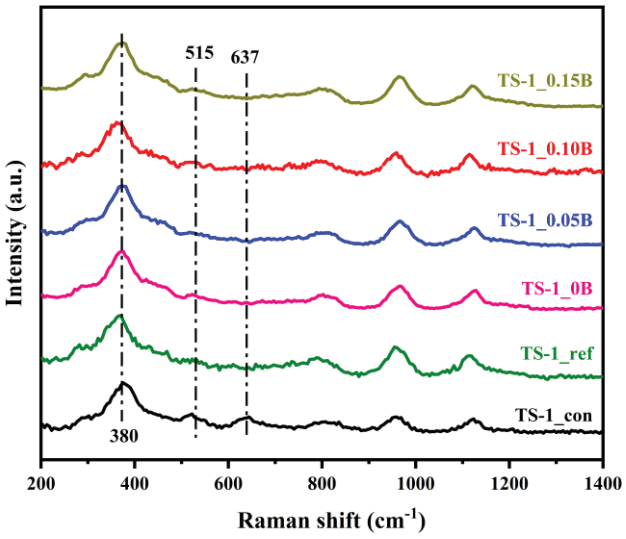

Figure 4. UV resonance Raman spectra excited at 325 nm.

Figure 5 shows the XPS spectra of various TS-1 zeolite samples. The symbolic peaks at 460 eV and 465 eV are attributed to the binding energies of Ti $2p_{3/2}$ and Ti $2p_{1/2}$, representing the tetrahedral-coordinated framework Ti species [46,47]. The peak at 458 eV

is assigned to the extra-framework Ti like anatase TiO_2 [48]. Deconvolution of the XPS spectra reveals that quite a number of anatase TiO_2 are present in the sample of TS-1_con. As for the TS-1_0.10B zeolite, the signal intensity related to anatase TiO_2 is nearly negligible, further confirming the high incorporation efficiency of Ti into the zeolitic framework through the polymer/TPABr composite precursor strategy.

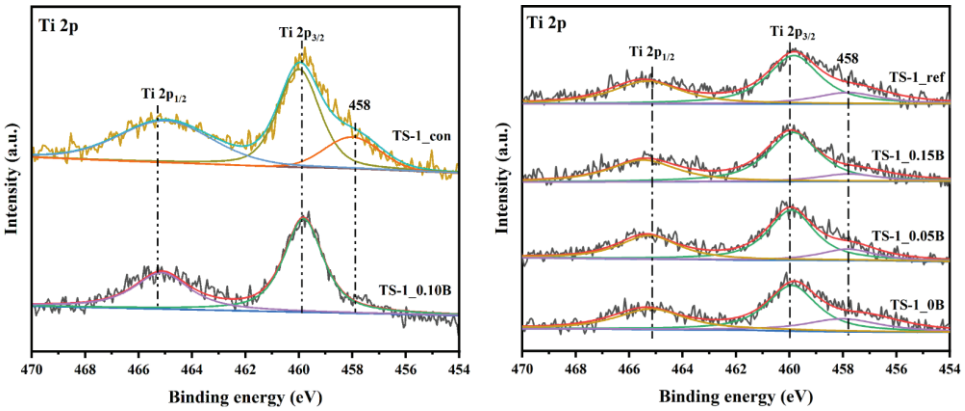

Figure 5. XPS spectra of Ti 2p spectra in TS-1 samples.

According to the above experimental results, it can be concluded here that the framework Ti-enriched TS-1 crystals could be efficiently synthesized by using Ti-BDO-Si/TPABr composites as precursors. The effective inhibition of extra-framework Ti could mainly be interpreted by the adopted strategy using Ti-diol-Si polymers as precursors. As proposed by Liu and colleagues, the Ti source and the Si source in the polymers are uniformly connected by BDO, easily leading to a good match in the hydrolysis rate between the Si source and the Ti source during the hydrothermal crystallization process [31]. Apparently, the addition of a certain amount of TPABr in the polymer precursor seems to increase the positive effect on the effective incorporation of Ti into the zeolitic framework and the generation of high-quality TS-1 zeolites with a smaller particle size.

3. Discussion of the Formation Process of the TS-1 Zeolites

To track the crystallization processes of the TS-1_0.10B sample, the solid products obtained at different crystallization stages (2–12 h) were collected and characterized by XRD, SEM, UV−Vis, and UV Raman measurements. The sample extracted at the early crystallization stage (2 h) exhibits amorphous features (Figure 6). After crystallization for 3 h, the diffraction peaks associated with the MFI structure begin to appear, and a large number of TS-1 zeolite crystals with a rough surface can be observed in the SEM images (Figure 7a–f), accompanied by the disappearance of the amorphous matrix (Figure 7b). After prolonging the crystallization time to 6 h, the XRD peaks become intensified, and the crystal size of the resultant TS-1 zeolites somewhat increases. After further extending the crystallization time, the relative crystallinity and morphology of the obtained TS-1 zeolites remain almost unchanged (Table S3). In addition, the UV−Vis DRS and UV resonance Raman spectra show that the coordination states of the Ti species remain consistent throughout the crystallization stages of 3 to 8 h, with the tetracoordinated titanium as the dominant species (Figures S3 and S4). These results clearly show that the amorphous particles formed at the initial stage could be rapidly transformed to the MFI phase during the hydrothermal synthesis process, and the crystallization of the TS-1 zeolites was basically completed within 6 h, much faster than that of the samples obtained by the conventional way.

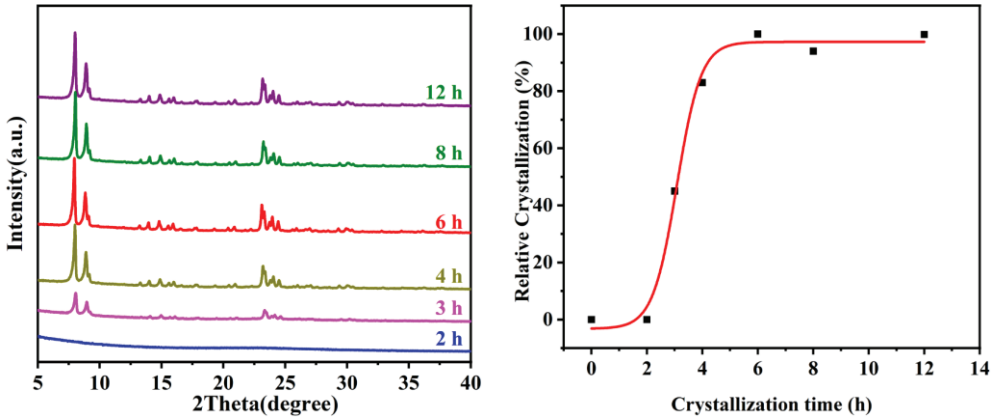

Figure 6. The evolution of XRD patterns of TS-1_0.10B as a function of crystallization time and the corresponding crystallization curve.

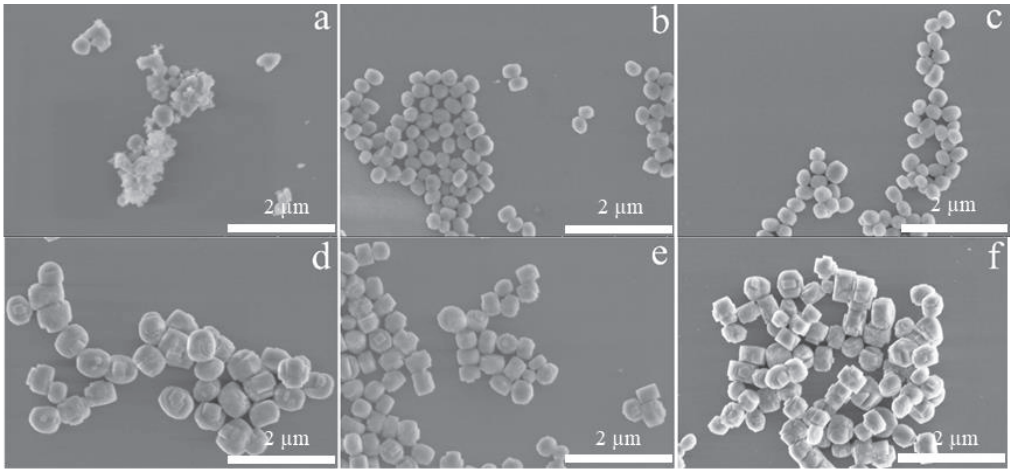

Figure 7. SEM images of TS-1_0.10B sample at different crystallization stages of (**a**) 2 h, (**b**) 3 h, (**c**) 4 h, (**d**) 6 h, (**e**) 8 h, and (**f**) 12 h.

It should be pointed out that, in general, the alkalinity of the synthesis system has an important effect on the crystal size of the final TS-1 product. Higher alkalinity usually favors the rapid hydrolysis and condensation of Si-O-Si bonds during the hydrothermal crystallization process, which can promote the formation of more structural units of the zeolite and accelerate the nucleation and crystal growth, thus easily forming primary crystallites with smaller particle sizes [49,50]. In the present synthesis system, the total amount of TPA^+ (TPABr and TPAOH) remains constant, and the alkalinity of the synthesis system should decrease somewhat with the decrease in TPAOH in the synthesis system (corresponding to the increase in the TPABr amount added into the composites). However, the change in the crystal size of the as-synthesized TS-1_xB zeolites show an opposite trend, decreasing obviously from ~800 nm (for TS-1_0B) to ~250 nm (for TS-1_0.15B), with a decrease in the alkalinity (TPAOH usage amount changed from 0.4 to 0.25). According to the crystallization kinetic experiments described above, the hydrothermal crystallization of the polymer/TPABr composite precursors proceeded very quickly, and a very high yield of zeolite (above 90%) was achieved in a short crystallization time (i.e., 6 h). A possible explanation is as follows: The addition of TPABr in the polymer composites may have increased the local concentration of TPA^+ surrounding the Si and Ti species during the initial stage of hydrothermal treatment. In this case, the hydrolysis-generated Si-OH and Ti-OH, which are detached from the Ti-BDO-Si polymers, could be easily transformed to TPA^+-tinanosilicate species through a direct interaction with the neighboring TPA^+ template, considerably improving the nucleation and crystal growth of the zeolites and

finally leading to the formation of smaller TS-1 crystals within a short crystallization time [29]. Similar cases have already been proposed for the template-induced synthesis of heteroatom zeolites with smaller particle size through the concentrated gel or dry gel conversion methods [19,51,52].

Notably, the reference sample TS-1_ref, which was synthesized by introducing the TPABr in the second stage of hydrothermal crystallization (rather than in the first stage of preparing the polymer precursor), shows a relatively large crystal size (700–900 nm). This result implies that the addition of TPABr in the polymer precursor (to form Ti-BDO-Si/TPABr composites) is beneficial for speeding up the generation of a large number of crystal nuclei, which could lead to the rapid formation of TS-1 crystals with a smaller particle size (300–500 nm). In general, the smaller crystal size of zeolite could provide more accessible active sites for reactants, as well as improve product diffusivity, thus possibly being beneficial to improvements in the catalytic performance of the zeolite-based catalysts [53–55].

Based on the above experimental results and the related literature [31], a possible schematic diagram of the polymer/TPABr precursor approach for synthesizing TS-1 zeolites is proposed (Scheme 1). In the first stage, the transesterification of the alkoxy groups of orthosilicate and butyl titanate with 1,4-butanediaol proceeds smoothly to form network-like polymers, since alkyl titanate may also serve as a catalyst to catalyze the reaction; meanwhile, pre-added TPABr compounds are embedded in the interspace of the polymer chains during the polymerization process, leading to the formation of the Ti-BDO-Si/TPABr composite precursors. In the second stage of the initial hydrothermal crystallization process, the pre-added TPABr accelerates the formation of TPA^+-tinanosilicate species, which is possibly related to the fact that a relatively high local concentration of TPA^+ is present near the Si and Ti precursors, leading to the rapid nucleation and growth of the zeolites under the basic environment arising from the addition of the TPAOH template. With a further prolonged crystallization time, relatively small TS-1 crystals with high crystallinity are rapidly formed as both the titanium source and the silicon source are equally detached from the polymer precursors, resulting in a good match for their hydrolysis and condensation rates to avoid the generation of extra-framework Ti species.

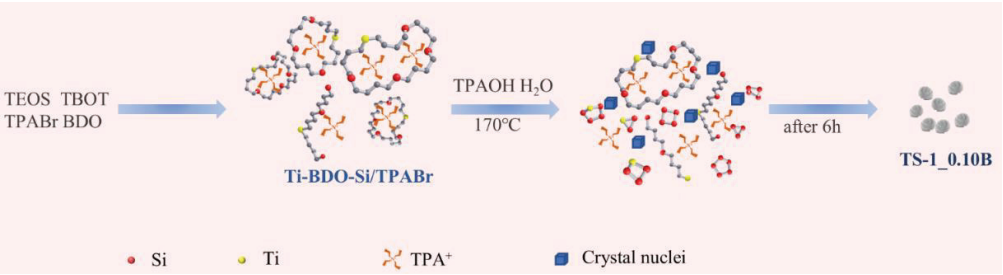

Scheme 1. Proposed schematic diagram of the synthesis process of TS-1 zeolites based on polymer/TPABr precursor approach.

4. Catalytic Performance

The catalytic properties of various TS-1 samples were evaluated for the epoxidation of 1-hexene with aqueous H_2O_2. As shown in Tables 2 and S4, the conventional TS-1_con zeolite exhibits relatively low catalytic activities under the tested conditions, giving a 31.8% conversion of 1-hexene after a 2 h reaction, which is quite similar to the TS-1 catalysts reported in the literature (Table S5) [56]. The conversion of 1-hexene could be improved to different extents upon the use of TS-1 zeolites synthesized with the polymer composite precursors as catalysts. Among them, the highest activity is obtained using the catalyst of TS-1_0.10B over a crystallization time of 6 h, with 49.7% 1-hexene conversion and 98.6% epoxide selectivity, respectively. The relatively low catalytic efficiency of TS-1_con might be mainly related to the presence of some anatase TiO_2, which can cause the ineffective decomposition of hydrogen peroxide as proposed in the previous literature [57]. In addition,

the reference sample of TS-1_ref, which was synthesized by adding TPABr in the second hydrothermal crystallization stage, shows a 34.6% conversion of 1-hexene after 2 h, which is still much lower than that of TS-1_0.10B. Concerning the fact that TS-1_ref is nearly free of anatase TiO_2, it can be deduced that other factors, such as the particle size or the crystallinity of the TS-1 zeolites, may also play critical roles in influencing the catalytic performance of the TS-1 zeolites.

Table 2. Catalytic results of 1-hexene epoxidation with H_2O_2 as oxidant of prepared TS-1 samples [a].

Catalyst	Conv./% mol	Sel./% mol
TS-1_con	31.8%	97.6%
TS-1_0B	35.6%	97.9%
TS-1_0.05B	36.1%	97.8%
TS-1_0.10B	49.7%	98.6%
TS-1_0.15B	42.0%	97.8%
TS-1_ref	34.6%	98.4%

[a] Reaction conditions: 50 mg of catalyst, CH_3OH 10 mL, 1-hexene 10 mmol, H_2O_2 10 mmol, 333 K, 2 h.

Figure 8 shows the conversion of 1-hexene as a function of time over the TS-1_con and TS-1_0.10B catalysts. It can be seen that the catalytic activity of TS-1_0.10B is just slightly higher than that of TS-1_con at the early reaction stage (e.g., 0.5 h), implying that the initial activities of these two catalysts are quite similar. With a further extension in the reaction time, the conversion of 1-hexene catalyzed by TS-1_con slowly increases, reaching 46% after 10 h; similar cases have already been widely reported over various TS-1 zeolites, which were synthesized through different approaches [58,59]. These phenomena could usually be explained by the invalid decomposition of H_2O_2 or the gradual deactivation of the TS-1 zeolites caused by the strong adsorption of some substances in the micropores. Interestingly, the conversion of 1-hexene catalyzed by TS-1_0.10B keeps rising with the prolonged reaction time, reaching a very high value of 75.4% after 10 h; meanwhile, the selectivity of epoxide still remains at around 98%, which is significantly higher than the catalytic performance of TS-1_con and those typical TS-1 zeolites reported in the related literature [19,56]. These results suggest that TS-1_0.10B has very high catalytic efficiency for H_2O_2 activation and also possesses an enhanced ability against deactivation, both of which are quite attractive features for the application in olefin epoxidation.

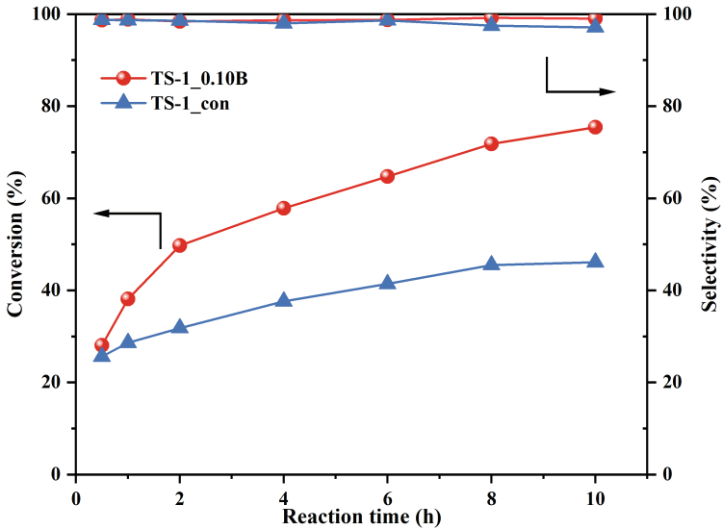

Figure 8. Conversion of 1-hexene as function of time in the H_2O_2-mediated epoxidation over TS-1_con and TS-1_0.1B catalyst.

The recycling experiments show that the TS-1_0.10B catalyst could be easily recovered after simple washing and calcination (Figure 9). Both the catalytic activity and epoxide

selectivity remain almost unchanged after recycling three times, indicating that the synthesized TS-1_0.10B catalyst has excellent recyclability and stability for the epoxidation of 1-hexene with H_2O_2 as the oxidant. These results suggest that the active center structure of TS-1_0.10B should be very stable, possibly related to the high crystallinity of the zeolite. Moreover, the additional catalytic tests reveal that TS-1_0.10B could also efficiently catalyze other epoxidation reactions such as the epoxidation of propylene with H_2O_2 as the oxidant, showing much better catalytic efficiency than the conventional TS-1 zeolites (Table S6).

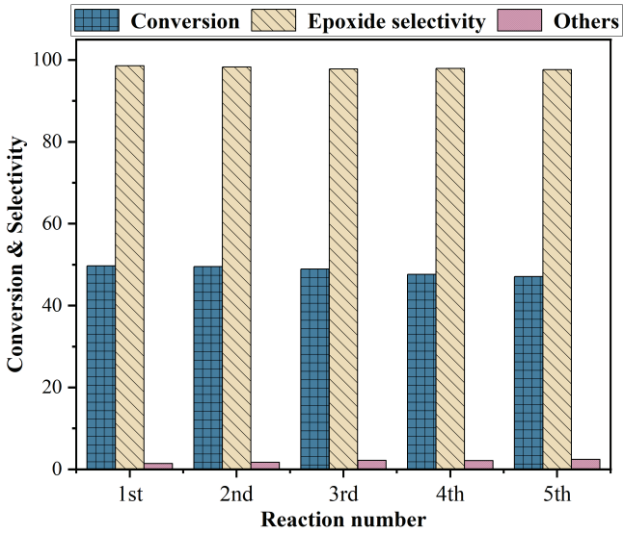

Figure 9. Recycling experiments of 1-hexene epoxidation catalyzed by TS-1_0.10B with H_2O_2 as the oxidant. Reaction conditions: catalyst 50 mg, 1-hexene 10 mmol, H_2O_2 10 mmol, CH_3OH 10 mL, temperature 313 K, 2 h.

The previous literature has revealed that the catalytic epoxidation performance of the TS-1 zeolites is very sensitive to the morphology, particle size, and crystallinity of the zeolite crystals, as well as the microstructure and environment of the Ti species [60]. For the epoxidation of 1-hexene, the relatively low catalytic activity of various TS-1 zeolites is mainly assigned to the ineffective decomposition of H_2O_2, as well as the repaid deactivation of the TS-1 zeolites caused by the block of zeolite pores/channel with epoxide products [61]. By decreasing the particle size of the TS-1 zeolites to nanoscale or constructing some mesopores over the TS-1 zeolite, the catalytic activity for 1-hexene could be somewhat improved; however, the epoxide selectivity commonly decreased, mainly due to the existence of relatively more defective sites (e.g., acidic Ti-OH in $[TiO_6]$ species) in the nanosized or hierarchical TS-1 zeolites [61].

In combination with the above characterization results and the catalytic data, it can be proposed that the relatively high catalytic efficiency of TS-1_0.10B should mainly be related to the positive features of zeolite, such as smaller crystal size, enriched framework Ti spices, and higher crystallinity. The relatively small crystal size is beneficial for improving the mass transport and diffusion ability for reagents and products, while the enriched framework TiO_4 species provides more catalytically active sites for the epoxidation of 1-hexene. Meanwhile, the high crystallinity of the zeolites and the lack of extra-framework Ti species could considerably reduce or even eliminate the undesirable active centers like defective Si-OH or Ti-OH, low-polymerized Ti species, or anatase TiO_2, considerably inhibiting the ineffective decomposition of hydrogen peroxide and/or the occurrence of other side reactions and leading to the improvement in catalytic activity, H_2O_2 utilization rate, and stability against deactivation.

5. Materials and Methods

5.1. Reactant Agents

The agents used were as follows: Tetraethyl orthosilicate (TEOS) (Sinopharm, Beijing, China); H_2O_2 (30 wt%, Sinopharm, Beijing, China); tetrapropylammonium bromide (TPABr) (A.R., Sinopharm, Beijing, China); 1,4-butanediol (BDO) (99%, Aladdin, Shanghai, China); tetrabutyl titanate (TBOT) (98%, Guangfu Fine Chemical Research Institute, Tianjin, China); tetrapropylammonium hydroxide (TPAOH) solution (25 wt%, Sinopharm, Beijing, China); methanol (Fuchen Chemical Reagent Co., Ltd. Tianjin, China); 1-hexene (99%, Shanghai Macklin Biochemical Co., Ltd., Shanghai, China); ethanol absolute (Jindong Tianzheng Fine Chemical Reagent Factory, Tianjin, China); and cyclopentene (98%, Shanghai Macklin Biochemical Co., Ltd., Shanghai, China).

5.2. Synthesis of Ti-BDO-Si/TPABr Composite Precursors

The composite precursors of Ti-BDO-Si/TPABr were synthesized by the transesterification of the alkoxy groups of ethyl orthosilicate and butyl titanate with 1,4-butanediol in presence of TPABr, following the procedure to synthesize Ti-diol-Si polymers [27]. The molar composition of the mixture was as follows: 1.0 SiO_2:1.0 BDO:0.02 TiO_2:x TPABr (x = 0, 0.05, 0.10 or 0.15). Typically, 0.185 g of TBOT was added dropwise to 5.0 g of ethanol with vigorous stirring in a round-bottom flask, then 2.445 g of BDO was added to form a clear solution, followed by the addition of a certain amount of TPABr. Subsequently, 5.653 g of TEOS was added to the above solution and stirred at 120 °C in an oil bath for 30 min. After that, the composite precursors composed of Ti-BDO-Si and TPABr were obtained.

5.3. Synthesis of TS-1 Zeolites from Polymer Composite Precursors

The polymer-based composite precursors obtained above were used as the titanium and silicon sources for the syntheses of TS-1 zeolites. The polymer composites containing different amounts of TPABr were directly added to the TPAOH solution with sufficient stirring. To ensure that the total concentration of TPA^+ remained constant, the molar ratio of SiO_2/TPAOH/H_2O was kept at 1.0:(0.4 − x):40 H_2O, while x is the molar ratio of TPABr/SiO_2 in the composite precursor as mentioned above. The resulting sol–gel solution was transferred to a PETE-lined stainless-steel autoclave and then hydrothermally crystallized at 170 °C for 6 h under static conditions. The solid product was washed thoroughly with deionized water and ethanol, centrifuged, dried in an oven at 80 °C overnight, and then calcined at 550 °C for 6 h. The final samples were denoted as TS-1_xB, where B represents the agent of TPABr, indicated as TS-1_0B, TS-1_0.05B, TS-1_0.10B, TS-1_0.15B, respectively.

To gain a clear understanding of the crystallization process of the zeolites synthesized from Ti-BDO-Si polymers, a series of TS-1_0.10B zeolites with different crystallization times were also synthesized by changing the conventional hydrothermal process time in the range of 2 h to 12 h.

For comparison, conventional TS-1 zeolite (named TS-1_con) was synthesized by the hydrothermal crystallization of the starting gel mixture with a molar composition of SiO_2: 0.02 TiO_2: 0.40 TPAOH: 40 H_2O at 170°C for 48 h, following a procedure as described in the previous literature [62].

To understand the role of TPABr, a reference sample named TS-1_ref was synthesized using a similar procedure as the one used for the synthesis of TS-1_0.10B. The main difference is that the agent of TPABr was not added to the synthesis system of the Ti-BDO-Si polymer, and it was added into the sol–gel synthesis system together with TPAOH in the second step, leading to a sol–gel solution with the molar ratio of TPABr/TPAOH/SiO_2 = 0.1:0.3:1.0.

5.4. Characterization

The X-ray diffraction (XRD) patterns of the as-synthesized samples were obtained utilizing an Empyrean XRD diffractometer (Cu Kα radiation, λ = 1.4518 Å) to verify the crystal structure and phase purity, employing a scanning rate at 10° min^{-1} between the

2θ angles of 5° and 40°. Relative crystallinity (RC) values for the resultant TS-1 samples were determined by assessing the total intensity of the diffraction peaks relative to the sample exhibiting the highest total intensity at 2θ values of 7.8°, 8.8°, 23.0°, 23.9°, and 24.4° [63].

Scanning electron microscopy (SEM) was used to analyze the crystal morphology and size of various samples on a SU-8020 electron microscope. The nitrogen adsorption–desorption isotherms were measured using a Micromeritics ASAP 2020N gas adsorption analyzer at 77 K after degassing the zeolite sample at 473 K for 6 h. The Ti/Si ratio of the various TS-1 samples was determined by inductively coupled plasma optical emission spectroscopy (ICP-OES) using a PerkinElmer emission spectrometer.

The Fourier transform infrared (FT-IR) spectra of the samples prepared by the KBr pellet technique were acquired using a Thermo Scientific NicoletTM 6700 spectrometer. The UV–Vis DRS (Diffuse Reflectance Spectroscopy) of the catalyst was recorded on a SHIMADZU U-4100 in the 200–500 nm range with $BaSO_4$ as reference. Ultraviolet resonance Raman spectra (UV Raman) were collected by using a HORIBA HR Evolution spectrometer at 325 nm excitation. X-ray photoelectron spectra (XPS) were obtained with an ESCALAB250 instrument, using X-ray monochromatization and operating at a constant power of 200 W.

5.5. Catalytic Tests

The catalytic epoxidation of 1-hexene with H_2O_2 (30 wt%) as the oxidant was carried out in a 25 mL round-bottom flask connected to a reflux condenser with magnetic stirring. In a typical operation, 10 mmol of 1-hexene, 10 mmol of H_2O_2 (30 wt%), 10 mL of methanol, and 50 mg of the catalyst were added in to the round-bottom flask. The glass stopper stuck in the neck of flask was coated with vacuum grease to ensure that the reaction system was tightly sealed during the reaction. After that, the epoxidation reaction was started by immersing the flask in an oil bath kept at 60 °C for 2 h. The products were quantitatively analyzed by a gas chromatograph (Fuli GC-9790II) equipped with a SE-54 capillary column and a flame ionization detector to calculate the conversion of 1-hexene and the selectivity of epoxides.

For the recycling tests, the filtered TS-1 catalysts were washed, dried in an oven at 80 °C, and then calcined at 550 °C in air for 6 h.

6. Conclusions

In summary, we found that high-quality TS-1 zeolites could be synthesized by employing a polymer/TPABr composite precursor strategy. The crystal size of the resultant zeolites, the coordination state of Ti species, and the incorporation rate of Ti may be adjusted to a certain extent through changes in the pre-addition amount of TPABr. The condition-optimized TS-1 zeolites with smaller particle size, as well as higher framework Ti content and crystallinity, exhibit excellent catalytic performance for the epoxidation of 1-hexene with H_2O_2 and achieves very high 1-hexene conversion and utilization rate of H_2O_2 under the test conditions, which is much better than the TS-1 zeolites synthesized by the conventional procedure. Although the synthesis procedure adopted in the present work is more complicated in comparison with the conventional synthesis methods reported in the literature, our current results clearly demonstrate that it is possible to further improve the catalytic efficiency of TS-1 zeolites by rationally optimizing the synthesis approach and conditions. More effort is still required in order to achieve good developments at the industrial level for practical application in the catalytic epoxidation of terminal olefins.

Supplementary Materials: The following supporting information can be downloaded at: https://www.mdpi.com/article/10.3390/catal14120939/s1, Table S1. The relative crystallinity of various TS-1 zeolite samples; Table S2. The compositions and the textural properties of TS-1_0.10B samples obtained at different crystallization stages; Table S3. The relative crystallinity of TS-1_0.10B samples obtained from different crystallization stages; Table S4. Catalytic results of 1-hexene epoxidation with H_2O_2 as oxidant of the prepared TS-1 samples; Table S5: Comparison catalytic performance of the

TS-1 catalyst with literature reported catalysts for epoxidation of 1-hexene; Table S6. XRD patterns of the as-synthesized TS-1 zeolites, **Figure S1**. Catalytic results of propylene epoxidation with H_2O_2 as oxidant; Figure S2. FT-IR patterns of the as-synthesized TS-1 zeolites; Figure S3. UV-vis spectra of the TS-1_0.10B samples with different crystallization time; Figure S4. UV-Raman spectra excited at 325 nm of the TS-1_0.10B samples with different crystallization time.

Author Contributions: Y.S.: writing—original draft, methodology, conceptualization, formal analysis. X.C.: partial characterization. J.Z.: investigation. C.B.: investigation. Z.D.: investigation. S.S.: investigation. M.J.: writing—review and editing, validation, and supervision. All authors have read and agreed to the published version of the manuscript.

Funding: We thank the National Natural Science Foundation of China (no. 22172058).

Data Availability Statement: Data are contained within the article or the Supplementary Materials.

Conflicts of Interest: The authors declare no competing financial interests.

References

1. Taramasso, M.; Perego, G.; Notari, B. Preparation of Porous Crystalline Synthetic Material Comprised of Silicon and Titanium Oxides. U.S. Patent 4,410,501, 18 October 1983.
2. Tsai, S.-T.; Chao, P.-Y.; Tsai, T.-C.; Wang, I.; Liu, X.; Guo, X.-W. Effects of pore structure of post-treated TS-1 on phenol hydroxylation. *Catal. Today* **2009**, *148*, 174–178. [CrossRef]
3. Wilkenhöner, U.; Langhendries, G.; van Laar, F.; Baron, G.V.; Gammon, D.W.; Jacobs, P.A.; van Steen, E. Influence of Pore and Crystal Size of Crystalline Titanosilicates on Phenol Hydroxylation in Different Solvents. *J. Catal.* **2001**, *203*, 201–212. [CrossRef]
4. Hu, Y.; Du, C.; Wang, T.; Luo, G. Highly efficient and greener synthesis of TS-1 in a flow system by recycling the mother liquid. *Microporous Mesoporous Mater.* **2019**, *288*, 109585. [CrossRef]
5. Zhang, L.; Zhu, X.; Wang, X.; Shi, C. The synthesis of pure and uniform nanosized TS-1 crystals with a high titanium content and a high space–time yield. *Inorg. Chem. Front.* **2021**, *8*, 5260–5269. [CrossRef]
6. Wróblewska, A.; Tołpa, J.; Kłosin, D.; Miądlicki, P.; Koren, Z.C.; Michalkiewicz, B. The application of TS-1 materials with different titanium contents as catalysts for the autoxidation of α-pinene. *Microporous Mesoporous Mater.* **2020**, *305*, 110384. [CrossRef]
7. Wróblewska, A.; Makuch, E.; Miądlicki, P. The studies on the limonene oxidation over the microporous TS-1 catalyst. *Catal. Today* **2016**, *268*, 121–129. [CrossRef]
8. Tekla, J.; Tarach, K.A.; Olejniczak, Z.; Girman, V.; Góra-Marek, K. Effective hierarchization of TS-1 and its catalytic performance in cyclohexene epoxidation. *Microporous Mesoporous Mater.* **2016**, *233*, 16–25. [CrossRef]
9. Feng, X.; Duan, X.; Yang, J.; Qian, G.; Zhou, X.; Chen, D.; Yuan, W. Au/uncalcined TS-1 catalysts for direct propene epoxidation with H_2 and O_2: Effects of Si/Ti molar ratio and Au loading. *Chem. Eng. J.* **2015**, *278*, 234–239. [CrossRef]
10. Xu, W.; Zhang, T.; Bai, R.; Zhang, P.; Yu, J. A one-step rapid synthesis of TS-1 zeolites with highly catalytically active mononuclear TiO_6 species. *J. Mater. Chem. A* **2020**, *8*, 9677–9683. [CrossRef]
11. Li, H.; Xu, B.; Deng, B.; Yan, X.; Zheng, Y. Epoxidation of 1-hexene with hydrogen peroxide over nitrogen-incorporated TS-1 zeolite. *Catal. Commun.* **2014**, *46*, 224–227. [CrossRef]
12. Wang, Y.Y.; Li, L.; Bai, R.S.; Gao, S.Q.; Feng, Z.C.; Zhang, Q.; Yu, J.H. Amino acid-assisted synthesis of TS-1 zeolites containing highly catalytically active TiO_6 species. *Chin. J. Catal.* **2021**, *42*, 2189–2196. [CrossRef]
13. Fan, W.; Fan, B.; Shen, X.; Li, J.; Wu, P.; Kubota, Y.; Tatsumi, T. Effect of ammonium salts on the synthesis and catalytic properties of TS-1. *Microporous Mesoporous Mater.* **2009**, *122*, 301–308. [CrossRef]
14. Yan, M.; Jin, F.; Ding, Y.; Wu, G.; Chen, R.; Wang, L.; Yan, Y. Synthesis of Titanium-Incorporated MWW Zeolite by Sequential Deboronation and Atom-Planting Treatment of ERB-1 as an Epoxidation Catalyst. *Ind. Eng. Chem. Res.* **2019**, *58*, 4764–4773. [CrossRef]
15. Chen, Z.; Zhang, L.; Yu, Y.; Liu, D.; Fang, N.; Lin, Y.; Xu, D.; Li, F.; Liu, Y.; He, M. TS-1 zeolite with homogeneous distribution of Ti atoms in the framework: Synthesis, crystallization mechanism and its catalytic performance. *J. Catal.* **2021**, *404*, 990–998. [CrossRef]
16. Van der Pol, A.J.H.P.; Verduyn, A.J.; van Hooff, J.H.C. Why are some titanium silicalite-1 samples active and others not? *Appl. Catal. A Gen.* **1992**, *92*, 113–130. [CrossRef]
17. Huang, D.-G.; Zhang, X.; Liu, T.-W.; Huang, C.; Chen, B.-H.; Luo, C.-W.; Ruckenstein, E.; Chao, Z.-S. Synthesis of High-Performanced Titanium Silicalite-1 Zeolite at Very Low Usage of Tetrapropyl Ammonium Hydroxide. *Ind. Eng. Chem. Res.* **2013**, *52*, 3762–3772. [CrossRef]
18. Chen, L.H.; Li, Y.; Su, B.L. Hierarchy in materials for maximized efficiency. *Natl. Sci. Rev.* **2020**, *7*, 1626–1630. [CrossRef]
19. Soekiman, C.N.; Miyake, K.; Hayashi, Y.; Zhu, Y.; Ota, M.; Al-Jabri, H.; Inoue, R.; Hirota, Y.; Uchida, Y.; Tanaka, S.; et al. Synthesis of titanium silicalite-1 (TS-1) zeolite with high content of Ti by a dry gel conversion method using amorphous TiO_2–SiO_2 composite with highly dispersed Ti species. *Mater. Today Chem.* **2020**, *16*, 100209. [CrossRef]
20. Zhu, L.; Zhang, J.; Wang, L.; Wu, Q.; Bian, C.; Pan, S.; Meng, X.; Xiao, F.-S. Solvent-free synthesis of titanosilicate zeolites. *J. Mater. Chem. A* **2015**, *3*, 14093–14095. [CrossRef]

21. Gordon, C.P.; Engler, H.; Tragl, A.S.; Plodinec, M.; Lunkenbein, T.; Berkessel, A.; Teles, J.H.; Parvulescu, A.N.; Coperet, C. Efficient epoxidation over dinuclear sites in titanium silicalite-1. *Nature* **2020**, *586*, 708–713. [CrossRef]
22. Zhang, F.; Guo, X.; Wang, X.; Li, G.; Zhou, J.; Yu, J.; Li, C. The active sites in different TS-1 zeolites for propylene epoxidation studied by ultraviolet resonance Raman and ultraviolet visible absorption spectroscopies. *Catal. Lett.* **2001**, *72*, 3–4.
23. Wang, B.; Guo, Y.; Zhu, J.; Ma, J.; Qin, Q. A review on titanosilicate-1 (TS-1) catalysts: Research progress of regulating titanium species. *Coord. Chem. Rev.* **2023**, *476*, 214931. [CrossRef]
24. Li, M.; Yan, X.; Zhu, M.; Zhou, D. Theoretical investigation on the spectroscopic properties and catalytic activities of the Ti-Hydroperoxo intermediates in titanosilicate zeolites. *Microporous Mesoporous Mater.* **2020**, *299*, 110133. [CrossRef]
25. Ramachandran, C.; Du, H.; Kim, Y.; Kung, M.; Snurr, R.; Broadbelt, L. Solvent effects in the epoxidation reaction of 1-hexene with titanium silicalite-1 catalyst. *J. Catal.* **2008**, *253*, 148–158. [CrossRef]
26. Zhao, P.; Li, Z.; Zhang, Y.; Cui, D.; Guo, Q.; Dong, Z.; Qi, G.; Xu, J.; Deng, F. Tuning Lewis acid sites in TS-1 zeolites for hydroxylation of anisole with hydrogen peroxide. *Microporous Mesoporous Mater.* **2022**, *335*, 111840. [CrossRef]
27. Li, Y.; Fan, Q.; Li, Y.; Feng, X.; Chai, Y.; Liu, C. Seed-assisted synthesis of hierarchical nanosized TS-1 in a low-cost system for propylene epoxidation with H_2O_2. *Appl. Surf. Sci.* **2019**, *483*, 652–660. [CrossRef]
28. Wang, H.; Du, G.; Chen, S.; Su, Z.; Sun, P.; Chen, T. Steam-assisted strategy to fabricate Anatase-free hierarchical titanium Silicalite-1 Single-Crystal for oxidative desulfurization. *J. Colloid Interface Sci.* **2022**, *617*, 32–43. [CrossRef]
29. Zhang, J.; Shi, H.; Song, Y.; Xu, W.; Meng, X.; Li, J. High-efficiency synthesis of enhanced-titanium and anatase-free TS-1 zeolite by using a crystallization modifier. *Inorg. Chem. Front.* **2021**, *8*, 3077–3084. [CrossRef]
30. Zhang, T.; Chen, X.; Chen, G.; Chen, M.; Bai, R.; Jia, M.; Yu, J. Synthesis of anatase-free nano-sized hierarchical TS-1 zeolites and their excellent catalytic performance in alkene epoxidation. *J. Mater. Chem. A* **2018**, *6*, 9473–9479. [CrossRef]
31. Xing, J.; Yuan, D.; Liu, H.; Tong, Y.; Xu, Y.; Liu, Z. Synthesis of TS-1 zeolites from a polymer containing titanium and silicon. *J. Mater. Chem. A* **2021**, *9*, 6205–6213. [CrossRef]
32. Gleeson, D.; Sankar, G.; Richard, C.; Catlow, A.; Meurig Thomas, J.; Spanó, S.; Bordiga, G.; Zecchina, A.; Lamberti, C. The architecture of catalytically active centers in titanosilicate (TS-1) and related selective-oxidation catalysts. *Phys. Chem. Chem. Phys.* **2000**, *2*, 4812–4817. [CrossRef]
33. Liu, Y.; Wang, F.; Zhang, X.; Zhang, Q.; Zhai, Y.; Lv, G.; Li, M.; Li, M. One-step synthesis of anatase-free hollow titanium silicalite-1 by the solid-phase conversion method. *Microporous Mesoporous Mater.* **2022**, *331*, 111676. [CrossRef]
34. Lesthaeghe, D.; Vansteenkiste, P.; Verstraelen, T.; Ghysels, A.; Kirschhock, C.E.A.; Martens, J.A.; Speybroeck, V.V.; Waroquier, M. MFI Fingerprint: How Pentasil-Induced IR Bands Shift during Zeolite Nanogrowth. *J. Phys. Chem. C* **2008**, *112*, 9186–9191.
35. Aziz, F.F.A.; Jalil, A.A.; Triwahyono, S.; Mohamed, M. Controllable structure of fibrous SiO_2–ZSM-5 support decorated with TiO2 catalysts for enhanced photodegradation of paracetamol. *Appl. Surf. Sci.* **2018**, *455*, 84–95. [CrossRef]
36. Liu, M.; Li, J.; Chen, X.; Song, J.; Wei, W.; Wen, Y.; Wang, X. Preparation of anatase-free hierarchical titanosilicalite-1 in favor of allyl chloride epoxidation. *Microporous Mesoporous Mater.* **2021**, *326*, 111388. [CrossRef]
37. Zuo, Y.; Chen, Y.; Li, T.; Yu, J.; Yang, H.; Liu, M.; Guo, X. Bulky macroporous titanium silicalite-1 free of extraframework titanium for phenol hydroxylation. *Microporous Mesoporous Mater.* **2022**, *336*, 111884. [CrossRef]
38. Bi, M.; Song, S.; Li, Z.; Zhang, B.; Zhao, L.; Guo, K.; Li, J.; Chen, L.; Zhao, Q.; Cheng, W.; et al. In situ encapsulated molybdovanaphosphodic acid on modified nanosized TS-1 zeolite catalyst for deep oxidative desulfurization. *Microporous Mesoporous Mater.* **2022**, *335*, 111799. [CrossRef]
39. Jiao, Y.; Adedigba, A.-L.; He, Q.; Miedziak, P.; Brett, G.; Dummer, N.F.; Perdjon, M.; Liu, J.; Hutchings, G.J. Inter-connected and open pore hierarchical TS-1 with controlled framework titanium for catalytic cyclohexene epoxidation. *Catal. Sci. Technol.* **2018**, *8*, 2211–2217. [CrossRef]
40. Zuo, Y.; Liu, M.; Ma, M.; Wang, Y.; Guo, X.; Song, C. Enhanced Catalytic Activity on Post-Synthesized Hollow Titanium Silicalite-1 with High Titanium Content on the External Surface. *ChemistrySelect* **2016**, *1*, 6160–6166. [CrossRef]
41. Zuo, Y.; Liu, M.; Zhang, T.; Hong, L.; Guo, X.; Song, C.; Chen, Y.; Zhu, P.; Jaye, C.; Fischer, D. Role of pentahedrally coordinated titanium in titanium silicalite-1 in propene epoxidation. *RSC Adv.* **2015**, *5*, 17897–17904. [CrossRef]
42. Tsunoji, N.; Opanasenko, M.V.; Kubů, M.; Čejka, J.; Nishida, H.; Hayakawa, S.; Ide, Y.; Sadakane, M.; Sano, T. Highly Active Layered Titanosilicate Catalyst with High Surface Density of Isolated Titanium on the Accessible Interlayer Surface. *ChemCatChem* **2018**, *10*, 2536–2540. [CrossRef]
43. Blasco, T.; Camblor, M.A.; Corma, A.; Perez-Pariente, J. The state of Ti in titanoaluminosilicates isomorphous with zeolite beta. *J. Am. Chem. Soc.* **1993**, *115*, 11806–11813. [CrossRef]
44. Zhang, T.; Zuo, Y.; Liu, M.; Song, C.; Guo, X. Synthesis of Titanium Silicalite-1 with High Catalytic Performance for 1-Butene Epoxidation by Eliminating the Extraframework Ti. *ACS Omega* **2016**, *1*, 1034–1040. [CrossRef] [PubMed]
45. Xiong, G.; Jia, Q.; Cao, Y.; Liu, L.; Guo, Z. The effect of acid treatment on the active sites and reaction intermediates of the low-cost TS-1 in propylene epoxidation. *RSC Adv.* **2017**, *7*, 24046–24054. [CrossRef]
46. Yang, D.; Wang, H.; Wang, W.; Peng, S.; Yang, X.; Xu, X.; Jia, S. Nickel-Modified TS-1 Catalyzed the Ammoximation of Methyl Ethyl Ketone. *Catalysts* **2019**, *9*, 1027. [CrossRef]
47. Hosseiniamoli, H.; Setiawan, A.; Adesina, A.A.; Kennedy, E.M.; Stockenhuber, M. The stability of Pd/TS-1 and Pd/silicalite-1 for catalytic oxidation of methane–understanding the role of titanium. *Catal. Sci. Technol.* **2020**, *10*, 1193–1204. [CrossRef]

48. Pang, C.; Xiong, J.; Li, G.; Hu, C. Direct ring C H bond activation to produce cresols from toluene and hydrogen peroxide catalyzed by framework titanium in TS-1. *J. Catal.* **2018**, *366*, 37–49. [CrossRef]
49. Huang, M.; Wen, Y.; Wei, H.; Zong, L.; Gao, X.; Wu, K.; Wang, X.; Liu, M. The Clean Synthesis of Small-Particle TS-1 with High-Content Framework Ti by Using NH_4HCO_3 and Suspended Seeds as an Assistant. *ACS Omega* **2021**, *6*, 13015–13023. [CrossRef]
50. Zhang, J.H.; Yue, M.B.; Wang, X.N.; Qin, D. Synthesis of nanosized TS-1 zeolites through solid transformation method with unprecedented low usage of tetrapropylammonium hydroxide. *Microporous Mesoporous Mater.* **2015**, *217*, 96–101. [CrossRef]
51. Smeets, V.; Boissière, C.; Sanchez, C.; Gaigneaux, E.M.; Peeters, E.; Sels, B.F.; Dusselier, M.; Debecker, D.P. Aerosol Route to TiO_2–SiO_2 Catalysts with Tailored Pore Architecture and High Epoxidation Activity. *Chem. Mater.* **2019**, *31*, 1610–1619. [CrossRef]
52. Li, R.; Linares, N.; Sutjianto, J.G.; Chawla, A.; Garcia-Martinez, J.; Rimer, J.D. Ultrasmall Zeolite L Crystals Prepared from Highly Interdispersed Alkali-Silicate Precursors. *Angew. Chem. Int. Ed.* **2018**, *57*, 11283–11288. [CrossRef] [PubMed]
53. Zhang, M.; Ren, S.; Guo, Q.; Shen, B. Synthesis of hierarchically porous zeolite TS-1 with small crystal size and its performance of 1-hexene epoxidation reaction. *Microporous Mesoporous Mater.* **2021**, *326*, 111395. [CrossRef]
54. Xue, T.; Liu, H.; Wang, Y.; Wu, H.; Wu, P.; He, M. Seed-induced synthesis of small-crystal TS-1 using ammonia as alkali source. *Chin. J. Catal.* **2015**, *36*, 1928–1935. [CrossRef]
55. Zhang, X.-F.; Yao, J.; Yang, X. Effects of crystal size and pore structure on catalytic performance of TS-1 in the isomerization of styrene oxide to phenyl acetaldehyde. *Microporous Mesoporous Mater.* **2017**, *247*, 16–22. [CrossRef]
56. Li, M.; Zhai, Y.; Zhang, X.; Wang, F.; Lv, G.; Rosine, A.; Li, M.; Zhang, Q.; Liu, Y. $(NH_4)_2SO_4$-assisted synthesis of thin-walled Ti-rich hollow titanium silicalite-1 zeolite for 1-hexene epoxidation. *Microporous Mesoporous Mater.* **2022**, *331*, 111655. [CrossRef]
57. Ruan, H.; Wang, K.; Bing, C.; Fan, X.; Lv, G.; Zhang, X.; Wang, F.; Wang, Y.; Cai, W. Investigation of the Ti active site in TS-1 for phenol hydroxylation via seed and dissolution-recrystallization methods. *Mol. Catal.* **2024**, *568*, 114524. [CrossRef]
58. Su, Y.; Li, F.; Zhou, Z.; Qin, J.; Wang, X.; Sun, P.; Wu, W. Acidic-treated TS-1 zeolites with high titanium for cyclohexanone efficient oximation. *Mol. Catal.* **2022**, *533*, 112752. [CrossRef]
59. Yang, J.; Liu, S.; Liu, Y.; Zhou, L.; Wen, H.; Wei, H.; Shen, R.; Wu, X.; Jiang, J.; Li, B. Review and perspectives on TS-1 catalyzed propylene epoxidation. *iScience* **2024**, *27*, 109064. [CrossRef]
60. Jiang, L.; Wang, F.; Zhai, Y.; Wang, K.; Xu, Z.; Zhang, X.; Li, M.; Li, M.; Zhang, X. Two-step synthesis of Ti-rich surface TS-1 with controllable microenvironment of titanium species. *Appl. Catal. A Gen.* **2023**, *651*, 119023. [CrossRef]
61. Potts, D.S.; Komar, J.K.; Jacobson, M.A.; Locht, H.; Flaherty, D.W. Consequences of Pore Polarity and Solvent Structure on Epoxide Ring-Opening in Lewis and Brønsted Acid Zeolites. *JACS Au* **2024**, *4*, 3501–3518. [CrossRef]
62. Lv, G.; Deng, S.; Yi, Z.; Zhang, X.; Wang, F.; Li, H.; Zhu, Y. One-pot synthesis of framework W-doped TS-1 zeolite with robust Lewis acidity for effective oxidative desulfurization. *Chem. Commun.* **2019**, *55*, 4885–4888. [CrossRef] [PubMed]
63. Rac, V.; Rakić, V.; Miladinović, Z.; Stošić, D.; Auroux, A. Influence of the desilication process on the acidity of HZSM-5 zeolite. *Thermochim. Acta* **2013**, *567*, 73–78. [CrossRef]

catalysts

MDPI

Article

Ru/Beta Zeolite Catalysts for Levulinic Acid Hydrogenation: The Importance of Catalyst Synthesis Methodology

Oana Adriana Petcuta [1], Nicolae Cristian Guzo [1], Mihai Bordeiasu [1], Adela Nicolaev [2], Vasile I. Parvulescu [1] and Simona M. Coman [1,*]

[1] Department of Inorganic Chemistry, Organic Chemistry, Biochemistry and Catalysis, Faculty of Chemistry, University of Bucharest, Bdul Regina Elisabeta 4-12, 030016 Bucharest, Romania; oana.petcuta@s.unibuc.ro (O.A.P.); nicolae.guzo@s.unibuc.ro (N.C.G.); mihai.bordeiasu@s.unibuc.ro (M.B.); vasile.parvulescu@chimie.unibuc.ro (V.I.P.)

[2] National Institute of Materials Physics, Atomistilor 405b, 077125 Magurele-Ilfov, Romania; adela.nicolaev@infim.ro

* Correspondence: simona.coman@chimie.unibuc.ro

Abstract: Ruthenium-based catalysts were prepared through a deposition–precipitation approach, taking beta zeolites with Si/Al ratios of 12.5, 18.5, and 150, respectively, as supports, and 1–3 wt% loadings of metal. Their activation was performed in the presence of either H_2 or $NaBH_4$. The dispersion of the Ru species and the acid–base properties were influenced by both the preparation method and the activation protocol. The catalysts reduced under H_2 flow presented well-dispersed Ru(0) and RuO_x nanoparticles, while the reduction with $NaBH_4$ led to larger RuO_x crystallites and highly dispersed Ru(0). These characteristics exerted an important role in the hydrogenation of levulinic acid (LA) to γ-valerolactone (GVL). The H_2 dissociation occurred via a heterolytic mechanism involving Lewis acid–base pairs associated with RuO_x and the framework oxygen (Si-O-Al) located near the zeolite pore edge. The Ru(0) nanoparticles activated the –C=O bond of the LA substrate, while the presence of the carrier zeolite Brønsted acid sites promoted the ring-closure esterification of the 4-hydroxyvaleric acid (4-HVA) intermediate to GVL. An optimal combination of these features was achieved for the catalyst with 3 wt% Ru and a Si/Al ratio of 150, which selectively converted LA (X_{LA} = 96.5%) to GVL (S_{GVL} = 97.8%) at 130 °C and 10 bars of H_2.

Keywords: beta zeolite; ruthenium; deposition–precipitation; levulinic acid; catalytic hydrogenation; gamma-valerolactone

1. Introduction

Due to its importance, catalytic hydrogenation for biomass valorization is one of the most significant examples requiring an efficient and suitable catalyst design, which is still a significant challenge [1,2]. In most of the reported procedures, conversion occurs as a multistep reaction (e.g., C=O saturation ring-opening and C-O cleavage) in multiphase systems. Therefore, reaching high selectivity to a particular product in the presence of conventional catalysts is a major challenge [3].

In this context, the selective hydrogenation of levulinic acid (LA) provides a good example [4]. Most of the reported investigations have focused on LA conversion to γ-valerolactone (GVL), which is a valuable chemical used as an additive for biodegradable fuels, a monomer for bulk polymers, and a solvent. With this aim, previous studies have shown that noble-metal-based catalysts, such as Ru [5–11], Au [12], Pd [13], and Pt [14], are

preferrable. Among these, ruthenium-based catalysts exhibit the highest activities [15,16]. To further improve their catalytic efficiency, various materials, such as carbon, alumina, titania, lamellar zeolites (MWW zeolites), mesoporous polyamides, and metal organic frameworks (MOFs), have been used as carriers [17–23].

Owing to their unique porous structure, shape selectivity, and medium–strong acidity, zeolites are the most commonly used solid catalysts in the traditional chemical industry, and recently in biomass valorization [24,25]. Zeolites are also efficient carriers for the dispersion of active metal or metal oxide phases. The resulting materials combine the acidic properties of zeolites with the redox properties of metals, thus affording improved catalytic properties for the reactions involved in biomass conversion [3,25]. Therefore, one of the investigated efforts aiming to improve the catalytic activity of metal-based catalysts focuses on bifunctional catalysts combining ruthenium as the metal and zeolites as supports. These catalysts have previously been prepared using a common impregnation method [26–29]. However, this preparation method has shown limited performance for Ru catalysts in LA hydrogenation. Despite this, only few reports have focused on the deposition–precipitation (DP) approach as an alternative to the impregnation method for producing catalysts with high efficiency in LA hydrogenation [23]. Compared to the impregnation method, the DP approach, which is widely used for the synthesis of nanostructured materials, could provide another way to prepare more uniformly dispersed metal nanoparticle catalysts [30]. Simultaneously, mesopores can be generated via desilication in an alkaline environment, improving the mass transfer of reactants, intermediates, and products through the pore system of the carrier [31,32].

Among zeolites, beta zeolites serve as attractive supports for many important biomass valorization applications because of their characteristics such as large channels, strong acid sites, and high thermal and chemical stability [33]. However, previous studies have demonstrated basicity for zeolites in the H-form. The contribution of lattice oxygen atoms to acid-catalyzed reactions has been suggested, where reactions proceed in a concerted manner [34]. In other words, zeolite lattice oxygen atoms may operate as base sites in combination with Brønsted acid sites. Thus, the lattice oxygen adjacent to Al on H-form zeolites possesses basicity and participates in several acid-catalyzed reactions. More recently, Kondo and co-workers [35] associated such base sites with framework oxygen bridging the silicon and aluminum (Si-O-Al) at the external surface zeolite pore edge, with the site density dependent on the zeolite's topology.

To the best of our knowledge, the study of activation protocols coupled with the effect of the preparation approach on the structure and performance of zeolite-based Ru catalysts for LA hydrogenation has never been reported. Herein, we attempt to synthesize Ru/Beta zeolite catalysts (Si/Al = 12.5, 18.5, and 150) with loadings of metal of 1, 2, and 3 wt% Ru, respectively, using the DP approach, followed by their activation through either reduction in a molecular hydrogen flow or direct chemical reduction with $NaBH_4$ as the reagent. The catalytic performances of the synthesized catalysts will be investigated for LA hydrogenation in 1,4-dioxane as the solvent. This study will mainly focus on (i) the influence of the activation protocol upon the structure of the catalysts and the chemical state of the Ru species, and (ii) on insights into the performances of the redox and acid–base sites for LA hydrogenation to GVL.

2. Results and Discussion

2.1. Catalyst Characterization

Figure 1 shows the XRD patterns of the pristine beta zeolite carriers with Si/Al ratios of 12.5, 18.5, and 150. The characteristic reflections of BEA18.5 and BEA12.5 are sharper and more intense, indicating highly regular structures and slightly larger crystals associated

with the higher Al content [36]. Additionally, the reflection lines are shifted to lower 2θ values, indicating an increase in unit cell size that corresponds to an increase in Al-O bonds (1.91 Å) compared to Si-O ones (1.69 Å) [36].

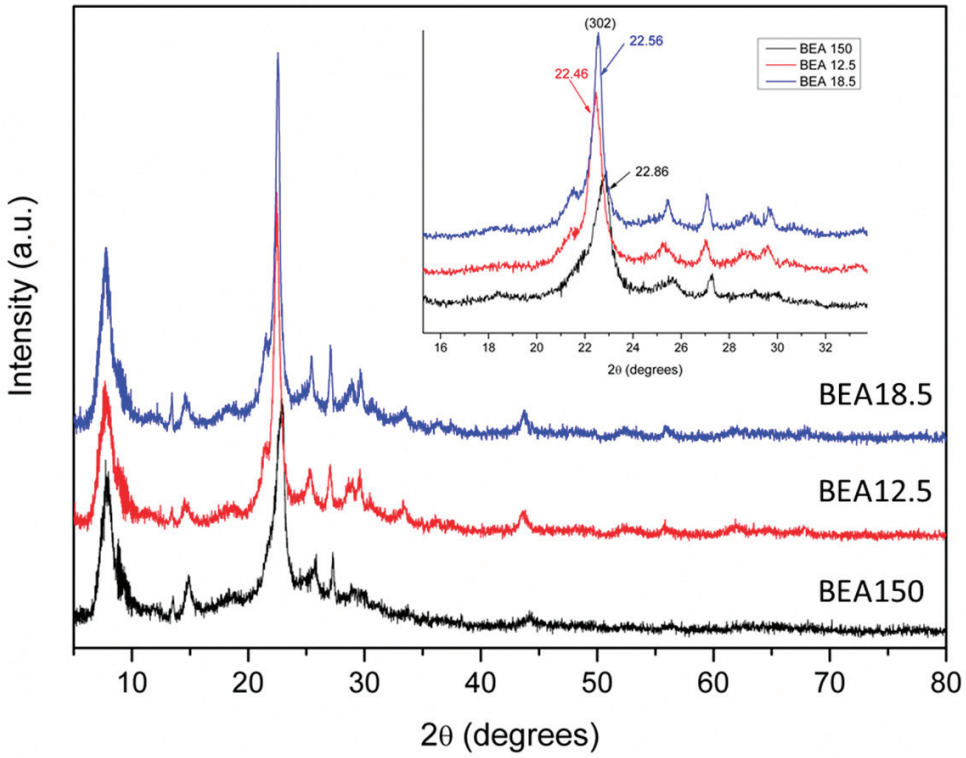

Figure 1. XRD patterns of pristine beta zeolites with different Si/Al ratios. Inset: XRD patterns of the BEA–zeolite samples in the 2θ = 16–30° range.

Further, the XRD patterns of the Ru/BEA catalysts preserved the typical diffraction lines of the beta zeolite carriers (Figure 2A–C). However, these showed an attenuation in their intensity, suggesting a partial loss of crystallinity.

The observed partial loss of crystallinity may be attributed to a desilication process occurring during the DP step. This is also consistent with the reports of Groen et al. [37], who suggested that the desilication of beta zeolites with a low Si/Al ratio (i.e., 12.5 and 18.5 in this work) is inhibited, owing to the relatively high concentration of Al (i.e., the negatively charged AlO_4^- tetrahedrons), which creates a more stable framework for the extraction of silicon. As an effect, the hydrolysis of the Si-O-Al bond in the presence of OH^- is hindered compared to the relatively easy cleavage of the Si-O-Si linkage in the absence of neighboring tetrahedra (i.e., BEA zeolite with a Si/Al ratio of 150).

The crystallinity of the Ru/BEA catalysts was determined by taking the highest intensity of the three characteristic lines of the beta zeolite carriers as a reference (i.e., 100% crystallinity). As Figure 1 shows, the crystallinity of the catalysts containing BEA12.5 and BEA18.5 carriers decreased to 83%, while that of Ru/BEA150 decreased to 59.7%. The advanced desilication of Ru/BEA150 is also confirmed by the shift in the reflection line at 2θ 22.86° (BEA150) to 22.57° (Ru/BEA150) (Figure 2C), which suggests an increase in the unit cell size due to the increased concentration of the longer Al-O bonds (1.91 Å). However, this process became even more prominent for the Ru/BEA catalysts subjected to reduction with $NaBH_4$ (i.e., 3Ru/BEA12.5-B, as illustrated in Figure 2A). In this case, the crystallinity of the beta zeolite support significantly decreased to 50.9%.

According to reports in the literature [23], during the DP approach, the formation of large metal nanoparticles is prevented by the gradual release of hydroxide ions and

the homogeneous precipitation of metal salt. However, the XRD patterns of the Ru/BEA catalysts (Figure 2A) revealed that the structure and, especially, the crystallite size of the ruthenium species are significantly influenced by reduction under a molecular hydrogen flow compared to chemical reduction with $NaBH_4$. As we have recently shown [38,39], Ru/BEA catalysts (1 and 3 wt% Ru and a Si/Al ratio of 12.5), prepared by a DP approach and activated by molecular hydrogen, were characterized by highly dispersed RuO_x species (not detectable in XRD patterns), alongside uniformly dispersed small metallic ruthenium particles. However, for these samples, it is difficult to calculate the size of the metallic ruthenium particles due to the ambiguous boundary of the characteristic diffraction lines. Thus, for the case of the 3Ru/BEA18.5, 2Ru/BEA150, and 3Ru/BEA150 catalysts, the size of the metallic ruthenium crystallites, calculated using the Debye–Scherrer Equation (2), ranged between 8 and 16 nm. Also, the formation of RuO_x species cannot be entirely ruled out. The absence of their characteristic diffraction lines from the recorded XRD patterns suggests either the presence of ruthenium oxide crystallites smaller than approximately 3 nm or the absence of this crystalline phase.

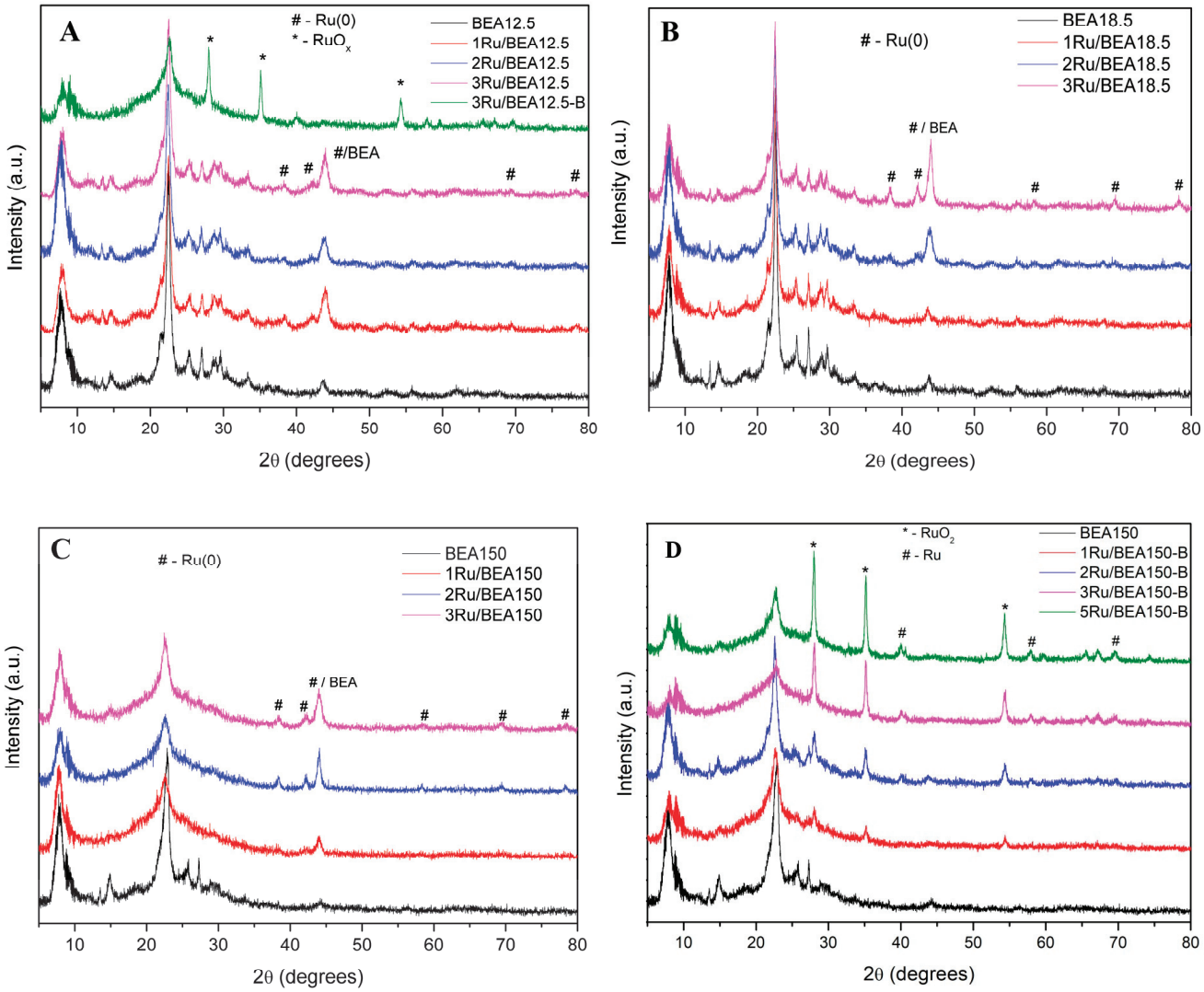

Figure 2. XRD patterns of (**A**) pristine BEA12.5 zeolite and Ru/BEA12.5 catalysts; (**B**) pristine BEA18.5 zeolite and Ru/BEA18.5 catalysts; (**C**) pristine BEA150 zeolite and Ru/BEA150 catalysts; and (**D**) pristine BEA150 zeolite and Ru/BEA150-B catalysts.

Contrarily to the reduction with hydrogen, the use of $NaBH_4$ promoted the formation of larger RuO_x crystallites (2θ = 28.1, 35.1, 44.0, and 54.4°, indexed to the (110), (101), (111), and (211) planes of anhydrous crystalline RuO_2 (ICDD-JCPDS Card No. 43-1027)). These appear to coexist with smaller metallic Ru(0) nanoparticles (Figure 2A,D). One possible explanation for the formation of larger RuO_x crystallites, measuring 15–16 nm in size, is the possible adsorption of borate species onto the ruthenium particles, generated through the hydrolysis of sodium borohydride. Also, in line with the findings of Liu et al. [40], this step may reduce the surface electron density and favor their aggregation.

The HR-XPS spectra of the Ru3d region for the 3Ru/BEA150 and 3Ru/BEA12.5-B catalysts are presented in Figure 3. In accordance with Balcerzak et al. [41], the spin–orbit split Ru3d doublet (i.e., Ru3d5/2 and Ru3d3/2) is resolved by applying a set of narrow (0.6–0.8 eV) symmetric components. For the 3Ru/BEA150 catalyst (Figure 3A), the Ru3d5/2 bands at 279.7 and 280.5 eV are attributed to metallic ruthenium and RuO_2, whereas for the 3Ru/BEA12.5-B catalyst (Figure 3B), the Ru3d5/2 bands are attributed to metallic ruthenium at 280.0 eV and RuOx at 281.7 eV. The Ru3d3/2 peak region is also populated with two ruthenium components, providing a fixed area ratio of the 3d5/2 to 3d3/2 corresponding components, equal to 3:2, and a constant value of their separation energy, equal to 4.15 eV. The C1s main C–C symmetric component is established at 284.6 eV to fully occupy the region envelope. An extra C1s component at 285.7 eV can be attributed to C-O bonds on the surface-adsorbed organic contaminants.

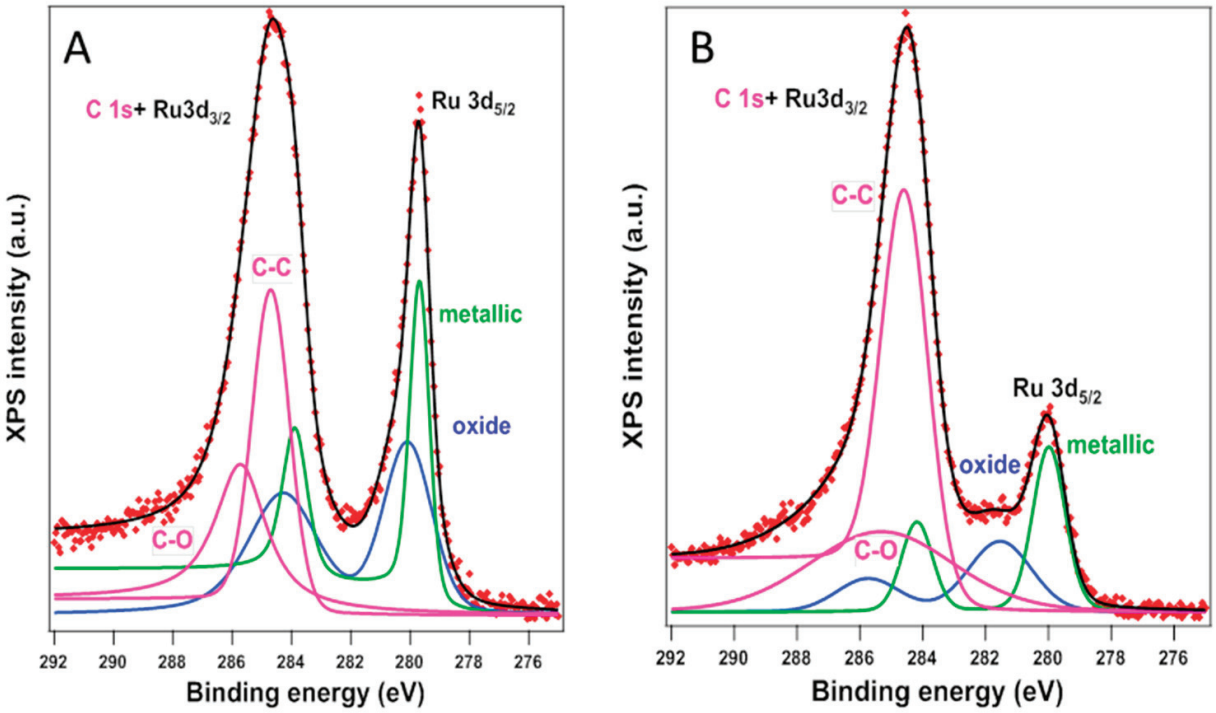

Figure 3. The XPS Ru3d spectra of 3Ru/BEA150 (**A**) and 3Ru/BEA12.5-B (**B**) catalysts.

It is worth noting that the reduction with molecular hydrogen preserved the RuOx species to a greater extent compared to the treatment with NaBH4, generating a higher reduction (Table 1, entries 2 and 4). However, these species were well dispersed in comparison with the large RuOx crystallites observed after the reduction with NaBH4 (XRD patterns, Figure 2A).

Table 1. Percentages and ratios of the Ru^0 and Ru^{x+} species, and the Si/Al ratio.

Catalysts	Ru3d		Ru^{x+}/Ru^0	Si/Al
	Ru^0, at%	Ru^{x+}, at%		
1Ru/BEA12.5 *	25.06	74.94	3.0	13.04
3Ru/BEA12.5 *	23.87	76.13	3.2	12.24
3Ru/BEA150	30.40	69.60	2.3	42.64
3Ru/BEA12.5-B	55.48	44.52	0.8	12.40

* Ref. [38].

The Si/Al ratio of the zeolite carrier also exhibited an important influence upon the nature of the ruthenium species. Thus, for the catalysts with Si/Al = 150, the percent of metallic ruthenium is higher compared to the samples with a Si/Al ratio of 12.5 (Table 1, entries 2 and 3). Also, a significant decrease in the Si/Al ratio from 150 to 42.55 (Table 1, entry 3) confirms, along with the XRD measurements, an advanced desilication of the BEA150 zeolite carrier during the DP approach. Changes also occurred in the surface loading of Na. While for the samples reduced by molecular hydrogen, a content of 1.0–1.22 at% Na (1072.2 eV) was evidenced, for 3Ru/BEA12.5-B, the XPS analysis indicated a higher surface loading of Na (16.28 at%) as Na[AlSi3O8] species, indicating an ion-exchange H^+/Na^+ process during the reduction step. No chlorine was evidenced, irrespective of the preparation procedure.

The N_2 adsorption–desorption isotherms of the Ru/BEA-150 catalysts are depicted in Figure 4, alongside the corresponding distribution of pore size (inset). According to the IUPAC classification, these isotherms correspond to a combination of typical Type IV and Type 3 (H3) hysteresis loops. These correspond to micropore filling at low pressures ($p/p_0 < 0.1$) and to hysteresis loops at higher pressures (p/p_0 of 0.45–0.90), illustrating a hierarchical porous system comprising both micro- and mesoporosity. In addition, near the saturation point (p/p_0 of 1.0), the N_2 adsorption–desorption isotherms also showed a sharp rise in the adsorbed amount, which is associated with condensation in the inter-particle voids (macropores).

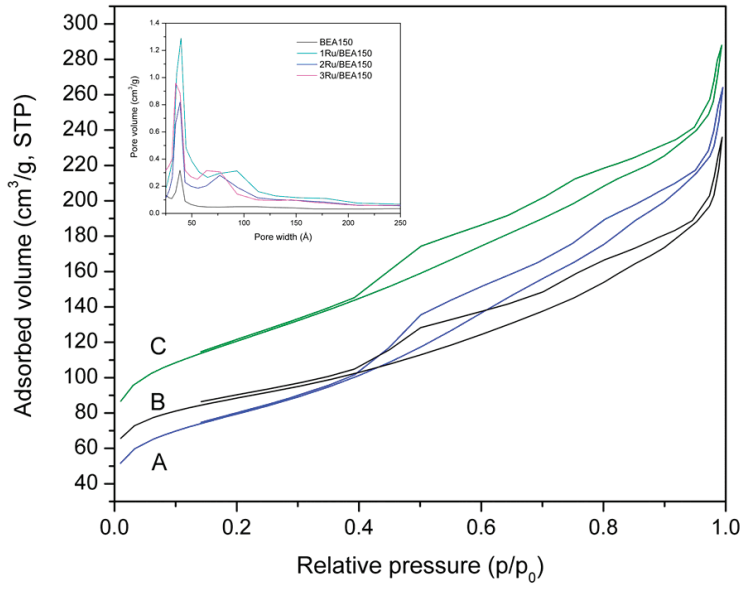

Figure 4. N_2 adsorption–desorption isotherms and pore size distribution profiles (BJH desorption data) of the representative supported Ru/BEA150 samples: 1Ru/BEA150 (**A**), 2Ru/BEA150 (**B**), and 3Ru/BEA150 (**C**).

The data compiled in Table 2 indicate that the deposition of ruthenium led to a decrease in surface area (Table 2, column 3). However, the micropore surface area (Table 2, column 5) experienced a more pronounced decline compared to the external surface (Table 2, column 4). This difference is attributed to the predominant deposition of the ruthenium species on the inner surface of the narrow zeolite pores. However, both the Langmuir and external (*t*-plot) surface areas of these catalysts confirm that the pores of the zeolite are only partly blocked.

Table 2. Textural properties of BEA and Ru/BEA samples.

Sample	S_{BET}, (m^2/g) *	S_{ext}, (m^2/g) **	S_{micro}, (m^2/g) **	V_{total}, (cm^3/g) ***	V_{meso}, (cm^3/g) ****	V_{micro}, (cm^3/g) *****	Pore Size Distribution, (nm) ******
BEA12.5	495	186	309	0.72	0.58	0.14	9.4; 31.5
1Ru/BEA12.5	415	168	247	0.65	0.54	0.11	9.3; 30.0
2Ru/BEA12.5	502	186	316	0.80	0.66	0.14	9.4; 31.5
3Ru/BEA12.5-B	262	172	90	0.38	0.34	0.04	4.0; 9.4
BEA150	497	133	364	0.29	0.12	0.17	3.8
1Ru/BEA150	281	217	64	0.35	0.32	0.03	3.9; 9.3
2Ru/BEA150	275	178	96	0.34	0.30	0.04	3.9; 7.7
3Ru/BEA150	421	273	148	0.38	0.31	0.07	3.9; 7.1

* Calculated by the BET method. ** External surface area calculated using the *t*-plot method. *** Total pore volume determined at a relative pressure (p/p_0) of 0.98. **** Mesopore volume calculated using the BJH method. ***** Micropore volume calculated using the *t*-plot method. ****** Mesopore diameter calculated using the BJH method.

The Ru/BEA catalysts also displayed the development of additional mesopores (Table 2, column 10), confirming a desilication process well correlated with the BEA Si/Al ratio. Thus, the external surface of Ru/BEA150 was significantly enlarged compared to that of the Ru/BEA12.5 catalysts (Table 2, column 4). This desilication process is consistent with the results of the XRD and XPS measurements.

2.2. Catalytic Activity

The Ru/BEA catalysts were evaluated during the hydrogenation of LA. Based on the fact that the kinetic diameter of LA is approximately 0.6 nm (6 Å) [42], and that its various intermediates and potential final products, including GVL, pentanoic acid, 1,2-pentandiol, and different hydrocarbons, have similar or smaller sizes, it was anticipated that the synthesized Ru/BEA zeolites developed through the DP approach (with abundant mesopores) would enhance the mass transport properties, thereby increasing the reaction efficiency.

For the hydrogenation of LA to GVL in water, alcohols, and alcohol/water mixtures, working with Ru catalysts supported on carbon, the literature highlights the significance of the reaction solvent [43,44]. Therefore, despite the limited solubility of hydrogen [45], water enhances the H-spillover effect on the catalyst surface [46], facilitating the adsorption of the reactant and reaction intermediates, thus leading to a faster reaction rate for LA and a higher yield of GVL [46,47]. However, the vulnerability of the zeolites' framework to the attack of the hot liquid water impedes their full utilization in aqueous phase processes. According to reports of Zhang et al. [48] the presence of hydrophilic moieties such as Brønsted acid sites (BAS), extra-framework Al, and silanol defects plays a crucial role influencing the zeolites' susceptibility to hot liquid water. Specifically, the density of the silanol defects has been found to be the most critical factor in this process. Moreover, the use of water as a solvent may also produce the hydrolysis of GVL to 4-hydroxy valeric

acid, which can be subsequently hydrogenated to 1,4-pentanediol [49]. Thus, in light of these findings, the reaction solvent 1,4-dioxane, i.e., a polar aprotic solvent with a polarity index of 4.8 (ε = 2.25), was selected. This solvent demonstrated the ability to enhance the stability of zeolites, while also providing the advantage of a significantly higher solubility for hydrogen [6]. It also allows work at a lower hydrogen pressure and practical benefits for the analysis of the reaction products [26,50].

The optimization of the reaction time and temperature was investigated for the 1Ru/BEA150 catalyst. At 10 bars of H_2 and 130 °C, the increase in the reaction time from 5 to 24 h led to a gradual increase in the conversion of LA, reaching 73.9% for a yield to GVL of 70.2% (S_{GVL} = 95.0%). Based on this, 24 h was established as a reference reaction time for further experiments. Then, the increase in the reaction temperature to 190 °C led to an increase in the conversion to 99.8%. However, due to the instability of 1,4-dioxane in the presence of acid catalysts at this temperature, the yield to GVL decreased to 79.5%, resulting in the formation of dioxane-derived byproducts, as also suggested by Luo et al. [26]. Based on these results, the optimal reaction temperature for further experiments was set to 130 °C.

Noteworthily, under these conditions, the selectivity to GVL was almost total. The only detected intermediate was 4-hydroxyvaleric acid (4-HVA). No intermediates, such as α-angelica lactone (α-AL) or GVL over-hydrogenation products (e.g., 1,4-pentanediol and valeric acid), were identified. The low amounts of 4-HVA may be related to a fast conversion of GVL, while the formation of α-AL requires an acid-catalyzed endothermic dehydration of LA at reaction temperatures higher than 180 °C. As the mass balance of the substrate and products (LA+GVL) was always higher than 93 % (determined by GC analysis), to compare the catalytic activity of the investigated catalysts, Table 3 compiles only the GVL yields.

Table 3. The influence of the support nature and ruthenium loading on catalytic activity and selectivity.

Catalyst *	X_{LA}, %	Y_{GVL}, %	S_{GVL}, %
1Ru/BEA12.5	3.9	3.6	93.3
2Ru/BEA12.5	4.9	4.6	94.0
3Ru/BEA12.5	5.4	5.1	95.0
3Ru/BEA12.5-B	0	-	-
1Ru/BEA18.5	7.9	7.4	94.0
2Ru/BEA18.5	10.5	10.1	96.1
3Ru/BEA18.5	15.1	14.5	96.3
1Ru/BEA150	73.9	70.2	95.0
2Ru/BEA150	87.6	84.1	96.0
3Ru/BEA150	96.5	94.4	97.8

* Reaction conditions: 116 mg (1 mmol) LA, 10 mg catalyst, 3.5 mL dioxane, 10 bar H_2, 130 °C, 24 h. Note: The difference in selectivity up to 100% is given by 4-hydroxyvaleric acid (4-HVA).

As Table 3 shows, the LA conversion was influenced by both the Ru loading and the Si/Al ratio of the zeolite carrier. Regardless of the Si/Al ratio, increasing the Ru loading from 1 to 3 wt% led to an increase in activity. Also, for the catalysts with the same loading of ruthenium, an increase in the conversion of LA was determined by increasing the Si/Al ratio from 12.5 to 150 (Table 3, entries 1–3). Across the Ru/BEA150 catalysts, the conversion of LA was in the range of 73.9–96.5% (Table 3, entries 8–10).

For both the most efficient catalyst (3Ru/BEA150, Table 3, entry 10) and the completely inactive one (3Ru/BEA12.5-B, Table 3, entry 4), the Ru^{x+}/Ru^0 ratio was less than 2.5

(Table 1, entries 3 and 4). So, the determined catalytic behavior is not strictly explained by the differences in the oxidation state of Ru, but also by differences in the size of the RuO_x crystallites. The larger ones (3Ru/BEA12.5-B) relate to a weaker metal–support interaction that, consequently, permeates a high probability of leaching during the reaction. A similar effect of the reduction step may be taken into consideration irrespective of the catalyst nature.

NH_3/CO_2-TPD measurements were conducted for the most efficient catalyst (i.e., 3Ru/BEA150), and the results were compared to those of the less effective ones (i.e., 1Ru/BEA18.5 and 3Ru/BEA12.5-B). For the investigated catalysts, the NH_3-TPD profiles showed different percentages of weak (50–200 °C, Table 4), medium (200–300 °C, Table 4,), and strong acid sites (300–400 °C, Table 4) (Figure 5A,B). Specifically, BEA12.5 and BEA18.5 (Figure 5A) exhibited three pronounced peaks at 103, 200, and 381 °C, indicating the presence of both weak and medium-strength acid sites. Following the ruthenium loading, the population of the weak acid sites was slightly declined, while the medium and strong acid sites (200 and 381 °C) disappeared. The latter were replaced by new medium-strength acid sites (peak at 248 °C) generated by the deposition of the RuO_x crystallites [51]. For the 3Ru/BEA150 catalyst, another peak was evidenced at 225 °C (Figure 5B).

Table 4. Acid–base properties of the 3Ru/BEA12.5-B, 3Ru/BEA150, and 1Ru/BEA18.5 catalysts, determined from NH_3/CO_2-TPD.

Sample	Acid Site Population, (μmols/g)			Total Acid Sites, (μmols/g)	Base Site Population, (μmols/g)			Total Base Sites (μmols/g)	Base–Acid Ratio
	Range of Temperature (°C)				Range of Temperature (°C)				
	50–200	200–300	300–400		100–200	200–400	>400		
BEA12.5	61.8	36.2 (200 °C)	10.2	98.3	50.0	-	-	50.0	0.51
3Ru/BEA12.5-B	60.8	24.2 (248 °C)	-	85.0	49.4	231.8 μ	43.9	325.0	3.82
BEA18.5	74.3	17.0 (200 °C)	15.8	107.1	60.2	-	-	60.2	0.56
1Ru/BEA18.5	71.2	51.7 (248 °C)	-	122.9	70.4	80.2	-	150.6	1.23
BEA150	158.9	-	-	158.9	68.4	18.2	-	86.6	0.54
3Ru/BEA150	133.4	95.5	-	228.9	194.4	118.5	-	312.9	1.37

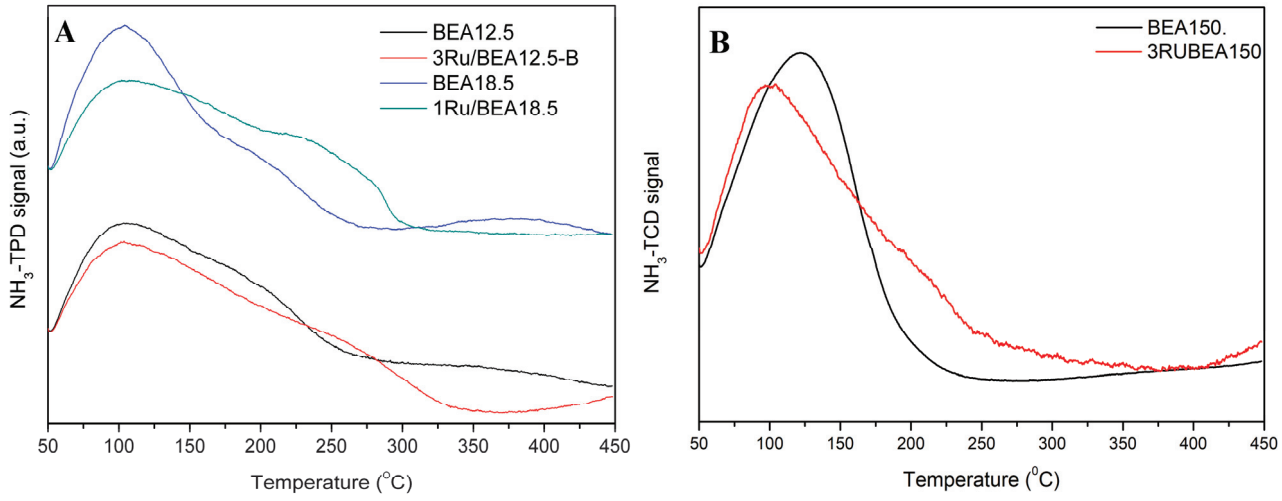

Figure 5. NH_3-TPD profiles for (**A**) 3Ru/BEA12.5-B, 1Ru/BEA18.5, and (**B**) 3Ru/BEA150 catalysts.

The CO_2-TPD profiles are depicted in Figure 6, and the surface features of the investigated samples are listed in Table 4. According to these profiles, the base sites can be classified into three categories: (i) weak base sites (100–200 °C), (ii) moderate-strength base sites (200–400 °C), and (iii) strong base sites (>400 °C) [52].

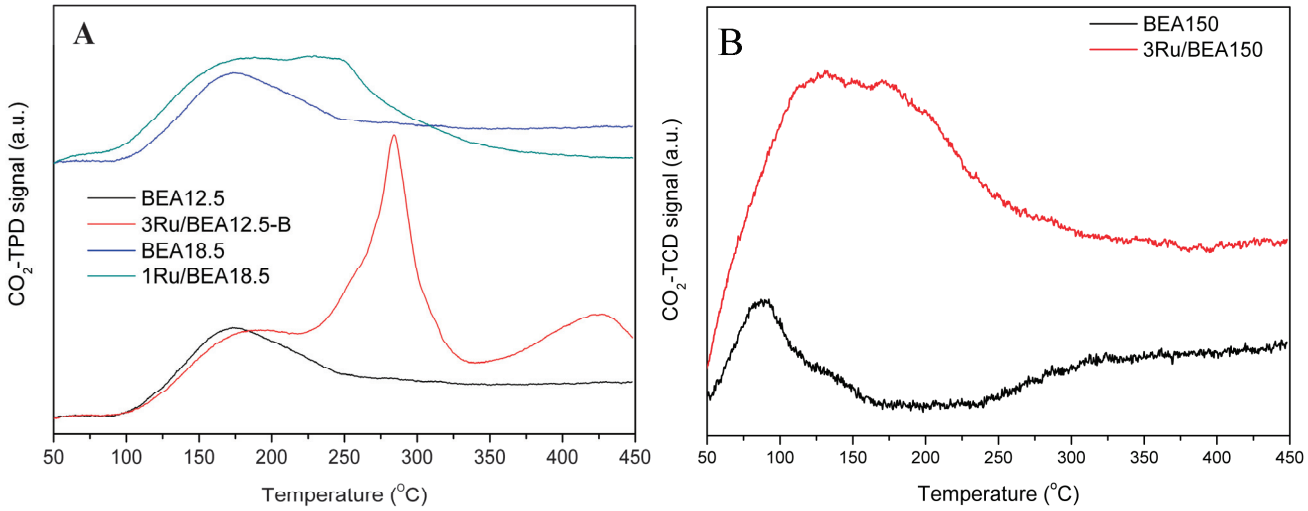

Figure 6. CO_2-TPD profiles for (**A**) 3Ru/BEA12.5-B, 1Ru/BEA18.5, and (**B**) 3Ru/BEA150 catalysts.

In our example, these new generated base sites with moderate strength (200–400 °C; 60.2 μmols/g CO_2 for 1Ru/BEA18.5 and 312.9 μmols/g for 3Ru/BEA150; Figure 6A,B and Table 4) can be associated with partial desilication, as also evidenced by the XRD and XPS measurements. As an effect, in accordance with the extent of desilication, new framework oxygen bridging the silicon and aluminum (Si-O-Al) was generated, which—in agreement with Kondo [35]—represents the basic lattice oxygen in H-BEA zeolite carriers. For 3Ru/BEA12.5-B, the CO_2-TPD profile revealed the presence of moderate-strength and strong base sites. The base strength of H-form zeolites is far weaker than that of conventional solid–base catalysts (alkali-cation-exchanged zeolites and metal oxides). Therefore, while the moderate-strength sites were attributed to the partial loss of zeolite crystallinity as an effect of the desilication, the strong base sites were attributed to the retention of Na^+ as a counter cation, balancing the negative charge of the aluminum tetrahedron during the reduction with $NaBH_4$ [53].

Previous studies suggested two different pathways for the production of GVL from LA [11,23]. These proposed (i) the hydrogenation of LA to 4-HVA, followed by dehydration to the GVL product (pathway 1, Scheme 1), and (ii) the acid-catalyzed endothermic dehydration of LA (temperatures higher than 180 °C) to α-AL via intra-molecular esterification, followed by hydrogenation to GVL (pathway 2, Scheme 1) [11,23]. However, the results collected in this study fit pathway 1, with 4-HVA serving as the intermediate (Scheme 1).

According to this, by hydrogenation, the keto functionality of LA is transformed into an alcohol group, resulting in the formation of the 4-HVA intermediate. This step can be achieved through either homo- [23] or heterolytic [11] H_2 dissociation.

While metallic ruthenium nanoparticles typically favor the homolytic dissociation of H_2 [54], in the case of the surface RuO_x species, due to their involvement in hydrogenation reactions, the mechanism of the reaction of the carbonyl group may be more complicated [15]. The support is not a spectator in this reaction. As previously shown in the hydrogenation of α,β-unsaturated aldehydes, an important effect upon the chemoselectivity to allylic alcohol is given by the existence of the Lewis acid site in the vicinity of the Ru(0) particles, which favors the heterolytic splitting of molecular hydrogen in

hydride–proton pairs [55]. In line with these findings, this study revealed the synergistic effect of Ru(0) nanoparticles activating the -C=O bond of the LA substrate and the Lewis acid–base pairs, which facilitated the heterolytic dissociation of H_2 into H^- and H^+. Specifically, the Lewis base, associated with the framework oxygen bridging the silicon and aluminum (Si-O-Al) situated near the zeolite pore edge on its external surface, can accept the generated protons, leaving the hydrides to the RuO_x (Lewis acid sites) (Figure 7). However, a homolytic mechanism for H_2 dissociation into 2H is also possible for metallic Ru nanoparticles.

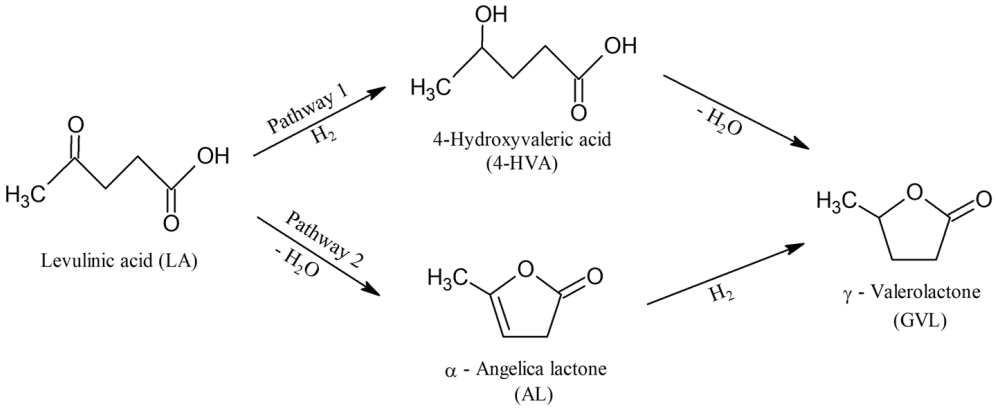

Scheme 1. Reaction pathways for the synthesis of GVL from LA.

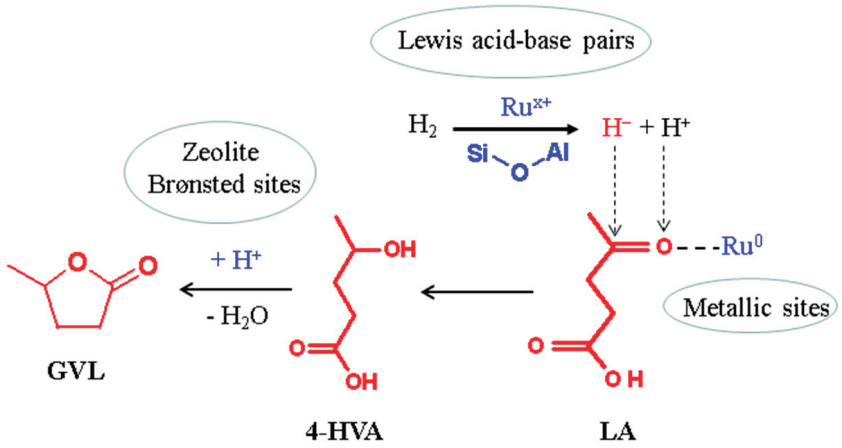

Figure 7. The proposed selective hydrogenation mechanism of LA to GVL through the heterolytic dissociation of H_2.

Following the conclusions of Ruppert et al. [56], the 4-HVA molecule, once formed, may undergo dehydration onto the Brønsted acid sites of the zeolite carrier. As a consequence, the GVL cyclic ester product is generated through a favorable intramolecular esterification process. Thus, the very high efficiency of 3Ru/BEA150 may be attributed to the optimal combination of the catalytic phase, which boasts a balanced Ru^{x+}/Ru^0 ratio of 1.3 (as determined by XPS), with the acid–base properties of the zeolite carrier provided by the Brønsted acid and bridged oxygen Lewis base sites.

Recyclability tests were conducted on the 3Ru/BEA150 catalyst, which displayed the highest catalytic efficiency. After 24 h, the catalyst was separated, washed, dried, and then utilized for another catalytic batch under identical reaction conditions. This process was repeated for five consecutive cycles. As illustrated in Figure 8, the catalyst maintained a high catalytic efficiency for five cycles, with only a slight deactivation in terms of the GVL production after the fourth cycle.

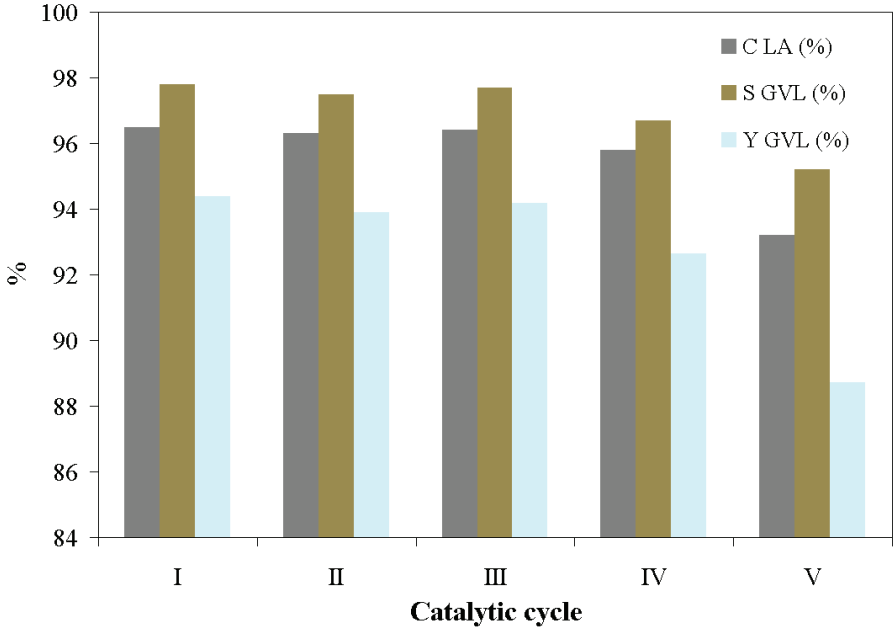

Figure 8. Recycling tests for 3Ru/BEA150 catalyst (1 mmol LA, 10 mg cat, 10 bar H_2, 130 °C, 24 h).

The stability of the investigated catalyst was further validated by the X-ray diffraction patterns (Figure 9) and infrared spectra (Figure 10) collected from both the fresh cycle and after the fifth cycle test.

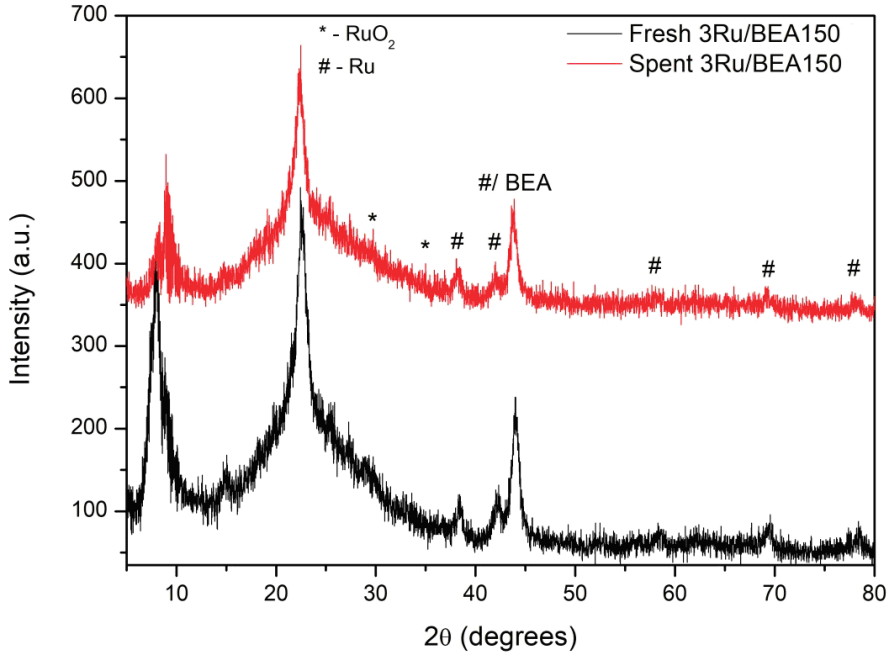

Figure 9. XRD patterns of the fresh and fifth cycles of the tested 3Ru/BEA150 catalyst.

The presence of lines characteristic of both the zeolite and Ru species in the DRIFT spectra after five recycling steps attests the high stability of the catalyst. However, the appearance of new bands in the 2750–3000 cm^{-1} region suggests the adsorption of organic molecules during the reaction, which is likely the primary cause of the gradual decline in catalyst efficiency after multiple catalytic cycles.

A stable and efficient bifunctional Ru/BEA catalyst was developed through the DP method and activation with molecular hydrogen, integrating the necessary catalytic characteristics for the LA conversion to GVL.

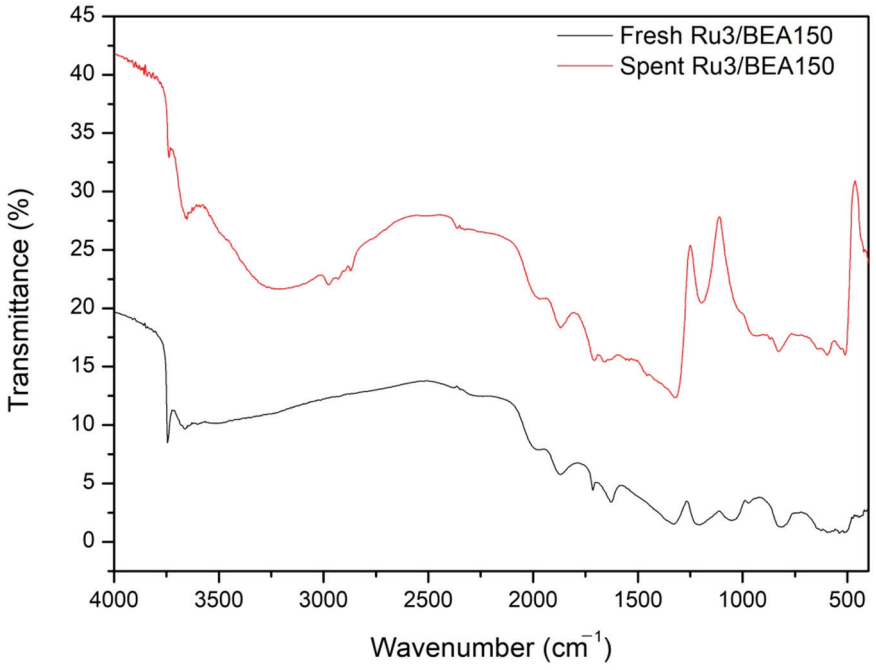

Figure 10. DRIFT spectra for the fresh and fifth cycles of the tested 3Ru/BEA150 catalyst.

Contrarily, the 3Ru/BEA12.5-B catalyst showed complete inactivity in the LA hydrogenation (Table 3, entry 4). This is attributed to the lack of catalyst stability, as proven by the XRD pattern of the spent catalyst (Figure 11). It shows no lines characteristic of RuO_x or metallic Ru(0) species.

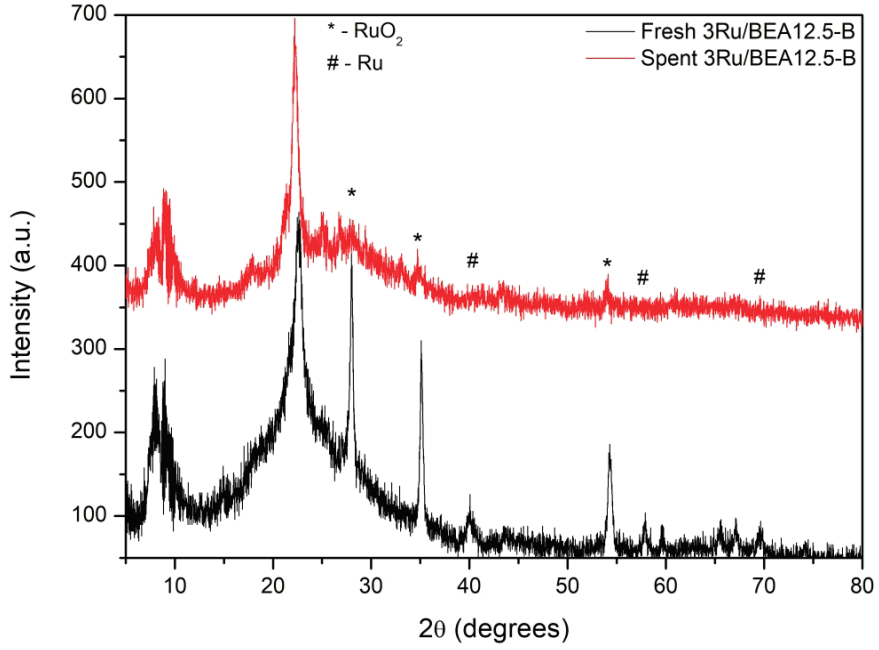

Figure 11. XRD patterns of fresh and 1st cycle of spent 3Ru/BEA12.5-B catalyst.

Therefore, it is likely that the primary cause for the rapid deactivation of the catalyst in LA conversion is an inadequate metal–support interaction. This is also confirmed by the

leaching of ruthenium species observed by UV-Vis spectroscopy (Figure 12), which revealed the presence of cationic ruthenium species in the reaction solution after the separation of the 3Ru/BEA12.5-B catalyst. The spectrum of $RuCl_3$ solution exhibits two signals: one located at 532 nm, assigned to a $\pi \rightarrow \gamma_5$ charge transfer, and the second one at 240 nm, due to the $\pi \rightarrow \gamma_3$ charge transfer typical of low-spin d complexes [57]. An absorption band around 360 nm also appeared in the spectrum due to the formation of $[RuCl_n(H_2O)_{6-n}]^{3-n}$ species. The UV-Vis spectra of the blank reaction (in the absence of the catalyst) indicate the presence of only levulinic acid (LA), with a maximum absorbance at 265 nm.

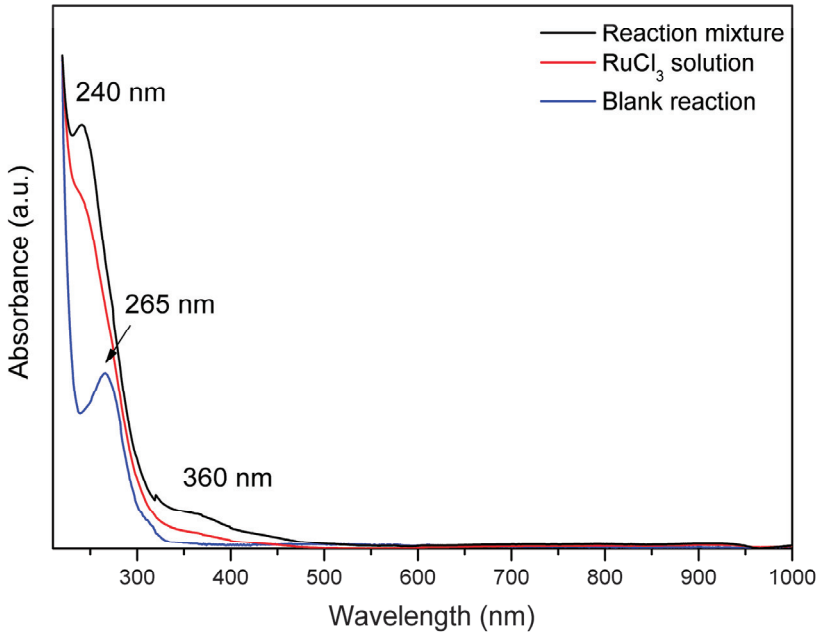

Figure 12. UV-Vis spectra of the aqueous $RuCl_3 \cdot 3H_2O$ solution, the reaction solution after the 1st cycle of the tested 3Ru/BEA12.5-B catalyst, and the reaction solution after blank reaction.

A significant proportion of H^+ acid sites were also lost due to an H^+/Na^+ ion-exchange process occurring during the catalyst reduction with the $NaBH_4$ reagent. This behavior was also proven by XPS and CO_2-TPD characterizations.

3. Materials and Methods

All chemicals and reagents were of analytical grade, purchased from Sigma-Aldrich (Saint Louis, MO, USA), and used without further purification.

3.1. Catalyst Preparation

Ru/BEA zeolite (Si/Al = 12.5, 18.5, and 150) catalysts with 1, 2, and 3 wt%Ru were synthesized by a deposition–precipitation (DP) method. In agreement with our previous work [38,39], in a typical preparation approach for the synthesis of the 1 wt% Ru-BEA catalyst, a solution of 26.1 mg $RuCl_3 \cdot 3H_2O$ (0.1 mmoles of $RuCl_3 \cdot 3H_2O$ in 60 mL H_2O) was added to a suspension of zeolite (1 g in 80 mL of H_2O) under stirring. Subsequently, a solution of NaOH (0.1 M) was added drop-wise until the pH reached 10. The mixture was then stirred for 24 h at room temperature. The same procedure was used to prepare catalysts with 2 and 3 wt% Ru. The Ru loading was adjusted by controlling the amount of the zeolite powder and the volume of the aqueous solution of $RuCl_3 \cdot 3H_2O$. The obtained solids were separated by centrifugation (6000 rpm for 35–40 min) and washed with an $AgNO_3$ reagent until a neutral pH was reached and until chlorine anions were absent from the rinse water. After washing, the catalysts were dried under vacuum at 110 °C.

The catalysts were then activated by calcination at 300 °C, for 4 h, followed by reduction with molecular hydrogen under a flow (H_2) (50 mL/min at 350 °C for 1 h, with a heating rate of 1 °C/min in a flow reactor). The obtained samples were denoted as xRu/BEAy, where x denotes the Ru content (1, 2 or 3 wt%) and y is the Si/Al ratio (12.5, 18.5, or 150).

For comparison, some Ru/BEA catalysts were directly reduced with $NaBH_4$ at room temperature. After drying, a portion of the recovered solid powder was added to 100 mL of a $NaBH_4$ ethanol solution (0.4 M), and the resulting mixture was stirred until bubble generation ceased (~4 h). The obtained catalysts were then separated from the solution by vacuum filtration, washed with deionized water until they reached a pH of ~7, then washed with 50 mL of ethanol, and finally dried at 110 °C overnight. The obtained catalysts are denoted as xRu/BEAy-B.

3.2. Catalyst Characterization

The synthesized Ru/BEA catalysts were characterized by X-ray diffraction (XRD), the adsorption–desorption of nitrogen at −196 °C, IR diffuse reflectance with Fourier transform (DRIFT) spectroscopy, NH_3/CO_2-TPD, and X-ray photoelectron spectroscopy (XPS). Powder X-ray diffraction (XRD) patterns were collected using a Shimadzu XRD-7000 apparatus with a Cu Kα monochromatic radiation of 1.5406 Å, 40 kV, and 40 mA at a scanning rate of 0.1 degree min^{-1} in the 2θ range of 5°–80°. The crystallinity of the samples was defined on the basis of the three characteristic diffraction lines of beta zeolite at Bragg angles of 7.6°, 21.2°, and 22.4°, and calculated using Formula (1) [58]:

$$\%Crystallinity = \frac{\sum_{i=1}^{3} intensity_i}{\left[\sum_{i=1}^{3} intensity_i\right] Ref} \times 100 \quad (1)$$

The average size of the metallic Ru crystallites in the Ru/BEA samples was determined using the Debye–Scherrer Equation (2) [59], taking the (002) reflection of Ru (2θ = 42.3°).

$$d = \frac{k\lambda}{\beta cos\theta} \quad (2)$$

where d is the crystallite size in nm; k = 0.94; λ is the wavelength of the X-ray (1.54178 Å); θ is the half-diffraction angle; and β is the full width at half maximum (FWHM) in radians at 2θ = 42.3°.

Textural characteristics (surface area, pore volume, and pore diameter) were determined from the nitrogen adsorption–desorption isotherms at −196 °C using a Micromeritics ASAP 2020 Surface Area and Porosity Analyzer (Micromeritics, Norcross, GA, USA). Prior to adsorption, all samples were systematically degassed at 200 °C under primary vacuum for 4 h. The surface area was calculated from the BET equation and the pore size distribution was determined based on the Barret–Joyner–Halenda (BJH) approach (Stone, UK), considering the desorption curves. DRIFT spectra were recorded and collected using a Bruker (Billerica, MA, USA) Tensor-II FTIR spectrometer at room temperature at a 4 cm^{-1} resolution in the range of 400–4000 cm^{-1}, and the final spectrum was obtained by averaging 32 scans. UV-vis spectra were recorded with a SPECORD 250-222P108 (Analytical Jena GmbH. KG, Jena, Germany) in the range of 200–1100 nm with a scan rate of 50 nm per second. CO_2- and NH_3-TPD measurements were performed using an AutoChem II 2920 station (Osaka, Japan). The samples (100−200 mg), placed in a U-shaped quartz reactor with an inner diameter of 0.5 cm, were pretreated under He (purity 5.0) at 120 °C for 1 h, and then exposed to a flow of CO_2 or a flow of NH_3 (1 vol%) in helium for 1 h. Subsequently, the samples were purged with a flow of He (50 mL × min^{-1}) for 20 min

at 25 °C in order to remove the weakly adsorbed species. TPD measurements were then started with a heating rate of 10 °C × min^{-1} up to 500 °C, where they were maintained for 30 min. The desorbed products were analyzed using GC-TCD chromatography. The amount of desorbed CO_2/NH_3, expressed as mmol of CO_2/NH_3 per gram of catalyst, was determined using a calibration curve. The X-ray photoelectron spectroscopy (XPS) analysis was performed on an AXIS Ultra DLD (Kratos Surface Analysis) setup (Kratos Analytical, Manchester, UK) using Al Kα1 (1486.74 eV) radiation produced by a monochromatized X-ray source at an operating power of 144 W (12 kV × 12 mA). The base pressure in the analysis chamber was ~1 × 10^{-9} mbar. XPS was performed to determine the surface chemical composition of the samples. All core-level spectra were deconvoluted using Voigt functions, singlets, or doublets (Lorentzian and Gaussian widths), with a distinct inelastic background for each component [60,61]. The minimum number of components was used to obtain a convenient fit. The binding energy scale was calibrated to the C 1 s standard value of 284.6 eV.

3.3. Catalytic Tests

The catalytic experiments were carried out in a stainless-steel autoclave (8 mL, HEL Instruments) under the following conditions: 116 mg of LA (1 mmol), 10 mg of the catalyst, and 3.5 mL of 1,4-dioxane. The system was flushed thrice with hydrogen and then pressurized to 10 bar. To exclude the influence of the external mass transfer limitations, the resulting mixture was stirred at a speed of 1200 rpm. The experiments were performed at 110–190 °C for 5–24 h. After the reaction, the autoclave was quickly cooled to room temperature, the catalyst was separated from the liquid phase by centrifugation (6000 rpm for 5 min), and the products were concentrated under vacuum at 60 °C.

The recovered products were silylated with 150 µL of a derivatization agent (N,O-bis (trimethylsilyl)trifluoroacetamide (BSTFA) with 1% trimethylchlorosilane (TMCS)) and 200 µL pyridine at 50 °C for 2 h. Afterwards, the obtained products were diluted with ethyl acetate (20 µL sample in 15 µL ethyl acetate) and analyzed by a Shimadzu gas chromatograph equipped with a flame-ionization detector (GC-FID) and a DB-5ms GC column (50 m × 0.2 mm × 0.33 µm) with a stationary phase composition of 5% diphenyl and 95% dimethylpolysiloxane. All samples were analyzed in triplicate. Product identification was performed using a Thermo Fischer Scientific (Waltham, MA, USA) Trace 1310 gas chromatograph coupled with an ISQ LT single-quadrupole mass spectrometer (GC-MS) equipped with a TG-5SILMS column (30 m × 0.25 mm × 0.25 µm).

LA conversion (X) and the selectivity to the reaction products (S_n) were calculated from the GC-FID chromatographic analysis using the following Equations (3):

$$X\% = \frac{n_i - n_t}{n_i} \times 100 \qquad S_n\% = \frac{Yield_n}{X} \times 100 \tag{3}$$

where n_i is initial moles of LA and n_t is moles of untransformed LA at time "t", as determined from the GC analysis.

4. Conclusions

In this study, Ru/BEA bifunctional catalysts were prepared by the deposition–precipitation (DP) method, and subsequently reduced with either molecular hydrogen or the $NaBH_4$ reagent. The characterization of the resulting catalysts demonstrated the formation of a hierarchically porous texture with both micro- and mesopores, limiting the steric and diffusional phenomena for both the substrate LA and reaction intermediates. The resulting hierarchical porosity made a significant part of the mesopore/external surface available, allowing a larger dispersion of the active catalytic phase.

The catalytic tests confirmed that the efficiency of Ru/BEA catalysts in LA hydrogenation is influenced by the activation protocol. For the activation with molecular hydrogen, the presence of highly dispersed Ru(0) nanoparticles and RuO_x crystallites led to a synergistic effect, converting LA into the 4-HVA intermediate, which further underwent dehydration to GVL on the Brønsted acid sites provided by the zeolite carrier. While it is not entirely ruled out that a homolytic dissociation of hydrogen could occur over metallic ruthenium nanoparticles, the presence of Lewis acid sites, such as RuO_x, and a high concentration of basic sites in the zeolite carrier, such as framework oxygen bridging the silicon and aluminum (Si-O-Al) at the external surface zeolite pore edge, suggest a possible heterolytic splitting of molecular hydrogen into hydride–proton pairs. However, it was proven that regardless of the hydrogen mechanism of dissociation, the presence of metallic ruthenium is essential for the activation of LA through the adsorption of carbonyl -C=O bonds.

The 3Ru/BEA150 catalyst demonstrated an exceptional ability to convert LA, achieving a conversion rate of 96.5% and a selectivity of 97.8% for GLV at 130 °C under 10 bars of H_2. This catalyst exhibited remarkable stability in the liquid phase, being efficient after five consecutive catalytic cycles without any significant change. The notable catalytic behavior that simultaneously provides high efficiency and stability at the same time in LA hydrogenation to GVL is, therefore, the result of the development of a tailor-made 3Ru/BEA150 catalyst with a combination of certain metallic/acid–base properties and a hierarchical micro/mesoporous structure.

The use of $NaBH_4$ in the reduction of the catalysts led to the formation of larger RuO_x crystallites and highly dispersed metallic Ru nanoparticles (i.e., 3Ru/BEA12.5-B, Ru/BEA150-B). The presence of such large particles suggests a weak metal–support interaction, which led to significant leaching during the reaction. Additionally, the high concentration of basic Na^+ sites on the zeolite carrier can be attributed to an ion-exchange H^+/Na^+ process during the chemical reduction. These two factors are likely responsible for the lack of catalytic efficiency observed in the studied synthesis.

Author Contributions: Conceptualization, O.A.P. and S.M.C.; methodology, O.A.P. and S.M.C.; validation, N.C.G., M.B. and A.N.; formal analysis, O.A.P. and A.N.; investigation, N.C.G., M.B. and A.N.; writing—original draft preparation, S.M.C.; writing—review and editing, V.I.P.; visualization, V.I.P. and S.M.C.; supervision, S.M.C.; funding acquisition, S.M.C. and N.C.G. All authors have read and agreed to the published version of the manuscript.

Funding: This research was funded by The Romanian Ministry of Research and Digitalization, grant number PNRR-III-C9-2022-I5-18, ResPonSE-Project, No. 760010/2022.

Data Availability Statement: The original contributions presented in this study are included in the article. Further inquiries can be directed to the corresponding author(s).

Acknowledgments: N.C.G. kindly acknowledges the Council of Doctoral Studies (C.S.U.D), University of Bucharest, Romania, for partial financial support.

Conflicts of Interest: The authors declare no conflicts of interest.

References

1. Li, N.; Wang, W.; Zheng, M.; Zhang, T. General Reaction Mechanisms in Hydrogenation and Hydrogenolysis for Biorefining. In *Catalytic Hydrogenation for Biomass Valorization*; Rinaldi, R., Ed.; RSC: London, UK, 2015; pp. 22–52.
2. Lazaridis, P.; Karakoulia, S.; Teodorescu, C.; Apostol, N.; Macovei, D.; Panteli, A.; Delimitis, A.; Coman, S.; Parvulescu, V.; Triantafyllidis, K. High hexitols selectivity in cellulose hydrolytic hydrogenation over platinum (Pt) vs. ruthenium (Ru) catalysts supported on micro/mesoporous carbon. *Appl. Catal. B* **2017**, *214*, 1–14. [CrossRef]
3. Sudarsanam, P.; Zhong, R.; Van den Bosch, S.; Coman, S.M.; Parvulescu, V.I.; Sels, B.F. Functionalised heterogeneous catalysts for sustainable biomass valorisation. *Chem. Soc. Rev.* **2018**, *47*, 8349–8402. [CrossRef]

4. Jin, X.; Yin, B.; Xia, Q.; Fang, T.; Shen, J.; Kuang, L.; Yang, C. Catalytic Transfer Hydrogenation of Biomass-Derived Substrates to Value-Added Chemicals on Dual-Function Catalysts: Opportunities and Challenges. *ChemSusChem* **2019**, *12*, 71–92. [CrossRef]
5. Alonso, D.M.; Wettstein, S.G.; Dumesic, J.A. Gamma-valerolactone, a sustainable platform molecule derived from lignocellulosic biomass. *Green Chem.* **2013**, *15*, 584–595. [CrossRef]
6. Tan, J.; Cui, J.; Deng, T.; Cui, X.; Ding, G.; Zhu, Y.; Li, Y. Water-Promoted Hydrogenation of Levulinic Acid to γ-Valerolactone on Supported Ruthenium Catalyst. *ChemCatChem* **2015**, *7*, 508–512. [CrossRef]
7. Wright, W.R.H.; Palkovits, R. Development of Heterogeneous Catalysts for the Conversion of Levulinic Acid to γ-Valerolactone. *ChemSusChem* **2012**, *5*, 1657–1667. [CrossRef] [PubMed]
8. Deng, J.; Wang, Y.; Pan, T.; Xu, Q.; Guo, Q.-X.; Fu, Y. Conversion of Carbohydrate Biomass to γ-Valerolactone by using Water-Soluble and Reusable Iridium Complexes in Acidic Aqueous Media. *ChemSusChem* **2013**, *6*, 1163. [CrossRef]
9. Piskun, A.S.; Van de Bovenkamp, H.H.; Rasrendra, C.B.; Winkelman, J.G.M.; Heeres, H.J. Kinetic modeling of levulinic acid hydrogenation to γ-valerolactone in water using a carbon supported Ru catalyst. *Appl. Catal. A* **2016**, *525*, 158–167. [CrossRef]
10. Wettstein, S.G.; Bond, J.Q.; Alonso, D.M.; Pham, H.N.; Datye, A.K.; Dumesic, J.A. RuSn bimetallic catalysts for selective hydrogenation of levulinic acid to γ-valerolactone. *Appl. Catal. B* **2012**, *117–118*, 321–329. [CrossRef]
11. Seretis, A.; Diamantopoulou, P.; Thanou, I.; Tzevelekidis, P.; Fakas, C.; Lilas, P.; Papadogianakis, G. Recent Advances in Ruthenium-Catalyzed Hydrogenation Reactions of Renewable Biomass-Derived Levulinic Acid in Aqueous Media. *Front. Chem.* **2020**, *8*, 221. [CrossRef]
12. Mustafin, K.; Cárdenas-Lizana, F.; Keane, M.A. Continuous Gas Phase Catalytic Transformation of Levulinic Acid to γ-Valerolactone over Supported Au Catalysts. *J. Chem. Technol. Biotechnol.* **2017**, *92*, 2221–2228. [CrossRef]
13. Feng, J.; Li, M.; Zhong, Y.; Xu, Y.; Meng, X.; Zhao, Z.; Feng, C. Hydrogenation of levulinic acid to γ-valerolactone over Pd@UiO-66-NH2 with high metal dispersion and excellent reusability. *Micropor. Mesopor. Mater.* **2020**, *294*, 109858. [CrossRef]
14. Nemanashi, M.; Noh, J.-H.; Meijboom, R. Hydrogenation of biomass-derived levulinic acid to γ-valerolactone catalyzed by mesoporous supported dendrimer-derived Ru and Pt catalysts: An alternative method for the production of renewable biofuels. *Appl. Catal. A* **2018**, *550*, 77–89. [CrossRef]
15. Michel, C.; Gallezot, P. Why Is Ruthenium an Efficient Catalyst for the Aqueous-Phase Hydrogenation of Biosourced Carbonyl Compounds? *ACS Catal.* **2015**, *5*, 4130–4132. [CrossRef]
16. Kasar, G.B.; Medhekar, R.S.; Bhosale, P.N.; Rode, C.V. Kinetics of Hydrogenation of Aqueous Levulinic Acid over Bimetallic Ru−Ni/MMT Catalyst. *Ind. Eng. Chem. Res.* **2019**, *58*, 19803–19817. [CrossRef]
17. Cao, W.; Luo, W.; Ge, H.; Su, Y.; Wang, A.; Zhang, T. UiO-66 derived Ru/ZrO_2@C as a highly stable catalyst for hydrogenation of levulinic acid to γ-valerolactone. *Green Chem.* **2017**, *19*, 2201–2211. [CrossRef]
18. Yan, L.; Yao, Q.; Fu, Y. Conversion of levulinic acid and alkyl levulinates into biofuels and high-value chemicals. *Green Chem.* **2017**, *19*, 5527–5547. [CrossRef]
19. Wang, Q.; Ling, X.; Ye, T.; Zhou, Y.; Wang, J. Ionic mesoporous polyamides enable highly dispersed ultrafine Ru nanoparticles: A synergistic stabilization effect and remarkable efficiency in levulinic acid conversion into γ-valerolactone. *J. Mater. Chem. A* **2019**, *7*, 19140–19151. [CrossRef]
20. Wojciechowska, J.; Jędrzejczyk, M.; Grams, J.; Keller, N.; Ruppert, A.M. Enhanced Production of γ-Valerolactone with an Internal Source of Hydrogen on Ca-Modified TiO_2 Supported Ru Catalysts. *ChemSusChem* **2019**, *12*, 639–650. [CrossRef] [PubMed]
21. Rivas, S.; Galletti, A.M.R.; Antonetti, C.; Licursi, D.; Santos, V.; Parajó, J.C. A Biorefinery Cascade Conversion of Hemicellulose-Free Eucalyptus Globulus Wood: Production of Concentrated Levulinic Acid Solutions for γ-Valerolactone Sustainable Preparation. *Catalysts* **2018**, *8*, 169. [CrossRef]
22. Guo, Y.; Li, Y.; Chen, J.; Chen, L. Hydrogenation of Levulinic Acid into γ-Valerolactone Over Ruthenium Catalysts Supported on Metal–Organic Frameworks in Aqueous Medium. *Catal. Lett.* **2016**, *146*, 2041–2052. [CrossRef]
23. Li, W.; Li, F.; Chen, J.; Betancourt, L.E.; Tu, C.; Liao, M.; Ning, X.; Zheng, J.; Li, R. Efficient and Sustainable Hydrogenation of Levulinic Acid to γ-Valerolactone in Aqueous Phase over Ru/MCM-49 Catalysts. *Ind. Eng. Chem. Res.* **2020**, *59*, 17338–17347. [CrossRef]
24. Jacobs, P.A.; Dusselier, M.; Sels, B.F. Will Zeolite-Based Catalysis be as Relevant in Future Biorefineries as in Crude Oil Refineries? *Angew. Chem. Int. Ed.* **2014**, *53*, 8621–8626. [CrossRef]
25. Sudarsanam, P.; Peeters, E.; Makshina, E.V.; Parvulescu, V.I.; Sels, B.F. Advances in porous and nanoscale catalysts for viable biomass conversion. *Chem. Soc. Rev.* **2019**, *48*, 2366–2421. [CrossRef]
26. Luo, W.; Deka, U.; Beale, A.M.; van Eck, E.R.H.; Bruijnincx, P.C.A.; Weckhuysen, B.M. Ruthenium-catalyzed hydrogenation of levulinic acid: Influence of the support and solvent on catalyst selectivity and stability. *J. Catal.* **2013**, *301*, 175–186. [CrossRef]
27. Abusuek, D.A.; Tkachenko, O.P.; Bykov, A.V.; Sidorov, A.I.; Matveeva, V.G.; Sulman, M.G.; Nikoshvili, L.Z. ZSM-5 as a support for Ru-containing catalysts of levulinic acid hydrogenation: Influence of the reaction conditions and the zeolite acidity. *Catal. Today* **2022**, *423*, 113885. [CrossRef]

28. Abusuek, D.A.; Nikoshvili, L.Z.; Sorokina, S.A.; Matveeva, V.G.; Sulman, M.G. Catalytic Hydrogenation of Levulinic Acid Using Ruthenium Dioxide Supported on Zeolites. *Chem. Eng. Trans.* **2021**, *88*, 277–282.
29. Piskun, A.; Winkelman, J.G.M.; Tang, Z.; Heeres, H.J. Support Screening Studies on the Hydrogenation of Levulinic Acid to γ-Valerolactone in Water Using Ru Catalysts. *Catalysts* **2016**, *6*, 131. [CrossRef]
30. Hu, L.; Wei, X.-Y.; Zong, Z.-M. Ru/Hβ catalyst prepared by the deposition-precipitation method for enhancing hydrodeoxygenation ability of guaiacol and lignin-derived bio-oil to produce hydrocarbons. *J. Energy Inst.* **2021**, *97*, 48–57. [CrossRef]
31. Feng, X.; Duan, X.; Cheng, H.; Qian, G.; Chen, D.; Yuan, W.; Zhou, X. Au/TS-1 catalyst prepared by deposition–precipitation method for propene epoxidation with H_2/O_2: Insights into the effects of slurry aging time and Si/Ti molar ratio. *J. Catal.* **2015**, *325*, 128–135. [CrossRef]
32. Wang, Z.; Brouri, D.; Casale, S.; Delannoy, L.; Louis, C. Exploration of the preparation of Cu/TiO_2 catalysts by deposition–precipitation with urea for selective hydrogenation of unsaturated hydrocarbons. *J. Catal.* **2016**, *340*, 95–106. [CrossRef]
33. Otomo, R.; Tatsumi, T.; Yokoi, T. Beta zeolite: A universally applicable catalyst for the conversion of various types of saccharides into furfurals. *Catal. Sci. Technol.* **2015**, *5*, 4001–4007. [CrossRef]
34. Chang, C.D.; Silvestri, A.J. The conversion of methanol and other O-compounds to hydrocarbons over zeolite catalysts. *J. Catal.* **1977**, *47*, 249–259. [CrossRef]
35. Osuga, R.; Yokoi, T.; Kondo, J.N. Probing the basicity of lattice oxygen on H-form zeolites using CO_2. *J. Catal.* **2019**, *371*, 291–297. [CrossRef]
36. Schröder, K.P.; Sauer, J. Preferred stability of aluminum-oxygen-silicon-oxygen-aluminum linkages in high-silica zeolite catalysts: Theoretical predictions contrary to Dempsey's rule. *J. Phys. Chem.* **1993**, *97*, 6579–6581. [CrossRef]
37. Groen, J.C.; Peffer, L.A.A.; Moulijn, J.A.; Pérez-Ramírez, J. On the Introduction of Intracrystalline Mesoporosity in Zeolites Upon Desilication in Alkaline Medium. *Micropor. Mesopor. Mater.* **2004**, *69*, 29–34. [CrossRef]
38. Podolean, I.; Dogaru, M.; Guzo, N.C.; Petcuta, O.A.; Jacobsen, E.E.; Nicolaev, A.; Cojocaru, B.; Tudorache, M.; Parvulescu, V.I.; Coman, S.M. Highly Efficient Ru-Based Catalysts for Lactic Acid Conversion to Alanine. *Nanomaterials* **2024**, *14*, 277. [CrossRef]
39. Petcuta, O.; Guzo, N.; Parvulescu, V.I.; Coman, S.M. *Bifunctional Ru/Beta Zeolite Catalysts for the Biomass Feedstock Upgrading*; BioMat Proceedings Book; NTNU: Trondheim, Norway, 2022; Available online: https://chimie.unibuc.ro/edu/greencam/index.php/summer-school-2022 (accessed on 1 November 2024).
40. Liu, J.; Lee, J.B.; Kim, D.H.; Kim, Y. Preparation of high concentration of silver colloidal nanoparticles in layered laponite sol. *Colloids Surf. A* **2007**, *302*, 276–279. [CrossRef]
41. Balcerzak, J.; Redzynia, W.; Tyczkowski, J. In-situ XPS analysis of oxidized and reduced plasma deposited ruthenium-based thin catalytic films. *Appl. Surf. Sci.* **2017**, *426*, 852–855. [CrossRef]
42. Jae, J.; Tompsett, G.A.; Foster, A.J.; Hammond, K.D.; Auerbach, S.M.; Lobo, R.F.; Huber, G.W. Investigation into the shape selectivity of zeolite catalysts for biomass conversion. *J. Catal.* **2011**, *279*, 257–268. [CrossRef]
43. Al-Shaal, M.G.; Wright, W.R.H.; Palkovits, R. Exploring the ruthenium catalysed synthesis of γ-valerolactone in alcohols and utilisation of mild solvent-free reaction conditions. *Green Chem.* **2012**, *14*, 1260–1263. [CrossRef]
44. Wei, Z.; Li, X.; Deng, J.; Wang, J.; Li, H.; Wang, Y. Improved catalytic activity and stability for hydrogenation of levulinic acid by Ru/N-doped hierarchically porous carbon. *Mol. Catal.* **2018**, *448*, 100–107. [CrossRef]
45. Shao, Y.; Wang, J.; Sun, K.; Gao, G.; Li, C.; Zhang, L.; Zhang, S.; Xu, L.; Hu, G.; Hu, X. Selective hydrogenation of furfural and its derivative over bimetallic NiFe-based catalysts: Understanding the synergy between Ni sites and Ni–Fe alloy. *Renew. Energy* **2021**, *170*, 1114–1128. [CrossRef]
46. Weng, R.; Yu, Z.; Xiong, J.; Lu, X. Effects of water in the heterogeneous catalytic valorization of levulinic acid into γ-valerolactone and its derivatives. *Green Chem.* **2020**, *22*, 3013–3027. [CrossRef]
47. Velisoju, V.K.; Peddakasu, G.B.; Gutta, N.; Boosa, V.; Kandula, M.; Chary, K.V.R.; Akula, V. Influence of Support for Ru and Water Role on Product Selectivity in the Vapor-Phase Hydrogenation of Levulinic Acid to γ-Valerolactone: Investigation by Probe-Adsorbed Fourier Transform Infrared Spectroscopy. *J. Phys. Chem. C* **2018**, *122*, 19670–19677. [CrossRef]
48. Zhang, L.; Chen, K.; Chen, B.; White, J.L.; Resasco, D.E. Factors that Determine Zeolite Stability in Hot Liquid Water. *J. Am. Chem. Soc.* **2015**, *137*, 11810–11819. [CrossRef]
49. Pinto, B.P.; Fortuna, A.L.L.; Cardoso, C.P.; Mota, C.J.A. Hydrogenation of Levulinic Acid (LA) to γ-Valerolactone (GVL) over Ni–Mo/C Catalysts and Water-Soluble Solvent Systems. *Catal. Lett.* **2017**, *147*, 751–757. [CrossRef]
50. Jiang, L.; Xu, G.; Fu, Y. A nitrogen-doped carbon modified nickel catalyst for the hydrogenation of levulinic acid under mild conditions. *Green Chem.* **2021**, *23*, 7065–7073. [CrossRef]
51. Hernando, H.; Moreno, I.; Fermoso, J.; Ochoa-Hernández, C.; Pizarro, P.; Coronado, J.M.; Čejka, J.; Serrano, D.P. Biomass catalytic fast pyrolysis over hierarchical ZSM-5 and Beta zeolites modified with Mg and Zn oxides. *Biomass Convers. Bioref.* **2017**, *7*, 289–304. [CrossRef]
52. Zeng, W.; Cheng, D.-G.; Chen, F.; Zhan, X. Catalytic Conversion of Glucose on Al–Zr Mixed Oxides in Hot Compressed Water. *Catal. Lett.* **2009**, *133*, 221–226. [CrossRef]

53. Groen, J.C.; Moulijn, J.A.; Pérez-Ramírez, J. Alkaline posttreatment of MFI zeolites. From accelerated screening to scale-up. *Ind. Eng. Chem. Res.* **2007**, *46*, 4193–4201. [CrossRef]
54. Aireddy, D.R.; Ding, K. Heterolytic Dissociation of H_2 in Heterogeneous Catalysis. *ACS Catal.* **2022**, *12*, 4707–4723. [CrossRef]
55. Coman, S.M.; Parvulescu, V.I. Heterogeneous Diastereoselective Catalysis—A Powerful Strategy Toward C(15) Stereoselectivity from PGF2α Analogues Structure. *Curr. Pharm. Des.* **2015**, *21*, 5558–5572. [CrossRef] [PubMed]
56. Ruppert, A.M.; Grams, J.; Jedrzejczyk, M.; Matras-Michalska, J.; Keller, N.; Ostojska, K.; Sautet, P. Titania-Supported Catalysts for Levulinic Acid Hydrogenation: Influence of Support and its Impact on γ-Valerolactone Yield. *ChemSusChem* **2015**, *8*, 1538–1547. [CrossRef]
57. Pârvulescu, V.; Coman, S.; Palade, P.; Macovei, D.; Teodorescu, C.; Filoti, G.; Molina, R.; Poncelet, G.; Wagner, F. Reducibility of ruthenium in relation with zeolite structure. *Appl. Surf. Sci.* **1999**, *141*, 164–176. [CrossRef]
58. Bhat, R.N.; Kumar, R. Synthesis of zeolite beta using silica gel as a source of SiO_2. *J. Chem. Technol. Biotechnol.* **1990**, *48*, 453–466. [CrossRef]
59. Zhang, Q.H.; Gao, L.; Guo, J.K. Effects of calcination on the photocatalytic properties of nanosized TiO_2 powders prepared by $TiCl_4$ hydrolysis. *Appl. Catal. B* **2000**, *26*, 207–215. [CrossRef]
60. Teodorescu, C.M.; Esteva, J.M.; Karnatak, R.C.; El Afif, A. An approximation of the Voigt I profile for the fitting of experimental X-ray absorption data. *Nucl. Instrum. Methods Phys. Res. Sect. A—Accel. Spectrom. Dect. Assoc. Equip.* **1994**, *345*, 141–147. [CrossRef]
61. Mardare, D.; Luca, D.; Teodorescu, C.M.; Macovei, D. On the hydrophilicity of nitrogen-doped TiO_2 thin films. *Surf. Sci.* **2007**, *601*, 4515–4520. [CrossRef]

catalysts

MDPI

Article

Effect of Metal Dispersion in Rh-Based Zeolite and SiO_2 Catalysts on the Hydroformylation of Olefin Mixtures from Fischer–Tropsch Synthesis

Yu Wang [1,2,†], Xuemin Cao [1,2,†], Yuting Dai [1,2], Tao Yan [1,2], Xiangjie Zhang [1,2], Huizi He [1,2], Yujie Xie [1,2], Tiejun Lin [3], Chang Song [1,2,*] and Peng He [1,2,*]

[1] State Key Laboratory of Coal Conversion, Institute of Coal Chemistry, Chinese Academy of Sciences, Taiyuan 030001, China; wangyu22@mails.ucas.ac.cn (Y.W.); caoxuemin21@mails.ucas.ac.cn (X.C.); daiyuting23@mails.ucas.ac.cn (Y.D.); yantao@sxicc.ac.cn (T.Y.); zhangxiangjie18@mails.ucas.ac.cn (X.Z.); hehuizi23@mails.ucas.ac.cn (H.H.); xieyujie23@mails.ucas.ac.cn (Y.X.)
[2] School of Chemical Engineering, University of Chinese Academy of Sciences, Beijing 100049, China
[3] CAS Key Laboratory of Low-Carbon Conversion Science and Engineering, Shanghai Advanced Research Institute, Chinese Academy of Sciences, Shanghai 201210, China; lintj@sari.ac.cn
* Correspondence: songchang@sxicc.ac.cn (C.S.); hepeng@sxicc.ac.cn (P.H.)
† These authors contributed equally to this work.

Abstract: This study investigates the hydroformylation of C_{5+} olefins derived from Fischer–Tropsch synthesis (FTS) using Rh-based catalysts supported on zeolites (MFI, MEL) and SiO_2. A series of catalysts were synthesized through two different methods: a one-pot hydrothermal crystallization process, which results in highly dispersed Rh species encapsulated within the zeolite framework (Rh@MFI, Rh@MEL), and an impregnation method that produces larger Rh nanoparticles exposed on the support surface (Rh/MFI, Rh/MEL, Rh/SiO_2). Characterization techniques such as BET, TEM, and FTIR were employed to evaluate different catalysts, revealing significant differences in the dispersion and accessibility of Rh species. Owing to its more accessible mesoporous structure, Rh/SiO_2 with a pore size of 5.6 nm exhibited the highest olefin conversion rate (>90%) and 40% selectivity to C_{6+} aldehydes. In contrast, zeolite-encapsulated catalysts exhibited higher selectivity for C_{6+} aldehydes (~50%) due to better confinement and linear aldehyde formation. This study also examined the influence of FTS byproducts, including paraffins and short-chain olefins, on the hydroformylation reaction. Results showed that long-chain paraffins had a negligible effect on olefin conversion, while the presence of short-chain olefins, such as propene, reduced both olefin conversion and aldehyde selectivity due to competitive adsorption. This work highlights the critical role of catalyst design, olefin diffusion, and feedstock composition in optimizing hydroformylation performance, offering insights for improving the efficiency of syngas-to-olefins and aldehydes processes.

Keywords: syngas; Fischer–Tropsch synthesis; hydroformylation; metal encapsulation; zeolite

1. Introduction

Syngas, a mixture of H_2 and CO, is primarily derived from carbonaceous resources such as coal, natural gas, and biomass [1–3]. It serves as a versatile feedstock for the production of high-value chemicals. Among the various conversion pathways, Fischer–Tropsch synthesis (FTS) is widely utilized to transform syngas into diverse products, including alkanes [4,5], olefins [6–8], and high-value feedstocks such as C_{6+} alcohols [9,10]. These C_{6+} alcohols have extensive applications, including their use as plasticizers, detergents, and pharmaceutical

precursors, with their value increasing proportionally to the carbon chain length [11–13]. Extensive research has focused on the conversion of syngas to alcohols, with particular emphasis on C_{6+} alcohols. However, this process involves competitive reaction pathways [14–16]. In a typical FTS sequence, CO is first dissociated on the catalyst surface to generate carbon species, followed by carbon–carbon coupling to elongate the chain. Non-dissociative CO insertion into the intermediate species and subsequent hydrogenation yield alcohols [17–20]. During this process, dissociative and non-dissociative CO activation compete. Stronger CO dissociation favors the production of long-chain olefins, whereas enhanced non-dissociative activation promotes the formation of lower-carbon alcohols [21]. Despite numerous advancements in catalyst design, the selectivity for C_{6+} alcohols remains below 30%, underscoring the challenge posed by this competitive reaction [16,17,22,23].

To address this challenge, a two-step reaction process has been proposed. In the first step, syngas is converted into C_{5+} olefins via FTS, and in the second step, the hydroformylation of the C_{5+} olefins produces C_{6+} aldehydes [24], which can then be readily hydrogenated to form alcohols. For this approach to be viable, the FTS reaction must achieve high selectivity for C_{5+} olefins to ensure a sufficient supply of feedstocks for hydroformylation. Recent studies have reported promising catalyst systems for this purpose [25–30]. For instance, the $NaRu/SiO_2$ catalyst has demonstrated remarkable efficiency in catalyzing syngas conversion, achieving over 70% selectivity for C_{5+} olefins [26]. Recently, Rh@MEL [31] and Rh@MFI [32] catalysts were developed to catalyze the hydroformylation of olefins with high selectivity of linear products, wherein the zeolite is no longer the catalyst but the scaffold to induce regioselectivity. Such catalyst system could induce further improved product selectivity to the final products. However, the Fischer–Tropsch process generates byproducts, such as short-chain olefins, alkanes, and water, which mix with C_{5+} olefins and serve as the feedstock for hydroformylation.

The complex composition of the feedstock raises several critical challenges. Byproducts from the FTS reaction, including short-chain olefins, alkanes, and water, may influence the hydroformylation of C_{5+} olefins, potentially affecting the overall reaction efficiency and selectivity. Consequently, the efficiency of hydroformylation with a mixed feedstock may not be comparable with that achieved with pure olefins. Additionally, the diffusion behavior of C_{5+} olefins is likely influenced by the properties of the hydroformylation catalyst, necessitating an exploration of various heterogeneous catalysts to determine their suitability for this process. Addressing these challenges is essential to enable a seamless tandem reaction using heterogeneous catalysts, representing a significant research gap that requires further investigation.

In this work, we investigated the catalytic hydroformylation performance of C_{5+} olefins within FTS product mixtures containing various components (mainly including long-chain alkanes, short-chain alkenes, and water). A series of Rh catalysts with differing Rh loading methods were synthesized to catalyze the hydroformylation reaction. Characterization techniques, including transmission electron microscopy (TEM) and diffuse reflectance infrared Fourier transform spectroscopy (DRIFTS), were employed to analyze the Rh particle size and spatial distribution within the catalysts. Feedstock mixtures with different compositions were used to systematically examine their effects on the hydroformylation process. The impact of diffusion behaviors of the long-chain olefins was evaluated by comparing catalysts with distinct Rh species positions within the catalyst structure. Additionally, the catalytic performance was studied in the presence of water or propene to assess their impact on the hydroformylation of C_{5+} olefins, as these molecules may compete with C_{5+} olefins for catalytic sites. Insights into the influence of feedstock diffusion, short-chain olefins, and water on the hydroformylation reaction provide valuable guidance for the future development of heterogeneous catalysts aimed at the efficient conversion of

FTS products to aldehydes. Such knowledge will be instrumental in the design of catalysts for the conversion of syngas into C_{6+} alcohols.

2. Results and Discussion

2.1. Catalyst Synthesis and Characterization

A series of Rh catalysts with varying Rh loading methods were synthesized to catalyze the hydroformylation reaction. Rh@MFI and Rh@MEL catalysts were prepared via a one-pot hydrothermal crystallization process, while Rh/MFI, Rh/MEL, and Rh/SiO_2 catalysts were synthesized using the impregnation method. The MFI and MEL zeolite supports were synthesized through the same one-pot hydrothermal crystallization process without metal loading, ensuring that the morphology of the zeolites remained consistent. The crystalline structures of the prepared catalysts were confirmed by powder X-ray diffraction (XRD) analysis (Figure 1). No characteristic peaks of SiO_2 were observed, confirming its amorphous nature. However, distinct peaks for RhO_2 were observed at 27° and 36°, indicating the presence of Rh species. The diffraction patterns of the Rh@MFI and Rh@MEL samples aligned well with the characteristic peaks of MEL and MFI, suggesting the successful formation of the zeolite structures during the hydrothermal crystallization process [31,32]. These diffraction patterns also confirmed that Rh loading did not alter the zeolite crystalline structures. A comparison of the XRD patterns of the catalysts synthesized via the impregnation and one-pot hydrothermal methods reveals that neither method affects the zeolite structure, and notably, peaks corresponding to Rh oxides were absent in the zeolite-supported catalysts, indicating better Rh dispersion compared with Rh/SiO_2.

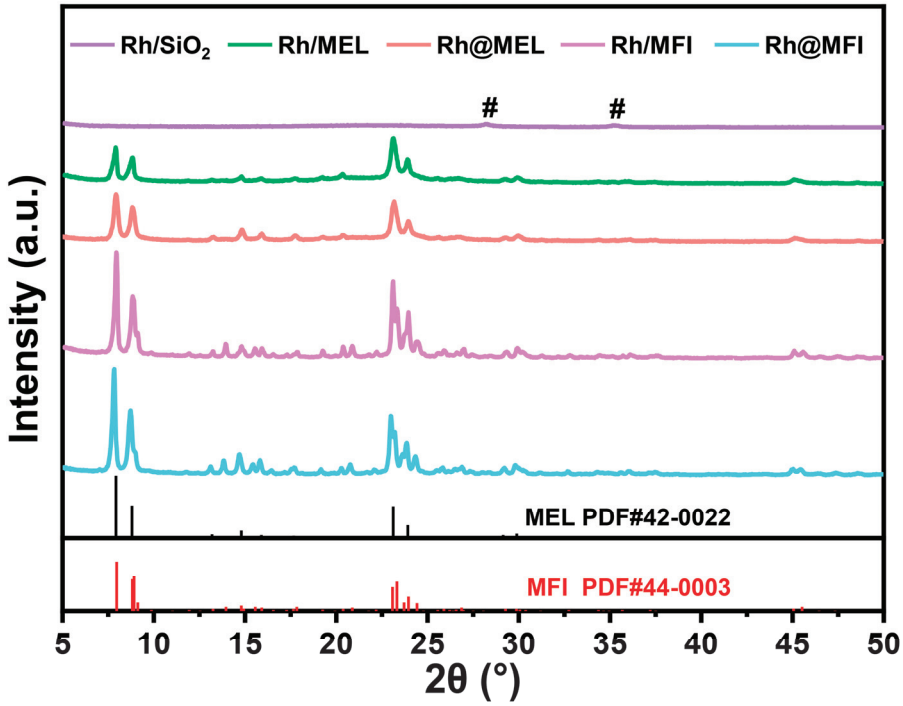

Figure 1. XRD patterns of different catalysts (symbol assignment: #-Rh_2O_3).

To examine the morphologies of the various catalysts, scanning electron microscopy (SEM) was performed, and the results are shown in Figure 2. The Rh@MEL and Rh/MEL samples exhibited a regular block-like shuttle shape, while the Rh@MFI and Rh/MFI samples displayed a block-like spherical shape [31,32]. These similar morphologies can be attributed to the identical one-pot hydrothermal synthesis conditions, with the exception of metal loading. The catalysts supported on the same type of zeolite exhibited similar

morphologies, providing a fair basis for comparing their catalytic performances. In contrast, the Rh/SiO_2 samples displayed irregular shapes due to the amorphous nature of the SiO_2 support. To further investigate the metal loading and porous structure of the catalysts, inductively coupled plasma optical emission spectrometry (ICP-OES) and N_2 physisorption (BET analysis) were employed to determine the elemental compositions and surface areas of the catalysts (Table 1). The ICP-OES results showed similar Rh loadings across the different catalyst types, ensuring a fair comparison of their catalytic activities in subsequent sections. The micropore volume in MFI and MEL zeolites was close to 97.5%, whereas in SiO_2, it was only 18%, with the majority of the pores being mesopores. The nitrogen adsorption−desorption isotherms also confirmed this point (Figure 3). As shown in Figure 3, the Rh/SiO_2 catalyst exhibits a distinct hysteresis loop, indicating that it is a mesoporous material. In contrast, no significant hysteresis loop is observed for the zeolite catalysts, suggesting the presence of a large number of uniformly distributed micropores within these catalysts. Moreover, the loading mode of Rh species does not affect the microporous structure of the zeolites. This is expected, as the channels of MFI and MEL zeolites feature 10-membered rings with a pore size of approximately 0.55 nm, while the pore size of the SiO_2 samples, as determined by BET analysis, is 5.6 nm. These results suggest that catalysts supported on MFI and MEL zeolites provide greater spatial confinement, thereby imposing a higher diffusion barrier for C_{5+} mixed olefins.

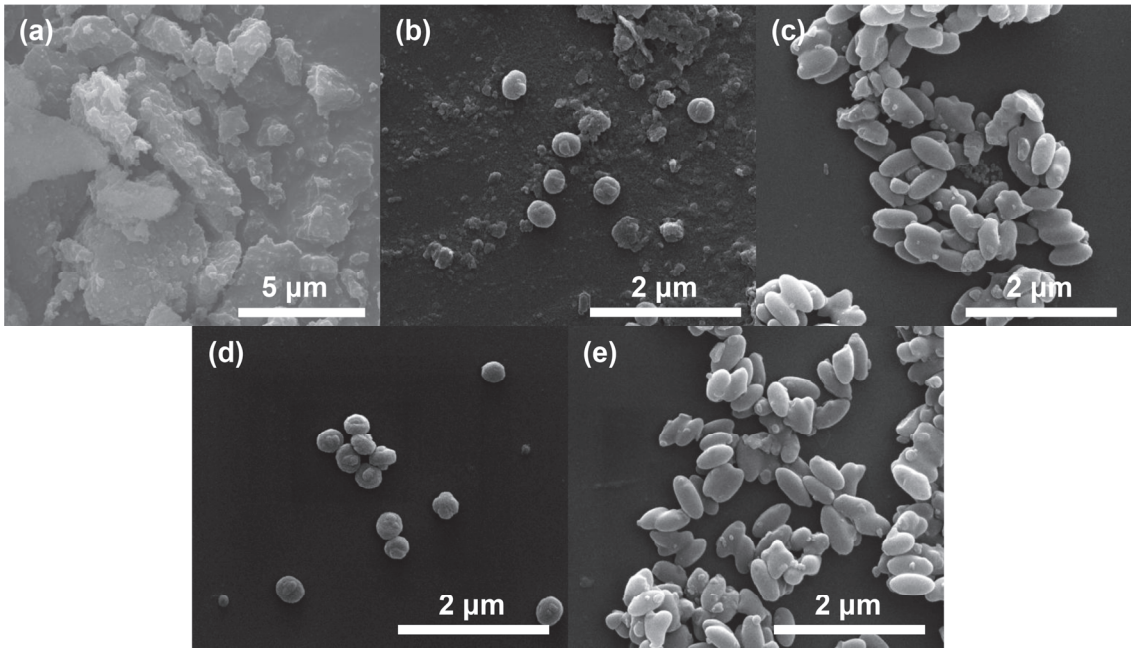

Figure 2. SEM images of (**a**) Rh/SiO_2, (**b**) Rh/MFI, (**c**) Rh/MEL, (**d**) Rh@MFI, and (**e**) Rh@MEL catalysts. The Rh@MEL and Rh/MEL samples are regular blocky fusiform. The Rh@MFI and Rh/MFI samples are massive and spherical. The Rh/SiO_2 sample has an irregular shape.

Table 1. Surface area and elemental composition analysis results of catalysts.

Catalysts	Surface Area (m^2/g)			Pore Sizes (nm)	ICP Elemental Analysis
	Total	External	Micro		Rh (wt %)
Rh@MFI	291	7	284	0.53	0.21
Rh@MEL	303	7	296	0.48	0.20
Rh/MFI	289	6	283	0.54	0.23
Rh/MEL	299	8	291	0.50	0.20
Rh/SiO_2	223	182	40	5.60	0.21

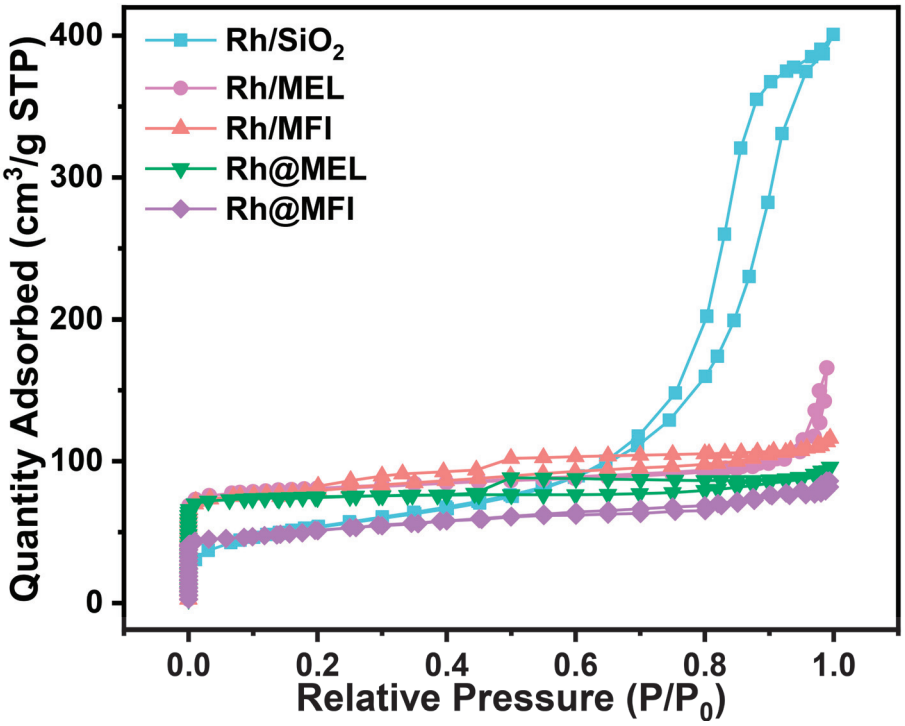

Figure 3. N_2 adsorption–desorption isotherms of different catalysts.

The characterization results above confirm that the synthesis of the catalyst supports met expectations, and the Rh loadings are consistent across the different catalysts. Given that the Rh species serve as the active sites for the hydroformylation reaction, it is essential to examine their dispersion within the catalysts. To investigate this, the catalysts were characterized using high-angle annular dark-field scanning transmission electron microscopy (HAADF-STEM) and transmission electron microscopy (TEM), with the results presented in Figure 4. TEM images of Rh/SiO_2, Rh/MFI, and Rh/MEL catalysts reveal distinct Rh clusters with sizes of 0.8 nm, 1.8 nm, and 1.2 nm, respectively. Compared with SiO_2, Rh species on MFI and MEL zeolites, when prepared via impregnation, exhibit larger particle sizes, suggesting that Rh species are better dispersed on SiO_2 than on MFI and MEL zeolites [33–36]. In contrast, no obvious Rh species are observed in the TEM images of Rh@MFI and Rh@MEL. However, energy dispersive X-ray spectroscopy (EDS) scanning images reveal a uniform distribution of Rh, indicating that the Rh species exist as sub-nanometer clusters or isolated Rh atoms, which are not readily observable in the STEM images. This finding aligns with the expectation that small Rh species may not be visible in high-resolution TEM images due to their extremely small size and uniform distribution within the zeolite supports [37–40].

Since Rh species were not detectable in the HAADF-STEM images of Rh@MFI and Rh@MEL catalysts, we employed CO adsorption FTIR to further confirm the dispersion of Rh and investigate its local environment. This technique can distinguish between isolated Rh atoms and Rh nanoparticles. Figure 5 shows the presence of three distinct IR bands. The band centered around 2055 cm^{-1} is attributed to CO linearly adsorbed on Rh clusters [41,42]. The bands at 2082 cm^{-1} and 2007 cm^{-1} correspond to the symmetric and asymmetric vibrations of geminal dicarbonyls on isolated Rh atoms [43,44]. A broad band spanning the 1900–2000 cm^{-1} region [45,46], which is associated with CO adsorbed in a bridge-like structure on Rh clusters, was almost absent. These findings confirm the presence of both isolated Rh atoms and Rh clusters in the Rh@MFI and Rh@MEL catalysts, with a notable proportion of isolated Rh atoms [47]. This result is consistent with the observations made in the HAADF-STEM analysis.

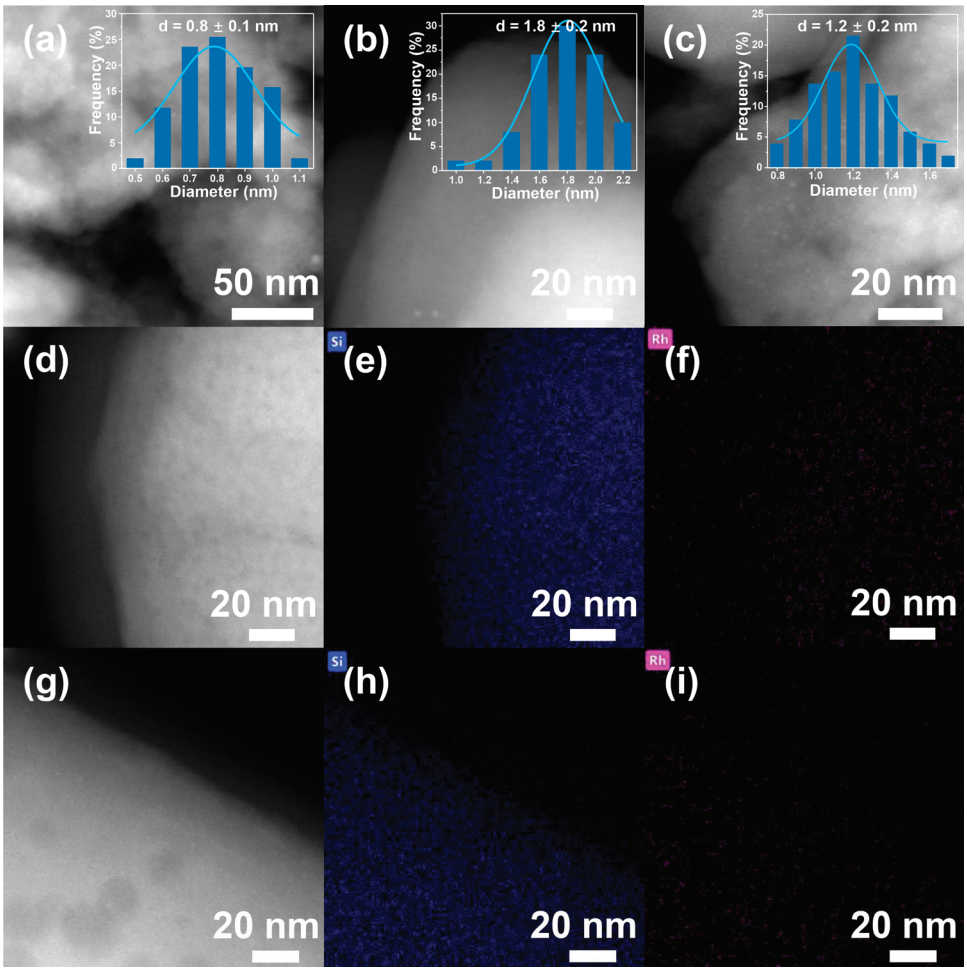

Figure 4. HAADF-STEM images and EDS analysis of different catalysts. HAADF-STEM images of (**a**) Rh/SiO_2, (**b**) Rh/MFI, and (**c**) Rh/MEL with the size distribution of Rh species. HAADF-STEM images of (**d**) Rh@MFI and (**g**) Rh@MEL catalysts and their EDS mapping images of (**e**,**h**) Si and (**f**,**i**) Rh.

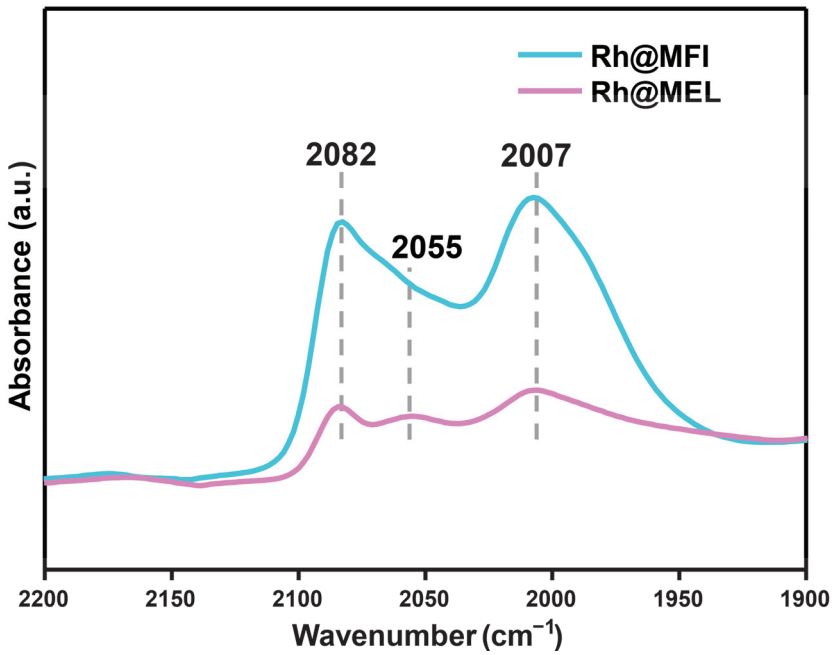

Figure 5. FTIR spectra of Rh@MFI and Rh@MEL catalysts upon CO absorption.

2.2. Catalytic Performance Evaluation

The $NaRu/SiO_2$ catalyst was utilized for the conversion of syngas into hydrocarbons, with a particular focus on maximizing the production of C_{5+} olefins. As demonstrated in a previous study [26], Na serves as a promoter by enhancing the dispersion of Ru nanoparticles. The uniform distribution of Na on the catalyst surface facilitates strong electronic interactions between Na and Ru nanoparticles. Na ions donate electrons to Ru atoms, enriching the Ru surface with electrons, which enhances CO adsorption at Ru sites while suppressing hydrogen reactivity. This electron transfer effect reduces the likelihood of secondary olefin hydrogenation, thereby increasing the olefin yield. Consequently, the $NaRu/SiO_2$ catalyst exhibits high selectivity for C_{5+} olefins during the catalytic conversion of syngas.

To optimize C_{5+} olefin production, the $NaRu/SiO_2$ catalyst with 5 wt% Ru loading and a Na/Ru molar ratio of 0.5 was employed for Fischer–Tropsch synthesis (FTS). The reaction was carried out under conditions of 260 °C, 1 MPa, and a H_2/CO ratio of 2 ($H_2/CO/N_2$ = 64/32/4). The results showed a CO conversion of 42.3% and an olefin selectivity of 66.4%, with C_{5+} olefins accounting for 50.8% of the olefin fraction. The selectivities for CH_4 and CO_2 were 3.0% and 2.7%, respectively (Figure 6a). The organic phase of the FTS products was then used as feedstock for the hydroformylation reaction. Specifically, 0.3 g of FTS products were mixed with 5 mL of toluene, and the reaction was carried out at 80 °C, 3 MPa, and a H_2/CO ratio of 1 ($H_2/CO/Ar$ = 45/45/10).

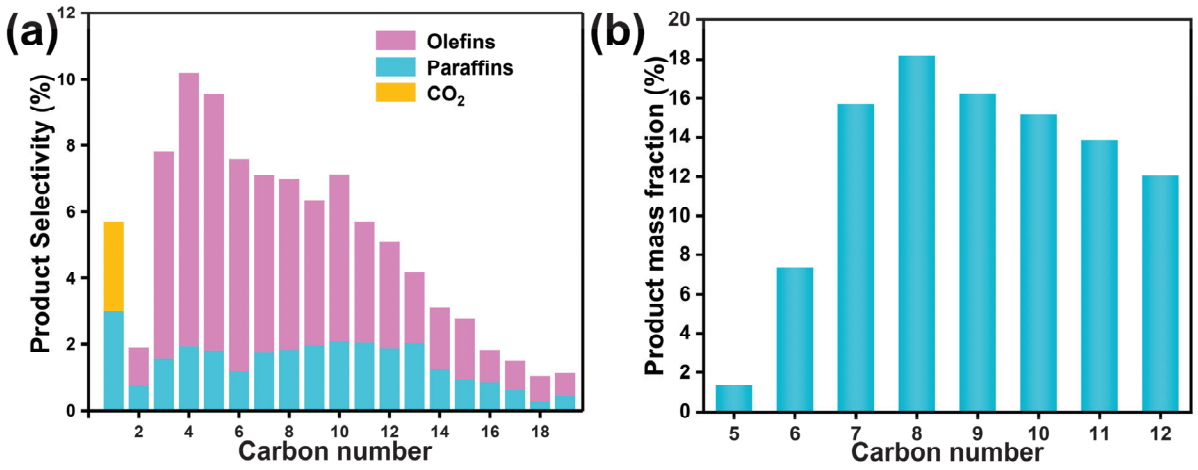

Figure 6. (**a**) Detailed product distribution (including CO_2) and (**b**) the mixed olefin of C_5–C_{12} with the same mass fraction in the organic phase of the FTS product.

To assess the effect of olefin diffusion on the reaction performance, a series of Rh catalysts with different Rh loading methods were employed. Rh@MFI and Rh@MEL catalysts were prepared via a one-pot hydrothermal crystallization process, resulting in highly dispersed Rh species encapsulated within the zeolite framework. This arrangement allows the zeolite framework to guide the reaction pathway of intermediates confined in the space between the zeolite structure and Rh centers, promoting the exclusive formation of linear aldehyde products [31,32]. In contrast, Rh/MFI, Rh/MEL, and Rh/SiO_2 catalysts were synthesized via impregnation, resulting in larger Rh nanoparticles exposed on the external surface of the support, where they are more accessible to olefin molecules. In the hydroformylation reaction, olefins must diffuse to the Rh sites for conversion into aldehydes. The kinetic diameters of normal olefins ranging from C_5 to C_{12} are between 0.4 and 0.6 nm. The zeolite structure may impede olefin diffusion, thus affecting their accessibility to catalytic sites [48,49].

The catalytic performances of these catalysts in the hydroformylation of C_{5+} mixed olefins are shown in Figure 7a. The Rh@MEL catalyst exhibited higher C_{5+} olefin conversion and C_{6+} aldehyde selectivity compared with Rh@MFI. Although both MFI and MEL zeolites are microporous materials with similar micropore volumes (Table 1), MEL zeolite features two sets of straight channels, while MFI has one straight and one sinusoidal channel [50–52]. The sinusoidal channels in MFI impose greater diffusion resistance for C_{5+} olefins, requiring the olefins to overcome additional barriers to access Rh sites. Consequently, Rh@MEL displayed higher catalytic activity compared with Rh@MFI.

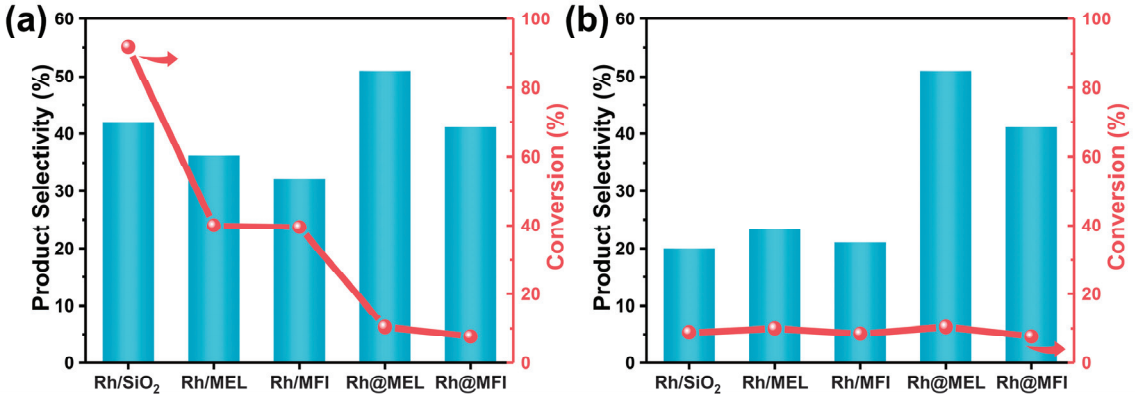

Figure 7. (**a**) The conversion and product selectivity of C_{5+} olefins catalyzed by different catalysts at the same time. (**b**) When the conversion rate is about 10%, the product selectivity of C_{6+} aldehyde in the hydroformylation of C_{5+} olefin catalyzed by different catalysts is obtained.

When Rh was loaded onto the support via the impregnation method (Rh/MEL, Rh/MFI, and Rh/SiO_2), the catalytic activity was significantly higher, indicating that olefin diffusion plays a critical role in determining catalytic performance. Olefin conversion was found to be higher over Rh/SiO_2 (>90%) than Rh/MEL and Rh/MFI. A plausible explanation for this is that a significant fraction of Rh atoms is embedded within the zeolite framework in Rh/MEL and Rh/MFI, making them less accessible to the olefin feedstock. In contrast, SiO_2 is mesoporous, and the Rh sites on SiO_2 are more easily reached by olefins, resulting in the higher conversion of C_{5+} olefins. This suggests that the zeolite framework introduces greater diffusion resistance for C_{5+} olefins. Despite the better Rh dispersion in the zeolite structure, the diffusion constraints make it more difficult for C_{5+} olefins to access these active sites, leading to lower activity in the hydroformylation reaction. Although the Rh@MEL catalyst displayed higher selectivity for C_{6+} aldehydes than Rh/SiO_2, the conversion of long-chain olefins was much lower over Rh@MEL. Therefore, enhanced feedstock diffusion is essential for efficient hydroformylation over Rh@MFI and Rh@MEL catalysts, which is crucial for the tandem conversion of syngas to aldehydes and alcohols.

To facilitate a more accurate comparison of the catalytic activities, we controlled the olefin conversion rate to approximately 10% and compared the selectivity of aldehydes with the results presented in Figure 7b. Similar to the findings above, the Rh@MFI and Rh@MEL catalysts exhibited higher selectivity. This is primarily attributed to the confinement effect within the zeolite channels, which restricts the isomerization of olefins within the pores, thereby facilitating their transformation into aldehydes. In contrast, the lack of such confinement on Rh/MEL, Rh/MFI, and Rh/SiO_2 catalysts allows olefins to more readily undergo isomerization, resulting in lower selectivity for aldehydes.

We compare the catalysts in this work with those in published works. For Rh/MEL, Rh/MF,I and Rh/SiO_2 catalysts, the selectivity of aldehyde is basically maintained between 35% and 50%, which is better than most catalysts prepared through the conventional impregnation method [32]. In contrast, the aldehyde selectivity of Rh@MEL and Rh@MFI

catalysts is almost the same as that of Rh@S-1 catalysts prepared through solvo-free hydrothermal synthesis methods reported in the literature [53], both of which are about 50%. However, the conversion rate of our catalyst is slightly lower than that of other Rh@MEL and Rh@MFI prepared through the same method [54]. We speculate that this is due to the effect of the concentration of specific olefins in the feedstock on their conversion and aldehyde selectivity. In the studies reported in the literature, the raw materials used were all single olefin instead of C_{5+} olefin mixture, which we believe is the reason why the aldehyde selectivity observed in this work is lower than that reported in the literature.

In addition to C_{5+} olefins, the organic phase of the FTS products also consists of paraffins of varying chain lengths and a significant proportion of short-chain olefins such as ethene and propene. These components can adsorb onto the active sites of the hydroformylation catalyst, reducing the availability of catalytic active sites for C_{5+} olefins and lowering their conversion. Furthermore, FTS generates substantial amounts of water, which can interact with the active sites of the hydroformylation catalyst, potentially altering the reaction pathways for C_{5+} olefins. To explore the effects of short-chain olefins, alkanes, and water on the hydroformylation of C_{5+} olefins, experiments were conducted using the organic phase of the FTS products obtained over the $NaRu/SiO_2$ catalyst. These studies aimed to evaluate how these substances influence catalytic performance and provide insights for optimizing the tandem reaction process.

To investigate the effect of water on hydroformylation, 1 mL of water was added to the reaction system. The results, shown in Figure 8a, indicate that water had a minimal impact on both the conversion of C_{5+} olefins and the selectivity for C_{6+} aldehydes. These findings suggest that water has a negligible influence under the conditions studied, supporting the feasibility of coupling the FTS and hydroformylation reactions for efficient syngas conversion to C_{6+} aldehydes.

The organic phase of the FTS products contains significant amounts of long-chain paraffins, which may influence the hydroformylation of long-chain olefins. To assess this, we prepared a mixture of C_5–C_{12} olefins that mirrored the mass distribution found in the FTS products (Figure 8b). Using this mixed olefin feedstock, hydroformylation was conducted at 80 °C, 3 MPa, and a H_2/CO ratio of 1 ($H_2/CO/Ar$ = 45/45/10). The results, shown in Figure 6b, indicate a slight increase in both the conversion of C_{5+} olefins and the selectivity for C_{6+} aldehydes compared with the control experiment using FTS products as feedstock. This modest improvement is likely due to the dilution effect of paraffins in the FTS products, which could have reduced the competition for catalytic sites. However, under the conditions of this study, the overall impact of long-chain alkanes on the hydroformylation of C_{5+} olefins was negligible.

To further explore the influence of short-chain olefins on the hydroformylation of C_{5+} olefins, propene was chosen as a co-fed component. The reaction was conducted with a gas feedstock composition of $H_2/CO/propylene/Ar$ = 45/45/2/8. The results, shown in Figure 8c, demonstrate that the presence of propene led to a decrease in both the conversion of C_{5+} olefins and the selectivity for C_{6+} aldehydes, compared with the control reaction ($H_2/CO/Ar$ = 45/45/10). A plausible explanation for this is that propene, due to its smaller molecular size and faster diffusion rate, is more readily adsorbed onto the catalyst's active sites. This preferential adsorption reduces the number of available active sites for C_{5+} olefins, thereby lowering their conversion. Furthermore, the reduced availability of catalytic sites may increase the likelihood of alternative reaction pathways for C_{5+} olefins, such as hydrogenation or isomerization, which can lead to a decrease in selectivity for C_{6+} aldehydes. These findings highlight the competitive adsorption effects of short-chain olefins and underscore the importance of catalyst design in tandem reactions. It

is crucial to optimize catalyst properties to minimize these competitive effects and enhance the selective conversion of C_{5+} olefins to C_{6+} aldehydes.

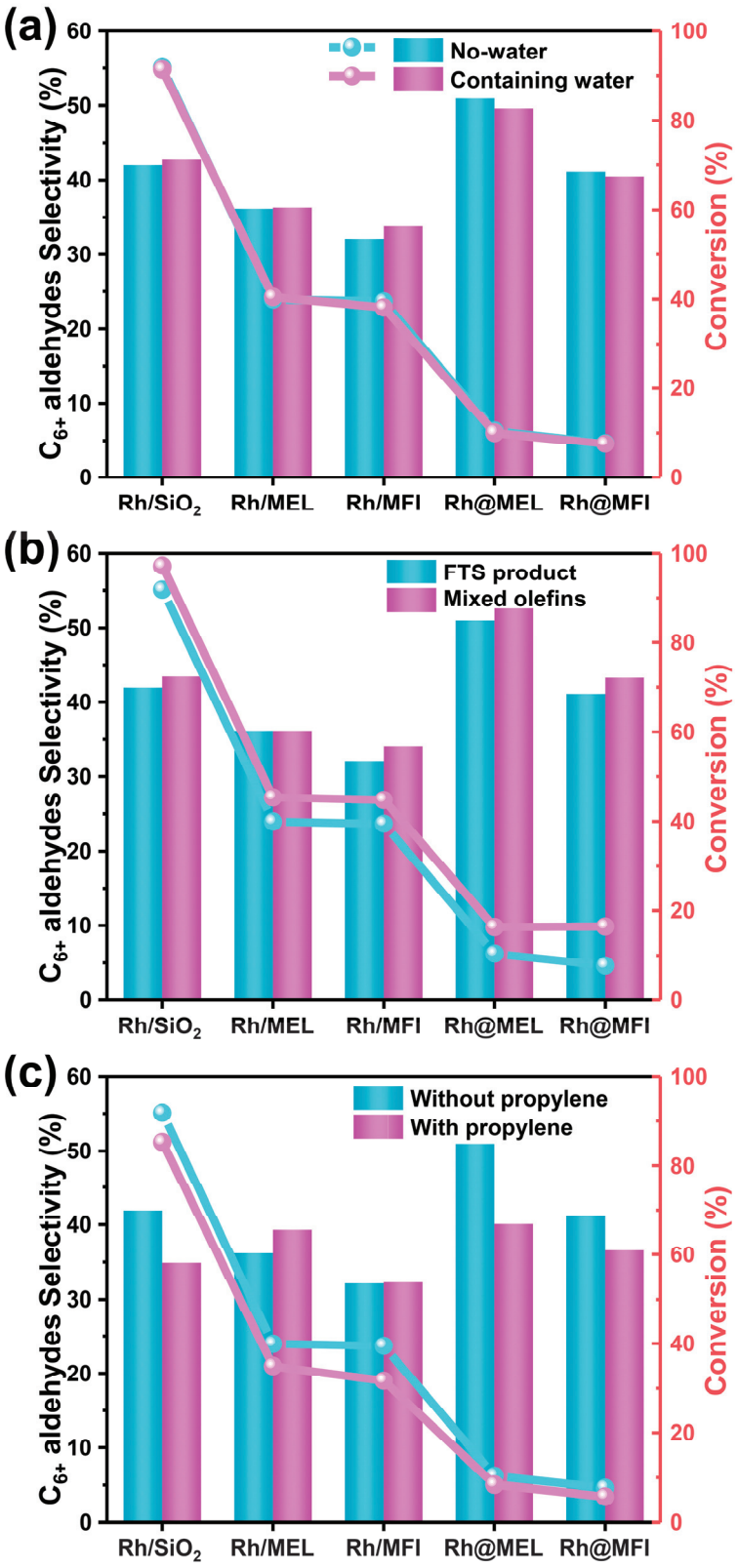

Figure 8. Conversions of C_{5+} olefins and the selectivity of C_{6+} aldehydes over various hydroformylation catalysts in the presence of (**a**) water, (**b**) alkane, and (**c**) propylene.

3. Experimental Section

3.1. Materials Synthesis

NaRu/SiO_2 Preparation: The catalyst was prepared by incipient wetness impregnation. First, 0.3173 g nitrosyl ruthenium nitrate (Ru $\geq$ 31.3%, Alfa) was dissolved in 5.3 mL deionized water to prepare a nitrosyl ruthenium nitrate solution according to the required volume for the incipient wetness impregnation of 2 g of aerosol silica (99.9%, Aladdin, Brussels, Belgium). Then 0.0437 g $NaNO_3$ (AR, Beijing Tongguang Fine Chemical Co., Beijing, China) was added to the nitrosyl ruthenium nitrate solution to form the impregnation precursor solution. In order to better dissolve ruthenium nitrosyl nitrate and $NaNO_3$, the precursor solution was ultrasonic for 30 min. Then the SiO_2 support was impregnated with the above precursor solution and stirred at room temperature until impregnated completely. The sample was dried at 80 °C for 12 h and calcined in air at 400 °C for 4 h to obtain a NaRu/SiO_2 catalyst.

Rh@MFI Preparation: An amount of 4.06 g of TPAOH (tetrapropyl ammonium hydroxide, 40 wt% in H_2O, Sigma-Aldrich, St. Louis, MO, USA), 0.0725 g of KOH (AR, Beijing Tongguang Fine Chemical Co.), and 9.05 g of deionized water were mixed at room temperature to obtain a TPAOH solution. Then, 4.17 g TEOS (tetraethyl orthosilicate, >99%, Alfa Aesar, Ward Hill, MA, USA) was added, and the mixture was stirred at room temperature for 6 h. A precursor of 0.0051 g $RhCl_3 \cdot xH_2O$ (for an Rh loading of 0.21%) dissolved in 0.1 mL deionized water and 0.1 mL EDA (ethylenediamine, $\geq$99.5%, Sigma-Aldrich) was prepared. The precursor solution was then added to the TEOS–TPAOH–water mixture and stirred for 30 min at room temperature. The resulting mixture was transferred to a 50 mL PTFE-lined autoclave and heated at 100 °C for 24 h under static conditions. Afterward, the product was washed with deionized water and ethanol (95%, Innochem, Beijing, China) until the pH reached 6–7, followed by drying at 60 °C overnight. The dried sample was calcined in a muffle furnace at 560 °C, with a ramping rate of 2 °C/min, for 8 h and reduced with H_2 (10% H_2 in Ar) at 500 °C for 4 h. The final catalyst was labeled Rh@MFI. The molar ratios of the raw materials used for the synthesis of the catalyst are as follows: 799 TPAOH: 2002 SiO_2: 129 KOH: 63811 H_2O: 1 Rh_2O_3: 150 EDA.

Rh@MEL Preparation: An amount of 3.88 g of TBAOH (tetrabutylammonium hydroxide, 40 wt% in H_2O, Sigma-Aldrich), 0.0303 g of KOH, and 2.32 g of deionized water were mixed at room temperature to obtain a TBAOH solution. Then, 4.13 g TEOS was added, and the mixture was stirred at room temperature for 6 h. A precursor of 0.0068 g $RhCl_3 \cdot xH_2O$ (for an Rh loading of 0.20%) dissolved in 0.1 mL deionized water and 0.1 mL EDA was prepared. The precursor solution was then added to the TEOS–TBAOH–water mixture and stirred for 30 min at room temperature. The resulting mixture was transferred to a 50 mL PTFE-lined autoclave and heated at 100 °C for 24 h under static conditions. Afterward, the product was washed with deionized water and ethanol until the pH reached 6–7, followed by drying at 60 °C overnight. The dried sample was calcined in a muffle furnace at 560 °C, with a ramping rate of 2 °C/min, for 8 h and reduced with H_2 (10% H_2 in Ar) at 500 °C for 4 h. The final catalyst was labeled Rh@MEL. The molar ratios of the raw materials used for the synthesis of the catalyst are as follows: 399 TBAOH: 1321 SiO_2: 36 KOH: 17215 H_2O: 1 Rh_2O_3: 100 EDA.

Rh/MEL, Rh/MFI, and Rh/SiO_2 Preparation: The catalysts were prepared through wetness impregnation. In the preparation process of Rh/MFI and Rh/MEL described above, no metal precursor solution was added, but the other processes remained the same, resulting in the preparation of MFI and MEL samples. In a typical synthesis process, 4.36 mg of $RhCl_3$ is dissolved in 1.45 mL of deionized water to prepare a metal precursor solution, and then 1 g MFI or MEL or SiO_2 samples are added to the solution and continuously stirred at room temperature until the impregnation is complete. The sample is then dried

at 80 °C for 12 h, calcined in air at 560 °C for 8 h, and finally reduced with H_2 (10% H_2 in Ar) at 500 °C for 4 h. The obtained samples were labeled as Rh/MFI, Rh/MEL, and Rh/SiO_2 catalysts.

3.2. Characterization Methods

Powder X-ray diffraction (XRD) patterns were measured using a Bruker D8 diffractometer (Bruker, Saarbrücken, Germany) using Cu Kα (λ = 0.15406 nm) radiation. The scanning range was 5–50° with a step size of 0.02°.

Inductively coupled plasma emission spectrometry (ICP-OES) analysis was performed using a PerkinElmer Optima 2100DV spectrometer (PerkinElmer, Waltham, MA, USA) equipped with a charge-coupled device detector to analyze the Rh content in the samples.

N_2 physical adsorption desorption analysis of Rh/SiO_2 was performed using a MicroActive ASAP 2420 physical adsorption analyzer (Micromeritics, Norcross, GA, USA), while the analyses of Rh/MFI, Rh/MEL, Rh@MFI, and Rh@MEL were performed using a MicroActive ASAP 2020 physical adsorption analyzer (Micromeritics, Norcross, GA, USA). Approximately 100 mg samples were pretreated under vacuum conditions at 350 °C for 5 h, and the N_2 isotherms were determined at −196 °C. The specific surface areas and pore size of Rh/SiO_2 were determined through the Brunauer–Emmett–Teller (BET) method and *t*-plot method, respectively. The surface areas of Rh/MFI, Rh/MEL, Rh@MFI, and Rh@MEL were determined through the Horvath–Kawazoe method.

Scanning electron microscopy (SEM) analysis was performed using an FEI Quanta 400 thermal field emission scanning electron microscope for electron microscopic observation at a voltage of 10 kV. Before microscope observation, an appropriate amount of the sample was put into a 10 mL centrifuge bottle with 5 mL of ethanol. The mixture was then subjected to ultrasound for 1 h to disperse the sample. A total of 5 drops of the mixture were added to a silicon support plate with a dropper. The silicon support plate with the sample was fixed to a conductive adhesive for gold spraying prior to the SEM analysis.

Transmission electron microscopy (TEM) and high-angle dark field scanning electron microscopy (HAADF-STEM) were used to observe the distribution of Rh species in the samples. A small number of samples were fully ground and dispersed in 7 mL dichloromethane (CH_2Cl_2) solution. After 30 min of ultrasound, 3–5 drops of suspension were applied to the ultrathin carbon film copper grid with an eyedropper. An FEI-Tecnai-Talos transmission electron microscope was used for observation with an acceleration voltage of 200 kV and a resolution of 1.4 Å.

Infrared spectra were collected using a Bruker VERTEX 70 infrared spectrometer (Bruker, Dresden, Germany). Spectra were obtained at a resolution of 4 cm^{-1}. The spectra of Rh@MEL and Rh@MFI catalysts upon CO adsorption were recorded in an environmental chamber. The sample (~30 mg) was first fully ground and pressed into translucent flakes. Then the sample was put into the chamber, heated to 500 °C under 10% H_2 (H_2/He = 10/90) flow, and pretreated for 1 h. Then it was cooled to room temperature and then purged with He for 10 min. After purging, the background spectrum was collected. CO flow was allowed into the sample chamber at a flow rate of 20 sccm for adsorption. During the CO adsorption process, the sample infrared spectra were collected every 30 s until the CO adsorption equilibrium (about 25 min). Then He flow was injected for purging. During the purging process, the infrared spectra of the sample were collected every 30 s until the spectrum was stable (about 25 min). The infrared spectrum of the sample after complete desorption was recorded.

3.3. Catalytic Performance Evaluation

Fischer–Tropsch Synthesis. The catalyst was evaluated using a micro-fixed bed reactor. The stainless-steel reaction tube had a quartz tube with an inner diameter of 6 mm, and the

stainless-steel tube was inserted into the quartz tube to detect the temperature. Typically, 0.1 g catalyst is diluted with 0.05 g silicon carbide, and the mixture is loaded into the constant temperature zone of the reactor. Before the catalytic reaction, the synthesis gas with a H_2/CO ratio of 2/1 (H_2/CO/N_2 = 64/32/4) was injected into the reactor at a flow rate of 5 mL/min (WHSV = 3000 mL/g_{cat}) after being reduced at 450 °C for 4 h with H_2 (40 mL/min). Unless otherwise specified, the reaction pressure is 1 MPa and the H_2/CO ratio is 2. After passing through a hot trap (393 K) and a cold trap (273 K), the gaseous effluent was analyzed online using an Agilent 6890N apparatus equipped with two detectors. A packed column (PoraPak Q) and two capillary columns (HP-PLOT/Q and HP-MOLESIEVE) were connected to a thermal conductivity detector (TCD) with Ar as the carrier gas for the analysis of H_2, N_2, CO, CH_4, and CO_2. An alumina capillary column (HP-AL/S) was connected to a flame ionization detector (FID) with N_2 as the carrier gas for the analysis of hydrocarbon gaseous products. The specific methods were as follows: The initial column temperature was set at 40 °C and held for 3 min, then ramped to 75 °C at a rate of 5 °C/min. The temperature was then increased to 200 °C at a rate of 10 °C/min, and held at 200 °C for 20 min. The split flow rate at the injection port was 37.9 mL/min with a split ratio of 4:1. Peak areas were obtained by integrating the peaks of each detected substance on the chromatogram. Since CH_4 was detectable on both the TCD and FID detectors, the peak areas of CH_4 from the two detectors were used to compare the results obtained from them. The molar fraction of each substance was determined using a calibration curve. The molar amount of each substance in the gas mixture was calculated per unit time based on the flow rate of the internal standard (N_2) and its chromatographic peak area. Finally, the conversion of feedstock molecules and the selectivity of products were calculated from the molar amount of each component in the gas mixture. The aqueous products, liquid oil products, and solid wax products were collected from a cold trap and a hot trap. The aqueous products and the liquid oil products were analyzed off-line using an Agilent 7890A gas chromatograph (Agilent Technologies, Santa Clara, CA, USA). An AB-InoWax column connected to an FID was employed with N_2 as the carrier gas for the analysis of the aqueous products. Additionally, an HP-PONA capillary column connected to an FID was employed with N_2 as the carrier gas for the analysis of the oil phase products. The solid wax products were analyzed off-line using an Agilent 8890 gas chromatograph. The wax product was dissolved in CS_2 and analyzed using an Ultra ALLOY$^+$-1 (Frontier Laboratories, Koriyama, Fukushima, Japan) column with an FID using N_2 as carrier gas.

CO conversion (X_{CO}) and product selectivity (S_i) were calculated using the following equation:

$$X_{CO} = \frac{F_{CO,in} - F_{CO,out}}{F_{CO,in}} \times 100\%$$

$$S_i = \frac{N_i \times n_i}{\sum(N_i \times n_i)} \times 100\%$$

where $F_{CO,in}$ and $F_{CO,out}$ represent moles of CO at the inlet and the outlet, respectively; S_i denotes the selectivity of product *i* on a carbon basis; N_i is the molar fraction of product *i*; and n_i is the carbon number of product *i*.

Hydroformylation Reaction. The catalyst was evaluated using a 50 mL high-pressure reactor. In a typical reaction, 5 mL of toluene is added to the high-pressure reactor as a solvent, followed by 0.03 g of catalyst and 0.3 g of feedstock (the organic phase product separated from the cold trap product from the FTS reactor). The reactor was sealed, purged 3 times with 1 MPa CO, filled with a 3 MPa H_2/CO ratio of 1 (H_2/CO/Ar = 45/45/10) syngas, heated to 80 °C, and maintained at a 1000 rpm stirring rate for 1 h. After the reaction, 1.5 g of the product was collected in a chromatographic bottle, which was subsequently analyzed via gas chromatography (Agilent 8890, equipped with an HP-5MS capillary

column). The tail gas was collected using a 30 mL gas sampling bag and analyzed using an Agilent 8890 GC equipped with both a TCD and an FID. The permanent gases (Ar, CO, and H_2) and hydrocarbons (including propene, propane) in the tail gas were separated by an HP-5MS and a GasPro capillary column, respectively. Ar was used as the internal standard for quantification. The specific methods were as follows: The initial column temperature was set at 50 °C and held for 5 min. Subsequently, the temperature was increased to 200 °C at a rate of 5 °C/min and held for 10 min. Finally, the temperature was raised to 250 °C at a rate of 10 °C/min and maintained at 250 °C for 10 min. The split flow rate at the injection port was 18.9 mL/min with a split ratio of 4:1. The peak area for each substance was obtained by integrating the chromatogram peaks. Subsequently, we employed GC–MS (Agilent 5977B GC/MSD, equipped with an HP-PONA capillary column) to identify individual components in the gaseous and liquid products, followed by the determination of the relative correction factors for each component. The specific methods are as follows: The initial column temperature was set at 30 °C and held for 10 min. Subsequently, the temperature was increased to 300 °C at a rate of 3 °C/min and maintained at 300 °C for 30 min. The split flow rate at the injection port was 15 mL/min with a split ratio of 50:1. The molar fraction of each substance in the gas product and the liquid product was determined using a calibration curve. The molar amounts of each substance in the gas product and liquid product were then calculated based on the internal standard and chromatographic peak areas. Finally, the conversion of raw materials and the selectivity of products were calculated based on the molar amount of each component. The conversion of C_{5+} olefins (X_{C5+}) and the selectivity of C_{6+} aldehydes (S_{C6+}) were calculated using the following equations:

$$X_{C5+} = \frac{F_{C5+,before} - F_{C5+,after}}{F_{C5+,before}} \times 100\%$$

$$S_{C6+} = \frac{F_{C6+}}{F_{C5+,before} - F_{C5+,after}} \times 100\%$$

where $F_{C5+,before}$ and $F_{C5+,after}$ represent the moles of C_{5+} olefins before and after the reaction, respectively, while F_{C6+} represents the moles of C_{6+} aldehydes after the reaction.

4. Conclusions

In this study, we investigated the catalytic conversion of syngas to C_{5+} aldehydes via hydroformylation, utilizing a series of Rh-based catalysts supported on different zeolite frameworks (MFI and MEL) and SiO_2. Our results demonstrate that the dispersion and accessibility of Rh species significantly influence the catalytic performance. The Rh@MFI and Rh@MEL catalysts, prepared via a one-pot hydrothermal crystallization process, exhibited higher selectivity for C_{6+} aldehydes (~50%), with Rh species being highly dispersed and confined within the zeolite frameworks. In contrast, catalysts prepared via impregnation, such as Rh/MFI, Rh/MEL, and Rh/SiO_2, displayed larger Rh nanoparticles (0.8–1.8 nm) exposed on the support surface, leading to a more accessible but less selective reaction pathway for C_{5+} olefins. The impact of olefin diffusion within the catalyst structure was a critical factor in determining the efficiency of the hydroformylation process. While zeolite-supported catalysts provided greater spatial confinement and enhanced selectivity for linear aldehyde formation, their performance was hindered by diffusion limitations, particularly in the case of MFI zeolite with a pore size of 0.55 nm. On the other hand, Rh/SiO_2 catalysts with a pore size of 5.6 nm, though exhibiting lower selectivity (~40%), showed higher olefin conversion (>90%) due to the more accessible mesoporous structure.

Moreover, this study explored the effect of FTS byproducts, including paraffins and short-chain olefins, on the hydroformylation reaction. Although the presence of long-chain paraffins had a negligible effect, the co-feeding of short-chain olefins, such as propene, reduced the catalytic efficiency of C_{5+} olefin conversion. This was attributed to competitive adsorption, where smaller olefins preferentially occupy active sites, thus hindering the conversion of longer olefins. Overall, this work highlights the importance of both catalyst design and reaction conditions in optimizing the hydroformylation of C_{5+} olefins. Further improvements in feedstock diffusion and catalyst accessibility, especially for zeolite-supported catalysts, could significantly enhance the tandem conversion of syngas to value-added aldehydes and alcohols. These findings provide valuable insights for the development of more efficient catalysts for syngas-based processes, paving the way for more sustainable and selective hydroformylation reactions.

Author Contributions: Conceptualization, P.H. and T.L.; investigation, Y.W.; software, X.C. and Y.D.; validation, Y.X. and C.S.; data curation, T.Y., X.Z. and H.H.; writing—original draft preparation, Y.W. and Y.D.; writing—review and editing, P.H.; project administration, C.S. All authors have read and agreed to the published version of the manuscript.

Funding: We acknowledge the support from the National Key R&D Program of China (No. 2023YFB4103102), National Natural Science Foundation of China (No. 92477203), Strategic Priority Research Program of the Chinese Academy of Sciences (No. XDA0400402), Beijing Natural Science Foundation (No. L245019), and Fundamental Research Program of Shanxi Province (Nos. YDZJSX2022A074, 202403021223010, and 202403021224011).

Data Availability Statement: Data are contained within the article.

Acknowledgments: We gratefully acknowledge Ying Liu and Xin Tong at Synfuels China Technology Co., Ltd., for the assistance in performing SEM and DRIFT analysis.

Conflicts of Interest: The authors declare no conflicts of interest.

References

1. Kang, J.; He, S.; Zhou, W.; Shen, Z.; Li, Y.; Chen, M.; Zhang, Q.; Wang, Y. Single-Pass Transformation of Syngas into Ethanol with High Selectivity by Triple Tandem Catalysis. *Nat. Commun.* **2020**, *11*, 827. [CrossRef] [PubMed]
2. Foit, S.R.; Vinke, I.C.; de Haart, L.G.J.; Eichel, R.A. Power-to-Syngas: An Enabling Technology for the Transition of the Energy System? *Angew. Chem. Int. Ed.* **2017**, *56*, 5402–5411. [CrossRef] [PubMed]
3. Jiao, F.; Li, J.; Pan, X.; Xiao, J.; Li, H.; Ma, H.; Wei, M.; Pan, Y.; Zhou, Z.; Li, M.; et al. Selective Conversion of Syngas to Light Olefins. *Science* **2016**, *351*, 1065–1068. [CrossRef]
4. Li, J.; He, Y.; Tan, L.; Zhang, P.; Peng, X.; Oruganti, A.; Yang, G.; Abe, H.; Wang, Y.; Tsubaki, N. Integrated Tuneable Synthesis of Liquid Fuels via Fischer–Tropsch Technology. *Nat. Catal.* **2018**, *1*, 787–793. [CrossRef]
5. Duyckaerts, N.; Bartsch, M.; Trotuş, I.T.; Pfänder, N.; Lorke, A.; Schüth, F.; Prieto, G. Intermediate Product Regulation in Tandem Solid Catalysts with Multimodal Porosity for High-Yield Synthetic Fuel Production. *Angew. Chem. Int. Ed.* **2017**, *56*, 11480–11484. [CrossRef] [PubMed]
6. Zhong, L.; Yu, F.; An, Y.; Zhao, Y.; Sun, Y.; Li, Z.; Lin, T.; Lin, Y.; Qi, X.; Dai, Y.; et al. Cobalt Carbide Nanoprisms for Direct Production of Lower Olefins from Syngas. *Nature* **2016**, *538*, 84–87. [CrossRef]
7. Cheng, K.; Gu, B.; Liu, X.; Kang, J.; Zhang, Q.; Wang, Y. Direct and Highly Selective Conversion of Synthesis Gas into Lower Olefins: Design of a Bifunctional Catalyst Combining Methanol Synthesis and Carbon–Carbon Coupling. *Angew. Chem. Int. Ed.* **2016**, *128*, 4803–4806. [CrossRef]
8. Torres Galvis, H.M.; Bitter, J.H.; Khare, C.B.; Ruitenbeek, M.; Dugulan, A.I.; de Jong, K.P. Supported Iron Nanoparticles as Catalysts for Sustainable Production of Lower Olefins. *Science* **2012**, *335*, 835–838. [CrossRef]
9. Ao, M.; Pham, G.H.; Sunarso, J.; Tade, M.O.; Liu, S. Active Centers of Catalysts for Higher Alcohol Synthesis from Syngas: A Review. *ACS Catal.* **2018**, *8*, 7025–7050. [CrossRef]
10. Luk, H.T.; Mondelli, C.; Ferre, D.C.; Stewart, J.A.; Perez-Ramirez, J. Status and Prospects in Higher Alcohols Synthesis from Syngas. *Chem. Soc. Rev.* **2017**, *46*, 1358–1426. [CrossRef] [PubMed]
11. Xiang, Y.; Kruse, N. Tuning the Catalytic CO Hydrogenation to Straight- and Long-Chain Aldehydes/Alcohols and Olefins/Paraffins. *Nat. Commun.* **2016**, *7*, 13058. [CrossRef] [PubMed]

12. Zhou, Z.; Zhang, K.; He, P.; Chang, H.; Zhang, M.; Yan, T.; Zhang, X.; Li, Y.; Cao, Z. Reactive Intermediate Confinement in Beta Zeolites for the Efficient Aerobic Epoxidation of α-Olefins. *Angew. Chem. Int. Ed.* **2025**, *64*, e202419900. [CrossRef] [PubMed]
13. Cai, Y.; Yin, A.; Zhang, X.; Wang, J.; Qin, X.; Yang, Y.; Qin, G.; Sun, X.; He, P.; Yang, Y. Carbon-Coated Ni-Fe Nanocatalysts: Bridging the Gap in Cinnamaldehyde Hydrogenation Performance and Durability. *Catalysts* **2023**, *13*, 1474. [CrossRef]
14. Liu, G.; Yang, G.; Peng, X.; Wu, J.; Tsubaki, N. Recent Advances in the Routes and Catalysts for Ethanol Synthesis from Syngas. *Chem. Soc. Rev.* **2022**, *51*, 5606–5659. [CrossRef] [PubMed]
15. Chen, Y.; Ma, L.; Zhang, R.; Ye, R.; Liu, W.; Wei, J.; Ordomsky, V.V.; Liu, J. Carbon-supported Fe Catalysts with Well-Defined Active Sites for Highly Selective Alcohol Production from Fischer-Tropsch Synthesis. *Appl. Catal. B Environ.* **2022**, *312*, 121393. [CrossRef]
16. Li, Y.; Zhao, Z.; Lu, W.; Jiang, M.; Li, C.; Zhao, M.; Gong, L.; Wang, S.; Guo, L.; Lyu, Y.; et al. Highly Selective Conversion of Syngas to Higher Oxygenates over Tandem Catalysts. *ACS Catal.* **2021**, *11*, 14791–14802. [CrossRef]
17. Zhao, Z.; Lu, W.; Yang, R.; Zhu, H.; Dong, W.; Sun, F.; Jiang, Z.; Lyu, Y.; Liu, T.; Du, H.; et al. Insight into the Formation of Co@Co2C Catalysts for Direct Synthesis of Higher Alcohols and Olefins from Syngas. *ACS Catal.* **2017**, *8*, 228–241. [CrossRef]
18. Martin, O.; Mondelli, C.; Cervellino, A.; Ferri, D.; Curulla-Ferré, D.; Pérez-Ramírez, J. Operando Synchrotron X-ray Powder Diffraction and Modulated-Excitation Infrared Spectroscopy Elucidate the CO_2 Promotion on a Commercial Methanol Synthesis Catalyst. *Angew. Chem. Int. Ed.* **2016**, *55*, 11031–11036. [CrossRef]
19. Xiang, Y.; Chitry, V.; Liddicoat, P.; Felfer, P.; Cairney, J.; Ringer, S.; Kruse, N. Long-Chain Terminal Alcohols through Catalytic CO Hydrogenation. *J. Am. Chem. Soc.* **2013**, *135*, 7114–7117. [CrossRef]
20. Bezemer, G.L.; Bitter, J.H.; Kuipers, H.P.C.E.; Oosterbeek, H.; Holewijn, J.E.; Xu, X.; Kapteijn, F.; van Dillen, A.J.; de Jong, K.P. Cobalt Particle Size Effects in the Fischer−Tropsch Reaction Studied with Carbon Nanofiber Supported Catalysts. *J. Am. Chem. Soc.* **2006**, *128*, 3956–3964. [CrossRef]
21. Li, Y.; Gao, W.; Peng, M.; Zhang, J.; Sun, J.; Xu, Y.; Hong, S.; Liu, X.; Liu, X.; Wei, M.; et al. Interfacial Fe5C2-Cu Catalysts toward Low-Pressure Syngas Conversion to Long-Chain Alcohols. *Nat. Commun.* **2020**, *11*, 61. [CrossRef] [PubMed]
22. Ge, Y.; Zou, T.; Martín, A.J.; Pérez-Ramírez, J. ZrO2-Promoted Cu-Co, Cu-Fe and Co-Fe Catalysts for Higher Alcohol Synthesis. *ACS Catal.* **2023**, *13*, 9946–9959. [CrossRef]
23. Lin, T.; Qi, X.; Wang, X.; Xia, L.; Wang, C.; Yu, F.; Wang, H.; Li, S.; Zhong, L.; Sun, Y. Direct Production of Higher Oxygenates by Syngas Conversion over a Multifunctional Catalyst. *Angew. Chem. Int. Ed.* **2019**, *58*, 4627–4631. [CrossRef] [PubMed]
24. Jeske, K.; Rösler, T.; Belleflamme, M.; Rodenas, T.; Fischer, N.; Claeys, M.; Leitner, W.; Vorholt, A.J.; Prieto, G. Direct Conversion of Syngas to Higher Alcohols via Tandem Integration of Fischer–Tropsch Synthesis and Reductive Hydroformylation. *Angew. Chem. Int. Ed.* **2022**, *61*, e202201004. [CrossRef]
25. An, Y.; Wang, X.; Yu, H.; Qi, X.; Lv, D.; Lin, T.; Zhong, L. Mn-Promoted Ru-Based Catalysts for Enhanced Fischer–Tropsch Synthesis of Olefins from Syngas. *ACS Catal.* **2023**, *13*, 13245–13256. [CrossRef]
26. Yu, H.; Wang, C.; Lin, T.; An, Y.; Wang, Y.; Chang, Q.; Yu, F.; Wei, Y.; Sun, F.; Jiang, Z.; et al. Direct Production of Olefins from Syngas with Ultrahigh Carbon Efficiency. *Nat. Commun.* **2022**, *13*, 5987. [CrossRef] [PubMed]
27. Yu, F.; Lin, T.; An, Y.; Gong, K.; Wang, X.; Sun, Y.; Zhong, L. Recent Advances in Co2C-Based Nanocatalysts for Direct Production of Olefins from Syngas Conversion. *Chem. Commun.* **2022**, *58*, 9712–9727. [CrossRef] [PubMed]
28. Xu, Y.; Li, X.; Gao, J.; Wang, J.; Ma, G.; Wen, X.; Yang, Y.; Li, Y.; Ding, M. A Hydrophobic FeMn@Si Catalyst Increases Olefins from Syngas by Suppressing C1 by-Products. *Science* **2021**, *371*, 610–613. [CrossRef] [PubMed]
29. Lin, T.; Yu, F.; An, Y.; Qin, T.; Li, L.; Gong, K.; Zhong, L.; Sun, Y. Cobalt Carbide Nanocatalysts for Efficient Syngas Conversion to Value-Added Chemicals with High Selectivity. *Acc. Chem. Res.* **2021**, *54*, 1961–1971. [CrossRef] [PubMed]
30. Zhai, P.; Xu, C.; Gao, R.; Liu, X.; Li, M.; Li, W.; Fu, X.; Jia, C.; Xie, J.; Zhao, M.; et al. Highly Tunable Selectivity for Syngas-Derived Alkenes over Zinc and Sodium-Modulated Fe5C2 Catalyst. *Angew. Chem. Int. Ed.* **2016**, *55*, 9902–9907. [CrossRef]
31. Zhang, X.; Yan, T.; Hou, H.; Yin, J.; Wan, H.; Sun, X.; Zhang, Q.; Sun, F.; Wei, Y.; Dong, M.; et al. Regioselective Hydroformylation of Propene Catalysed by Rhodium-Zeolite. *Nature* **2024**, *629*, 597–602. [CrossRef] [PubMed]
32. Dou, X.; Yan, T.; Qian, L.; Hou, H.; Lopez-Haro, M.; Marini, C.; Agostini, G.; Meira, D.M.; Zhang, X.; Zhang, L.; et al. Regioselective Hydroformylation with Subnanometre Rh Clusters in MFI Zeolite. *Nat. Catal.* **2024**, *7*, 666–677. [CrossRef]
33. Sun, Q.; Wang, N.; Yu, J. Advances in Catalytic Applications of Zeolite-Supported Metal Catalysts. *Adv. Mater.* **2021**, *33*, 2104442. [CrossRef] [PubMed]
34. Wang, H.; Wang, L.; Xiao, F.-S. Metal@Zeolite Hybrid Materials for Catalysis. *ACS Cent. Sci.* **2020**, *6*, 1685–1697. [CrossRef] [PubMed]
35. Liu, L.; Corma, A. Confining Isolated Atoms and Clusters in Crystalline Porous Materials for Catalysis. *Nat. Rev. Mater.* **2020**, *6*, 244–263. [CrossRef]
36. Babucci, M.; Guntida, A.; Gates, B.C. Atomically Dispersed Metals on Well-Defined Supports including Zeolites and Metal–Organic Frameworks: Structure, Bonding, Reactivity, and Catalysis. *Chem. Rev.* **2020**, *120*, 11956–11985. [CrossRef] [PubMed]

37. Liu, L.; Lopez-Haro, M.; Lopes, C.W.; Li, C.; Concepcion, P.; Simonelli, L.; Calvino, J.J.; Corma, A. Regioselective Generation and Reactivity Control of Subnanometric Platinum Clusters in Zeolites for High-Temperature Catalysis. *Nat. Mater.* **2019**, *18*, 866–873. [CrossRef]
38. Yan, T.; Hou, H.; Wu, C.; Cai, Y.; Yin, A.; Cao, Z.; Liu, Z.; He, P.; Xu, J. Unraveling the Molecular Mechanism for Enhanced Gas Adsorption in Mixed-Metal MOFs via Solid-State NMR Spectroscopy. *Proc. Natl. Acad. Sci. USA* **2024**, *121*, e2312959121. [CrossRef] [PubMed]
39. Dou, X.; Li, W.; Zhang, K.; Hou, H.; He, Z.; Zhu, C.; Meira, D.M.; Lopez-Haro, M.; Xia, Z.; He, P.; et al. Size-Dependent Structural Features of Subnanometer PtSn Catalysts Encapsulated in Zeolite for Alkane Dehydrogenation. *ACS Catal.* **2024**, *14*, 2859–2871. [CrossRef]
40. Gong, N.; Qin, G.; Li, P.; Zhang, X.; Chen, Y.; Yang, Y.; He, P. Enhanced Stability and Selectivity in Pt@MFI Catalysts for n-Butane Dehydrogenation: The Crucial Role of Sn Promoter. *Catalysts* **2024**, *14*, 760. [CrossRef]
41. Qi, L.; Das, S.; Zhang, Y.; Nozik, D.; Gates, B.C.; Bell, A.T. Ethene Hydroformylation Catalyzed by Rhodium Dispersed with Zinc or Cobalt in Silanol Nests of Dealuminated Zeolite Beta. *J. Am. Chem. Soc.* **2023**, *145*, 2911–2929. [CrossRef] [PubMed]
42. Matsubu, J.C.; Yang, V.N.; Christopher, P. Isolated Metal Active Site Concentration and Stability Control Catalytic CO_2 Reduction Selectivity. *J. Am. Chem. Soc.* **2015**, *137*, 3076–3084. [CrossRef] [PubMed]
43. McClure, S.M.; Lundwall, M.J.; Goodman, D.W. Planar Oxide Supported Rhodium Nanoparticles as Model Catalysts. *Proc. Natl. Acad. Sci. USA* **2010**, *108*, 931–936. [CrossRef] [PubMed]
44. Yates, D. Ultradispersed Rhodium Rafts: Their Existence and Topology. *J. Catal.* **1979**, *57*, 41–63. [CrossRef]
45. Chen, M.; Gupta, G.; Ordonez, C.W.; Lamkins, A.R.; Ward, C.J.; Abolafia, C.A.; Zhang, B.; Roling, L.T.; Huang, W. Intermetallic Nanocatalyst for Highly Active Heterogeneous Hydroformylation. *J. Am. Chem. Soc.* **2021**, *143*, 20907–20915. [CrossRef] [PubMed]
46. Huang, N.; Liu, B.; Lan, X.; Wang, T. Insights into the Bimetallic Effects of a RhCo Catalyst for Ethene Hydroformylation: Experimental and DFT Investigations. *Ind. Eng. Chem. Res.* **2020**, *59*, 18771–18780. [CrossRef]
47. Li, C.; Wang, W.; Yan, L.; Ding, Y. A Mini Review on Strategies for Heterogenization of Rhodium-Based Hydroformylation Catalysts. *Front. Chem. Sci. Eng.* **2017**, *12*, 113–123. [CrossRef]
48. Cnudde, P.; De Wispelaere, K.; Vanduyfhuys, L.; Demuynck, R.; Van der Mynsbrugge, J.; Waroquier, M.; Van Speybroeck, V. How Chain Length and Branching Influence the Alkene Cracking Reactivity on H-ZSM-5. *ACS Catal.* **2018**, *8*, 9579–9595. [CrossRef] [PubMed]
49. Yoo, K.; Tsekov, R.; Smirniotis, P.G. Experimental Proof for Resonant Diffusion of Normal Alkanes in LTL and ZSM-12 Zeolites. *J. Phys. Chem. B* **2003**, *107*, 13593–13596. [CrossRef]
50. Zhang, K.; Dou, X.; Zhou, Z.; Wang, Y.; Hou, H.; Meira, D.M.; Liu, L.; He, P. Tuning the Size and Spatial Distribution of Pt in Bifunctional Pt-zeolite Catalysts for Direct Coupling of Ethane and Benzene. *Chem. Eng. J.* **2024**, *497*, 154874. [CrossRef]
51. Chen, Z.; Zhao, W.; Zhang, H.; Ren, J.; He, P. Influence of Intracrystalline Diffusion Constraints Enhanced by Channel Fluctuation on Zeolite Catalyst Performance in Isomerization and Aromatization. *Fuel* **2024**, *362*, 130797. [CrossRef]
52. Zhang, K.; Dou, X.; Hou, H.; Zhou, Z.; Lopez-Haro, M.; Meira, D.M.; Liu, P.; He, P.; Liu, L. Generation of Subnanometer Metal Clusters in Silicoaluminate Zeolites as Bifunctional Catalysts. *JACS Au* **2023**, *3*, 3213–3226. [CrossRef] [PubMed]
53. Fang, Y.; Zhao, H.; Guo, X.; He, Y.; Yang, G.; Tsubaki, N. Silicalite-1 Encapsulated Rhodium Nanoparticles for Hydroformylation of 1-hexene. *Catal. Today* **2023**, *410*, 150–156. [CrossRef]
54. Dou, X.; Yan, T.; Li, W.; Zhu, C.; Chen, T.; Lo, B.T.W.; Marini, C.; Xiao, H.; Liu, L. Structure–Reactivity Relationship of Zeolite-Confined Rh Catalysts for Hydroformylation of Linear α-Olefins. *J. Am. Chem. Soc.* **2025**, *147*, 2726–2736. [CrossRef]

catalysts

MDPI

Article

Unravel the Roles of the Acid Sites in Different Pore Channels of HZSM-5 Catalyst on Ethanol Conversion to Light Olefin

Wei Xia *, Xinrui Wang, Di Wang, Zhenhua Jiang, Yanli Zhang, Shuangshuang Li, Mingyuan Dong, Kun Chen and Dong Liu

State Key Laboratory of Heavy Oil Processing, College of Chemistry and Chemical Engineering, China University of Petroleum (East China), Qingdao 266580, China; wxr13015164529@163.com (X.W.); wang_di_19@163.com (D.W.); jzh000906@163.com (Z.J.); qustzyl@126.com (Y.Z.); sshuangg@126.com (S.L.); dmydsg666@163.com (M.D.); chenkun@upc.edu.cn (K.C.); liudong@upc.edu.cn (D.L.)
* Correspondence: xiawei@upc.edu.cn; Tel.: +86-532-86984615

Abstract: Catalytic conversion of bioethanol is a promising production method for preparing light olefin. However, the role of acid sites in different pore channels of HZSM-5 catalyst is not clear. The roles of acid sites in different channels of HZSM-5 catalyst on the conversion of ethanol to ethylene and propylene was investigated by density functional theory (DFT). The results show that the conversion of ethanol to ethylene mainly occurs at the acid site of the sinusoidal channel (T11) of HZSM-5, and the conversion of ethanol to propylene mainly occurs at the acid site of the straight channel (T10) of HZSM-5 catalyst. The adsorption and diffusion behaviors of ethylene and propylene in straight and sinusoidal channels of HZSM-5 were simulated by the molecular dynamics method. The results show that for the adsorption of ethylene and propylene, the acid sites of sinusoidal channel (T11) with SiO_2/Al_2O_3 = 128 is more conducive to improving the selectivity of ethylene, and the acid sites of straight channel (T10) with SiO_2/Al_2O_3 = 128 is more conducive to improving the propylene selectivity. For the diffusion of ethylene and propylene, the acid sites in the straight channel (T10) of HZSM-5 (SiO_2/Al_2O_3 = 128) are more beneficial to improve propylene selectivity.

Keywords: ethanol; light olefin; HZSM-5 catalyst; acid sites; pore channels

1. Introduction

The light olefins mainly include ethylene and propylene, which are important raw materials for chemical production. With the rapid development of the economy and industry, the demand for light olefins is increasing rapidly. In addition, some catalytic cracking (FCC) processes specially used for propylene production have been developed and industrialized [1,2]. When ZSM-5 is mixed with FCC catalyst, olefins in FCC gasoline fractions are converted into light olefins containing propylene [3–5]. Ali et al. [6] discovered that the distributions of acidic sites and ZSM-5 morphology significantly altered local residence time and resulted in different selectivity to aromatics and heavier hydrocarbons during gas-phase CO_2 conversion, which provided an efficient approach for direct CO_2 conversion to aromatics. Depending on the choice of the metal, metal oxide, and zeolite, light olefins, long-chain linear a-olefins, long-chain paraffins, aromatics, alcohols, and acids can be selectively produced [7]. Iwamoto et al. [8] developed a Ni-M41 catalyst for converting ethanol into ethylene, which reached the maximum ethylene yield at 673 K and 2000–3000 h^{-1}.

The adjustment of aluminum in HZSM-5 catalyst has also attracted extensive attention of researchers. Sazama et al. [9] found that for the same SiO_2/Al_2O_3 ratio and crystal size, Al pair is more conducive to oligomerization and hydrogen transfer reaction of 1-butene, while single Al is more conducive to cracking of 1-butene. Structure directing- agent (SDA) and sodium cation have a certain influence on the position of Al atom in the framework of ZSM-5 synthesis. Yokoi et al. [10] found that Al atoms on H-ZSM-5 synthesized by using tetrapropylammonium (TPA) cation structure directing-agent (SDA) were mainly located at the channel intersections in the absence of Na cations. Janda et al. [11] adjusted the distribution of aluminum in HZSM-5 by increasing the aluminum content, so that most of the aluminum was located at the intersection of channels, which was beneficial to dehydrogenation rather than cracking of n-butane. Liang et al. [12] found that HZSM-5 catalyst prepared with ethyl orthosilicate as a silicon source has more acid sites at channel intersections and higher selectivity for ethylene and aromatic hydrocarbons; HZSM-5 catalyst prepared with silica sol as a silicon source has more acid sites with straight channels and sinusoidal channels and has higher selectivity for propylene and higher olefins. Kim et al. [13] successfully prepared HZSM-5 molecular sieves with different distributions of Al atoms in the framework by adjusting the crystallization temperature. Wang et al. [14] studied the product distribution of methanol to olefins (MTO) on HZSM-5 by DFT calculation and found that the product distribution based on aromatic hydrocarbon and olefin ring was obviously different. Although people have conducted a lot of experimental research on the ETO process on HZSM-5 catalyst, the role of acid sites in different channels of HZSM-5 catalyst in the reaction of ethanol to light olefins is still unclear.

Different pore structures and acid site distributions of HZSM-5 catalyst have significant effects on the adsorption and diffusion behavior of reactants, which in turn affects the selectivity of the products. Therefore, understanding the adsorption and diffusion behavior of ethylene and propylene on the HZSM-5 catalyst is of great significance for optimizing the catalyst design and improving the reaction selectivity. However, the Roles of the acid sites in different pore channels of HZSM-5 catalyst on ethanol conversion to light olefin have not been systematically investigated up to now. In this work, DFT was used to calculate the energy required to catalyze the conversion of ethanol to ethylene and propylene at the acid sites of the straight, sinusoidal, and intersection channels of the HZSM-5 zeolite. The reaction path of ethanol conversion to ethylene and propylene on HZSM-5 catalyst is based on our previous work [15] and the work of Yin et al. [16] (as shown in Figure 1). The adsorption and diffusion behaviors of ethylene and propylene on different pore acid sites of HZSM-5 catalyst were simulated by molecular dynamics method, and the effects of different pore acid sites on the selectivity of ethylene and propylene were discussed.

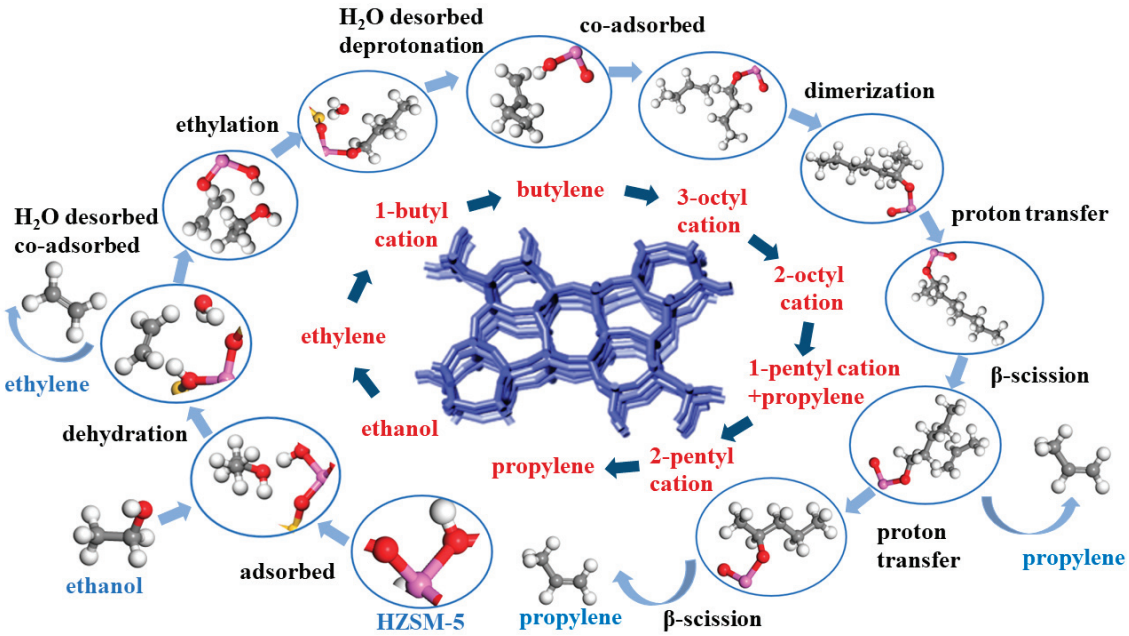

Figure 1. Reaction path of ethanol conversion to ethylene and propylene on HZSM-5 catalyst. The yellow, red, gray, pink, and white balls represent the Si, O, C, Al, and H atoms, respectively.

2. Results and Discussion

2.1. DFT Simulation Results

Based on our previous work [15] and the work of Yin et al. [16], the reaction path of ethanol conversion to ethylene and propylene is proposed. The specific process is as follows: Ethanol is initially adsorbed on the acid site of HZSM-5 catalyst, in which the hydroxyl group of ethanol interacts with hydrogen protons in the HZSM-5 catalyst, resulting in the production of ethylene and water. The resultant ethylene and reactant ethanol are co-adsorbed on the surface of the HZSM-5 molecular sieve, leading to ethylation reactions that give rise to 1-butyl cations. Subsequently, a proton is lost from the methyl group to form butylene. Some butylene undergoes dimerization with 1-butylcation, resulting in the formation of 3-octyl cations. Proton transfer occurs within these 3-octyl cations, leading to their conversion into 2-octyl cations, and 2-octyl cations are decomposed by β-scission to form propylene and 1-pentyl cations. 1-pentyl cations undergo proton transfer to form the 2-pentyl cations, and the 2-pentyl cations undergo β-scission to form propylene.

Eight reaction processes involve eight transition states (TSs), as shown in Figure 2. The activation barrier of a single step of each TS is calculated as the energy difference between a TS and its previous intermediate. The energy barrier differences of all TSs are shown in Figure 2. The reaction free energy barriers of three different channels were compared, and then the most favorable channel for the conversion of ethanol into ethylene and propylene was selected.

Figure 3 shows the channels that require the least energy for each step of converting ethanol into ethylene and propylene at T10, T11, and T12 acid sites of HZSM-5 catalyst.

As shown in Figure 3, the energy required to catalyze the dehydration of ethanol to ethylene on the acid site of the sinusoidal channel of HZSM-5 molecular sieve is the lowest, so the acid site of the sinusoidal channel of HZSM-5 molecular sieve is more conducive to the conversion of ethanol to ethylene. In the process of producing ethylene from ethanol, HZSM-5 catalyst with more sinusoidal pore acid sites can be selected. For the conversion of ethanol to propylene, the rate-determining step of the reaction path is β-scission. The straight channel acid site of HZSM-5 molecular sieve catalyzes the conversion of ethanol to propylene, and the energy required for β-scission is the lowest, so the straight channel acid site of HZSM-5 molecular sieve is more favorable for catalyzing the conversion of ethanol

to propylene. In the process of producing propylene from ethanol, HZSM-5 catalyst with more straight channel acid sites can be selected.

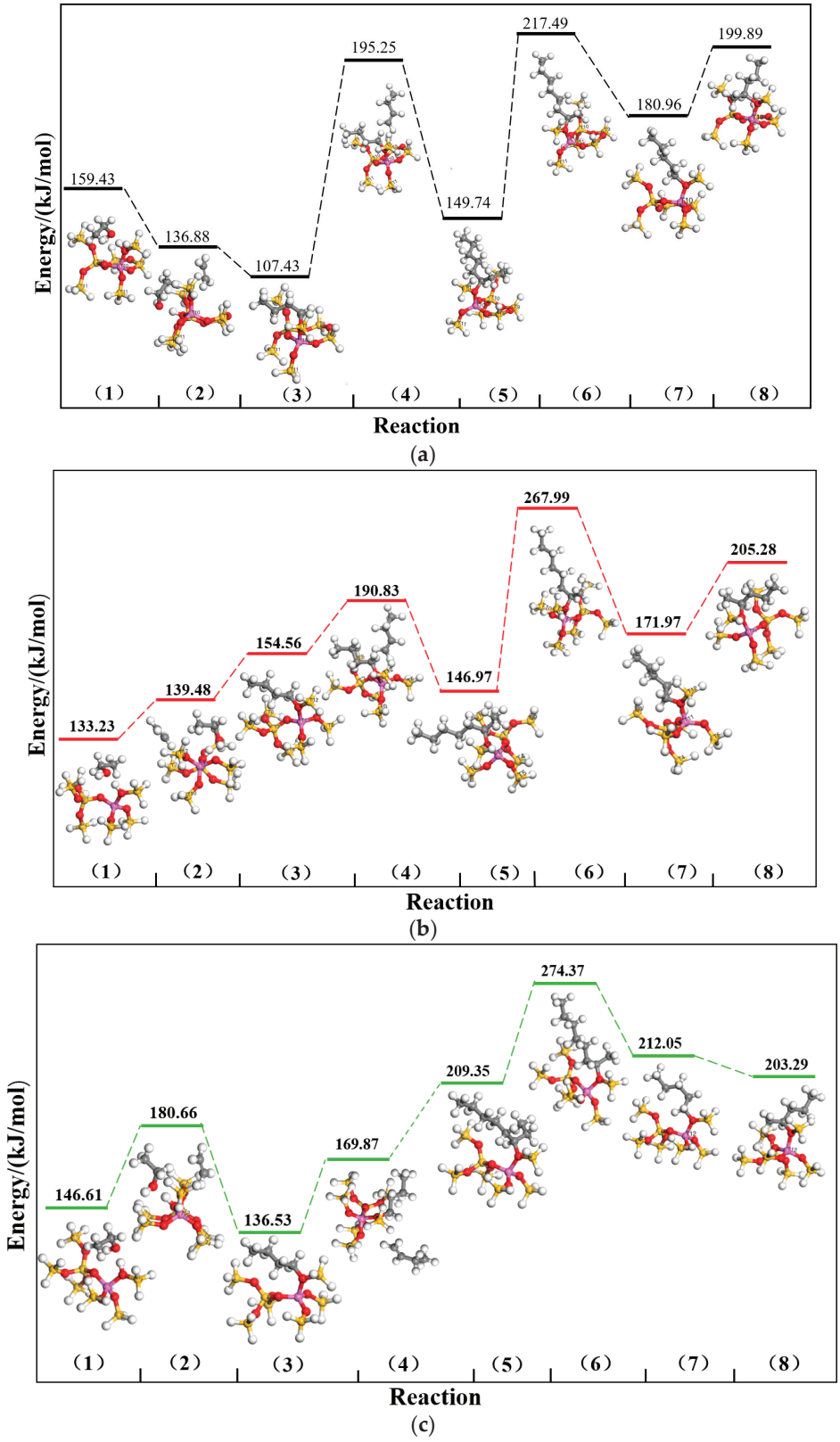

Figure 2. Free energy distribution of HZSM-5 catalyst in catalytic conversion of ethanol to propylene at acid sites of different channels. (**a**) straight channel, (**b**) sinusoidal channel, and (**c**) intersection channel. (1), (2), (3), (4), (5), (6), (7), and (8), respectively, represent dehydration, ethylation, deprotonation, dimerization, proton transfer, β-scission, proton transfer, β-scission steps.

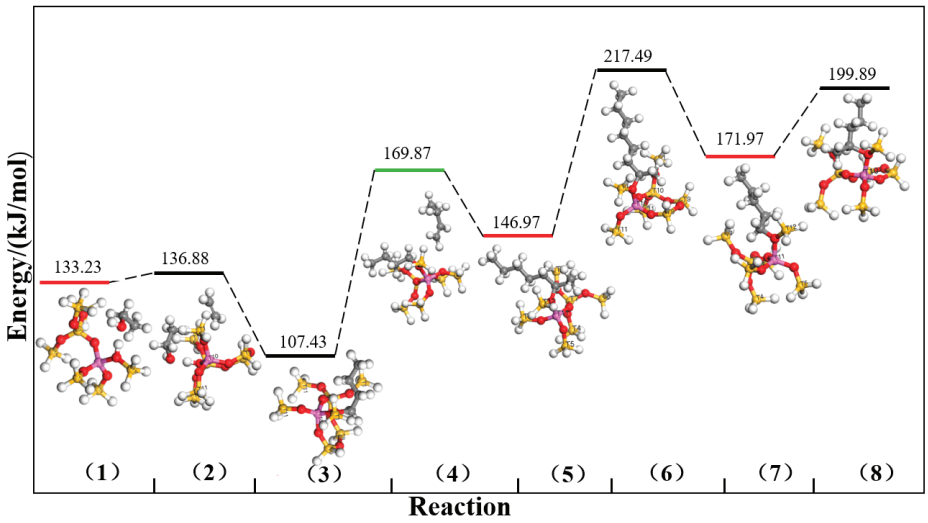

Figure 3. Diagram of the energy required for each reaction to preferentially occur in the channel (The black line represent straight channel, the red line represent sinusoidal channel, and the green line represent intersection channel). (1), (2), (3), (4), (5), (6), (7), and (8), respectively, represent dehydration, ethylation, deprotonation, dimerization, proton transfer, β-scission, proton transfer, β-scission steps.

The smaller the front orbital energy gap difference (ΔE) (LUMO-HOMO), the easier the electron transition and the stronger the reactivity. Eight reaction steps in the reaction pathway were calculated (Table 1). From the energy gap value of ΔE (LUMO-HOMO), it can be seen that the energy gap value of dehydration reaction is the smallest in the acid site of the sinusoidal channel of HZSM-5 molecular sieve, indicating that the dehydration reaction is the most reactive in the acid site of the sinusoidal channel, and the dehydration reaction preferentially occurs in the acid site of the sinusoidal channel. The energy gap value of β-scission reaction is the smallest at the acid site of the straight channel, indicating that β-scission reaction is the most reactive at the acid site of the straight channel, and β-scission reaction preferentially occurs at the acid site of the straight channel. The obtained results are consistent with the above DFT calculation results. The conversion of ethanol to ethylene takes place preferentially at the acid site of sinusoidal channel, and the conversion of ethanol to propylene takes place preferentially at the acid site of straight channel.

Table 1. Front molecular orbital energy gap difference of reaction pathway.

Channels	ΔE (kJ/mol)							
	Dehydration	Ethylation	Deprotonation	Dimerization	Proton Transfer	β-Scission	Proton Transfer	β-Scission
Straight channel	499.03	474.25	456.06	478.90	469.82	463.29	470.74	456.34
Sinusoidal channel	486.05	483.46	470.54	463.20	460.45	467.68	465.16	482.78
Intersection channel	498.93	494.57	480.54	440.86	490.83	476.20	482.77	480.04

2.2. Dynamics Simulation Result

The adsorption behavior of single-component ethylene and propylene on HZSM-5 catalyst with different SiO_2/Al_2O_3 ratios and different channels was simulated at a temperature of 823 K and a pressure of 0–1000 kPa. The simulation results are presented in Figures 4 and 5, and Table 2. The Langmuir adsorption model (Equation (1)) was used to analyze the adsorption data of ethylene and propylene, as shown in Figure 4.

$$Q = \frac{Q_m bp}{1 + bp} \quad (1)$$

where Q is the adsorption capacity in cm^3/g, Q_m is the saturated adsorption capacity in cm^3/g, b is the adsorption equilibrium constant in kPa^{-1}, and p is the partial pressure of the components in kPa.

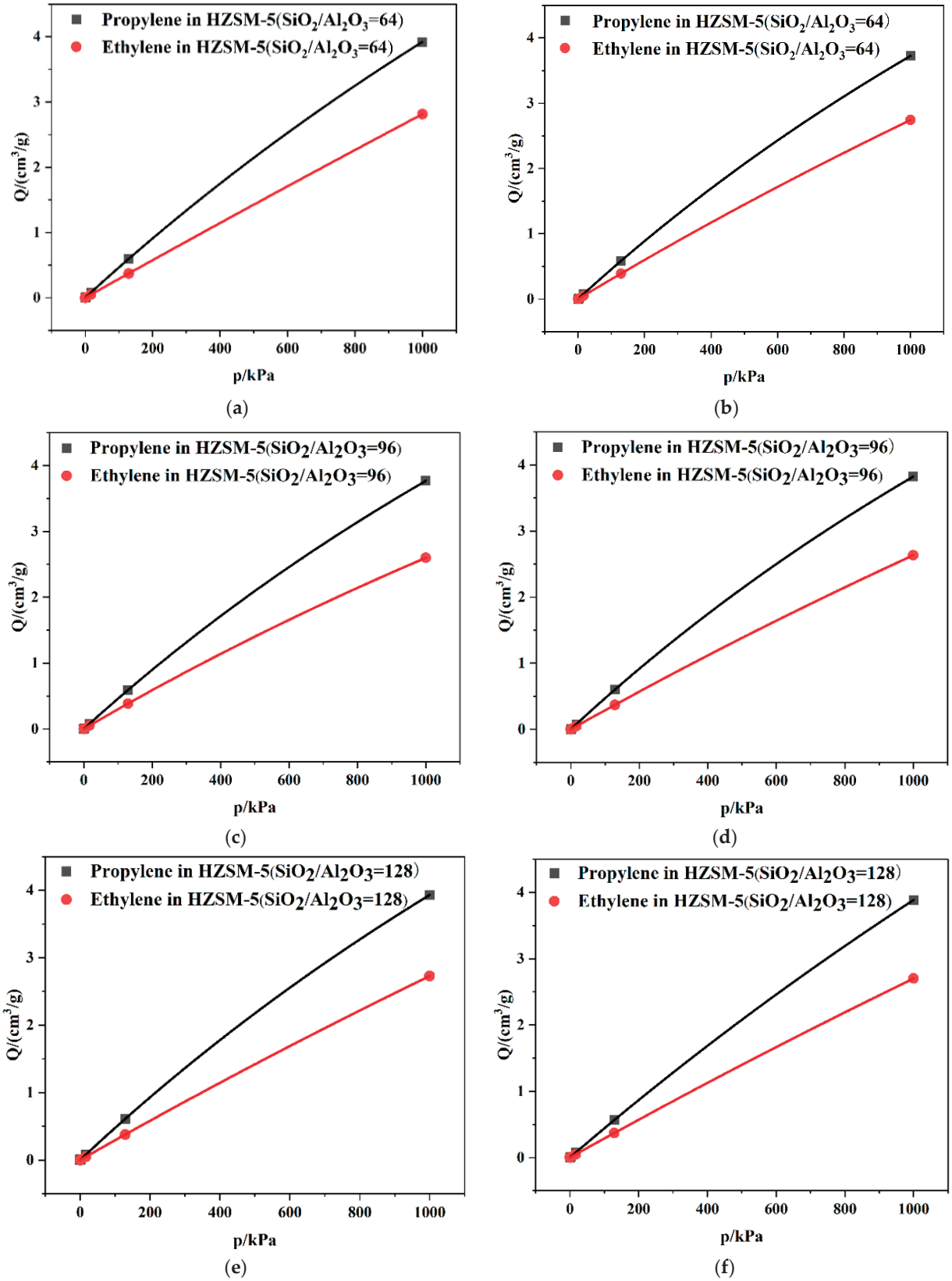

Figure 4. Langmuir isotherm of pure components adsorbed in T10 straight channel (**a**,**c**,**e**) and T11 sinusoidal channel (**b**,**d**,**f**) of HZSM-5 catalyst.

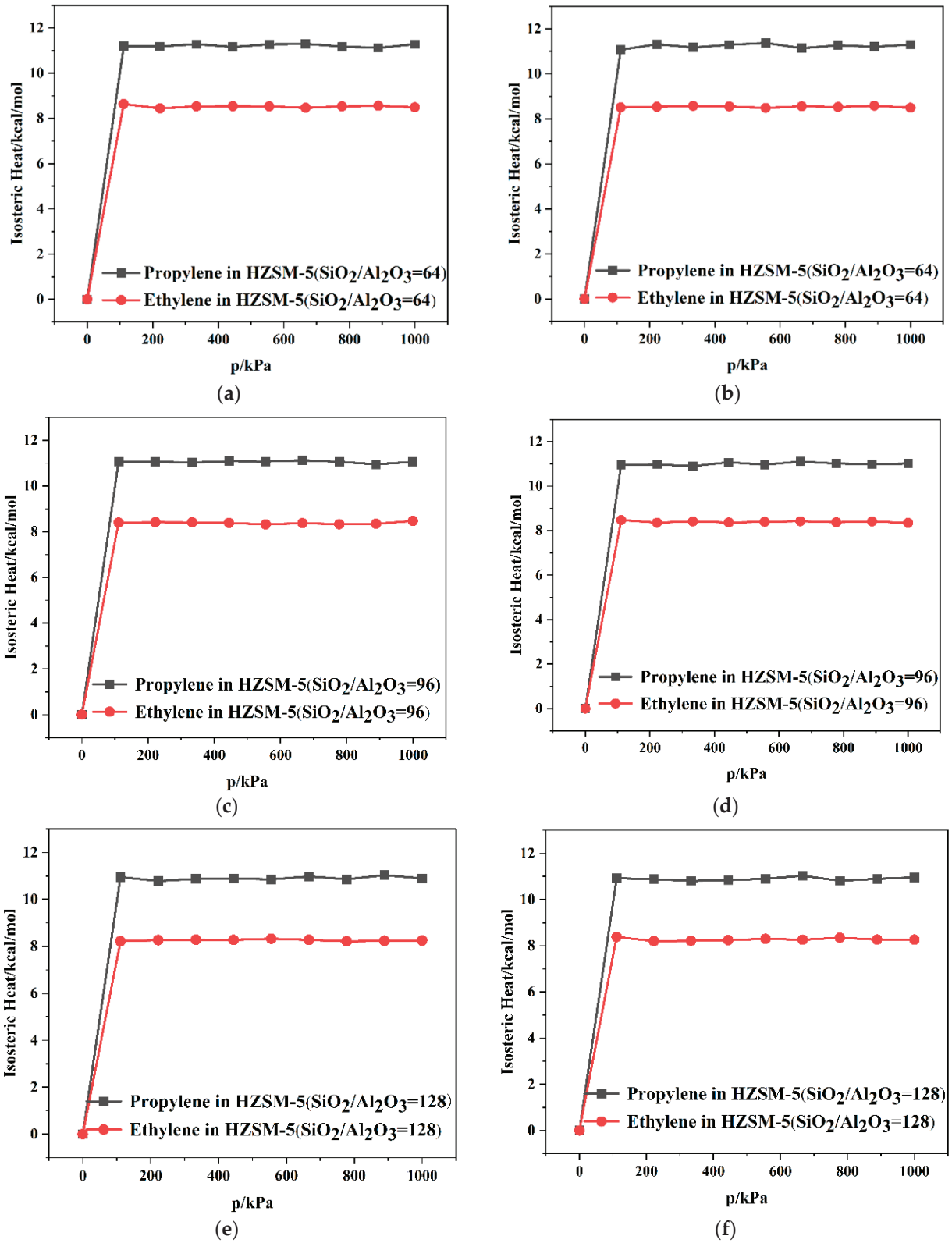

Figure 5. The Isosteric Heat of pure components in T10 straight channel (**a**,**c**,**e**) and T11 sinusoidal channel (**b**,**d**,**f**) of HZSM-5 catalyst.

As shown in Figure 4, the adsorption of ethylene and propylene on HZSM-5 molecular sieves was monolayer adsorption, and the adsorption followed the Langmuir adsorption model. Propylene is loaded more than ethylene in both straight and sinusoidal channels of

HZSM-5 catalyst. This is mainly due to the fact that propylene (3.4 Å diameter) has a larger molecular structure with more carbon atoms than ethylene (2.8 Å diameter).

Table 2. Adsorption parameters of pure components of ethylene and propylene.

SiO_2/Al_2O_3	Channel	Langmuir Constant b ($kPa^{-1} \times 10^{-4}$)		Isosteric Heat (kcal/mol)		Average Loading (per cell)	
		C_3H_6	C_2H_4	C_3H_6	C_2H_4	C_3H_6	C_2H_4
64	T10	2.78	2.55	11.10	8.86	7.65	5.73
	T11	2.80	2.63	11.34	8.51	8.19	5.78
96	T10	2.60	2.52	11.06	8.47	7.91	5.84
	T11	2.63	2.58	11.01	8.34	7.68	5.66
128	T10	2.73	2.38	10.89	8.25	8.00	5.56
	T11	2.70	2.48	10.56	8.26	7.97	5.58

The isosteric heat of adsorption is an important thermodynamic parameter for designing gas separation systems. As shown in Figure 5, the adsorption process of ethylene and propylene on the HZSM-5 catalyst is exothermic, and the isosteric adsorption heat of propylene is obviously higher than that of ethylene, which is consistent with Pham et al. [17]. With the increase of adsorption amount, the adsorbate molecules reach saturation, the adsorption heat of adsorbate molecules basically remains unchanged, and the adsorption heat of propylene fluctuates at 11.0 kcal/mol, while the adsorption heat of ethylene is at 8.0 kcal/mol.

As shown in Table 2, with the increase of SiO_2/Al_2O_3, the Langmuir constant of ethylene in sinusoidal channel (T11) of HZSM-5 catalyst decreases, which is beneficial to the desorption of ethylene and improves the selectivity of ethylene; the Langmuir constant of propylene in the straight channel (T10) of HZSM-5 catalyst decreases, which is beneficial to the desorption of propylene and improves the selectivity of propylene. Among the three kinds of SiO_2/Al_2O_3 studied, the Langmuir constant of HZSM-5 catalyst with SiO_2/Al_2O_3 = 128 is smaller, so the acid sites of sinusoidal channels of HZSM-5 catalyst with SiO_2/Al_2O_3 = 128 are more conducive to improving ethylene selectivity; the acid sites of straight channels of HZSM-5 catalyst with SiO_2/Al_2O_3 = 128 are more conducive to improving propylene selectivity.

The adsorption behavior of binary mixtures of ethylene and propylene on HZSM-5 catalyst with straight (T10) and sinusoidal (T11) channels of HZSM-5 (SiO_2/Al_2O_3 = 64, 96, 128) at 823 K was investigated, and the results are shown in Figures 6 and 7, and Table 3.

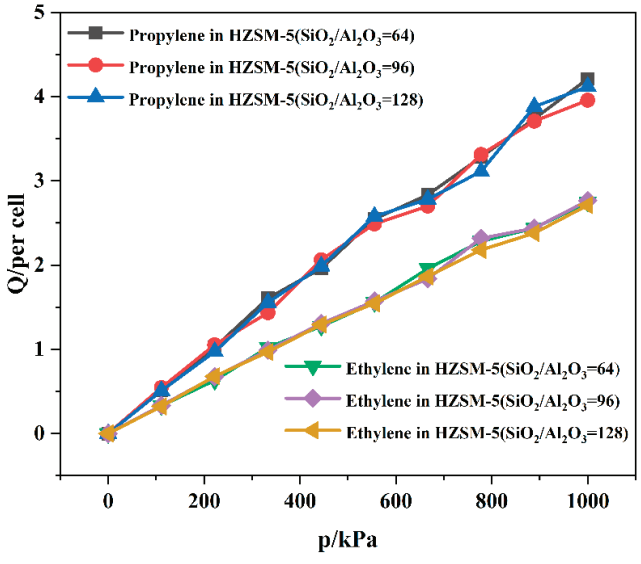

(**a**)

Figure 6. *Cont.*

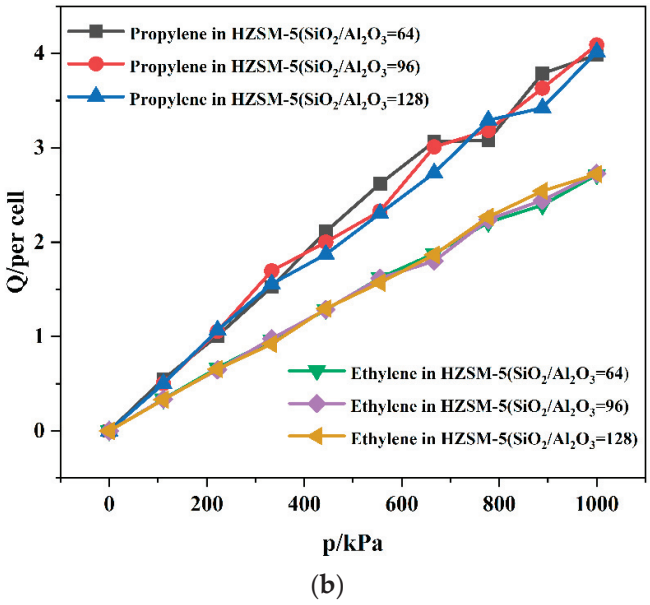

(**b**)

Figure 6. Adsorption isotherm of adsorption for binary mixture in T10 straight channel (**a**) and T11 sinusoidal channel (**b**) of HZSM-5 catalyst.

As shown in Figures 6 and 7, and Table 3, compared with the adsorption of pure components, the adsorption amount of propylene and ethylene in binary mixture is reduced. As shown in Table 3, the interaction between propylene and HZSM-5 catalyst skeleton is the weakest in the straight channel (T10) with SiO_2/Al_2O_3 = 128 and the strongest in the sinusoidal channel (T11) with SiO_2/Al_2O_3 = 64. At the sinusoidal channel (T11) with SiO_2/Al_2O_3 = 64, the interaction between ethylene and HZSM-5 catalyst skeleton is the strongest, and at the sinusoidal channel (T11) with SiO_2/Al_2O_3 = 128, the interaction between ethylene and HZSM-5 catalyst skeleton is the weakest. Therefore, propylene is more likely to desorb on the straight channel (T10) of HZSM-5 with SiO_2/Al_2O_3 = 128 in the adsorption of binary mixtures, which is more conducive to improving the selectivity of propylene. Ethylene is more likely to be desorbed from the sinusoidal channel (T11) of HZSM-5 with SiO_2/Al_2O_3 = 128, which is more conducive to improving the selectivity of ethylene.

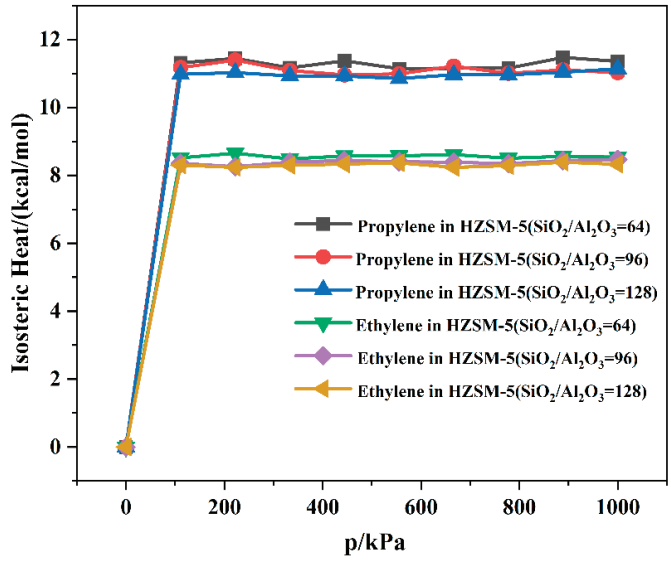

(**a**)

Figure 7. *Cont.*

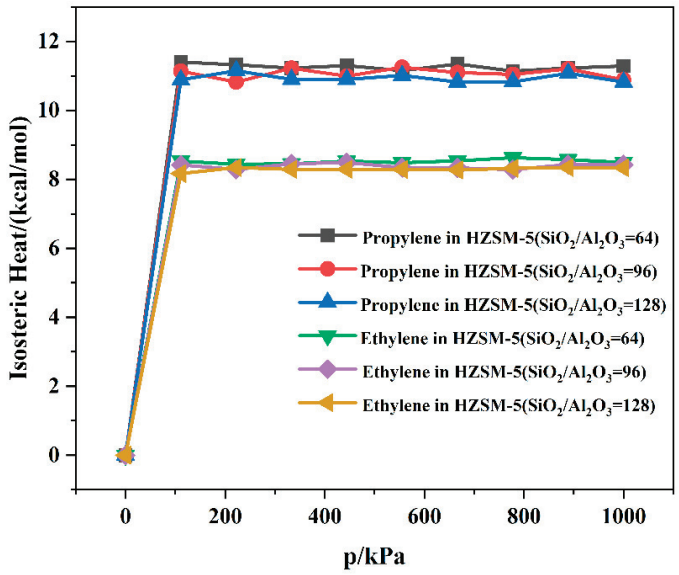

(**b**)

Figure 7. The Isosteric Heat of adsorption for binary mixture in T10 straight channel (**a**) and T11 sinusoidal channel (**b**) of HZSM-5 catalyst.

Table 3. Adsorption parameters of binary mixture of ethylene and propylene.

SiO_2/Al_2O_3	Channel	Langmuir Constant b ($kPa^{-1} \times 10^{-4}$)		Isosteric Heat (kcal/mol)		Average Loading (per Cell)	
		C_3H_6	C_2H_4	C_3H_6	C_2H_4	C_3H_6	C_2H_4
64	T10	1.61	1.14	11.24	8.49	4.21	2.75
	T11	3.21	1.49	11.19	8.53	3.98	2.71
96	T10	2.29	1.04	10.91	8.44	3.95	2.76
	T11	2.53	1.07	10.90	8.30	4.09	2.73
128	T10	1.50	1.30	10.96	8.33	3.88	2.71
	T11	1.91	0.64	10.96	8.35	4.02	2.72

The Mean Squared Displacement (MSD) is the deviation of the component's position from the reference position over time. The MSD indicates the ability of the component to migrate on a specific time scale and can be used to determine the time-dependent diffusion coefficient. The diffusion coefficient is calculated using the Einstein equation [18], as shown in Equation (2).

$$D = \frac{1}{2dN} \lim_{t \to \infty} \frac{d}{dt} \sum_{i=1}^{N} \left\langle \left[\vec{r_i}(t) - \vec{r_i}(0) \right]^2 \right\rangle \quad (2)$$

where D is the diffusion coefficient, t is the time, N is the number of target molecules in the system, and $\vec{r_i}(t)$ and $\vec{r_i}(0)$ are the coordinates of the ith particle at moments t and 0, respectively.

As shown in Figure 8, the MSD curves of pure component ethylene are higher than pure component propylene, attributed to the stronger interaction of propylene with the HZSM-5 sieve framework. The diffusion coefficients of HZSM-5 catalyst with different silica–aluminum ratios and different channels for ethylene and propylene are listed in Table 4. Wang et al. [19] reported diffusion coefficients of 1.95×10^{-8} m^2/s and 0.87×10^{-8} m^2/s for pure ethylene and pure propylene, respectively, in ZSM-5 at 873 K, which is consistent with the present results. As shown in Table 4, for the diffusion of pure components, the diffusion coefficient of ethylene is larger than that of propylene, which is

consistent with the adsorption simulation results, indicating that the generated ethylene diffuses more easily from the HZSM-5 catalyst channels in the ETO reaction. The reason for the higher ethylene yield than propylene in the ETO reaction was further explained from the diffusion point of view.

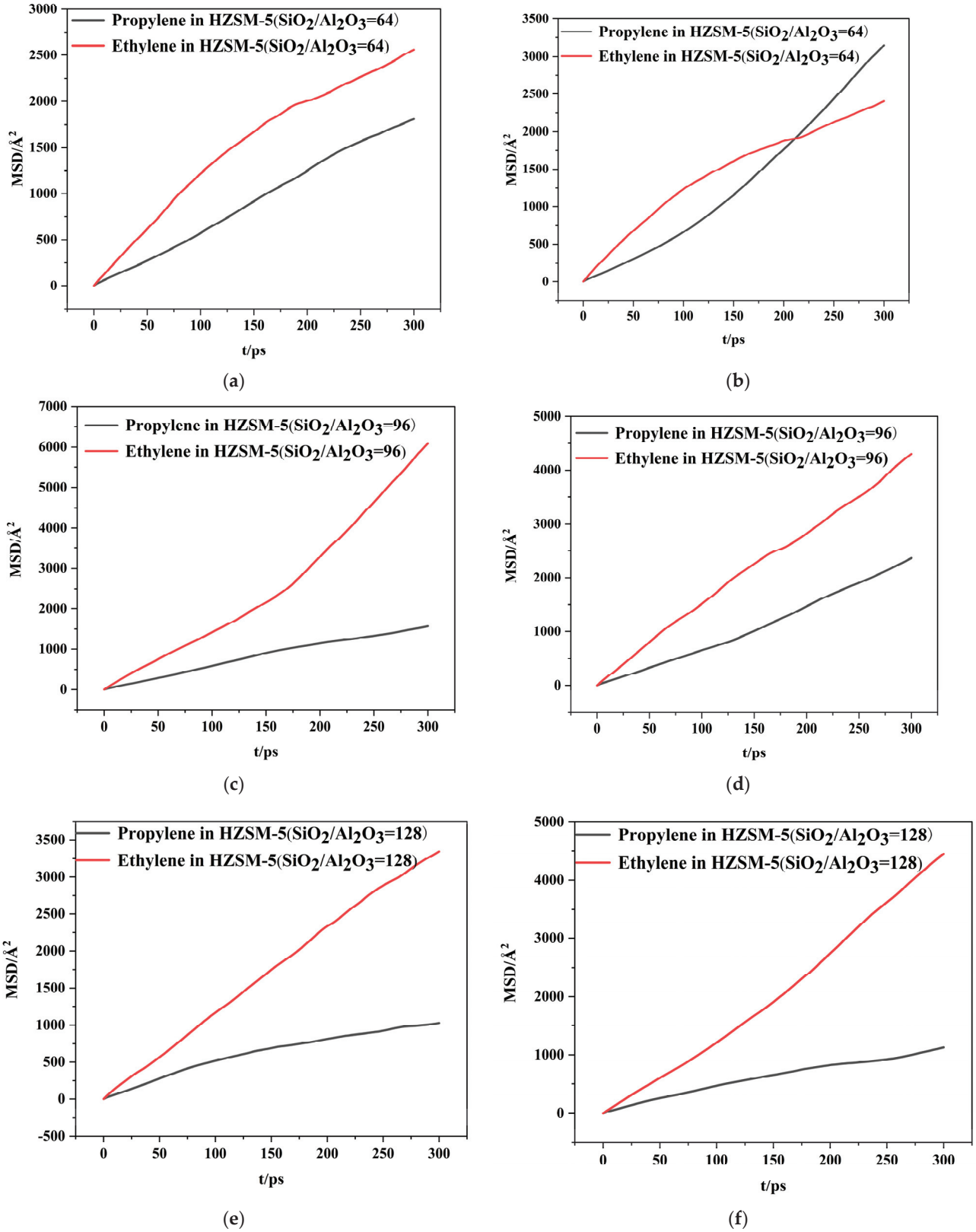

Figure 8. The MSD curve of pure components in T10 straight channel (**a**,**c**,**e**) and T11 sinusoidal channel (**b**,**d**,**f**) of HZSM-5 catalyst.

Table 4. Diffusion coefficient of pure components of ethylene and propylene.

SiO_2/Al_2O_3	Channel	Diffusion Coefficients $\times 10^{-8}$(cm^2/s)	
		C_3H_6	C_2H_4
64	T10	1.05	1.38
	T11	1.77	1.24
96	T10	0.87	3.27
	T11	1.32	2.30
128	T10	0.55	1.89
	T11	0.59	2.50

Radial distribution function (RDF) can be used to describe the spatial structure of a particle system, such as the average distance between particles and the degree of aggregation between particles. It is defined as the ratio of the number of particles neighboring a given particle at a distance of r to the total number of particles in the system, and its formula is shown in Equation (3).

$$\mathrm{RDF(r)} = \frac{4\pi r^2 n(r)}{N} \tag{3}$$

where n(r) is the particle number density at distance r, and N is the total number of particles in the system.

The spacing distributions of ethylene and propylene molecules with acid site H protons were statistically analyzed using RDF, and the calculated results are shown in Figure 9. The RDF plots of ethylene and propylene on the structure of HZSM-5 catalyst with different SiO_2/Al_2O_3 ratios and different channels exhibit a similar trend, with a high probability of finding ethylene or propylene molecules at a distance of 2.70 Å, and a low probability of finding ethylene or propylene molecules at distances exceeding 7 Å. Thus, the adsorption location is close to the zeolite backbone.

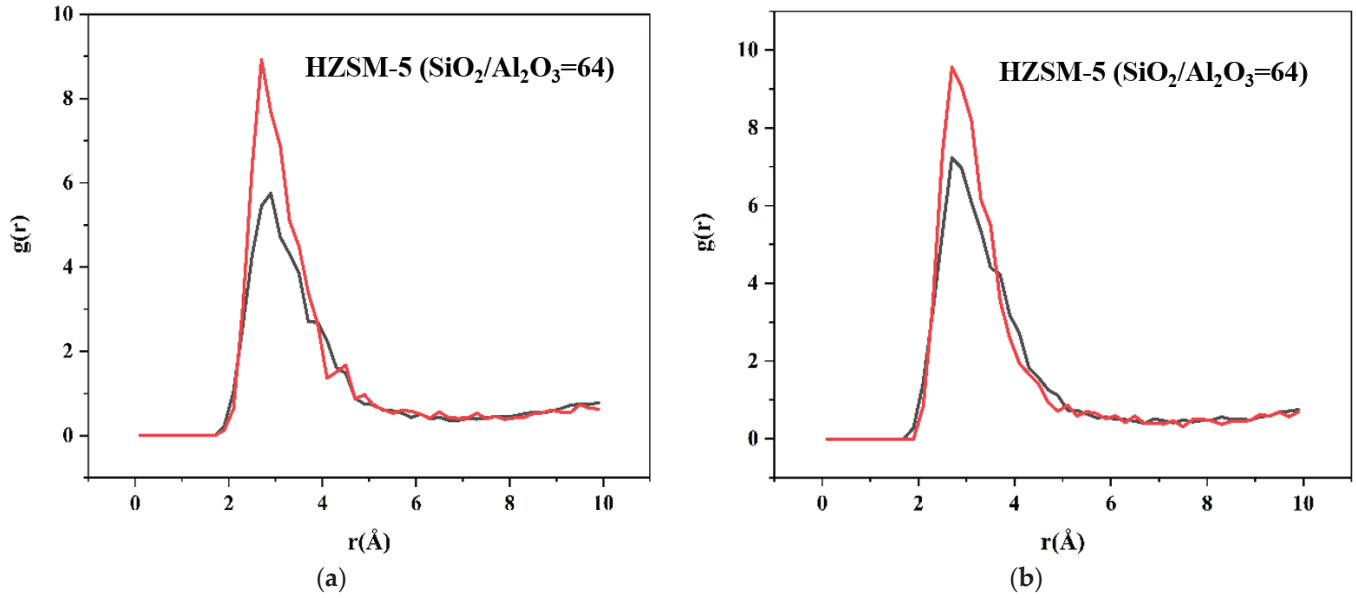

Figure 9. *Cont.*

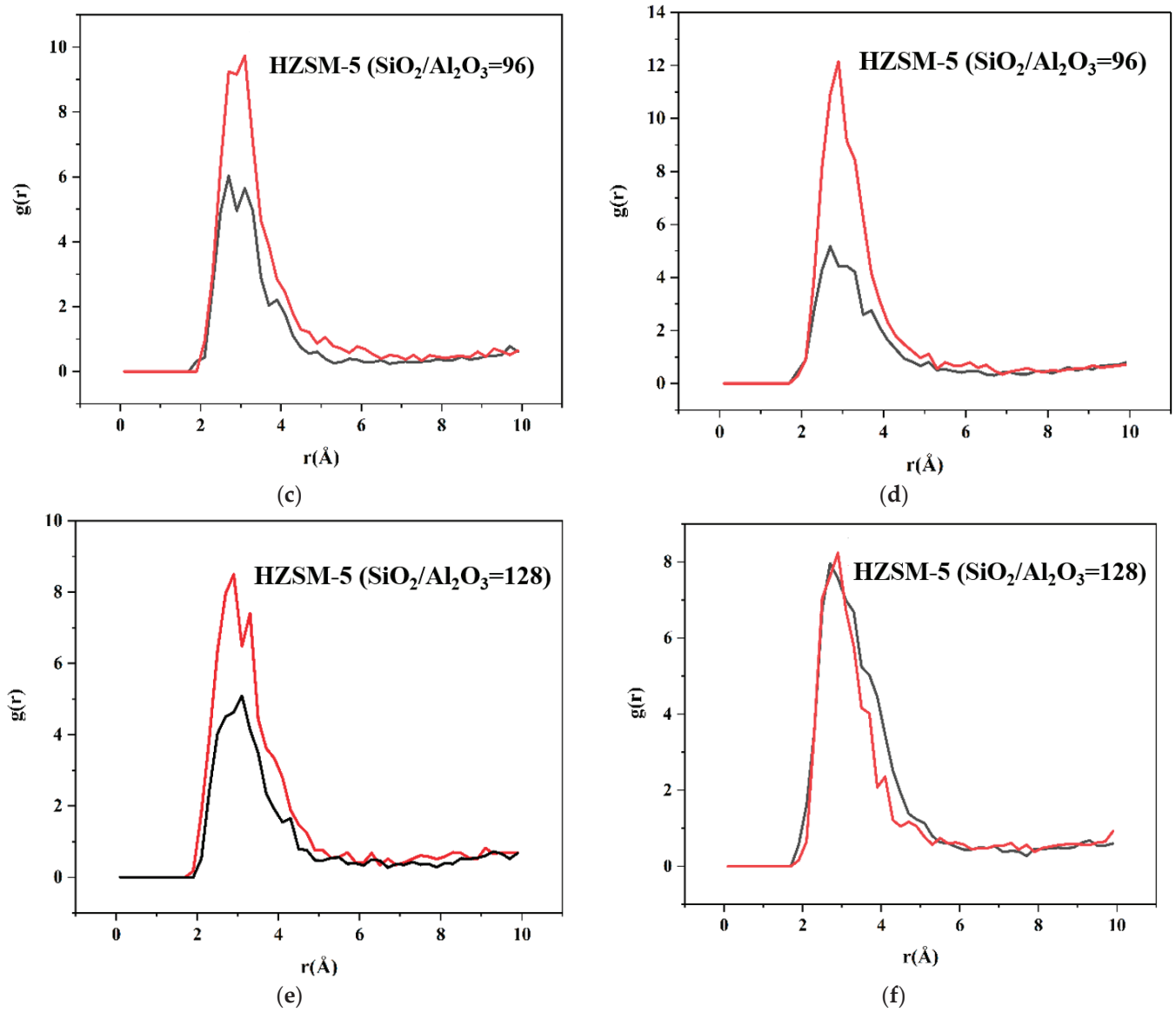

Figure 9. RDF of pure components in T10 straight channel (**a**,**c**,**e**) and T11 sinusoidal channel (**b**,**d**,**f**) of HZSM-5 catalyst. red line: ethylene; black line: propylene.

As shown in Table 5, for the diffusion of the mixture of ethylene and propylene, the diffusion coefficient of ethylene is greater than that of propylene, so there is more interaction between propylene molecules and HZSM-5 catalyst. In HZSM-5 (SiO_2/Al_2O_3 = 128), the highest diffusion coefficient was found for propylene and the lowest for ethylene, which is beneficial to propylene production.

Table 5. Diffusion coefficient of ethylene and propylene in binary mixture.

SiO_2/Al_2O_3	Channel	Diffusion Coefficient $\times 10^{-8}$ (cm^2/s)	
		C_3H_6	C_2H_4
64	T10	0.69	2.51
	T11	0.85	2.48
96	T10	0.47	1.55
	T11	1.00	2.69
128	T10	1.36	1.12
	T11	1.58	1.58

Diffusion selectivity refers to the separation of different components due to different diffusion rates on the adsorbent surface during the adsorption separation of a mixture. The results of adsorption selectivity (α) and diffusion selectivity (S) [20,21] of ethylene/propylene binary gas mixtures in HZSM-5 catalyst framework were calculated by Equations (4) and (5) and the results are shown in Table 6.

$$S = D_{C_3H_6}/D_{C_2H_4} \quad (4)$$

$$\alpha = \frac{y_{C_3H_6}/y_{C_2H_4}}{x_{C_3H_6}/x_{C_2H_4}} \quad (5)$$

where $D_{C_2H_4}$, $D_{C_3H_6}$ are the diffusion coefficients of ethylene and propylene, $y_{C_2H_4}$, $y_{C_3H_6}$ are the adsorption loadings of ethylene and propylene, and $x_{C_2H_4}$, $x_{C_3H_6}$ are the molar fractions of ethylene and propylene.

Table 6. The diffusion selectivity (S) and adsorption selectivity (α) for binary mixture in the studied structures.

SiO_2/Al_2O_3	Channel	$S_{C_3H_6/C_2H_4}$	$\alpha_{C_3H_6/C_2H_4}$
64	T10	0.27	1.53
	T11	0.34	1.47
96	T10	0.30	1.43
	T11	0.37	1.50
128	T10	1.21	1.43
	T11	1.00	1.48

As shown in Table 6, the diffusion selectivity of propylene to ethylene increased with the increase of SiO_2/Al_2O_3 ratio, and the maximum diffusion selectivity to propylene in HZSM-5 (SiO_2/Al_2O_3 = 128) straight channel (T10) was 1.21, which is beneficial to the separation of propylene and improves the selectivity of propylene. In HZSM-5 (SiO_2/Al_2O_3 = 128) straight channel (T10), propylene has less selectivity for ethylene adsorption. Therefore, in the straight channel (T10) of HZSM-5 (SiO_2/Al_2O_3 = 128), it is more beneficial to improve the selectivity of propylene.

3. Computational Methods

3.1. DFT Simulation Calculation

The GGA-PBE functional and high-precision DNP basis set were employed for calculation using the All Electron method with a real space Orbital Cutoff of 4.5 Å. The convergence standard was set to Fine with allowable deviations of total energy, gradient, and structure displacement at 10^{-5} Ha, 0.002 Ha·Å^{-1}, and 0.005 Å, respectively. Transition state search and reaction energy barrier calculations were performed using the Complete LST/QST method with a Medium accuracy setting allowing for deviations in total energy (2×10^{-5} Ha), gradient (0.004 Ha·Å^{-1}), and structure displacement (0.005 Å). The acid sites in the straight channel, sinusoidal channel and intersection channel of zeolite HZSM-5 are simulated by strategically placing an aluminum atom at the T10, T11, and T12 positions, respectively [22,23] (Figure 10).

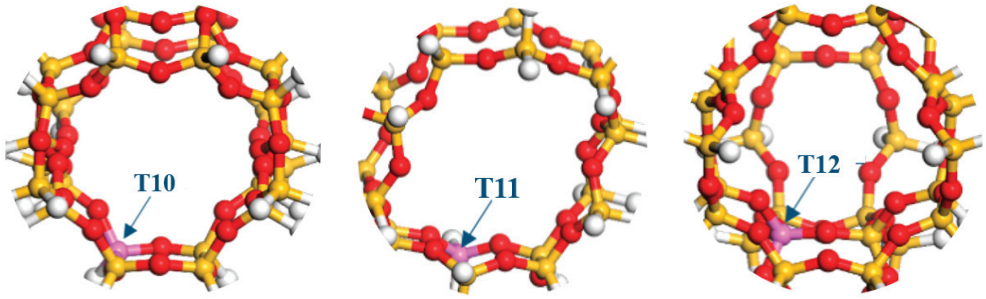

Figure 10. Models illustrating the straight channel, sinusoidal or and intersection channel (T10, T11, and T12 sites, respectively) of HZSM-5 catalyst. The yellow, red, pink, and white balls represent the Si, O, Al, and H atoms, respectively.

Equation (6) below calculates the energy required for the reactants to the transition state on the HZSM-5 catalyst:

$$\Delta E = (E_{TS} - E_R) \cdot 2625.50184 \quad (6)$$

where ΔE represents the energy required for the reactant to the transition state, $kJ \cdot mol^{-1}$, ΔE_R represents the total energy of the reactants adsorbed on the catalyst, and Ha; ΔE_{TS} represents the total energy of the transition state adsorbed on the catalyst, Ha.

3.2. Molecular Dynamic Simulation

The original cell of ZSM-5 molecular sieve was obtained from the International Zeolite Association (IZA), and the 2 × 2 × 2 (a = 40.180 Å, b = 39.476 Å, and c = 26.284 Å) cell was modeled in Materials Studio 2018 software. Replacing the silicon atoms at the T10 and T11 sites with aluminum atoms and adjusting the charge of each atom of the molecular sieve, the charge of all Al atoms is 1.4 Å, the charge of all O atoms is −1.2 Å, and the charge of all Si atoms is 2.4 Å. Six molecular sieve model structures with SiO_2/Al_2O_3 = 64, 96, and 128 were constructed, respectively (Figure 11).

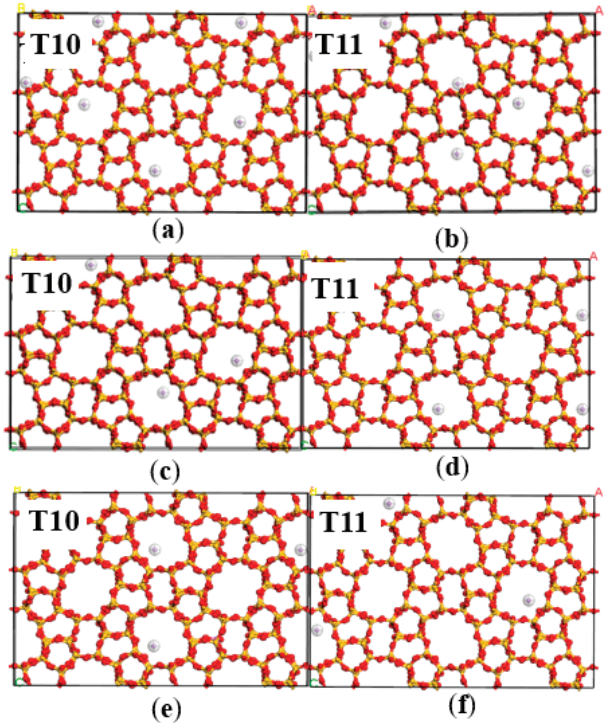

Figure 11. T10, T11 channel supercell of HZSM-5 with different SiO_2/Al_2O_3 ratios (**a**,**b**) SiO_2/Al_2O_3 = 64, (**c**,**d**) SiO_2/Al_2O_3 = 96, (**e**,**f**) SiO_2/Al_2O_3 = 128.

The Sorption module in Materials Studio 2018 was used for adsorption calculations. The Compass force field was selected for the calculation. Charges were managed using the Forcefield Assigned method. Van der Waals potential was calculated using the Atom Based method, and Ewald method was employed for electrostatic interactions with an accuracy of 0.042 J/mol. The simulation consisted of 10^6 steps, with the first 10^5 steps dedicated to achieving equilibrium.

Molecular dynamic calculations for diffusion were performed in the Forcite module of the Materials Studio 2018, with Dynamics selected for the computational task, Medium accuracy, a value of 12.5 Å for the cutoff distance, a time step of 1.0 fs, and a total simulation time of 2500 ps. The NVE system was used, and the Nose method was employed for the temperature control.

4. Conclusions

The catalytic behavior of T10, T11, and T12 acid sites (representing straight channel, sinusoidal channel, and intersection channel, respectively) of HZSM-5 catalyst on the reaction network of ethanol conversion to ethylene and propylene was studied by DFT. The results show that the conversion of ethanol to ethylene occurs preferentially at the acid site of the sinusoidal channel (T11); the conversion of ethanol to propylene takes place preferentially at the acid site of the straight channel (T10). The adsorption and diffusion behavior of ethylene and propylene in the straight and sinusoidal channels of HZSM-5 catalyst was simulated by molecular dynamics method. The results show that for the adsorption of pure components and binary mixtures, the acid sites of sinusoidal channel (T11) with SiO_2/Al_2O_3 = 128 are more conducive to improving the selectivity of ethylene, and the acid sites of straight channel (T10) with SiO_2/Al_2O_3 = 128 are more conducive to improving the selectivity of propylene. For the diffusion of pure components and binary mixtures, the diffusion coefficient of ethylene is greater than that of propylene. The diffusion selectivity of propylene to ethylene increases with the increase of SiO_2/Al_2O_3 ratio. Therefore, in the straight channel (T10) of HZSM-5 (SiO_2/Al_2O_3 = 128), it is more beneficial to improve propylene selectivity.

Author Contributions: The contributions of the authors for the manuscript are the following: conceptualization, W.X. and D.L.; methodology, W.X. and K.C.; software, X.W. and S.L.; validation, D.W.; formal analysis, D.W. and X.W.; investigation, Z.J.; resources, Z.J. and M.D.; data curation, Y.Z. and S.L.; writing—original draft, X.W., Y.Z. and S.L.; writing—review and editing, K.C. and D.L.; visualization, M.D.; supervision, W.X.; project administration, W.X.; funding acquisition, W.X. All authors have read and agreed to the published version of the manuscript.

Funding: This work is a project sponsored by the National Natural Science Foundation of China (Grant 21978327).

Data Availability Statement: The data presented in this study are available within the article.

Conflicts of Interest: The authors declare no conflicts of interest.

References

1. Alotibi, M.F.; Alshammari, B.A.; Alotaibi, M.H.; Alotaibi, F.M.; Alshihri, S.; Navarro, R.M. ZSM-5 zeolite based additive in FCC process: A review on modifications for improving propylene production. *Catal. Surv. Asia* **2020**, *24*, 1–10. [CrossRef]
2. Corma, A.; Corresa, E.; Mathieu, Y.; Sauvanaud, L.; Al-Bogami, S.; Al-Ghrami, M.S.; Bourane, A. Crude oil to chemicals: Light olefins from crude oi. *Catal. Sci. Technol.* **2017**, *7*, 12–46. [CrossRef]
3. Louwen, J.N.; Van Eijck, L.; Vogt, C.; Vogt, E.T.C. Understanding the activation of ZSM-5 by phosphorus: Localizing phosphate groups in the pores of phosphate-stabilized ZSM-5. *Chem. Mater.* **2020**, *32*, 9390–9403.
4. Degnan, T.; Chitnis, G.; Schipper, P.H. History of ZSM-5 fluid catalytic cracking additive development at Mobil. *Microporous Mesoporous Mater.* **2000**, *35*, 245–252.

5. Buchanan, J.J.C.T. The chemistry of olefins production by ZSM-5 addition to catalytic cracking units. *Catal. Today* **2000**, *55*, 207–212.
6. Ali, M.; Zafar, F.; Shen, D.; Wang, X.; Bae, J.W. Contributions of ZSM-5 morphology over hybridized ZnO-ZrO_2/ZSM-5 for direct CO_2 hydrogenation activity to aromatics. *Fuel* **2024**, *378*, 132925. [CrossRef]
7. Ahmed, S.; Sugiarto, J.R.; Yoon, W.; Irshad, M.; Jo, H.; Bibi, S.S.; Kim, S.K.; Khan, M.K.; Kim, J. High-yield pentanes-plus production via hydrogenation of carbon dioxide: Revealing new roles of zirconia as promoter of iron catalyst with long-term stability. *J. Energy Chem.* **2025**, *102*, 431–442.
8. Iwamoto, M.J. Selective catalytic conversion of bio-ethanol to propene: A review of catalysts and reaction pathways. *Catal. Today* **2015**, *242*, 243–248.
9. Sazama, P.; Dědeček, J.; Gábová, V.; Wichterlová, B.; Spoto, G.; Bordiga, S. Effect of aluminium distribution in the framework of ZSM-5 on hydrocarbon transformation. Cracking of 1-butene. *J. Catal.* **2008**, *254*, 180–189. [CrossRef]
10. Yokoi, T.; Mochizuki, H.; Namba, S.; Kondo, J.N.; Tatsumi, T. Control of the Al distribution in the framework of ZSM-5 zeolite and its evaluation by solid-state NMR technique and catalytic properties. *J. Phys. Chem. C* **2015**, *119*, 15303–15315.
11. Janda, A.; Bell, A.T. Effects of Si/Al ratio on the distribution of framework Al and on the rates of alkane monomolecular cracking and dehydrogenation in H-MFI. *J. Am. Chem. Soc.* **2013**, *135*, 19193–19207. [CrossRef]
12. Liang, T.; Chen, J.; Qin, Z.; Li, J.; Wang, P.; Wang, S.; Wang, G.; Dong, M.; Fan, W.; Wang, J. Conversion of methanol to olefins over H-ZSM-5 zeolite: Reaction pathway is related to the framework aluminum siting. *ACS Catal.* **2016**, *6*, 7311–7325. [CrossRef]
13. Sungtak, K.; Gyungah, P.; Hee, W.M.; Geunjae, K.; Ki, K.S. Control of hierarchical structure and framework-Al distribution of ZSM-5 via adjusting crystallization temperature and their effects on methanol conversion. *ACS Catal.* **2019**, *9*, 2880–2892.
14. Wang, S.; Chen, Y.; Wei, Z.; Qin, Z.; Ma, H.; Dong, M.; Li, J.; Fan, W.; Wang, J. Polymethylbenzene or alkene cycle theoretical study on their contribution to the process of methanol to olefins over H-ZSM-5 zeolite. *J. Phys. Chem. C* **2015**, *119*, 28482–28498. [CrossRef]
15. Xia, W.; Ma, C.; Huang, Y.; Li, S.; Wang, X.; Chen, K.; Liu, D. Bioethanol conversion into propylene over various zeolite catalysts: Reaction optimization and catalyst deactivation. *Nanomaterials* **2022**, *12*, 2746. [CrossRef] [PubMed]
16. Yin, J.; Guo, X.; Sun, Y.; Han, S.; Li, Q. Understanding the nanoconfinement effect on the ethanol-to-propene mechanism catalyzed by acidic ZSM-5 and FAU zeolites. *J. Phys. Chem. C* **2021**, *125*, 310–334. [CrossRef]
17. Pham, T.D.; Lobo, R.F.J.M.; Materials, M. Adsorption equilibria of CO_2 and small hydrocarbons in AEI, CHA, STT, and RRO-type siliceous zeolites. *Microporous Mesoporous Mater.* **2016**, *236*, 100–108. [CrossRef]
18. Keyvanloo, Z.; Pour, A.N.; Moosavi, F.; Shahri, S.M.K. Molecular dynamic simulation studies of adsorption and diffusion behaviors of methanol and ethanol through ZSM-5 molecular sieve. *J. Mol. Graph. Modell.* **2022**, *110*, 108048.
19. Wang, C.; Li, B.; Wang, Y.; Xie, Z. Insight into the topology effect on the diffusion of ethene and propene in zeolites: A molecular dynamics simulation study. *J. Energy Chem.* **2013**, *22*, 914–918. [CrossRef]
20. Martin-Calvo, A.; Van der Perre, S.; Claessens, B.; Calero, S.; Denayer, J.F.M. Unravelling the influence of carbon dioxide on the adsorptive recovery of butanol from fermentation broth using ITQ-29 and ZIF-8. *Phys. Chem. Chem. Phys.* **2018**, *20*, 9957–9964. [CrossRef]
21. Gee, J.A.; Chung, J.; Nair, S.; Sholl, D.S. Adsorption and diffusion of small alcohols in zeolitic imidazolate frameworks ZIF-8 and ZIF-90. *J. Phys. Chem. C* **2013**, *117*, 3169–3176.
22. Wang, S.; Li, Z.; Qin, Z.; Dong, M.; Li, J.; Fan, W.; Wang, J. Catalytic roles of the acid sites in different pore channels of H-ZSM-5 zeolite for methanol-to-olefins conversion. *Chin. J. Catal.* **2021**, *42*, 1126–1136. [CrossRef]
23. Wang, S.; Li, S.; Zhang, L.; Qin, Z.; Chen, Y.; Dong, M.; Li, J.; Fan, W.; Wang, J. Mechanistic insights into the catalytic role of various acid sites on ZSM-5 zeolite in the carbonylation of methanol and dimethyl ether. *Catal. Sci. Technol.* **2018**, *8*, 3193–3204. [CrossRef]

catalysts

MDPI

Article

Hydrocracking of Polyethylene to Gasoline-Range Hydrocarbons over a Ruthenium-Zeolite Bifunctional Catalyst System with Optimal Synergy of Metal and Acid Sites

Qing Du [1,2], Xin Shang [1,*], Yangyang Yuan [3,*], Xiong Su [1,*] and Yanqiang Huang [1]

[1] State Key Laboratory of Catalysis, Dalian Institute of Chemical Physics, Chinese Academy of Sciences, Dalian 116023, China; qingdu@dicp.ac.cn (Q.D.); yqhuang@dicp.ac.cn (Y.H.)
[2] University of Chinese Academy of Sciences, Beijing 100049, China
[3] Hangzhou Institute of Advanced Studies, Zhejiang Normal University, Hangzhou 311231, China
* Correspondence: shangxin@dicp.ac.cn (X.S.); yuanyangyang@zjnu.edu.cn (Y.Y.); suxiong@dicp.ac.cn (X.S.); Tel.: +86-411-84379015 (Xiong Su)

Abstract: Chemical recycling of plastic waste, especially polyolefins, into valuable liquid fuels is of considerable significance to address the serious issues raised by their threat on environmental and human health. Nevertheless, the construction of efficient and economically viable catalytic systems remains a significant hurdle. Herein, we developed an efficient bifunctional catalyst system comprising γ-Al_2O_3-supported ruthenium nanoparticles (Ru/γ-Al_2O_3) and β-zeolite for the conversion of polyolefins into gasoline-range hydrocarbons. A yield of $C_{5–12}$ paraffins up to 73.4% can be obtained with polyethene as the reactant at 250 °C in hydrogen. The Ru sites primarily activate the initial cleavage of C–H bonds of polymer towards the formation of olefin intermediates, which subsequently go through further cracking and isomerization over the acid sites in β-zeolite. Employing in situ infrared spectroscopy and probe–molecule model reactions, our investigation reveals that the optimized proportion and spatial distribution of the dual catalytic sites are pivotal in the tandem conversion process. This optimization synergistically regulates the cracking kinetics and accelerates intermediate transfer, thereby minimizing the production of side $C_{1–4}$ hydrocarbons resulting from over-cracking at the Ru sites and enhancing the yield of liquid fuels. This research contributes novel insights into catalyst design for the chemical upgrading of polyolefins into valuable chemicals, advancing the field of plastic waste recycling and sustainable chemical production.

Keywords: polyolefin; hydrocracking; ruthenium; β-zeolite; bifunctional catalysts

1. Introduction

The surge of plastic waste due to the rapid development of human life has led to gradually increasing threats on the environment and human health [1–3]. The predominated polyolefins in the wastes featuring stable C–C and the C–H skeleton are subject to difficult natural degradation [4,5]. The common disposal methods via landfilling and incineration have raised serious concerns regarding the accumulation of microplastics and excessive carbon emissions. In this context, it is urgent to achieve manual recycling of polyolefins, in which chemical upgrading through hydrocracking with green hydrogen is of prominent significance, as it can be efficiently conducted under relatively moderate conditions with considerable production of valuable chemicals and fuels [6–9].

Noble metals, such as Pt and Ru, are widely used in the hydrocracking of polyolefins due to their ability to efficiently activate hydrogen molecules and catalyze the cleavage

of both C–C and C–H, which are prevalent in polyolefin monomers [10–13]. However, despite their significant hydrogenation capabilities, catalysts based on these noble metals often face challenges in optimizing product selectivity by controlling reaction and diffusion kinetics [14–16]. Thus, aluminosilicate zeolite materials featuring ordered porous structures have been commonly introduced into the catalytic systems as a second active component to enhance the preferential production of specific hydrocarbons. The confined microenvironment and abundant acid sites are conducive to modulating the transferring and transformation of certain intermediates via imposing spatial restriction and inducing the formation of specific carbocations, whereby prompting the cracking, oligomerization, isomerization, aromatization, and other complex reactions [17–19]. In these cases, a key challenge lies in rationally arranging the metal and acid sites within multifunctional catalytic systems to establish enhanced synergy, ensuring not only high atomic utilization efficiency of noble metals but also precise control over reaction pathways. Several recent studies have employed bifunctional catalysts with Pt metal center and acid sites in close contact for reinforced tandem processes to enhance the production of liquid fuels [20–22], whereas Li et al. also reported a Pt@S-1 + Beta zeolite with metal and acid sites spatially separated for well-matched reaction steps delivering narrowed product distribution [23]. Owing to the higher activity of Ru for the C–C scission under desired moderate conditions, the Ru-based bifunctional catalysts for polyolefin hydrocracking have also been studied recently [24–26], in which the interplay between Ru and acid sites has not been fully understood, especially regarding the production of liquid fuels. The excessive terminal C–C scission over Ru sites would always lead to more methane with high H_2 consumption that undermines the selectivity of value-added liquid hydrocarbons [27,28], which could be potentially circumvented by constructing metal–acid bifunctional catalysts and rationally tuning the synergy between them.

Herein, we developed a bifunctional catalytic system containing Ru nanoparticles supported on γ-Al_2O_3 and abundant acid sites within β-zeolite for hydrocracking polyolefins. It is disclosed that spatially separated Ru and acid sites with an appropriate proportion are conducive to the effective cleavage of C–H and C–C bonds. The mechanism investigation through in situ infrared spectroscopy and probe–molecule model reactions implies that the optimal synergy of Ru and acid sites considerably contributes to the enhanced tandem process involves initial C–H bond activation and pre-cracking over Ru/γ-Al_2O_3, followed by transferring to the acid sites within β-zeolite for subsequent β-scission and isomerization to produce gasoline-range hydrocarbons, while inhibiting over-cracking of intermediates over Ru sites. This catalytic system not only significantly boosts the yield of $C_{5–12}$ gasoline-range hydrocarbons up to 73.4% for the low-density polyethylene (LDPE) hydrocracking at 250 °C but also offers a promising platform for the conversion of other ubiquitous polyolefins, such as linear low-density polyethylene (LLDPE) and polypropylene (PP). This work may offer new insights into the design of Ru-based bifunctional catalysts potentially applied in the chemical upgrading of polyolefin waste into valuable chemicals.

2. Results and Discussion

2.1. Catalytic Performance

A series of Ru-based catalysts were evaluated in a stainless steel batch reactor under a high-pressure hydrogen atmosphere, where a mixture of LDPE and catalyst was placed and heated to a certain reaction temperature for the hydrocracking reactions (details in Section 3). The performances of LDPE hydrocracking and the product distribution over various catalysts are shown in Figures 1A, S6 and S7. The mixture of β-zeolite and SiO_2 exhibits the conversion of LDPE as low as 17% and a broad product distribution with 37.4% $C_{5–12}$ branched alkanes, while the mixture of Ru/γ-Al_2O_3 and SiO_2 delivers a significantly higher conversion at 51.8% with predominate straight-chain alkanes beyond C_{13} (52.8%).

$Ru/\gamma\text{-}Al_2O_3$ combined with β-zeolite, in contrast, not only enhances the conversion of LDPE up to 56.1% but also dramatically narrows the product distribution and promotes the selectivity of $C_{5–12}$ gasoline branched liquid fuels as high as 63.9%. Interestingly, despite possessing similar active components, the catalyst via loading Ru onto β-zeolite and mixing with $\gamma\text{-}Al_2O_3$ ($Ru/\beta(25) + \gamma\text{-}Al_2O_3$) results in much lower conversion and selectivity compared with the above $Ru/\gamma\text{-}Al_2O_3$ + β-zeolite. By calculating the TOF on $Ru/\gamma\text{-}Al_2O_3$ + β(25) and $Ru/\beta(25) + \gamma\text{-}Al_2O_3$, they are 78.8 $g_{Gasline}\ h^{-1}\ g_{Ru}{}^{-1}$ and 50.5 $g_{Gasline}\ h^{-1}\ g_{Ru}{}^{-1}$ respectively. This result further demonstrates that separating Ru sites from acid sites can promote Ru-zeolite synergy and correspondingly facilitate the hydrogenolysis of polyolefins. In addition, the bifunctional catalysts comprising $Ru/\gamma\text{-}Al_2O_3$ and other zeolites (MOR, ZSM-5, and Y) are also evaluated and exhibit inferior performances in both the conversion of LDPE and selectivity of $C_{5–12}$ hydrocarbons (Figure S6), suggesting the critical importance of zeolite topology and acid properties.

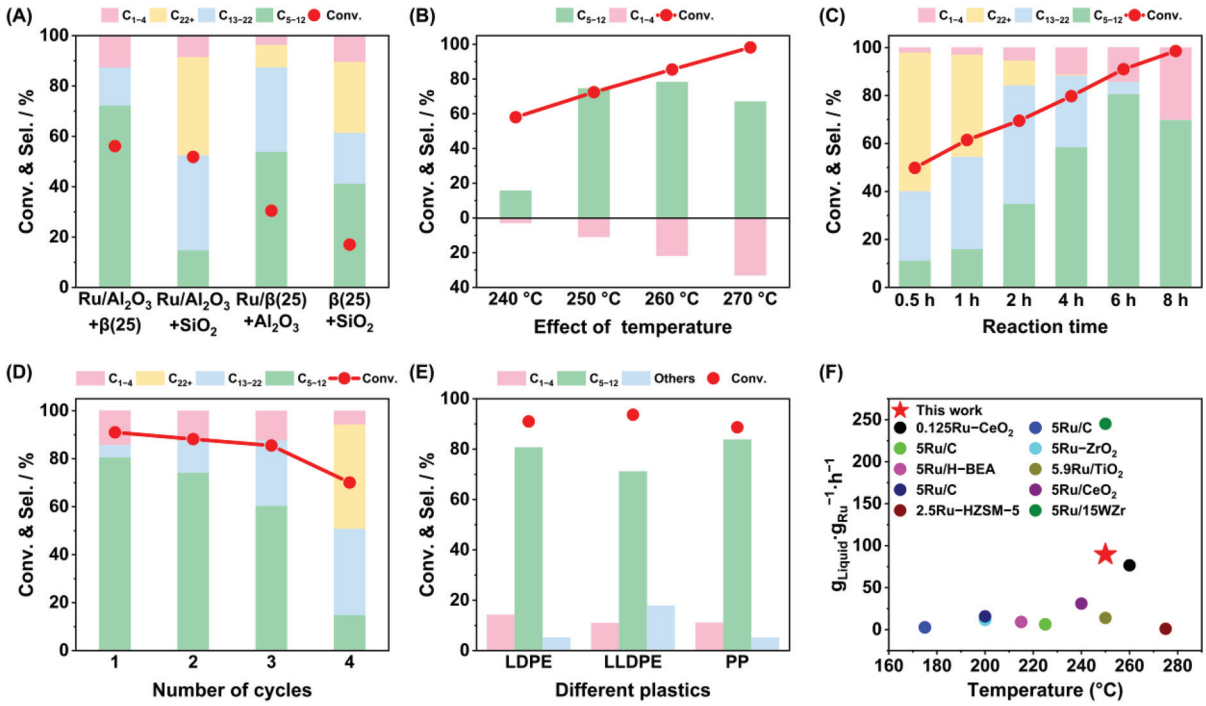

Figure 1. (**A**) Hydrocracking performance of LDPE on different catalysts (conditions: 250 °C, 2 MPa H_2, 6 h, 500 rpm, Ru loading 1.8 wt%); (**B**) Hydrocracking performance of LDPE by composite catalysts at different temperatures (conditions: 3 MPa H_2, 6 h, 600 rpm, $1.8Ru/\gamma\text{-}Al_2O_3$:β(25) = 1:1); (**C**) Hydrocracking performance of LDPE by composite catalysts at different times (conditions: 250 °C, 3 MPa H_2, 6 h, 600 rpm, $3.0Ru/\gamma\text{-}Al_2O_3$:β(25) = 1:1); (**D**) Number of cycles of composite catalysts (conditions: 250 °C, 3 MPa H_2, 6 h, 600 rpm, $3.0Ru/\gamma\text{-}Al_2O_3$:β(25) = 1:1); (**E**) Hydrocracking performance of composite catalysts for different polyolefin feedstocks (conditions: 250 °C, 3 MPa H_2, 6 h, 600 rpm, $3.0Ru/\gamma\text{-}Al_2O_3$:β(25) = 1:1); (**F**) Performances in hydrogenation cracking among recently reported state-of-the-art Ru-based catalytic systems [29–38].

We also examined the performance of the optimal $Ru/\gamma\text{-}Al_2O_3$ + β-zeolite system under varying conditions, including stirring speed, pressure, and temperature, all of which significantly influence batch reactions. As shown in Figure S8A, the mass transfer of reactants in the viscous reaction system enhances with the increase of stirring speed from 500 to 600 revolutions per minute (rpm), especially at the initial stage, leading to improved conversion of LDPE. However, further increasing the stirring speed to 700 rpm slightly reduces both conversion and $C_{5–12}$ hydrocarbon selectivity, likely due to decreased reactant residence time on the catalyst surface [39], which negatively impacts gas–liquid

phase mass transfer. Additionally, raising the hydrogen pressure from 1 MPa to 3 MPa significantly improves the conversion of LDPE from 53.5% to 72.5% and the selectivity of the $C_{5–12}$ product from 44.5% to 75.4% (Figure S8B). This may be contributed by a positive shift of the thermodynamic equilibrium and enriched active hydrogen species on the catalyst surface. However, further increasing hydrogen pressure to 4 MPa degrades the conversion of LDPE to 69.1% and the selectivity of $C_{5–12}$ to 70.8%, which may be caused by competitive adsorption of hydrogen and reactants on the catalyst surface [40]. Therefore, the optimal stirring speed and hydrogen pressure are 600 rpm and 3 MPa H_2, respectively. The conversion of LDPE almost linearly increases from 58.0% to 98.2% with the reaction temperature rising up from 240 °C to 270 °C, yet the selectivity of $C_{5–12}$ hydrocarbons goes through an initial dramatic elevation from 15.7% to 78.3% and a subsequent gradual decrease to 67.0% with a surge of $C_{1–4}$ hydrocarbons up to 33.0% (Figure 1B). It is plausible that the increased temperature would kinetically accelerate the cleavage of C–H and C–C bonds, whereas the excessively high temperature could also prompt intensive side reactions due to the iterative and uncontrollable cracking, leading to short-chain products [41].

We further monitored the catalytic performance of Ru/γ-Al_2O_3 + β-zeolite under optimal operation conditions along the extended reaction time from 0.5 h to 8 h. As shown in Figure 1C, approximately 50% LDPE conversion was achieved within 30 min, with C_{22+} as the primary product. Subsequently, the conversion keeps increasing with gradually decreased mean carbon number of hydrocarbon products. The highest selectivity of $C_{5–12}$ products up to 80.7% is achieved after a 6 h reaction, while further extending the reaction time to 8 h leads to possible secondary cracking of $C_{5–12}$ gasoline alkanes towards $C_{1–4}$ gaseous hydrocarbons due to the excessive residue time of intermediates and products on the catalysts. These results indicate that the hydrocracking reactions follow a typical tandem pathway involving consecutive C–C bond cleavage, transforming long-chain polymers into hydrocarbons with significantly shorter carbon chains. In this context, controlling the reaction time is crucial for regulating the product distribution under given conditions.

We also examined the recyclability through the cyclic experiments. As shown in Figure 1D, the conversion of LDPE and selectivity of $C_{5–12}$ gasoline hydrocarbons in the second use show a little decrease by 2.8% and 6.5%, respectively, while only the selectivity of $C_{5–12}$ is subjected to a significant decline by 13.8% in the third use. However, in the fourth use, the conversion of LDPE decreases by ~20% with even more dramatically decreased selectivity of $C_{5–12}$ hydrocarbons by ~65% compared to the first use. Instead, the distribution of the products is shifted towards predominantly heavier C_{22+} hydrocarbons. We rationally attribute this deactivation to the possible aggregation of Ru particle and carbon deposition on the catalyst (Figures S14 and S15).

The Ru/γ-Al_2O_3 + β-zeolite bifunctional catalyst demonstrates versatility in its application to the hydrocracking of various polyolefin feedstocks, including LLDPE and PP, achieving substantial yields of $C_{5–12}$ hydrocarbons, reaching 66.7% and 74.3%, respectively, as evidenced in Figure 1E. In comparison to the cutting-edge Ru-based catalysts recently reported in the literature, our developed catalyst maintains a superior specific activity under analogous moderate reaction conditions, specifically for the synthesis of liquid fuels. This superior performance underscores the high atom utilization efficiency of Ru within our catalytic system, positioning it as a promising candidate for potential industrial applications, as further illustrated in Figure 1F.

2.2. Effects of Metal–Acid Synergy

The above results of catalytic performance have indicated that the cooperation of metal Ru and acid sites of β-zeolite plays a critical role in enhancing the production of gasoline-range

hydrocarbons from polyolefin hydrocracking under specific conditions. To gain deep insight into the underlying mechanisms of such synergy between Ru metal acid sites for more rational design and optimization of the bifunctional catalysts, we employed advanced characterization techniques to further investigate the detailed structure–activity relationship.

A series of xRu/γ-Al_2O_3 (x represents the loading of Ru) catalysts with varied Ru loadings from 0.6 wt% to 3.0 wt% were prepared, and the actual Ru contents were quantified by inductively coupled plasma atomic emission spectroscopy (ICP-AES) and summarized in Table S2. Transmission electron microscopy (TEM) tests were conducted to characterize the morphology of xRu/γ-Al_2O_3. As shown in Figures 2A,B and S10, all samples demonstrate Ru nanoparticles uniformly dispersed on γ-Al_2O_3, with the mean particle size increasing from 0.97 nm to 1.39 nm as the Ru loading increases from 0.6 wt% to 3.0 wt%. X-ray diffraction (XRD) patterns (Figure 2C) of all samples exhibit prominent characteristic diffraction peaks of the support γ-Al_2O_3, while no significant diffraction peaks attributed to metallic Ru or Ru oxides can be distinguished, which might be ascribed to the high dispersion and small particle size of Ru species (<2 nm) [42]. We also measured the specific area and pore structure of xRu/γ-Al_2O_3 samples by N_2 physical adsorption and desorption tests (Figure 2D, Table S1). The incorporation of Ru species has a minimal effect on the specific surface area and pore volume of the γ-Al_2O_3 support, with the mesoporous structure remaining intact, as evidenced by the similar hysteresis loops observed at a relative pressure range of P/P^0 from 0.8 to 1.0.

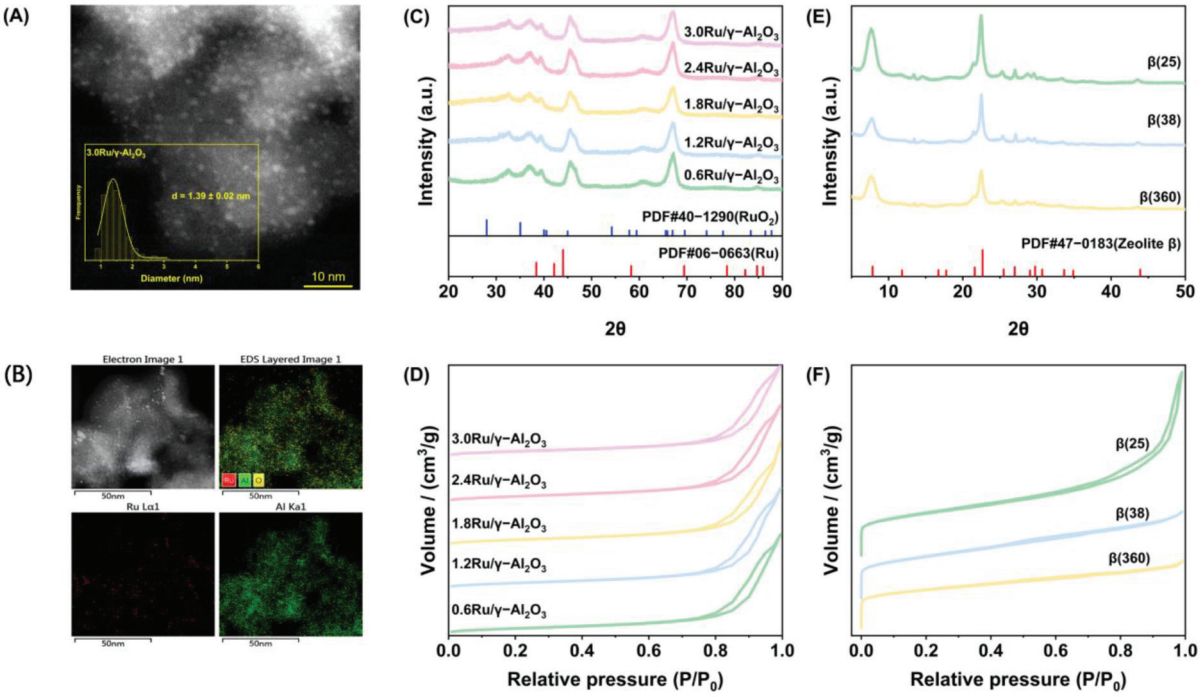

Figure 2. (**A**,**B**) TEM images and EDS elemental analysis of 3.0Ru/γ-Al_2O_3; (**C**) XRD patterns and (**D**) N_2 physical adsorption and desorption isotherms of xRu/γ-Al_2O_3; (**E**) XRD patterns; and (**F**) N_2 physical adsorption and desorption isotherms of β-zeolites with different Si/Al ratios.

To elucidate the influence of acid properties on the catalytic performance, we further introduced several β-zeolites (β(y), y represents the ratio of SiO_2/Al_2O_3) of different Si/Al ratios. XRD patterns of all zeolites exhibit characteristic diffraction peaks consistent with the database (Figure 2E). N_2 physisorption–desorption isotherms of all samples show a steep increase at a relative pressure P/P^0 of approximately 0, indicating the filling of micropores (Figure 2F). The significant hysteresis loop at P/P^0 = 0.6–1.0 for β(25) manifests the presence of mesopores probably derived from the aggregation of nanosized zeolite

crystals, while there are only a few mesopores for β(38) and β(360), as verified by the much smaller hysteresis loops. Correspondingly, the surface area and pore volume of these zeolites also have certain discrepancies, as summarized in Table S1.

First, we employed *x*Ru/γ-Al_2O_3 catalysts with varying Ru loadings, combined with the same β(25) catalyst, to investigate the structure–activity relationship of Ru sites in the conversion of LDPE. The catalytic performance results are shown in Figure 3A. With the Ru loading increased from 0.6 wt% to 3.0 wt%, the conversion of LDPE keeps increasing from 28.6% to 91.0%, while the selectivity of $C_{5–12}$ hydrocarbons also grows from 21.8% to the highest value of 80.7%. In contrast, the specific activity normalized by the Ru mass goes through an initial elevation from 32.5 g g_{Ru}^{-1} h^{-1} at 0.6 wt% to 100.7 g g_{Ru}^{-1} h^{-1} at 1.8 wt%, followed by a continuous decrease to 84.1 g g_{Ru}^{-1} h^{-1} at 3.0 wt% (Figure 3A). In situ CO adsorption infrared spectroscopy (CO-IR) was conducted to investigate the structure of surface Ru sites (Figure 3B). All *x*Ru/γ-Al_2O_3 catalysts exhibit three similar ν_{CO} bands at 2120 cm^{-1}, 2060 cm^{-1}, and 1990 cm^{-1}. The bands at 2120 cm^{-1} attributed to tricarbonyl CO species adsorption on partially oxidized Ru^{n+} species ($Ru^{n+}(CO)_3$, n = 1–3). The band centered at 2060 cm^{-1} consists of two characteristic peaks at 2068 cm^{-1} and 2050 cm^{-1} (the fitting results are shown in Figure S11), which the peak at 2068 cm^{-1} is attributed to dicarbonyl CO species adsorbed on the metallic Ru (Ru^0-$(CO)_2$), and the peak at 2050 cm^{-1} is assigned to linearly adsorbed CO on metallic Ru (Ru^0-CO) [43–46]. By deconvolving and fitting the four bands (Figure S11 and Table S3), it is evident that metallic Ru species dominate the catalyst surface, with their proportion only slightly increasing from 92.4% to 93.6% as the Ru loading rises from 0.6 wt% to 3.0 wt%. This indicates that pre-reduction in an H_2 atmosphere effectively generates metallic Ru surfaces in all cases, which are likely the active centers responsible for the hydrocracking reactions.

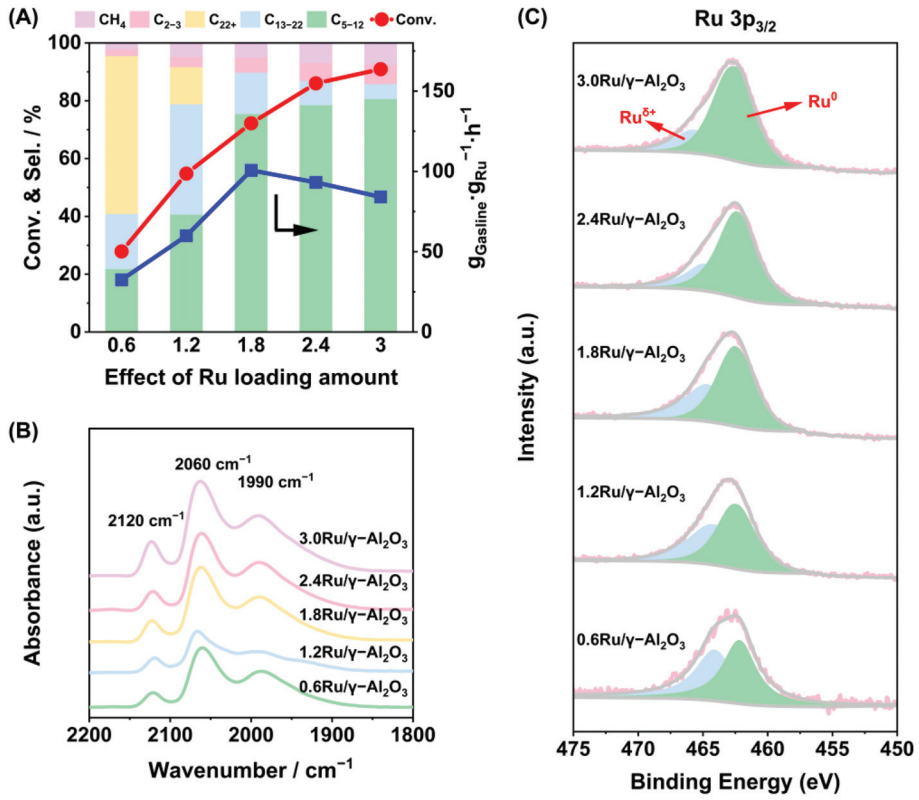

Figure 3. (**A**) The effect of Ru loading in the composite catalyst on the hydrocracking performance of LDPE and the specific activity of Ru loading with respect to gasoline yield (conditions: 250 °C, 3 MPa H_2, 6 h, 600 rpm, *x*Ru/γ-Al_2O_3:β(25) = 1:1); (**B**) In situ CO adsorption infrared spectroscopy of *x*Ru/γ-Al_2O_3; (**C**) X-ray photoelectron spectroscopy of *x*Ru/γ-Al_2O_3.

To elucidate the chemical state of Ru in the xRu/γ-Al_2O_3, Ru $3p_{3/2}$ X-ray photoelectron spectroscopy (XPS) characterization was performed. As shown in Figure 3C, the signals of xRu/γ-Al_2O_3 can be deconvolved and fitted into two sets of peaks. The peaks at 462.5 eV can be attributed to the metallic Ru (Ru^0), while the minor peaks at 465.7 eV correspond to partially oxidized Ru ($Ru^{\delta+}$) [47,48]. The proportion of Ru species was calculated based on the integrated peak area and summarized in Table S3. With Ru loading increasing from 0.6 wt% to 3.0 wt%, the proportion of metallic Ru^0 species increased from 50.9% to 79.0%. These values are significantly lower than those measured in CO-IR, which should be ascribed to the deeper detection distance of XPS (~3 nm) in comparison with the CO-IR only involving outermost atomic layers of catalysts. Additionally, quite a few small metallic Ru^0 species are subject to easier oxidization under atmospheric conditions during the transfer and preparation process of samples for XPS. According to the TEM results, the size of Ru nanoparticles also increases from 0.97 nm to 1.39 nm as the Ru loading increases. We can reasonably correlate the increased metallic Ru^0 species with the intensified aggregation of Ru particles. Ru^0 can realize hydrocracking of polyolefin by dissociating hydrogen into active H atoms and reducing the activation energy of C-C bond breakage [49,50]. With the increase of Ru loading, the proportion of Ru^0 increases, which is more conductive to the activation of C–H and C–C bonds. In this context, the xRu/γ-Al_2O_3 catalysts with low Ru loading of 0.6 wt% and 1.2 wt% exhibit lower specific activity compared to those with higher Ru loading, despite the enhanced accessibility of Ru atoms in Ru/γ-Al_2O_3 with smaller particle sizes. In addition, the emergence of oxidized Ru species can be attributed to the charge transfer at the metal–support interface, which shows an enhancement at low Ru loading. The relatively strong interaction between Ru and γ-Al_2O_3 facilitate the electron transfer from Ru to support Ru-O-Al bonds [51,52], whereas the electron-deficient Ru species may not favor the activation of H_2 molecules and C–H and C–C bonds in polyolefins, as suggested by previous studies [53–55]. The $Ru^{\delta+}$, which is more prevalent at low Ru loading, mainly promotes the fracture of the internal C–C bond and thus inhibits the generation of methane [15,56]. This is because the internal C atoms have a higher electron density than terminal C atoms, making $Ru^{\delta+}$ more inclined to bind to the internal C atoms. Consequently, the tendency of terminal C–C bond breakage and the selectivity of methane increase with increasing Ru loading.

To investigate the effect of acid sites, we further employed the β-zeolites of different Si/Al ratios with the same 3.0Ru/γ-Al_2O_3 in the conversion of LDPE. As shown in Figure 4A, increasing the Si/Al ratio of β-zeolite from 25 to 360 dramatically reduces the conversion of LDPE from 72.5% to 52.5% and the selectivity of gasoline hydrocarbons ($C_{5–12}$) from 75.4% to 12.9%. NH_3-temperature programmed desorption (NH_3-TPD) characterization reveals that all β-zeolites (Figure 4B) exhibit two desorption peaks within a range of 100 °C and 500 °C, corresponding to the weak and strong acid centers. The total acid amounts are calculated to be 1198 mmol g^{-1}, 1059 mmol g^{-1}, and 205 mmol g^{-1} for β(25), β(38), and β(360), respectively (Table S4). Pyridine-infrared (Py-IR) spectroscopy was employed to discriminate different acid centers in β-zeolites, where the peaks at 1454 cm^{-1} and 1544 cm^{-1} are attributed to the adsorption of pyridine on Lewis and Brønsted acid sites, respectively. As shown in Figure 4C and summarized in Table S4, β(360) zeolite displays notably reduced peak intensities at 1454 cm^{-1} and 1544 cm^{-1}, indicative of a minimal presence of acid sites attributable to the lower proportion of framework Al atoms [57]. In contrast, there is almost the same area of the peaks at 1544 cm^{-1} for β(25) and β(38), while the peak of β(25) at 1454 cm^{-1} is significantly higher. This indicates that there is little discrepancy in the number of Brønsted acid sites for β(25) and β(38), corresponding to the similar amount of strong acid sites, as shown in the NH_3-TPD results. Rationally correlating these results with the catalytic activity shown in Figure 4A, it is found that the

productivity of $C_{5–12}$ hydrocarbons from LDPE hydrocracking is primarily enhanced by the strong Brønsted acid sites, while the moderate Lewis acid sites show minor effect on the apparent performance, as β(25) and β(38) with distinct amounts of Lewis acid sites offer quite similar activity for the production of $C_{5–12}$ hydrocarbons. It is plausible that the carbocation-based reactions controlled by the Brønsted acid centers impose a prominent effect on the kinetic behaviors of the intermediates within the β-zeolites.

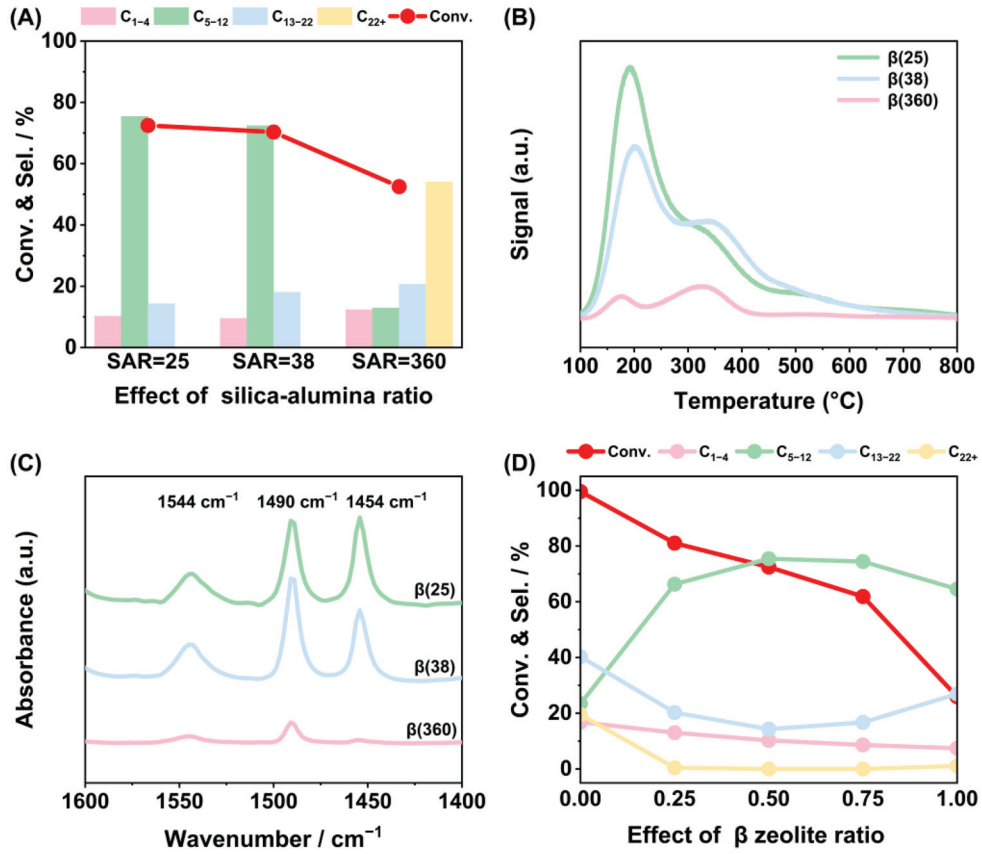

Figure 4. (**A**) The effect of the Si/Al ratio of β-zeolite on the hydrocracking performance of LDPE (conditions: 250 °C, 3 MPa H_2, 6 h, 600 rpm, 1.8Ru/γ-Al_2O_3:β(y) = 1:1); (**B**) NH_3-TPD; and (**C**) Py-IR spectra of β-zeolites with different Si/Al ratios.; and (**D**) The effect of the proportion of β-zeolite on the hydrocracking performance of LDPE (conditions: 250 °C, 3 MPa H_2, 6 h, 600 rpm, Ru loading 1.8 wt%, the Si/Al ratio of β-zeolite is 25).

Besides the optimization of individual Ru/γ-Al_2O_3 and β-zeolites, the synergy could also be influenced by the proportion of dual components. As shown in Figure 4D, the sole 1.8Ru/γ-Al_2O_3 gives the highest conversion of LDPE up to 99.5%, yet exhibiting poor selectivity of $C_{5–12}$ hydrocarbons at 23.4%. With the ratio of β-zeolites increasing, the conversion of LDPE demonstrates a gradual decline, while the selectivity of $C_{5–12}$ hydrocarbons goes through an initial promotion to 75.4% at the conversion of 72.5% and a subsequent decrease to 64.6% at the conversion of 25.9%. The yield of $C_{5–12}$ gasoline hydrocarbons reaches the highest value of 54.7% with 1.8Ru/γ-Al_2O_3 and β-zeolite mixed in a 1:1 ratio. These results imply that Ru/γ-Al_2O_3 primarily contributes to the hydrocracking reaction, as it possesses much higher activity than that of β-zeolite. The introduction of β-zeolite might not only catalyze the carbocation-based cracking reactions but also tailor the products' distribution through regulating the kinetics behaviors regarding the transferring and transformation of the intermediates.

2.3. Reaction Mechanisms

Now that we have demonstrated that the synergy of metal–acid sites should play a vital role in the catalytic hydrocracking of LDPE, the corresponding reaction mechanisms should also be elucidated for the rational design of catalysts specialized in the critical kinetic process. We first studied the hydrocracking of LDPE at the initial reaction stage to obtain the performance close to kinetic region. As depicted in Figure 5A, during the initial 0.5 h of reaction, the conversion of LDPE and the product distribution on the Ru/γ-Al_2O_3 + β-zeolite and Ru/γ-Al_2O_3 + SiO_2 catalysts are nearly identical. In contrast, the β-zeolite + SiO_2 catalyst exhibits extremely poor activity. These observations indicate that the majority of LDPE is initially activated and transformed on the Ru/γ-Al_2O_3 catalyst via a hydrocracking mechanism, attributable to the significantly superior capability of metallic Ru in activating the H_2, C–H, and C–C bonds within the LDPE molecules. In addition, the pore opening of narrow size in the range of 0.5–1.2 nm greatly restricts the diffusion of reactants into the channels of β-zeolite (Figure S12) and the corresponding accessibility of acid sites to the specific C–H and C–C bonds in bulk molecules. Thus, we speculate that the β-zeolites demonstrate negligible activity until smaller hydrocarbon intermediates are formed from LDPE hydrocracking over Ru/γ-Al_2O_3.

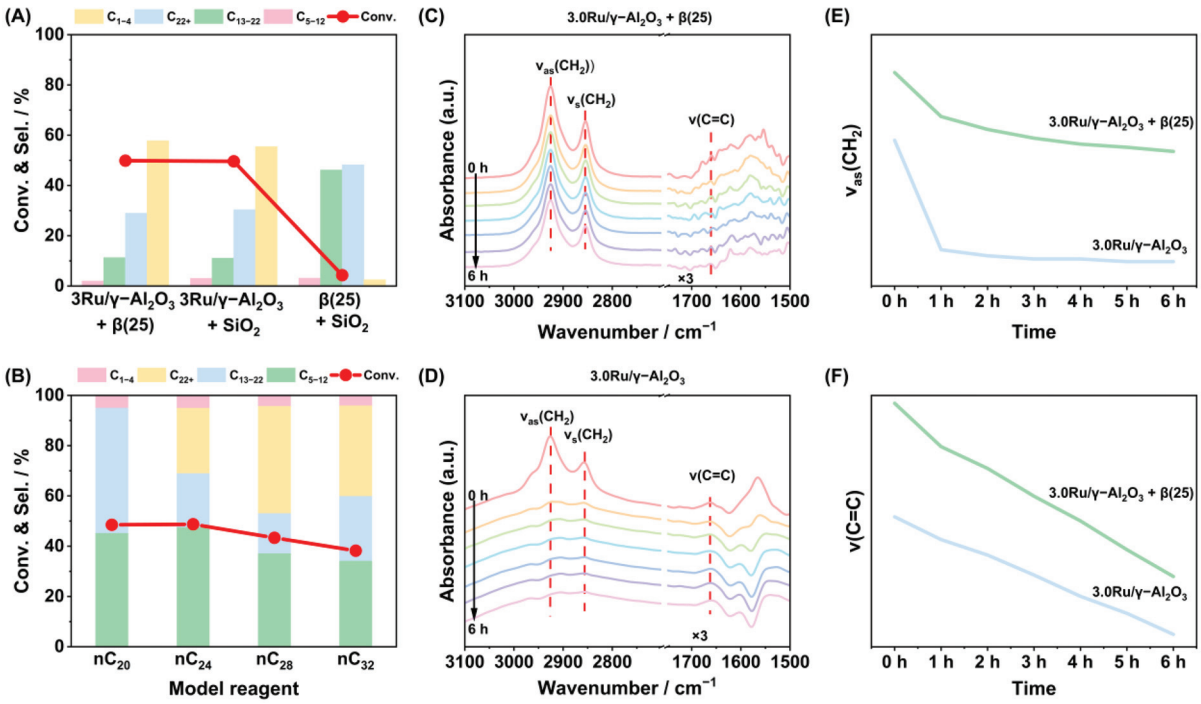

Figure 5. (**A**) The effect of different catalysts on the hydrocracking performance of LDPE (conditions: 250 °C, 3 MPa H_2, 600 rpm, 0.5 h); (**B**) The catalytic performance of β(25) + SiO_2 on model reactants with different carbon numbers (conditions: 250 °C, 3 MPa H_2, 600 rpm, 0.5 h); (**C**,**D**) In situ infrared spectra of LDPE hydrocracking on mixtures of 3.0Ru/γ-Al_2O_3 and β-zeolite, and on 3.0Ru/γ-Al_2O_3 alone; (**E**,**F**) The curves of the intensity changes of $\nu_{as}(CH_2)$ and ν(C=C) over time.

This reaction pathway has been further elucidated through the use of $C_{20–32}$ *n*-alkanes as model reactants, with β-zeolite as the catalyst (Figure 5B). The decreased conversion of alkanes from 48.5% to 38.2% with enlengthened carbon chains from C_{20} to C_{32} also implies that the acid-catalyzed behaviors in β-zeolite are highly dependent on the molecular size of reactants. A detailed analysis of the product distribution, using C_{24} alkane as a representative reactant (Figure S9), reveals the absence of C_1 products and the presence of only minimal C_2 products, alongside a significant yield of C_{22} and C_{23} hydrocarbons. These findings lead us to infer that long-chain hydrocarbons initially undergo protonation

at the acidic sites of β-zeolite, resulting in the formation of carbocation intermediates. These intermediates are primarily subject to skeletal isomerization and β-scission, while the terminal cleavage of C–C bonds is intrinsically suppressed. The formation of $C_{22–23}$ hydrocarbons also suggests that there might be oligomerization reactions of short-chain carbocations at Brønsted acid sites [58].

To further comprehend the reaction pathways of LDPE hydrocracking on Ru/γ-Al_2O_3 and β-zeolite catalysts, in situ infrared experiments were employed to monitor the changes of intermediates in reaction. As shown in Figure 5C,D, there are obvious adsorption bands at 2925 cm^{-1} and 2854 cm^{-1} assigned to C–H asymmetric and symmetric stretching vibration ($\nu_{as}(CH_2)$ and $\nu_s(CH_2)$) of the LDPE skeleton, respectively, during the hydrocracking of LDPE on both Ru/γ-Al_2O_3 and Ru/γ-Al_2O_3 + β-zeolite [59,60]. Signals assigned to C=C vibration at 1660 cm^{-1} also emerge even before the onset of the hydrocracking reaction, suggesting that they might be attributed to the formation of alkene intermediates in the heating period in the absence of a H_2 atmosphere. As the reaction proceeds, both peaks assigned to LDPE and alkene intermediates undergo a gradual decline, indicating that the LDPE is converted into volatile hydrocarbons that diffuse away from the catalyst surface rapidly. The quick consumption of alkene implies that the H_2 atmosphere might kinetically promote the transformation of intermediates. Interestingly, we notice that the decrease of C–H peaks is significantly slower on Ru/γ-Al_2O_3 + β-zeolite in comparison with Ru/γ-Al_2O_3, while the descent of C=C peaks almost has an identical rate (Figure 5E,F). This suggests that Ru/γ-Al_2O_3, primarily adept at hydrogen activation, plays a pivotal role in the elimination of unsaturated alkene intermediates. In contrast, β-zeolite is in favor of the transferring of certain intermediates into the channels for more moderate and controllable cracking and isomerization reactions, thereby prolonging the residue time of hydrocarbons in the Ru/γ-Al_2O_3 + β-zeolite and preventing the excessive cracking over Ru/γ-Al_2O_3.

Based on the preceding discourse, we posit a potential reaction mechanism for the bifunctional catalytic system comprising Ru/γ-Al_2O_3 and β-zeolite, as depicted in Figure 6. Ru/γ-Al_2O_3 firstly transform LDPE into long-chain olefin intermediates with its prominent capability to activate H_2 molecules and C–C and C–H bonds. Once the intermediates are tailored to specific dynamic diameters close to the pore opening of β-zeolite, they are diffused into the channels and undergo isomerization, β-scission, and oligomerization reactions at the strong Brønsted acid sites. The optimal acid properties and the confinement effect of the pores and channels in β-zeolite are harnessed to selectively produce $C_{5–12}$ hydrocarbons. Within this context, the unsaturated intermediates are subjected to hydrogenation at the Ru metal sites, ultimately resulting in the production of gasoline-ranged alkanes. The meticulously regulated synergy between the Ru and acid sites is chiefly responsible for the high selectivity of the target products, achieved through a controlled cleavage of C–C bonds, thereby mitigating excessive cracking and the resultant formation of $C_{1–4}$ gaseous byproducts. This proposed mechanism highlights the sophisticated interplay between the catalytic components and their collective contribution to the enhanced efficiency and selectivity of the chemical recycling process.

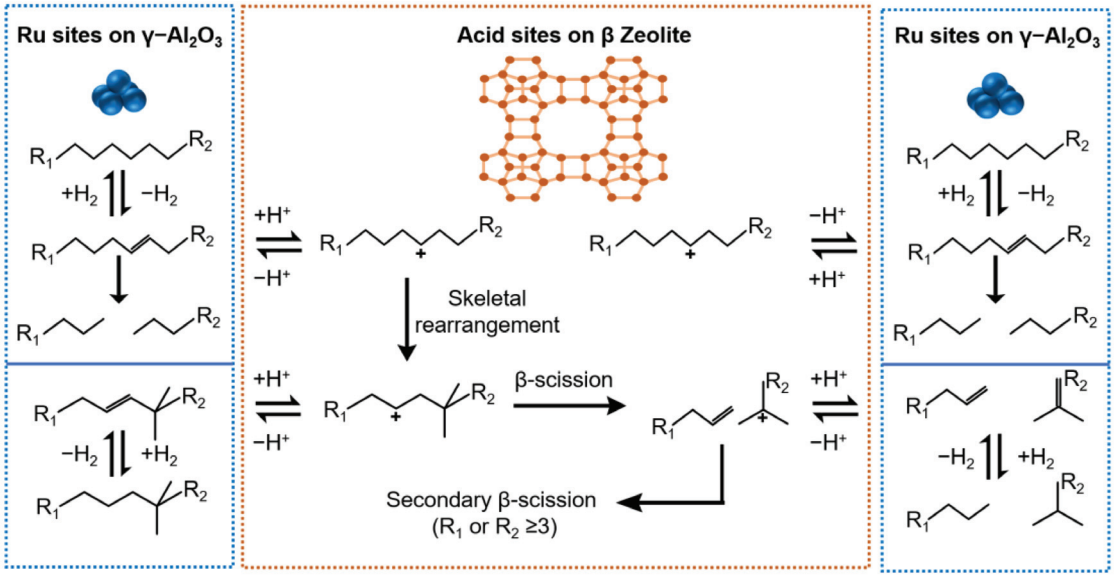

Figure 6. Mechanism of hydrocracking of LDPE on composite catalysts.

3. Materials and Methods

3.1. Materials

$RuCl_3 \cdot xH_2O$ (35.0–42.0% Ru basis), $NH_3 \cdot H_2O$, cyclohexane (HPLC grade, ≥99.9%), mesitylene (GC standard, ≥99%), C_7–C_{40} saturated alkane mixture (certified reference material, 1000 μg ml^{-1} each component in hexane), *n*-eicosane (AR grade, ≥99%), *n*-tetracosane (AR grade, 99%), *n*-octacosane (AR grade, ≥97%), *n*-dotriacontane (AR grade, ≥98%), and nano-alumina (99.99% metals basis, γ-phase, 20 nm) were purchased from Aladdin Co., Ltd. (Fukuoka, Japan) β zeolites (Ammonium, S.A.) with Si/Al molar ratios of 25, 38, and 360 were purchased from Alfa Co., Ltd. (Shanghai, China). Low-density polyethylene, linear low-density polyethylene, and polypropylene (average Mw250,000 by GPC) were purchased from Macklin Co., Ltd. (Shanghai, China).

3.2. Synthesis of Catalysts

Synthesis of xRu/γ-Al_2O_3 (x represents the loading of Ru): $RuCl_3 \cdot xH_2O$ was dissolved in an aqueous solution containing a small amount of HCl via sonication, which was then mixed with 20 mL of water to obtain a homogeneous solution (denoted as solution A). Then, 2 g of γ-Al_2O_3 (after calcined in air at 400 °C for 2 h) was mixed with 50 mL of water and uniformly dispersed by stirring, and 1.8 mL of ammonia solution was added (denoted ad solution B). The $RuCl_3$ solution was pumped into solution B using a constant flow pump at a flow rate of 5 mL min^{-1} and 25 °C under vigorous stirring. The suspension was further stirred at room temperature for 3 h, followed by filtering and drying at 120 °C overnight. The sample was reduced at 400 °C for 2 h in a 10% H_2/Ar atmosphere to remove NH_4Cl and reduce the active metal Ru.

Synthesis of Ru/β-zeolite: β-zeolites were initially calcined in air at 550 °C for 6 h and then dispersed in 100 mL of water, followed by mixing with a certain amount of $RuCl_3$ aqueous solution under 25 °C stirring in a water bath at 60 °C overnight. The solvent was removed using a rotary evaporator at 60 °C, and the sample was dried in an oven at 120 °C overnight. Before use, it was reduced at 400 °C for 2 h in a 10% H_2/Ar atmosphere.

3.3. Reaction Test

The hydrocracking of polyolefin was conducted in a high-pressure stainless steel vessel reactor (50 mL). The inner diameter and height of the reactor used in the experiment

were ϕ34 mm and 78 mm, and the distance between the bottom of the stirring paddle and the thermocouple and the bottom of the reactor was about 5 mm, as shown in Figure S1. The catalysts were pre-ground to less than 60 mesh and the particle size was small enough to eliminate possible internal diffusion effects [61,62]. About 4 g of polyolefin powder was mixed with Ru/γ-Al_2O_3 and zeolite, according to the ratio of reactant to catalyst (10:1). The mixture was ground uniformly in a mortar and then placed into the reactor vessel and sealed. The atmosphere inside the reactor was flushed by the reaction gas (H_2) five times, pressurized to required reaction pressure, and held for a period. The reactor temperature was ramped to 240–270 °C within 0.5 h, while mechanical stirring was performed at a speed of 500–700 rotations per minute (rpm).

After the reaction was complete, the reactor was cooled in an ice-water bath rapidly until the temperature inside the reactor dropped below 20 °C. The gaseous products were collected using a gas sampling bag, analyzed using gas chromatography-flame ionization detection (GC-FID), and quantified with C_1-C_8 *n*-alkane standard gas. The liquid products were dissolved with cyclohexane as a solvent and mesitylene as an internal standard. The mixture was sonicated and then centrifuged. The supernatant was taken for gas chromatography-mass spectrometry (GC-MS) analysis. The residue was dried at 85 °C and then collected, and the solid was weighed.

For the recyclability test, the cyclohexane extract was centrifuged to obtain the used catalyst, which was then dried at 85 °C to remove cyclohexane. Before each use, the catalyst was reduced at 400 °C for 2 h in a 10% H_2/Ar atmosphere in a tubular furnace.

The conversion, selectivity, degree of branching, carbon balance, and mass balance in this work were calculated as follows. The carbon balance and mass balance were above 80% for all tests. The difference value from 100% is possibly ascribed to the partial carbon deposition on the solid catalyst and inevitable loss of products in the sample transferring steps.

$$\text{Conversion}(\%) = \frac{\text{mass of initial PE} - \text{mass of residual PE}}{\text{mass of initial PE}} \times 100\% \quad (1)$$

$$\text{Selectivity}(\%) \text{ of } C_i = \frac{\text{mass of } C_i}{\text{mass of } \sum C_i} \times 100\% \quad (2)$$

$$\text{Degree of branching}(\%) = \frac{\text{mass of } \sum \text{isoC}_i}{\text{mass of } \sum \text{isoC}_i + \text{mass of } \sum \text{nC}_i} \times 100\% \quad (3)$$

$$\text{Carbon balance}(\%) = \frac{\text{mass of carbon in product}}{\text{mass of carbon in initial PE}} \times 100\% \quad (4)$$

$$\text{Mass balance}(\%) = \frac{\text{mass of product} + \text{mass of residual PE}}{\text{mass of initial PE} + \text{mass of } H_2 \text{ consumption}} \times 100\% \quad (5)$$

3.4. Catalyst Characterization

Inductively coupled plasma atomic emission spectrometry (ICP-AES): The content of different elements in the catalysts was determined using a Avio 550 Max (PerkinElmer, Waltham, MA, USA) inductively coupled plasma optical emission spectrometer.

X-ray diffraction (XRD): XRD patterns were recorded using a Empyrean (Malvern Panalytical, Shanghai, China) diffractometer with a Cu Kα (λ = 0.154 nm) radiation source, operating at 40 kV and 40 mA, with a 2θ range of 5–90°.

NH_3-temperature programmed desorption (NH_3-TPD): The samples were pretreated at 400 °C for 1 h under a helium flow of 30 mL min^{-1}, then cooled to 100 °C. After the baseline stabilized, NH_3 was adsorbed to saturation. The samples were then heated to

800 °C at a rate of 10 °C min^{-1} under a helium flow for TPD experiments. The effluent was detected using mass spectrometry.

CO-pulse adsorption: Before CO injection, the samples were reduced at 400 °C for 1 h under a 10% H_2/Ar flow of 30 mL min^{-1} with a heating rate of 5 °C min^{-1}. The samples were then purged with helium at 30 mL min^{-1} for 1 h. CO pulses were sent to the catalyst, and the CO adsorption curves were measured using a thermal conductivity detector until no further CO was adsorbed.

N_2 physical adsorption and desorption: The specific surface area and porosity of the catalysts were determined using Quantachrome instruments through N_2 adsorption–desorption isotherms. The catalysts were degassed at 300 °C for 4–6 h, followed by the acquisition of the adsorption isotherms.

Transmission electron microscopy (TEM): TEM images were obtained using a JEM-2100 F (JEOL Ltd., Tokyo, Japan) microscope with an acceleration voltage of 100 kV. The samples were dispersed in ethanol and dropped onto carbon-coated copper TEM grids.

X-ray photoelectron spectroscopy (XPS): XPS was performed on a Escalab 250 Xi^+ (Thermo Fisher, Waltham, MA, USA) spectrometer using Al Kα radiation at an operating voltage of 15 kV and a current of 20 mA. The binding energy scale was calibrated by setting the C1s transition to 284.8 eV.

Thermo-gravimetric analysis (TGA): TGA was conducted using an STA449F5-Thermoster (Netzsch, Shanghai, China) thermogravimetric analyzer with air as the carrier gas. Approximately 10 mg of the sample was loaded into a ceramic crucible and placed on the balance. The temperature was programmed to increase, and the weight changes were recorded as a function of temperature and time.

Infrared spectroscopy of pyridine adsorption (Py-IR): The samples were pressed into pellets and treated under vacuum at 450 °C for 0.5 h. Pyridine was introduced into the sample cell at room temperature until adsorption saturation was reached. Then, under high vacuum, the samples were heated at a rate of 10 °C min^{-1} to 150 °C, 250 °C, 350 °C, and 450 °C for 0.5 h each to desorb unstable adsorbed species at the corresponding temperatures, followed by scanning of the infrared signals of the samples.

CO adsorption–desorption in situ diffuse reflectance infrared Fourier transform spectroscopy (CO-DRIFTS): CO-DRIFTS was collected on a NICOLET iS20 (Thermo Fisher, Waltham, MA, USA) FTIR spectrometer equipped with a mercury cadmium telluride detector. Before testing, the samples were pretreated in 5% H_2/He at 200 °C for 0.5 h and cooled to room temperature under the same atmosphere. Background spectra were collected with a resolution of 4 cm^{-1} and 32 scans under a He atmosphere. Then, 10% CO/He was introduced into the chamber, and spectra were collected at 20 °C. After adsorption saturation, CO flow was stopped, and the chamber was purged with He while continuing to collect spectra until no bands attributable to gaseous CO remained.

In situ IR Spectroscopy: In situ infrared cell in diffuse reflection mode was used in this experiment, as shown in Figure S2. Infrared spectra were collected by the NICOLET iS20 (Thermo Fisher, Waltham, MA, USA) FTIR spectrometer equipped with a mercury cadmium tellurium detector. The crucible in the in situ cell is $\phi 6 \times 4.5$ mm in size, and the temperature is measured by a thermocouple placed inside the in situ cell and controlled by an external temperature controller. The gas enters the in situ cell through the intake pipe and then directly exits the outlet pipe and is discharged into the tail gas without detection and analysis. LDPE was dissolved in toluene at 100 °C to obtain a solution with concentration of 5 mg LDPE mL^{-1}. A layer of KBr of 5 mm height was placed at the bottom of the crucible, followed by the addition of 10 mg of catalyst. The mixture was then pressed flat and placed in the in situ cell. The catalyst was reduced in situ at 250 °C for 30 min. After reduction, the catalyst background was collected, and the temperature was decreased

to 100 °C. The crucible was taken out, and 20 μL of the LDPE solution was gently pipetted onto the catalyst surface in the crucible. The crucible was then reinserted into the in situ cell, which was purged with helium gas at 100 °C for 1 h. The atmosphere was then switched to hydrogen, and the temperature was increased to 250 °C at a rate of 5 °C min^{-1}. In situ IR spectra of LDPE degradation were collected.

4. Conclusions

In this work, we developed a bifunctional catalytic system containing Ru nanoparticles supported on γ-Al_2O_3 and abundant acid sites within β-zeolite for hydrocracking of polyolefins. It is disclosed that spatially separated Ru and acid sites with an appropriate proportion is conducive to the effective cleavage of C–H and C–C bonds. The mechanism investigation through in situ infrared spectroscopy and probe–molecule model reactions implies that the optimal synergy of Ru and acid sites considerably contributes to the enhanced tandem process involves initial C–H bond activation and pre-cracking over Ru/γ-Al_2O_3, followed by transfer to the acid sites within β-zeolite for subsequent β-scission and isomerization to produce gasoline-range hydrocarbons while inhibiting over-cracking of intermediates over Ru sites. Through fully leveraging the unique properties of Ru/γ-Al_2O_3 and β-zeolite catalysts, this catalytic system not only achieves a top-level yield of $C_{5–12}$ gasoline-range hydrocarbons up to 73.4% for the LDPE hydrocracking at 250 °C but also holds a promise in the conversion of other ubiquitous polyolefins. This work may offer new insights for the design of Ru-based bifunctional catalysts and contribute to the chemical upgrading of polyolefin waste into valuable chemicals.

Supplementary Materials: The following supporting information can be downloaded at: https://www.mdpi.com/article/10.3390/catal15040335/s1. Figure S1: Diagram of the high-pressure reactor; Figure S2: Diagram of in situ infrared cell (A) and temperature controller (B); Figure S3: In situ infrared background spectra of different materials (A–C); Figure S4: Blank test (containing only LDPE and SiO_2 or γ-Al_2O_3) results of LDPE hydrocracking (conditions: 250 °C, 3 MPa H_2, 600 rpm, 6 h); Figure S5: Hydrocracking performance (A) and product distribution (B,C) of LDPE on different supports (conditions: 250 °C, 2 MPa H_2, 6 h, 500 rpm, Ru loading 1.8 wt%); Figure S6: (A–D) The hydrocracking performance and product distribution of LDPE using different zeolite mixtures with 1.8Ru/γ-Al_2O_3 (conditions: 250 °C, 2 MPa H_2, 500 rpm, 6 h); Figure S7: (A–D) Product distribution on different catalysts (conditions: 250 °C, 2 MPa H_2, 500 rpm, 6 h); Figure S8: (A,B) The effect of stirring speed and hydrogen pressure on the hydrocracking of LDPE (conditions: 250 °C, 6 h, 1.8Ru/γ-Al_2O_3:β(25) = 1:1); Figure S9: The carbon number distribution of effluents in the hydrocracking of *n*-tetracosane (nC_{24}) on the β(25) + SiO_2 catalyst (conditions: 250 °C, 3 MPa H_2, 600 rpm, 0.5 h); Figure S10: TEM images of 0.6Ru/γ-Al_2O_3 (A), 1.2Ru/γ-Al_2O_3 (B), 1.8Ru/γ-Al_2O_3 (C) and 2.4Ru/γ-Al_2O_3 (D); Figure S11: Fitting results of CO adsorption and desorption infrared for different loadings of Ru/γ-Al_2O_3; Figure S12: Pore size distribution curves of β-zeolites; Figure S13: XRD patterns of 3.0Ru/γ-Al_2O_3 + β(25) before and after the reaction; Figure S14: TEM images of 3.0Ru/γ-Al_2O_3 + β(25) after 1 (A), 2 (B), 3 (C) and 4 (D) reaction cycles; Figure S15: Thermogravimetric analysis (TGA) of 3.0Ru/γ-Al_2O_3 + β(25) after the reaction; Figure S16: A magnification of Figure 2B, which is the EDS elemental analysis of 3.0Ru/γ-Al_2O_3; Table S1: Summary of specific surface area and pore volume of *x*Ru/γ-Al_2O_3 and β-zeolites; Table S2: Summary of *x*Ru/γ-Al_2O_3 characterization obtained by ICP, TEM and CO pulsed chemisorption; Table S3: Summary of *x*Ru/γ-Al_2O_3 characterization obtained by CO-DRIFTS and XPS; Table S4: Summary of acid properties of β-zeolites catalysts.

Author Contributions: Conceptualization, Q.D.; formal analysis, Q.D. and X.S. (Xin Shang); investigation, Q.D.; data curation, Q.D.; writing—original draft preparation, Q.D.; writing—review and editing, X.S. (Xin Shang), Y.Y. and X.S. (Xiong Su); supervision, Y.H. and X.S. (Xiong Su); project administration, X.S. (Xiong Su); funding acquisition, X.S. (Xin Shang), X.S. (Xiong Su) and Y.H. All authors have read and agreed to the published version of the manuscript.

Funding: This research was funded by the National Natural Science Foundation of China for Single-Atom Catalysis (22388102), the Strategic Priority Research Program of the Chinese Academy of Sciences (XDA29040600), the National Natural Science Foundation of China (22478383, 22408360), the Postdoctoral Fellowship Program of China Postdoctoral Science Foundation (No. GZC20241676), and the China Postdoctoral Science Foundation (No. 2024M753164).

Data Availability Statement: The data that support the findings of this study are available from the authors upon reasonable request.

Acknowledgments: The authors appreciate the financial support from the funding sources mentioned above.

Conflicts of Interest: The authors declare no conflicts of interests.

References

1. Microplastics are everywhere—We need to understand how they affect human health. *Nat. Med.* **2024**, *30*, 913.
2. Geyer, R.; Jambeck, J.R.; Law, K.L. Production, use, and fate of all plastics ever made. *Sci. Adv.* **2017**, *3*, e1700782. [CrossRef] [PubMed]
3. Kots, P.A. Close-loop chemical recycling unlocked via waste polyolefins-ethylene co-metathesis. *Chem Catal.* **2024**, *4*, 101194.
4. Cen, Z.; Han, X.; Lin, L.; Yang, S.; Han, W.; Wen, W.; Yuan, W.; Dong, M.; Ma, Z.; Li, F.; et al. Upcycling of polyethylene to gasoline through a self-supplied hydrogen strategy in a layered self-pillared zeolite. *Nat. Chem.* **2024**, *16*, 871–880.
5. Selvam, E.; Yu, K.; Ngu, J.; Najmi, S.; Vlachos, D.G. Recycling polyolefin plastic waste at short contact times via rapid joule heating. *Nat. Commun.* **2024**, *15*, 5662. [CrossRef]
6. Odenweller, A.; Ueckerdt, F. The green hydrogen ambition and implementation gap. *Nat. Energy* **2025**, *10*, 110–123.
7. Aydogdu, A.C.; Erkmen, B.; Suerkan, A.; Ezdesir, A.; Guliyev, B.; Celik, G. Chemical upcycling of polyolefins into liquid refinery feedstock from the circularity and chemical engineering aspects. *J. Environ. Chem. Eng.* **2024**, *12*, 113430. [CrossRef]
8. Munyaneza, N.E.; Ji, R.; DiMarco, A.; Miscall, J.; Stanley, L.; Rorrer, N.; Qiao, R.; Liu, G. Chain-length-controllable upcycling of polyolefins to sulfate detergents. *Nat. Sustain.* **2024**, *7*, 1681–1690.
9. Tan, Y.; Cheng, Y.; Xu, J.; Wang, H. Catalytic chemical recycling and upcycling of polyolefin plastics. *Giant* **2024**, *19*, 100307. [CrossRef]
10. Sun, J.A.; Kots, P.A.; Hinton, Z.R.; Marinkovic, N.S.; Ma, L.; Ehrlich, S.N.; Zheng, W.; Epps, T.H.; Korley, L.T.J.; Vlachos, D.G. Size and Structure Effects of Carbon-Supported Ruthenium Nanoparticles on Waste Polypropylene Hydrogenolysis Activity, Selectivity, and Product Microstructure. *ACS Catal.* **2024**, *14*, 3228–3240.
11. Hu, Q.; Qian, S.; Wang, Y.; Zhao, J.; Jiang, M.; Sun, M.; Huang, H.; Gan, T.; Ma, J.; Zhang, J.; et al. Polyethylene hydrogenolysis by dilute RuPt alloy to achieve H_2-pressure-independent low methane selectivity. *Nat. Commun.* **2024**, *15*, 10573. [CrossRef] [PubMed]
12. Nguyen-Phu, H.; Kwon, T.; Kim, T.; Thi Do, L.; Hyuk Kang, K.; Ro, I. Investigating the influence of Ru structures and supports on hydrogenolysis of polyethylene plastic waste. *Chem. Eng. J.* **2023**, *475*, 146076. [CrossRef]
13. Wu, X.; Tennakoon, A.; Yappert, R.; Esveld, M.; Ferrandon, M.S.; Hackler, R.A.; LaPointe, A.M.; Heyden, A.; Delferro, M.; Peters, B.; et al. Size-Controlled Nanoparticles Embedded in a Mesoporous Architecture Leading to Efficient and Selective Hydrogenolysis of Polyolefins. *J. Am. Chem. Soc.* **2022**, *144*, 5323–5334. [PubMed]
14. Nakagawa, Y.; Oya, S.; Kanno, D.; Nakaji, Y.; Tamura, M.; Tomishige, K. Regioselectivity and Reaction Mechanism of Ru-Catalyzed Hydrogenolysis of Squalane and Model Alkanes. *ChemSusChem* **2016**, *10*, 189–198.
15. Cheng, L.; Tian, S.; Liang, D.; Gu, J.; Chen, R.; Chen, X.; Yuan, H.; Chen, Y. Enhanced hydroconversion of polyethylene via dual-functional catalysis: Exploiting ZSM-22 pore-mouth catalysis and Ru electronic effect. *Chem. Eng. J.* **2024**, *486*, 150332. [CrossRef]
16. Sun, C.; Wang, J.; Wang, J.; Shakouri, M.; Shi, B.; Liu, X.; Guo, Y.; Hu, Y.; Wu, X.-P.; Wang, Y. Pt enhanced C–H bond activation for efficient and low-methane-selectivity hydrogenolysis of polyethylene over alloyed $RuPt/ZrO_2$. *Appl. Catal. B* **2024**, *353*, 124046. [CrossRef]
17. Nadhifah, N.; Jovita, S.; Subagyo, R.; Utami, D.I.; Agustina, K.R.; Holilah, H.; Asikin-Mijan, N.; Bahruji, H.; Nugraha, R.E.; Jalil, A.A.; et al. Mesoporous aluminosilicate from metakaolin with natural surfactants for waste cooking oil conversion to hydrocarbon fuels via low-temperature pyrolysis. *Case Stud. Chem. Environ. Eng.* **2025**, *11*, 101111. [CrossRef]
18. Ezenwa, S.; Gounder, R. Advances and challenges in designing active site environments in zeolites for Brønsted acid catalysis. *Chem. Commun.* **2024**, *60*, 12118–12143.

19. Al Aslani, I.; Lezcano, G.; Colom, J.M.; Alahmadi, A.; Shoinkhorova, T.; Dikhtiarenko, A.; Cui, M.; Alfilfil, L.; Morales Osorio, I.; Almajnouni, K.; et al. Reaction network and kinetic modeling for the direct catalytic cracking of Arabian light crude oil to chemicals. *Chem. Eng. J.* **2024**, *498*, 154981. [CrossRef]
20. Wu, X.; Wang, X.; Zhang, L.; Wang, X.; Song, S.; Zhang, H. Polyethylene Upgrading to Liquid Fuels Boosted by Atomic Ce Promoters. *Angew. Chem. Int. Ed.* **2024**, *63*, e202317594. [CrossRef]
21. Liu, S.; Kots, P.A.; Vance, B.C.; Danielson, A.; Vlachos, D.G. Plastic waste to fuels by hydrocracking at mild conditions. *Sci. Adv.* **2021**, *7*, eabf8283. [CrossRef] [PubMed]
22. Wang, S.; Wang, W.; Chu, M.; Gao, D.; Wang, Y.; Lv, Y.; Wang, R.; Song, L.; Zhao, H.; Chen, J.; et al. Ultra-Narrow Alkane Product Distribution in Polyethylene Waste Hydrocracking by Zeolite Micro-Mesopore Diffusion Optimization. *Angew. Chem. Int. Ed.* **2024**, *63*, e202409288. [CrossRef]
23. Li, L.; Luo, H.; Shao, Z.; Zhou, H.; Lu, J.; Chen, J.; Huang, C.; Zhang, S.; Liu, X.; Xia, L.; et al. Converting Plastic Wastes to Naphtha for Closing the Plastic Loop. *J. Am. Chem. Soc.* **2023**, *145*, 1847–1854. [PubMed]
24. Zhang, Z.; Wang, J.; Ge, X.; Wang, S.; Li, A.; Li, R.; Shen, J.; Liang, X.; Gan, T.; Han, X.; et al. Mixed Plastics Wastes Upcycling with High-Stability Single-Atom Ru Catalyst. *J. Am. Chem. Soc.* **2023**, *145*, 22836–22844.
25. Zhao, M.; Chu, X.; Wang, F.; Fang, Y.; Sun, L.; Xie, Q.; Zhang, L.-l.; Song, S.; Zhang, H.; Wang, X. Enhancing the Conversion Efficiency of Polyethylene to Methane through Codoping of Mn Atoms into Ru Centers and CeO_2 Supports. *J. Am. Chem. Soc.* **2024**, *146*, 33104–33111.
26. Zhang, X.; Gan, Q.; Zhou, P.; Chen, Z.; Zhang, Z.; Lu, G.-P. Boosting strong metal-support interactions between Ru and sodium titanate nanowire for hydrogenolysis of polyolefins under mild conditions. *Appl. Catal. B* **2024**, *344*, 123626. [CrossRef]
27. Conk, R.J.; Hanna, S.; Shi, J.X.; Yang, J.; Ciccia, N.R.; Qi, L.; Bloomer, B.J.; Heuvel, S.; Wills, T.; Su, J.; et al. Catalytic deconstruction of waste polyethylene with ethylene to form propylene. *Science* **2022**, *377*, 1561–1566.
28. Jia, X.; Qin, C.; Friedberger, T.; Guan, Z.; Huang, Z. Efficient and selective degradation of polyethylenes into liquid fuels and waxes under mild conditions. *Sci. Adv.* **2016**, *2*, e1501591. [CrossRef]
29. Chen, L.; Meyer, L.C.; Kovarik, L.; Meira, D.; Pereira-Hernandez, X.I.; Shi, H.; Khivantsev, K.; Gutiérrez, O.Y.; Szanyi, J. Disordered, Sub-Nanometer Ru Structures on CeO_2 are Highly Efficient and Selective Catalysts in Polymer Upcycling by Hydrogenolysis. *ACS Catal.* **2022**, *12*, 4618–4627.
30. Chen, L.; Zhu, Y.; Meyer, L.C.; Hale, L.V.; Le, T.T.; Karkamkar, A.; Lercher, J.A.; Gutiérrez, O.Y.; Szanyi, J. Effect of reaction conditions on the hydrogenolysis of polypropylene and polyethylene into gas and liquid alkanes. *React. Chem. Eng.* **2022**, *7*, 844–854.
31. Rorrer, J.E.; Troyano-Valls, C.; Beckham, G.T.; Román-Leshkov, Y. Hydrogenolysis of Polypropylene and Mixed Polyolefin Plastic Waste over Ru/C to Produce Liquid Alkanes. *ACS Sustain. Chem. Eng.* **2021**, *9*, 11661–11666. [CrossRef]
32. Tamura, M.; Miyaoka, S.; Nakaji, Y.; Tanji, M.; Kumagai, S.; Nakagawa, Y.; Yoshioka, T.; Tomishige, K. Structure-activity relationship in hydrogenolysis of polyolefins over Ru/support catalysts. *Appl. Catal. B* **2022**, *318*, 121870. [CrossRef]
33. Rorrer, J.E.; Ebrahim, A.M.; Questell-Santiago, Y.; Zhu, J.; Troyano-Valls, C.; Asundi, A.S.; Brenner, A.E.; Bare, S.R.; Tassone, C.J.; Beckham, G.T.; et al. Role of Bifunctional Ru/Acid Catalysts in the Selective Hydrocracking of Polyethylene and Polypropylene Waste to Liquid Hydrocarbons. *ACS Catal.* **2022**, *12*, 13969–13979. [CrossRef]
34. Kots, P.A.; Liu, S.; Vance, B.C.; Wang, C.; Sheehan, J.D.; Vlachos, D.G. Polypropylene Plastic Waste Conversion to Lubricants over Ru/TiO_2 Catalysts. *ACS Catal.* **2021**, *11*, 8104–8115. [CrossRef]
35. Rorrer, J.E.; Beckham, G.T.; Román-Leshkov, Y. Conversion of Polyolefin Waste to Liquid Alkanes with Ru-Based Catalysts under Mild Conditions. *JACS Au* **2020**, *1*, 8–12. [CrossRef]
36. Nakaji, Y.; Tamura, M.; Miyaoka, S.; Kumagai, S.; Tanji, M.; Nakagawa, Y.; Yoshioka, T.; Tomishige, K. Low-temperature catalytic upgrading of waste polyolefinic plastics into liquid fuels and waxes. *Appl. Catal. B* **2021**, *285*, 119805. [CrossRef]
37. Lee, W.-T.; van Muyden, A.; Bobbink, F.D.; Mensi, M.D.; Carullo, J.R.; Dyson, P.J. Mechanistic classification and benchmarking of polyolefin depolymerization over silica-alumina-based catalysts. *Nat. Commun.* **2022**, *13*, 4850. [CrossRef]
38. Wang, C.; Xie, T.; Kots, P.A.; Vance, B.C.; Yu, K.; Kumar, P.; Fu, J.; Liu, S.; Tsilomelekis, G.; Stach, E.A.; et al. Polyethylene Hydrogenolysis at Mild Conditions over Ruthenium on Tungstated Zirconia. *JACS Au* **2021**, *1*, 1422–1434. [CrossRef]
39. Zhang, Y.; Zhang, L.; Wang, H.; Ma, X.; Yu, S.; Yan, Y.; Bu, H. Comparative Study on the Power Consumption and Flow Field Characteristics of a Three-Blade Combined Agitator. *Processes* **2021**, *9*, 1962. [CrossRef]
40. Zhang, X.; Pan, L.; Wang, L.; Zou, J.-J. Review on synthesis and properties of high-energy-density liquid fuels: Hydrocarbons, nanofluids and energetic ionic liquids. *Chem. Eng. Sci.* **2018**, *180*, 95–125.
41. Ma, Q.; Cheng, J.; Wu, X.; Xie, J.; Zhang, R.; Mao, Z.; Yang, H.; Fan, W.; Zeng, J.; Bitter, J.H.; et al. C–C bond coupling with sp^3 C–H bond via active intermediates from CO_2 hydrogenation. *Nat. Commun.* **2025**, *16*, 140. [CrossRef] [PubMed]
42. O'Connell, K.; Regalbuto, J.R. High Sensitivity Silicon Slit Detectors for 1 nm Powder XRD Size Detection Limit. *Catal. Lett.* **2015**, *145*, 777–783. [CrossRef]

43. Meng, Q.; Liu, H.; Xu, K.; Wang, W.; Jia, C. CeO_2 modified Ru/γ-Al_2O_3 catalysts for ammonia decomposition reaction. *J. Rare Earths* **2023**, *41*, 801–809. [CrossRef]
44. Chin, S.Y.; Williams, C.T.; Amiridis, M.D. FTIR Studies of CO Adsorption on Al_2O_3- and SiO_2-Supported Ru Catalysts. *J. Phys. Chem. B* **2005**, *110*, 871–882. [CrossRef]
45. Xiao, H.; Zhang, J.; Du, C.; Zheng, Y.; Fang, J.; Li, S.; Zhang, C. Tailoring the Electronic Ru-Al_2O_3 Interaction to Regulate Reaction Barriers for Selective Hydrogenolysis of Aromatic Ether. *ACS Sustain. Chem. Eng.* **2023**, *11*, 1305–1310. [CrossRef]
46. Zhou, J.; Gao, Z.; Xiang, G.; Zhai, T.; Liu, Z.; Zhao, W.; Liang, X.; Wang, L. Interfacial compatibility critically controls Ru/TiO_2 metal-support interaction modes in CO_2 hydrogenation. *Nat. Commun.* **2022**, *13*, 327. [CrossRef]
47. Chen, M.; Liu, L.; Chen, X.; Qin, X.; Li, K.; Zhang, J.; Bao, X.; Ma, L.; Zhang, C. Effects of Ru particle size over TiO_2 on the catalytic performance of CO_2 hydrogenation. *Appl. Surf. Sci.* **2024**, *654*, 159460. [CrossRef]
48. Lin, L.; Pei, C.; Ding, R.; Li, Y.; Park, H.S.; Yu, X. Ru nanoclusters coupling with hierarchical phosphorus and oxygen dual-doped carbon nanotube architectures for effective hydrogen evolution reaction. *Int. J. Hydrogen Energy* **2023**, *48*, 20350–20358. [CrossRef]
49. Flaherty, D.W.; Hibbitts, D.D.; Iglesia, E. Metal-Catalyzed C–C Bond Cleavage in Alkanes: Effects of Methyl Substitution on Transition-State Structures and Stability. *J. Am. Chem. Soc.* **2014**, *136*, 9664–9676. [CrossRef]
50. Tran, V.T.; Gurak, J.A.; Yang, K.S.; Engle, K.M. Activation of diverse carbon–heteroatom and carbon–carbon bonds via palladium(ii)-catalysed β-*X* elimination. *Nat. Chem.* **2018**, *10*, 1126–1133. [CrossRef]
51. Jiang, W.; Cao, J.-P.; Zhu, C.; Zhao, M.; Ni, Z.-H.; Zhao, X.-Y.; Xie, J.-X.; Zhao, L.; Zhao, Y.-P.; Bai, H.-C. Catalytic hydrogenation of aromatic ring over ruthenium nanoparticles supported on α-Al_2O_3 at room temperature. *Appl. Catal. B* **2022**, *307*, 121137. [CrossRef]
52. Ahmadi, M.; Mistry, H.; Roldan Cuenya, B. Tailoring the Catalytic Properties of Metal Nanoparticles via Support Interactions. *J. Phys. Chem. Lett.* **2016**, *7*, 3519–3533. [PubMed]
53. Ran, H.; Zhang, S.; Ni, W.; Jing, Y. Precise activation of C–C bonds for recycling and upcycling of plastics. *Chem. Sci.* **2024**, *15*, 795–831. [PubMed]
54. Li, R.; Ban, T.; Zhao, D.; Lin, J.; Liu, Z.; Wang, L.; Huang, X.; Tao, Z.; Wang, G. Defect engineering and Ni promoter synergistically accelerating electron transfer to Ru0 sites in UiO-66(Ce) for dicyclopentadiene hydrogenation under mild condition. *Nano Res.* **2024**, *17*, 9550–9563. [CrossRef]
55. Tu, W.; Chu, M.; Wang, X.; Wang, X.; Li, Y.; Yang, W.; Cao, M.; Wang, L.; Li, Y.; Sham, T.-K.; et al. SMSI-induced charge transfer for selective hydrogenolysis of polyolefins. *Appl. Catal. B* **2023**, *339*, 123122. [CrossRef]
56. Lu, S.; Jing, Y.; Jia, S.; Shakouri, M.; Hu, Y.; Liu, X.; Guo, Y.; Wang, Y. Enhanced Production of Liquid Alkanes from Waste Polyethylene via the Electronic Effect-Favored Csecondary−Csecondary Bond Cleavage. *ChemCatChem* **2023**, *15*, e202201375. [CrossRef]
57. Zhong, X.; Liu, J.; Gao, L.; Chen, J.; Wang, X.; Zhang, Y.; Wu, Y.A.; Shakeri, M.; Zhang, X.; Zhang, B. Constructing the Al deficiency in Si-O(H)-Al units based on Pt/ZSM-5 for enhanced hydrocracking of polyethylene into high-quality liquid fuel. *Nano Res.* **2024**, *17*, 10088–10098.
58. Blomsma, E.; Martens, J.A.; Jacobs, P.A. Reaction Mechanisms of Isomerization and Cracking of Heptane on Pd/H-Beta Zeolite. *J. Catal.* **1995**, *155*, 141–147.
59. Du, B.; Chen, X.; Ling, Y.; Niu, T.; Guan, W.; Meng, J.; Hu, H.; Tsang, C.W.; Liang, C. Hydrogenolysis-Isomerization of Waste Polyolefin Plastics to Multibranched Liquid Alkanes. *ChemSusChem* **2023**, *16*, e202202035. [CrossRef]
60. Zhou, Q.M.; Wang, D.L.; Wang, Q.Y.; He, K.L.; Lim, K.H.; Yang, X.; Wang, W.J.; Li, B.G.; Liu, P.W. Mechanistic Understanding of Efficient Polyethylene Hydrocracking over Two-Dimensional Platinum-Anchored Tungsten Trioxide. *Angew. Chem. Int. Ed.* **2023**, *62*, e202305644. [CrossRef]
61. Albahar, M.; Li, C.; Zholobenko, V.L.; Garforth, A.A. The effect of ZSM-5 zeolite crystal size on p-xylene selectivity in toluene disproportionation. *Microporous Mesoporous Mater.* **2020**, *302*, 110221. [CrossRef]
62. Wu, H.; Duan, A.; Zhao, Z.; Xu, C.; Jiang, G.; Liu, J.; Wei, Y.; Li, J.; Chi, K.; Guo, J. Restricted diffusion of model sulfides over a NiMo/BK catalyst under hydrodesulfurization reaction conditions. *RSC Adv.* **2017**, *7*, 44340–44347.

catalysts

MDPI

Article

Direct Conversion of 1,3-Butanediol to 1,3-Butadiene over ZSM-22 Catalysts: Influence of the Si/Al Ratio

Loïc Eloi [1,2], Jeroen Poissonnier [2], Arne De Landsheere [1,2], Dhanjay Sharma [1], Jaouad Al Atrach [3], Valérie Ruaux [3], Valentin Valtchev [3,4], Maarten K. Sabbe [1,2], Joris W. Thybaut [2] and An Verberckmoes [1,*]

[1] Industrial Catalysis and Adsorption Technology (INCAT), Ghent University, Valentin Vaerwyckweg 1, 9000 Ghent, Belgium; loic.eloi@ugent.be (L.E.); arne.delandsheere@ugent.be (A.D.L.); dhananjay.ssd@gmail.com (D.S.); maarten.sabbe@ugent.be (M.K.S.)
[2] Laboratory for Chemical Technology (LCT), Ghent University, Technologiepark 125, 9052 Ghent, Belgium; jeroen.poissonnier@ugent.be (J.P.); joris.thybaut@ugent.be (J.W.T.)
[3] Laboratoire Catalyse et Spectrochimie, ENSICAEN, Centra National de la Recherche Scientifique De Caen (CNRS), Université de Caen, 6 Boulevard Maréchal Juin, 14050 Caen, France; jaouad.al-atrach@ensicaen.fr (J.A.A.); valerie.ruaux@ensicaen.fr (V.R.); valentin.valtchev@ensicaen.fr (V.V.)
[4] Faculty of Chemistry and Pharmacy, University of Sofia, 1126 Sofia, Bulgaria
* Correspondence: an.verberckmoes@ugent.be

Abstract

ZSM-22 zeolites with different Si/Al ratios (38, 50, 80) were prepared via a hydrothermal synthesis method, investigated for the catalytic dehydration of 1,3-butanediol (1,3-BDO) to butadiene (BD) at 300 °C. The catalytic performance of the synthesized materials was related to their properties and compared to a commercial ZSM-22 zeolite (Si/Al = 30). ZSM-22 (50) exhibited a quick decline in conversion, a lower BD selectivity, and higher propylene selectivity compared to the other materials, which could be attributed to the presence of strong Lewis acid sites and silanol nests. The Lewis sites favor the cracking of the intermediate 3-buten-1-ol (3B1OL) into propylene, while the silanol nests interact with the free hydroxyl group of 3B1OL, potentially inhibiting further dehydration towards BD. The highest initial BD yield of 74% was observed over ZSM-22 (80), while the highest initial BD productivity of 2.7 $g_{BD} \cdot g^{-1}_{cata} \cdot h^{-1}$ was achieved over ZSM-22 (38). After 22 h time on stream (TOS), c-ZSM-22 and ZSM-22 (38) outperformed previously reported catalysts from the literature, with productivities amounting to 1.3 $g_{BD} \cdot g^{-1}_{cata} \cdot h^{-1}$ and 1.2 $g_{BD} \cdot g^{-1}_{cata} \cdot h^{-1}$, respectively, at a site time of 6.6 $mol_{H+} \cdot s \cdot mol^{-1}_{1,3\text{-BDO}}$.

Keywords: 1,3-butanediol; 1,3-butadiene; dehydration; ZSM-22; zeolites; acid catalyst

1. Introduction

Short-chain olefins (C_2–C_4) are among the most important platform chemicals in the petrochemical industry and are predominantly produced by steam cracking. They are fundamental building blocks for producing various plastics and synthetic rubbers. Their global demand has been steadily increasing over the years, driven by their widespread applications in the electronic and automotive industries, among others [1]. Among these olefins, 1,3-butadiene (BD) is a key building block in the petrochemical industry. It is predominantly used as a precursor in the production of styrene-butadiene rubber (SBR), polybutadiene rubber, and acrylonitrile butadiene styrene polymer (ABS) [2,3]. The ethylene demand heavily affects the current supply and price of butadiene [4]. More than 90% of butadiene is produced as a by-product of naphtha steam cracking in ethylene plants, which is accompanied by a high carbon footprint with cradle-to-gate CO_2 emissions

amounting to 1.2–1.8 ton_{CO2}/ton_{BD} [5]. However, recent technological advancements in North America have rendered shale gas as an economically more favorable feedstock, while European crackers are transitioning to liquefied petroleum gas as a primary feedstock [6,7]. These trends have significantly reduced the global supply of BD. Hence, the butadiene market faces a dual challenge of ensuring a sufficient butadiene supply while mitigating carbon emissions, making the development of a bio-based alternative technology of prime importance.

The ethanol-to-butadiene (ETB) route via the Lebedev process is a widely investigated alternative for BD production. However, this complex process involves several catalytic reactions, including dehydrogenation, aldol condensation, hydrogenation, and dehydration [8]. Moreover, the reaction generally occurs at high temperatures (>400 °C) over promoted (Zr, Ag, Cu or Au) MgO/SiO_2 catalysts exhibiting low BD productivities of 0.2 $g_{BD}\cdot g^{-1}{}_{cata}\cdot h^{-1}$ and BD yields of approximately 50% [2,9]. In contrast, obtaining BD from butanediol (BDO) isomers (1,4-, 2,3-, and 1,3-BDO) involves only two consecutive dehydrations, which facilitates the catalyst design for this type of reaction. Additionally, it has been demonstrated that these BDO isomers can be obtained from the microbial fermentation of sugars [10–17], positioning the acid-catalyzed dehydration of BDO as a promising sustainable alternative for BD production. Since cyclodehydration of 1,4-BDO and pinacol rearrangement of 2,3-BDO yield tetrahydrofuran and methylethylketone as major products, respectively [18–22], 1,3-BDO becomes an attractive feedstock for the on-purpose production of 1,3-butadiene. Moreover, this specific butanediol isomer can be produced via gas fermentation by *Cupriavidus Necator* using CO_2 as the sole carbon source [23], highlighting the potential value of 1,3-BDO as a sustainable feedstock for the on-purpose BD production.

The catalytic dehydration of 1,3-BDO into BD proceeds via two consecutive dehydration steps, generating unsaturated alcohols (UOLs) as intermediates: 2-buten-1-ol (2B1OL), 3-buten-1-ol (3B1OL), and 3-buten-2-ol (3B2OL). However, several side reactions can occur depending on the catalyst properties, including 1,3-BDO dehydrogenation into methyl vinyl ketone (MVK), see Figure 1. MVK hydrogenation results in methyl ethyl ketone (MEK) and 2-butanol. Moreover, 2B1OL and 3B1OL can be hydrogenated, resulting in the formation of 1-butanol, which can be converted into butanal via dehydrogenation. Finally, 3B1OL is prone to cracking via the reverse Prins reaction, generating propylene and formaldehyde [24,25]. Various solid acid catalysts have been investigated for the catalytic dehydration of 1,3-BDO, including silica-alumina, Al-SBA-15, and zeolites [24–32]. These works have implemented several strategies to fine-tune the catalyst properties to increase the BD yield. According to the work of Pera-Titus [28], Brønsted acid sites with a medium strength are responsible for a high BD selectivity. This hypothesis is also supported by the reports of Padro et al. [30] and Sato et al. [31], which demonstrated that Brønsted acid sites favor the dehydration of the UOLs towards BD, while Lewis acid sites facilitate the cracking of 3B1OL. The best-performing materials from these works are tungstophosphoric acid supported on SiO_2 (initial BD yield and productivity amounting to 75% and 1.92 $g_{BD}\cdot g^{-1}{}_{cata}\cdot h^{-1}$, respectively, at 300 °C) [30], WO_3-modified SiO_2 (BD yield and productivity after 5 h TOS of 73.4% and 0.17 $g_{BD}\cdot g^{-1}{}_{cata}\cdot h^{-1}$, respectively, at 300 °C) [31], and Ag-modified silica-alumina (BD yield and productivity after 5 h TOS of 68.9% and 1.33 $g_{BD}\cdot g^{-1}{}_{cata}\cdot h^{-1}$, respectively, at 250 °C) [32]. Despite the improvements in BD yields and selectivities, the overall productivity remains limited, particularly in long-term experiments. Most catalysts are evaluated within the first 5 h time on stream TOS, making it difficult to assess their potential for industrial application. Notably, $Y_2Zr_2O_3$ has been reported at 375 °C with BD yields of 95% and 87% after 10 and 30 h TOS, respectively.

Nevertheless, its productivity remains low, with values of 0.38 and 0.35 $g_{BD} \cdot g^{-1}_{cata} \cdot h^{-1}$ at 10 and 30 h TOS, respectively [33].

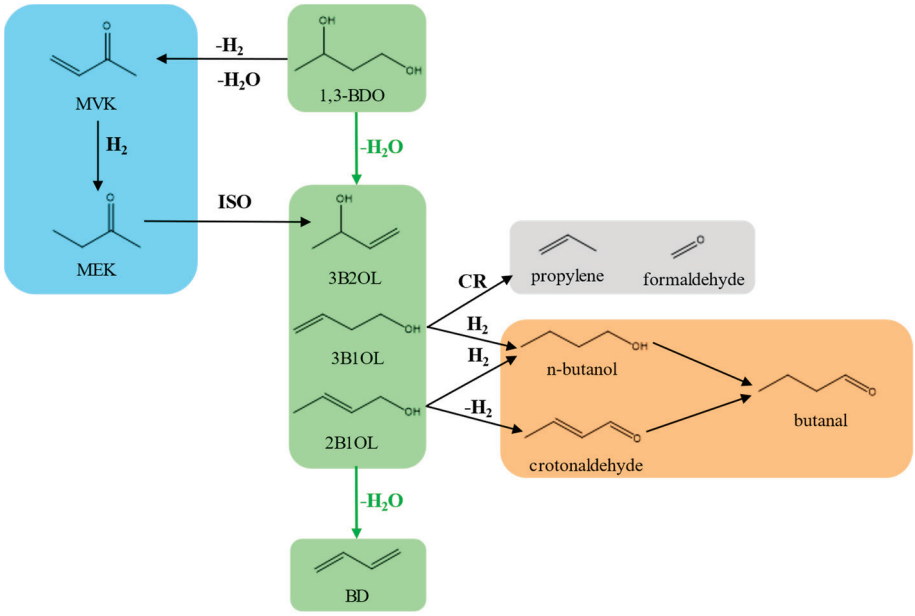

Figure 1. Schematic overview of the consecutive dehydration of 1,3-BDO to BD, including side reactions. CR = cracking and ISO = isomerization.

Additionally, in the case of zeolites, the topology has been identified as a determining factor for BD selectivity. Lee et al. [25] demonstrated that zeolites with a 1D and 2D topology, such as ZSM-22 and FER, suppress 3B1OL cracking, thereby increasing the BD selectivity. Although BD yields over 65% have been reported over ZSM-22 (Si/Al = 160) and FER (Si/Al = 130), the BD productivity remains relatively low (e.g., productivity of 0.59 $g_{BD} \cdot g^{-1}_{cata} \cdot h^{-1}$ after 10 h TOS over FER (Si/Al = 130) at 300 °C). In contrast, ZSM-5 has bigger pores compared to ZSM-22 and FER, which makes it possible for 3B1OL to coordinate its hydroxyl group with the negatively charged pi cloud of the C=C double bond, causing this intermediate to be less active for dehydration. This observation positions 1D and 2D zeolites as better alternatives for BD production from 1,3-BDO. However, no further investigations into these types of zeolites has been carried out.

Pera-Titus and coworkers have thoroughly investigated the influence of the Si/Al ratio in ZSM-5 on the dehydration behavior of 1,3-BDO [28], aiming at unraveling the correlation between the acid properties and the catalytic performance to improve the BD yield. These authors reported that higher Si/Al ratios are favorable for BD selectivity. Moreover, higher Si/Al ratios are favorable for the catalyst stability. For instance, ZSM-5 (Si/Al = 130) achieved a BD yield of 60% at 300 °C with a BD productivity amounting to 0.48 $g_{BD} \cdot g^{-1}_{cata} \cdot h^{-1}$ after 8 h time on stream (TOS) [25]. However, no studies on the influence of the acid properties of 1D or 2D zeolites on the catalytic dehydration of 1,3-BDO have been conducted yet. It is, therefore, an interesting strategy to investigate the influence of acid density in ZSM-22 zeolites on BD selectivity.

In this study, the influence of the acid properties of ZSM-22 on the catalytic dehydration of 1,3-BDO is investigated. Via an in-house recipe from our research group, ZSM-22 zeolites are synthesized with a similar crystal shape and size as investigated for the dehydration of 1,3-BDO by Lee et al. [25], but with lower Si/Al ratios, i.e., 38, 50, and 80. The structural properties are thoroughly analyzed through X-ray diffraction (XRD), scanning electron microscopy (SEM), Ar sorption, inductively coupled plasma mass spectroscopy (ICP-MS), ^{27}Al and ^{29}Si solid-state magic angle spinning nuclear magnetic resonance spec-

troscopy (MAS-NMR), and in situ Fourier transform infrared spectroscopy (FTIR) with pyridine as a probe molecule to determine the acid sites. Moreover, adsorption experiments with 3B1OL as a probe molecule are performed to gain insight into the adsorption behavior of this unsaturated alcohol within a zeolite framework, since this intermediate is prone to cracking. All these properties are compared to commercial ZSM-22, which is used as reference material. Finally, the catalysts are screened over a long period (up to 22 h) to investigate the influence of the acid properties on the BD yield and the long-term productivity behavior is compared to literature-reported catalysts.

2. Results and Discussion

2.1. Characterization of the Zeolite Materials

The normalized XRD patterns of both the commercially available ZSM-22 and the synthesized ZSM-22 zeolites with varying Si/Al ratios are depicted in Figure 2. All samples exhibit diffraction patterns consistent with those reported by Zhai and coworkers [34], characterized by well-defined peaks at 2θ = 8.1°, 20.3°, 24.2°, 24.6°, 25.7°, and 35.6°, which are indicative of the TON topology [35]. It is worth noting that no additional sharp peaks corresponding to impurities such as ZSM-5 and cristobalite were observed in the range of 2θ = 5–30°. This indicates that the addition of seeds during synthesis promotes the formation of pure ZSM-22. The average crystal size of the zeolites determined by the Scherrer equation for 2θ = 35.6° amounts to 77 nm for c-ZSM-22, 63 nm for ZSM-22 (38), 69 nm for ZSM-22 (50), and 76 nm for ZSM-22 (80), which is summarized in Table S1. The smaller value for the average crystal size of ZSM-22 (38) and ZSM-22 (50) can be attributed to the higher alkaline content in the precursor gel, which increased the number of nucleation sites [36].

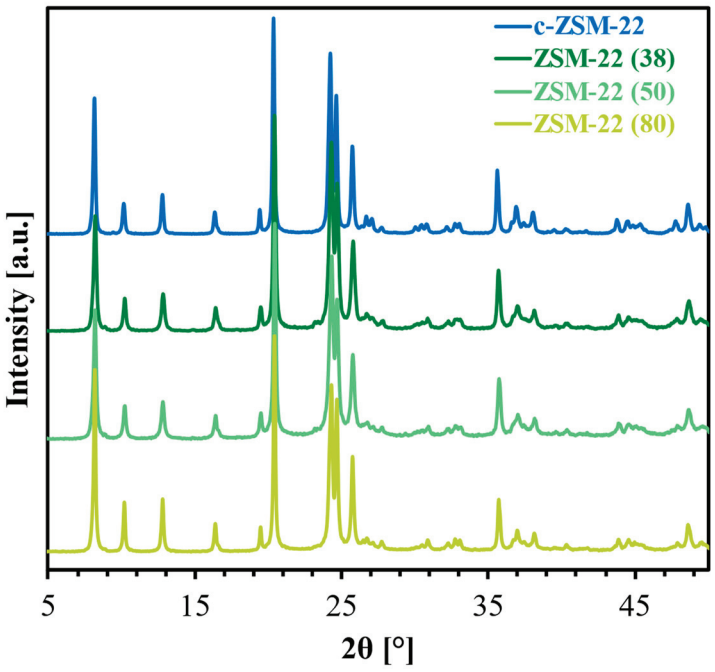

Figure 2. Normalized XRD patterns of the ZSM-22 zeolites studied in this work.

Figure 3 presents the SEM images of c-ZSM-22, ZSM-22 (38), ZSM-22 (50), and ZSM-22 (80). The commercial sample (see Figure 3a) consists of short prismatic crystals with dimensions ranging between 100 and 600 nm in length (more detailed in Figure S3.2), which are densely stacked together into agglomerated clusters with overall dimensions between 3 and 10 μm (Table S1). The crystal width, which is approximately 60–80 nm,

is consistent with the values calculated by the Scherrer equation. In contrast, the ZSM-22 zeolites synthesized in this work (Figure 3b–d) exhibit a different morphology. They consist of discrete nanorods stacked together to form elongated needle-like bundles with dimensions between 2.5 and 4 μm in length. The nanorods themselves have a length of ~200 nm and widths between 60 and 100 nm (Figure S3.2), which is in good agreement with the calculated widths by the Scherrer equation. As can be seen from Figure 3b–d, the nanorods are closely aligned, resulting in dense needle-like bundles exhibiting widths between 250 and 500 nm, which is consistent with previous observations by Zhai and coworkers [34]. However, they reported smaller bundles, which could be attributed to the lower rotation speed of 50 rpm used during the synthesis in their work. The rotation speed of 100 rpm in our work could facilitate the deposition of zeolite crystals on the wall of the Teflon liners, which favors particle growth. The dense needle-like bundles further agglomerate into spherical clusters of about 10 μm width (Figure S3.1).

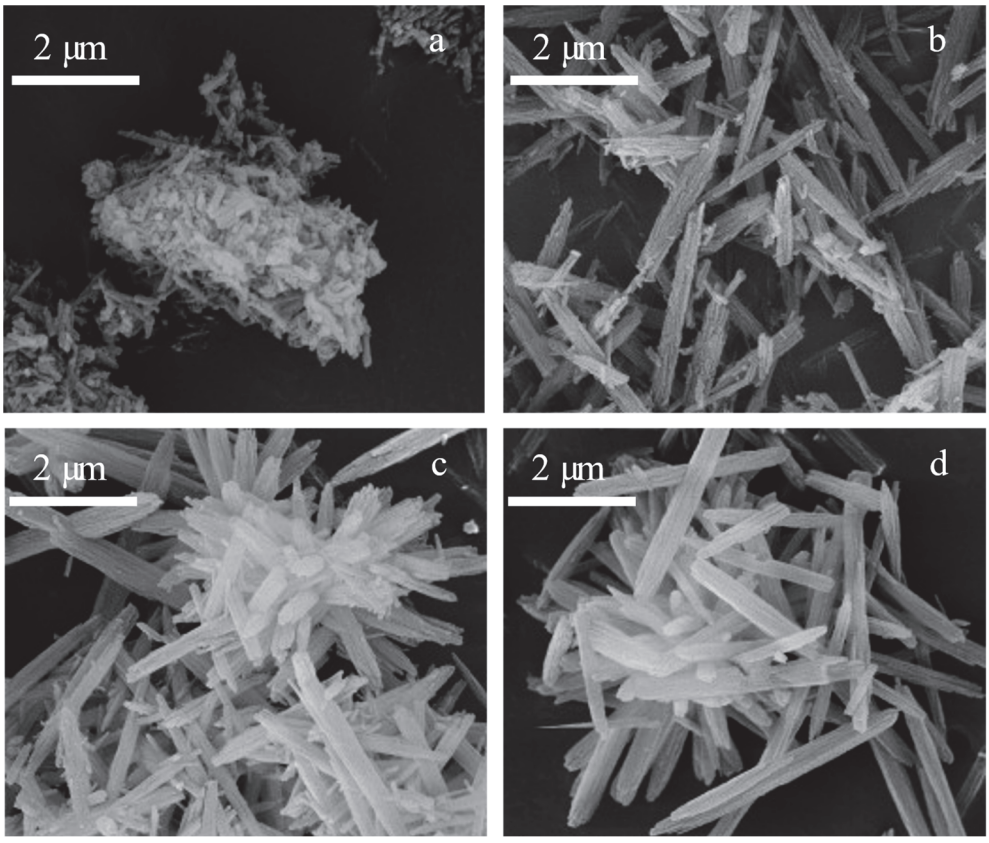

Figure 3. SEM images of (**a**) c-ZSM-22, (**b**) ZSM-22 (38), (**c**) ZSM-22 (50), and (**d**) ZSM-22 (80).

The normalized ^{27}Al MAS NMR spectra of the ZSM-22 zeolites, as depicted in Figure 4a, exhibit a dominant peak at 58 ppm. This is characteristic to tetrahedrally coordinated Al species, indicating that the majority of the Al atoms is successfully incorporated into the zeolite framework. Additionally, a broad signal centered at 8 ppm for ZSM-22 (50), which is less pronounced in the other materials. This could be associated with octahedrally coordinated Al, i.e., extra-framework alumina, which acts as Lewis acid sites [37]. After normalization, the ^{29}Si MAS NMR spectra can be deconvoluted into seven peaks (Figure S4). Two peaks are located in the region between −99 and −105 ppm, which are attributed to Si(1Al) coordination, while five bands are located between −106 ppm and −115 ppm, corresponding to Si(0Al) coordination [38,39]. The analysis of the deconvoluted bands reveals Si/Al ratios of 32, 40, 53, and 87 for c-ZSM-22, ZSM-22 (38), ZSM-22 (50), and ZSM-22 (80), respectively, which is consistent with the ICP-MS results (Table 1). The

lower Si/Al ratios compared to the targeted ratio in the synthesis gel are also reported for other ZSM-22 zeolites [34,35], and can be explained by the presence of K^+ cations in the synthesis mixture. In the presence of hydroxides, the Si-O-Si and Si-O-Al bonds are assembled around alkali cations such as the K^+ ions originating from the applied KOH, to form aluminosilicate oligomers. Due to the high charge density of these cations, a higher amount of Al atoms is incorporated into the zeolite framework to compensate for the positive charge. Moreover, the dissolution of colloidal silica is slow, which results in a lower incorporation of Si in the zeolite framework [40,41].

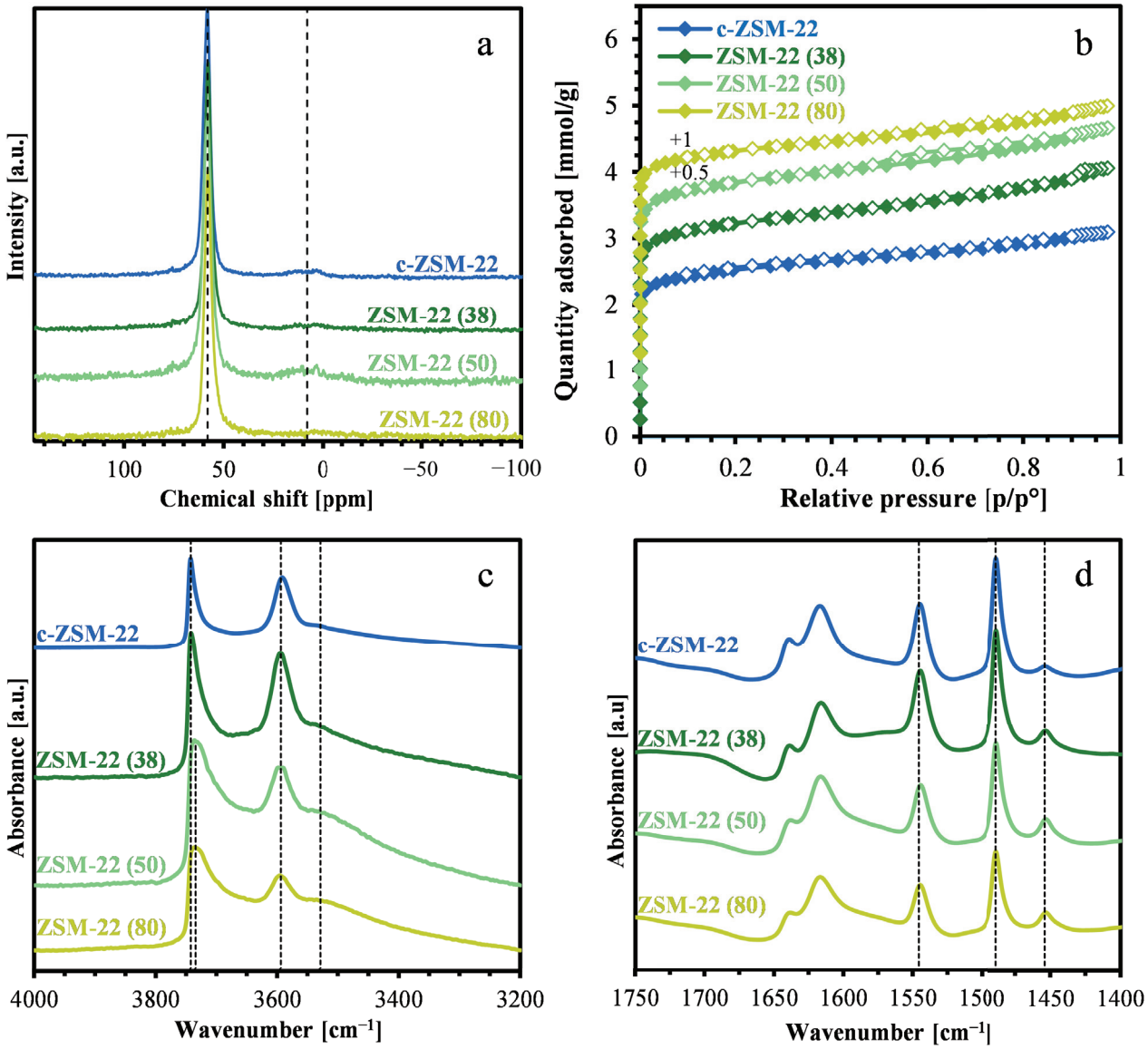

Figure 4. Normalized ^{27}Al MAS NMR spectra (**a**), Ar sorption isotherms (**b**), normalized in situ FTIR spectra of the dehydrated zeolite samples at 150 °C, after activation at 450 °C under vacuum (**c**), and normalized in situ Py-FTIR spectra after desorption at 300 °C (**d**) of c-ZSM-22, ZSM-22 (38), ZSM-22 (50), and ZSM-22 (80).

Figure 4b presents the argon sorption isotherms of all ZSM-22 zeolites investigated in this study. For clarity, the isotherms of ZSM-22 (50) and ZSM-22 (80) have been lifted by 0.5 and 1.0 mmol/g, respectively. According to the IUPAC classification, all zeolites exhibit type Ia isotherms, characterized by a steep Ar uptake at very low pressures ($p/p^\circ < 0.05$). This type of isotherm is related to microporous materials predominantly composed of narrow micropores (pore widths below 1 nm). In addition, all self-synthesized materials

exhibit a small hysteresis loop at high relative pressures ($p/p^\circ > 0.90$), suggesting the presence of intercrystalline mesopores, which are formed by the dense aggregation of the zeolite particles, as depicted in Figure 3. These types of isotherms are typically observed in ZSM-22 zeolites obtained via the hydrothermal synthesis method [34,35,42–46]. The textural properties of all materials (specific surface area and pore volumes) are listed in Table 1. The in-house prepared ZSM-22 samples exhibit a comparable specific surface area, which is higher than the commercially available ZSM-22 zeolite. Additionally, their micropore volume exceeds that of c-ZSM-22 by more than 25%.

Table 1. Physicochemical properties of the catalysts used in this study.

Sample	Si/Al^{ICP-MS}	Ar-Sorption			Brønsted Acid Sites [µmol/g]		Lewis Acid Sites [µmol/g]	
		S_{BET} [m^2/g]	V_{tot} [cm^3/g]	V_{micro} [cm^3/g]	T_{evac} = 150 °C	T_{evac} = 300 °C	T_{evac} = 150 °C	T_{evac} = 300 °C
c-ZSM-22	30	216	0.09	0.07	128	110	14	9
ZSM-22 (38)	38	280	0.12	0.09	136	110	27	15
ZSM-22 (50)	50	289	0.12	0.09	105	86	29	24
ZSM-22 (80)	80	291	0.11	0.09	87	71	26	13

The normalized FTIR spectra of the zeolites in the region corresponding to the ν(OH) stretching vibrations are presented in Figure 4c, and their deconvoluted spectra are reported in the Supporting Information (Figures S5.1–S5.4). All samples exhibit a prominent band between 3750 and 3720 cm^{-1}, indicating the presence of isolated silanol groups [40,47–50]. The c-ZSM-22 and ZSM-22 (38) spectra contain a sharp peak centered at 3743 cm^{-1}. In contrast, the spectra of ZSM-22 (50) and ZSM-22 (80) exhibit a broad band around 3735 cm^{-1}, with a tail extending towards lower wavenumbers related to looser stretch vibrations. The band can be decomposed into three main peaks at 3742 cm^{-1}, 3730 cm^{-1}, and 3710 cm^{-1} for all zeolite materials. According to the literature [48,51], the bands between 3745 cm^{-1} and 3740 cm^{-1} are assigned to isolated silanols on the external surface of the zeolites, while the bands between 3730 and 3700 cm^{-1} correspond to isolated silanol groups in the micropore channels. The band around 3730 cm^{-1} is related to hydroxyl groups linked to Si connected to Al atoms (silanol-Al), which are sometimes hypothesized to be tri-coordinated in the zeolite framework, i.e., Lewis acid sites [48,51]. It is worth noting that c-ZSM-22 and ZSM-22 (38) mainly exhibit external silanol groups, while the self-synthesized materials primarily contain isolated silanol groups inside the zeolite channels, which is also reflected in the long tail towards lower energy-stretching vibrations. Moreover, the band at 3743 cm^{-1} is more pronounced in the deconvoluted spectra of c-ZSM-22 and ZSM-22 (38) in Figures S5.1 and S5.4. Additionally, all samples exhibit a strong band at 3600 cm^{-1}, which corresponds to isolated bridged hydroxyl groups (Al-O(H)-Si) within the zeolite framework, and are attributed to strong Brønsted acid sites [47–49,52,53]. Furthermore, a broad band at 3530 cm^{-1} is observed for the materials synthesized in this work, which is associated with strong hydrogen bonding of internally located Si-OH groups. These silanol groups are typically formed due to framework defects, such as the absence of a T atom in the zeolite framework, and are commonly referred to as silanol nests [50,52]. It is noticeable that the amount of silanol nests decreases in the following order—ZSM-22 (50) > ZSM-22 (80) > ZSM-22 (38)—which is reflected in the values of the peak areas (summarized in Table S1) of the deconvoluted bands of Figures S5.1–S5.4.

The normalized FTIR spectra of the zeolites recorded after pyridine adsorption at 150 °C and subsequent evacuation at 300 °C are depicted in Figure 4d. The interaction of pyridine with the zeolite surface results in several characteristic peaks between 1700 cm^{-1} and 1400 cm^{-1}. The coordination of pyridine to Lewis acid sites results in two bands at

1454 cm^{-1} and 1618 cm^{-1}, while the protonation of pyridine on Brønsted acid sites results in two peaks at 1545 cm^{-1} and 1639 cm^{-1}. An additional band at 1489 cm^{-1} can also be detected, which is attributed to overlapping contributions of pyridine interacting with Lewis and Brønsted acid sites [54]. Due to the overlap of the ν_{8a} bands between 1600 cm^{-1} and 1640 cm^{-1}, deconvolution and integration of the signals at 1454 cm^{-1} and 1545 cm^{-1} is used to determine the amount of Lewis (A_L) and Brønsted (A_B) acid sites, respectively. Table 1 summarizes the results after pyridine evacuation at 150 °C and 300 °C. All zeolites have an $A_B/(A_B+A_L)$ ratio between 0.77 and 0.90 after evacuation at 150 °C, which increases to a value between 0.78 and 0.92 when the temperature is increased to 300 °C, reflecting the Brønsted nature of the acid sites. Interestingly, ZSM-22 (50) contains a similar amount of acid sites as c-ZSM-22 and ZSM-22 (38), but contains more Lewis acid sites. Additionally, the acid strength can be estimated by comparing the amounts of pyridine remaining on the acid sites after evacuation at 150 °C and 300 °C, i.e., by the $A_{B,300}/A_{B,150}$ and $A_{L,300}/A_{L,150}$ ratios for Brønsted and Lewis acid sites, respectively, which is presented in Table S1 [30]. All zeolites exhibit a comparable, high Brønsted acid strength, which is reflected by the $A_{B,300}/A_{B,150}$ ratios between 0.81 and 0.86. However, while c-ZSM-22, ZSM-22 (38), and ZSM-22 (80) exhibit a comparable medium Lewis acid strength, i.e., an $A_{L,300}/A_{L,150}$ ratio with values between 0.50 and 0.65, ZSM-22 (50) contains stronger Lewis acid sites, reflected by the $A_{L,300}/A_{L,150}$ ratio of 0.82.

Three unsaturated alcohols are generated during the dehydration of 1,3-BDO to BD, i.e., 2B1OL, 3B1OL, and 3B2OL. It is known that 3B1OL is the only one of the intermediates that can coordinate its hydroxyl group to its internal C=C bond within the zeolite pores, which could make the molecule less active for further dehydration towards BD (Figure S6) [25]. To investigate the adsorption behavior of this unsaturated alcohol in ZSM-22, the adsorption was monitored by in situ FTIR experiments. Figure 5 presents the normalized FTIR spectra of 3B1OL adsorbed on all the catalysts investigated in this work. The bands observed between 2750 cm^{-1} and 3100 cm^{-1} correspond to the ν(CH) stretching vibrations of the unsaturated alcohol and are consistent with previous literature [25]. In the ν(OH) stretching region, several additional bands can be observed compared to the reference spectrum. Upon the adsorption of 3B1OL at room temperature followed by evacuation, the band at 3743 cm^{-1} remains unchanged, indicating no interaction between the isolated silanol groups and 3B1OL. In contrast, the band between 3600 and 3590 cm^{-1}, related to Brønsted acid sites, has almost completely disappeared, suggesting a strong interaction between the unsaturated alcohol and these acid sites [55]. Additionally, a sharp peak is noticeable in the spectra of c-ZSM-22 at 3695 cm^{-1}, while this appears to be a shoulder in ZSM-22 (38). This peak could be associated with the interaction between the hydroxyl group of the unsaturated alcohol and the silicate wall inside the zeolite channels [56]. Furthermore, a broad band centered at 3540 cm^{-1} emerges in all samples, which is assigned to weakly perturbed hydroxyl groups. It has been proposed that this band is associated with the interaction of the hydroxyl group of the alcohol and the Brønsted acid site of the zeolite [55]. Interestingly, the intensity of this band does not directly correlate with the acid density, since a more prominent band is observed in the order of ZSM-22 (80) > ZSM-22 (50) > ZSM 22 (38) > c-ZSM-22, suggesting that additional effects within the zeolite pores are present. One possible explanation is the formation of hydrogen bonds between the 3B1OL molecules. Di Iorio et al. [57] reported that in more hydrophobic zeolites, a band near 3510 cm^{-1} becomes more pronounced upon 2-butanol adsorption. They attributed this band to the formation of hydrogen bonds between alcohol dimers because similar behavior has been observed for short-chain alcohols (C1–C4) in non-polar solvents. Since ZSM-22 (80) contains less Al, it is, therefore, more hydrophobic, and similar intermolecular interactions might contribute to the increased intensity of the band located at 3540 cm^{-1}.

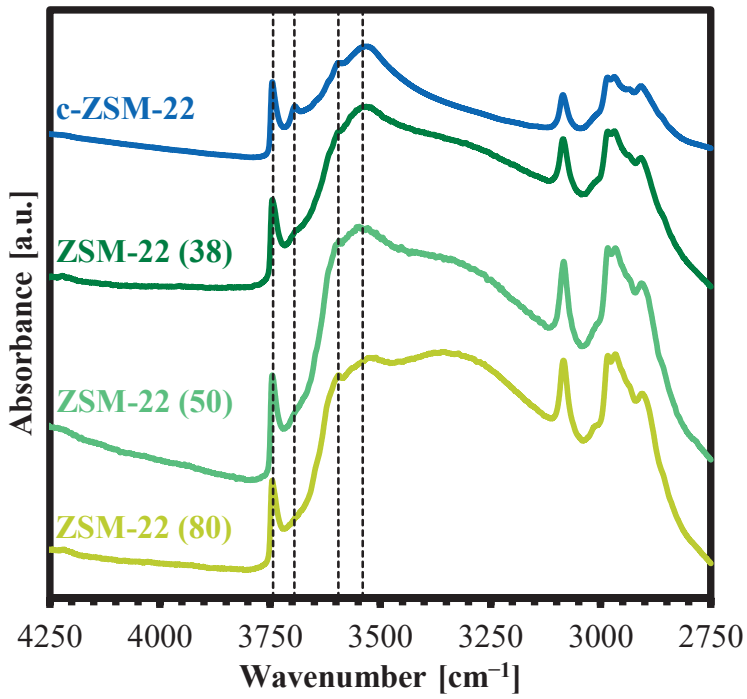

Figure 5. Normalized FTIR spectra of adsorbed 3-buten-1-ol on c-ZSM-22, ZSM-22 (38), ZSM-22 (50), and ZSM-22 (80) at 0.5 Torr and room temperature, followed by desorption under vacuum (10^{-3} Torr) at room temperature.

Finally, a broad band centered at 3300 cm^{-1} is observed in ZSM-22 (50) and ZSM-22 (80), while this is less pronounced in ZSM-22 (38) and absent in c-ZSM-22. Di Iorio and coworkers [57] observed a similar band between 3300 and 3400 cm^{-1} for 2-butanol adsorption in Beta zeolites. They attributed this peak to hydrogen bond formation between the hydroxyl group of the alcohols and zeolite defects such as Si-OH groups, resulting in the formation of dimeric and polymeric 2-butanol, resembling a liquid-like phase of bulk 2-butanol within the zeolite framework. Similarly, the band centered at 3300 cm^{-1} in Figure 5 resembles the ν(OH) stretching vibration related to hydrogen bonding in liquid 3B1OL. Since ZSM-22 (50) and ZSM-22 (80) contain more silanol nests than ZSM-22 (38), it can be suggested that there might be an interaction between the silanol nests and the free hydroxyl group of 3B1OL, resulting in a disordered liquid-like phase of hydrogen bonds.

2.2. Catalytic Results: Dehydration of 1,3-Butanediol into Butadiene

Figure 6 presents the 1,3-BDO conversion and product selectivities as a function of time on stream (TOS) during the vapor phase dehydration of 1,3-BDO over the zeolite materials at 300 °C, while Table 2 lists the relevant catalytic performance indicators of the zeolites after 1 h and 22 h TOS. In all cases, the major products detected were butadiene, propylene, 3-buten-1-ol, and methyl ethyl ketone, while only small amounts (selectivity < 1.5%) of butanal were observed. Additionally, no 3-buten-2-ol nor 2-buten-1-ol were present in the product pool. During the acid-catalyzed dehydration of 1,3-BDO, the secondary alcohol 3B2OL is more favorable to be dehydrated. Therefore, it is evident that 3B2OL is the least probable reaction intermediate, which could explain its absence in the reactor effluent. Additionally, according to Zaitsev's rule, dehydration of 1,3-BDO results in the formation of the most substituted unsaturated alcohol, i.e., 2B1OL, compared to 3B1OL. However, no 2B1OL is observed in the product pool, which could be related to its high reactivity towards further dehydration into butadiene in the presence of Brønsted acid sites [27,58]. The presence of propylene is related to the cracking of 3B1OL, while the formation of MEK

is directly formed from 1,3-BDO after a cascade of dehydration and dehydrogenation-hydrogenation reactions (Figure 1) [24,30].

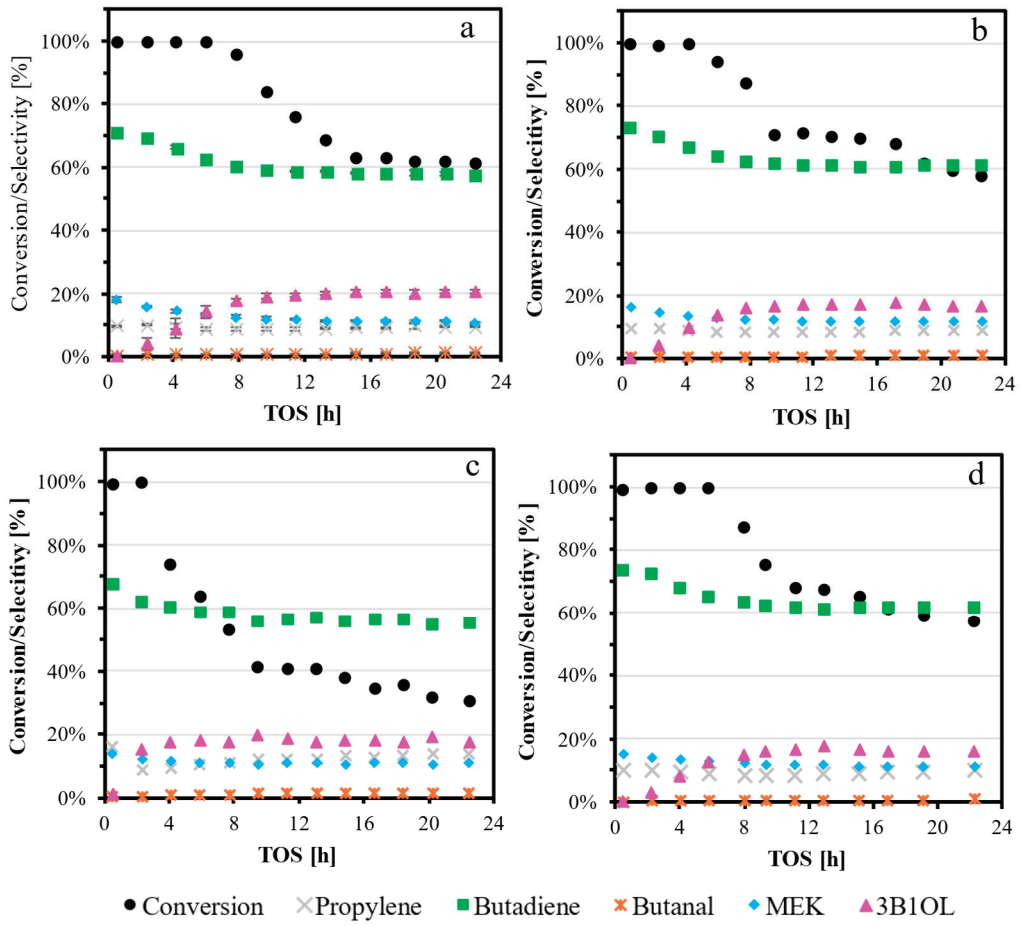

Figure 6. 1,3-BDO conversion and product selectivities as a function of time on stream over (**a**) c-ZSM-22, (**b**) ZSM-22 (38), (**c**) ZSM-22 (50), and (**d**) ZSM-22 (80) at 300 °C and a total pressure of 5 bar. The reactant feed contains 20 wt.% 1,3-BDO in dioxane. The feed rate for c-ZSM-22 and ZSM-22 (38) was 1.5 g/h, while this was 0.8 g/h for ZSM-22 (50) and ZSM-22 (80).

Table 2. Catalytic performance and butadiene productivity of all zeolites used for the dehydration of 1,3-BDO at 1 h and 22 h TOS. The reaction is performed at 300 °C, and the reactant feed consists of 20 wt.% 1,3-BDO in dioxane. The feed rate for c-ZSM-22 and ZSM-22 (38) was 1.5 g/h, while this was 0.8 g/h for ZSM-22 (50) and ZSM-22 (80).

Zeolite	TOS [h]	Conversion [%]	Selectivity [%]					Productivity [$g_{BD} \cdot g^{-1}_{cata} \cdot h^{-1}$]
			PE	BD	BuAL	MEK	3B1OL	
c-ZSM-22	1	100	10	71	0	18	0	2.5
	22	61	10	58	1	11	21	1.3
ZSM-22 (38)	1	100	10	73	0	16	0	2.7
	22	58	9	61	1	12	17	1.2
ZSM-22 (50)	1	99	16	68	0	14	1	2.0
	22	31	14	55	2	11	18	0.5
ZSM-22 (80)	1	99	10	74	0	15	0	1.4
	22	57	10	62	1	11	16	0.7

Both commercial ZSM-22 and ZSM-22 (38) achieve full BDO conversion during the first 5 h TOS, which then gradually decreases as the reaction proceeds. The initial BD selectivity over c-ZSM-22 and ZSM-22 (38) amounts to 71% and 73%, respectively. After 15 h TOS, the commercial sample stabilizes at a conversion of 62%, which is maintained for the remaining 7 h. However, ZSM-22 (38) reaches a stable conversion of 70% after 9 h TOS, which is maintained for 8 h before further deactivation occurs. After 22 h TOS, the conversion reaches a value of 58% over ZSM-22 (38). Once a stable regime of product selectivity is obtained, only minor differences in product distribution are observed between c-ZSM-22 and ZSM-22 (38). For instance, c-ZSM-22 exhibits a lower BD and MEK selectivity than ZSM-22 (38), but produces more 3B1OL. No difference in propylene or butanal selectivity is observed. The similar behavior in the product distribution might be associated with the nature, strength, and number of acid sites. It is known that Lewis acid sites favor the cracking of 3B1OL, while Brønsted acid sites promote its further dehydration to BD [30]. Since both catalysts exhibit a similar distribution of acid sites (Table 1), a similar product selectivity can be expected. However, ZSM-22 (38) exhibits weaker Lewis acid sites, which contribute to a reduced 3B1OL cracking, resulting in a slightly higher BD selectivity (Table 2). Although both zeolites exhibit a stable conversion regime, deactivation of ZSM-22 (38) is observed. This could be attributed to the bigger particle size of ZSM-22 (38) (2–4 μm), which is built up from stacked nanorods to form elongated needle-like bundles. As a result, ZSM-22 (38) exhibits longer diffusion path lengths for reactants and reaction products. Therefore, it might be more difficult for the coke precursors to reach the external surface, which could lead to deactivation by coke buildup inside the zeolite channels [59].

ZSM-22 (80) exhibits a similar behavior to that of c-ZSM-22 and ZSM-22 (38). Full 1,3-BDO conversion is achieved within the first 6 h TOS, with an initial BD selectivity of 74%. However, a rapid decline in conversion is observed, reaching 68% after 11 h TOS. This is followed by a gradual decrease to 57% at 22 h, similarly to the trend observed for ZSM-22 (38), which could be attributed to the similar acid properties, i.e., acid strength and the number of Brønsted acid sites. The catalyst deactivation could be associated with the morphology of ZSM-22 (80). Similarly to ZSM-22 (38), bigger particles are observed for ZSM-22 (80), which might hinder the diffusion of reactants, reaction products, and coke precursors [60,61]. Moreover, ZSM-22 (80) contains a higher amount of silanol nests (Figure 4c and Table S1), which could trap these coke precursors and enhance carbon deposition inside the pores, decreasing the accessibility towards other acid sites [28,59]. Additionally, as depicted in Figure 5, hydrogen bonding of 3B1OL (peak at 3300 cm^{-1}) occurs, which is suggested to be related to the interaction of 3B1OL's hydroxyl group with silanol nests. This could result in trapping of this unsaturated alcohol, making the hydroxyl group of 3B1OL not available for dehydration. Consequently, 3B1OL might crack, which can react further to produce coke precursors, which the silanols could retain.

In contrast to the other zeolites, ZSM-22 (50) can only maintain full conversion during the first 3 h TOS, after which it rapidly declines, reaching a value of 40% after 9 h TOS. The conversion keeps decreasing during the overall experiment and reaches a value of 31% after 22 h TOS. Furthermore, this zeolite exhibits an overall lower BD selectivity compared to the other catalysts. This is accompanied by a notably higher selectivity towards propylene ($C_{3=}$), suggesting a shift in the reaction pathway, possibly due to differences in acid site distribution or strength. As depicted in Figure 3, ZSM-22 (50) comprises particles of size similar to those in ZSM-22 (38), resulting in a longer diffusion path length compared to c-ZSM-22. Moreover, ZSM-22 (50) contains an increased amount of isolated silanol groups, which are known to be related to catalyst deactivation due to coke formation during the conversion of methanol to olefins [60]. Additionally, more silanol nests can be observed in ZSM-22 (50) (Figure 4c and Table S1), which are responsible for trapping and stabilizing

coke precursors. Similarly to ZSM-22 (80), the interaction between 3B1OL and the silanol nests might cause the hydroxyl group of 3B1OL to be less active for dehydration, and favor cracking and formation of coke precursors. The combination of those defects with longer diffusion path lengths in ZSM-22 (50) compared to c-ZSM-22 could explain the rapid decrease in conversion. As can be seen in Table S1, ZSM-22 (50) contains a higher amount of Lewis acid sites, which are also stronger ($A_{L,300}/A_{L,150}$ ratio of 0.82) compared to c-ZSM-22, ZSM-22 (38), and ZSM-22 (80) ($A_{L,300}/A_{L,150}$ ratio of 0.65, 0.55, and 0.50, respectively). This could lead to more cracking of 3B1OL instead of dehydration, which explains the increased amount of propylene over this catalyst.

To obtain a more accurate comparison of the catalytic performance of the zeolite materials, the productivity of each catalyst was calculated and compared both among the tested zeolites and with previously reported catalysts. Both the productivity at early TOS and after 22 h TOS were considered and are listed in Table 2. Initial productivities of 2.5 $g_{BD}\cdot g^{-1}_{cata}\cdot h^{-1}$ and 2.7 $g_{BD}\cdot g^{-1}_{cata}\cdot h^{-1}$ are observed for c-ZSM-22 and ZSM-22 (38), respectively, outperforming all previously reported catalysts. The initial productivities of ZSM-22 (50) and ZSM-22 (80) are comparable to those observed for commercial SiO_2/Al_2O_3 and $H_3PW_{12}O_{40}/SiO_2$. Although ZSM-22 (38), ZSM-22 (50) and ZSM-22 (80) exhibit comparable 1,3-BDO conversion and BD selectivity at 1 h TOS, a notable difference can be observed in their productivity. This is attributed to the lower acid site density in the two latter catalysts compared to ZSM-22 (38), as summarized in Table 1. Since productivity is expressed per gram of catalyst, the reduced number of active sites in ZSM-22 (50) and ZSM-22 (80) leads to an overall lower productivity, despite similar activity. It is important to note that productivity values calculated at (near) complete conversion represent a lower estimate. This implies that a smaller amount of catalyst could potentially achieve the same conversion and, consequently, a higher productivity.

Although the BD yield of all ZSM-22 zeolites decreases over time, and higher BD yields can be achieved over other types of catalysts (e.g., $Y_2Zr_2O_7$ and WO_3/SiO_2), the overall BD productivity of ZSM-22 (50) and ZSM-22 (80) after 22 h TOS remains comparable to other zeolite materials documented in the literature (e.g., 0.48 $g_{BD}\cdot g^{-1}_{cata}\cdot h^{-1}$ over ZSM-5 (130) after 8 h TOS and 0.59 $g_{BD}\cdot g^{-1}_{cata}\cdot h^{-1}$ over FER (130) after 10 h TOS) [25,28]. Moreover, the BD productivities of c-ZSM-22 and ZSM-22 (38) after 22 h TOS surpass all previously reported catalysts. Furthermore, since productivity in the literature is mostly reported between 0 and 10 h TOS, the values observed in this work demonstrate the enhanced performance of ZSM-22 zeolites over prolonged reaction times. Consequently, these catalysts could serve as a more efficient option for sustainable BD production.

3. Materials and Methods

3.1. Materials

A commercial sample of NH_4-ZSM-22 (<0.1 wt.% Na_2O) was obtained from Bonding Chemical (Si/Al = 30–40). This zeolite was calcined under air at 550 °C (heating ramp of 1 °C·min^{-1} from room temperature) for 4 h to obtain the protonic form, i.e., H-ZSM-22. This sample is referred to as c-ZSM-22. Potassium hydroxide (KOH, 85%), aluminum sulfate ($Al_2(SO_4)\cdot nH_2O$, 98%), 1,6-diaminohexane (DAH, 98%), colloidal silica (Ludox AS-40, 40 wt.% in water), ammonium nitrate (NH_4NO_3, 98%), and 1,3-butanediol (99.5%) were purchased from Merck Life Science. 1,4-dioxane (99.9%) was purchased from Chem-Lab Analytical. All chemicals are used without any further purification.

3.2. Catalyst Preparation

In this study, ZSM-22 zeolites with a targeted Si/Al ratio of 45, 70, and 100 were synthesized using the hydrothermal synthesis method reported by Zhai et al. [34], with

some slight adjustments. First, three homogeneous solutions were prepared: KOH, DAH, and $Al_2(SO_4)\cdot nH_2O$ were dissolved in water under continuous stirring (400 rpm). Additionally, colloidal silica was diluted in water under the same stirring conditions. Subsequently, the DAH solution was added to the KOH solution, followed sequentially by the $Al_2(SO_4)\cdot nH_2O$ solution and diluted colloidal silica, with 10 min of continuous stirring at 400 rpm between each addition. The molar composition of this precursor gel was xAl/90Si/yKOH/27DAH/3600H_2O with x = 2, 1.3, or 0.9 and y = 15, 15, or 12 to obtain a Si/Al ratio of 45, 70, or 100, respectively. After all the solutions were added, the pH was verified to ensure this was between 12 and 13. The resulting mixture was then aged for 3.5 h under continuous stirring at 200 rpm, after which seeds (c-ZSM-22) were added to the precursor gel. The amount of seeds was 5 wt.% with respect to the Si content in the gel. The suspension was then stirred for another 30 min to achieve complete homogenization. Crystallization was carried out in 100 mL Teflon-lined stainless-steel autoclaves under continuous stirring at 100 rpm using a Nabertherm oven and a MIXcontrol 20 stirring plate. ZSM-22 (45) was crystallized for 48 h at 160 °C, while ZSM-22 (70) and ZSM-22 (100) were crystallized for 36 h at 150 °C. After crystallization, the zeolites were recovered, washed three times with distilled water, dried at 100 °C for 20 h, and calcined under air (Nabertherm muffle furnace) at 550 °C (heating ramp 1 °C·min^{-1}) for 8 h to remove the structure-directing agent. The K-ZSM-22 zeolites were then three times ion-exchanged using 1 M NH_4NO_3 (10 mL/g zeolite) for 2 h at 50 °C under continuous stirring (200 rpm). NH_4-ZSM-22 was then recovered via centrifugation and washed until the pH of the washing water was neutral. Finally, the zeolites were dried at 100 °C for 20 h and calcined under air at 550 °C (heating ramp of 1 °C·min^{-1} from 100 °C) for 8 h to obtain H-ZSM-22.

3.3. Catalyst Characterization

The crystal structure of the zeolites was identified by X-ray powder diffraction (XRD) using a Bruker D8 Advance diffractometer (Bruker, Billerica, MA, USA) with Cu Kα radiation (λ = 1.54 Å). The XRD patterns were collected in a 2θ range of 5–90° with a scan rate of 1°/min and steps of 0.02°. The Scherrer equation was used to estimate the average crystal size of the zeolite particles

$$d = \frac{K\lambda}{\beta\cos\theta} \quad (1)$$

where d is the average crystal size in nanometers, K is a dimensionless shape factor with a value of 1, λ is the wavelength of the X-rays (0.154 nm), β is the full-width at half maximum, and θ is Bragg's angle. In this study, 2θ = 35.6° was chosen, which relates to the [002] crystallographic plane.

Scanning electron microscopy (SEM) with a JSM-IT800 (JEOL, Tokyo, Japan) was performed to gain insight into the crystal morphology and size of the zeolites.

The Si/Al ratio was determined for all samples through inductively coupled plasma mass spectrometry. Before analysis, the sample was added to a Teflon liner with a mixture of fluoric acid and aqua regia, which was then heated at 110 °C for one hour to digest the sample completely. After cooling, the fluoric acid was neutralized with a solution of boric acid. The prepared solution was then analyzed using a 7900 ICP-MS from Agilent Technologies (Waltham, MA, USA).

Solid-state magic angle spinning nuclear magnetic resonance spectroscopy (MAS-NMR) was used to determine the local ^{27}Al and ^{29}Si environments in the zeolites. All MAS NMR experiments were performed on a Bruker AVANCE 500 NB, using 4 mm rotors and a rotational speed of 12 kHz. ^{27}Al MAS NMR was recorded at 130.30 MHz, using $Al(NO_3)_3$ as a reference for the chemical shift. ^{29}Si MAS NMR was performed at 99.35 MHz, using

tetramethyl silane (TMS) as a reference for the chemical shift. The framework Si/Al ratio can be calculated by using the following equation

$$\mathrm{Si/Al} = \frac{\sum_{n=0}^{4} I_{Si(nAl)}}{\sum_{n=0}^{4} \frac{n}{4} \times I_{Si(nAl)}} \quad (2)$$

where n is the number of adjacent Al nuclei, and I is the peak area of the corresponding spectrum signal in the ^{29}Si MAS NMR spectrum.

Argon sorption experiments were performed at −186 °C using a Micromeritics 3FLEX instrument to determine the zeolites' specific surface area and pore volume. Prior to the analysis, the catalyst sample (100 mg) was degassed at 350°C overnight under vacuum to remove any adsorbed impurities. The specific surface area was determined via the Brunauer–Emmett–Teller (BET) method, applying the criteria of Rouquerol to increase the accuracy of the measurements. The micropore surface area and volume were calculated by the t-plot method, and the total pore volume (V_{tot}) was determined by the amount of adsorbed argon at a relative pressure (p/p°) of 0.97.

In situ Fourier transform infrared spectroscopy (FTIR) experiments were performed on a Nicolet iS60 spectrometer (Thermo Fisher Scientific, Waltham, MA, USA)with a resolution of 4 cm^{-1}. The samples were pressed under 1 ton into self-supported wafers (20 mg, 16 mm diameter) before loading to a carrousel, which is a transmission-type in situ cell designed to accommodate up to 12 self-supported sample disks. The samples were then activated at 450 °C for 2 h (temperature ramp 1 °C·min^{-1}) under a 10^{-6} Torr vacuum. In situ FTIR of dehydrated samples was acquired at 150 °C (reference) to reveal the acid sites and silanol groups. The quantification of the Brønsted and Lewis acid sites was performed by Py-FTIR. The probe molecule was adsorbed at 150 °C and an equilibrium pressure of 1 Torr. The spectra were subsequently recorded after evacuation at 150 °C and 300 °C. The FTIR spectra were obtained by subtracting the reference from the spectra of interest. The amount of acid sites was determined using the integrated bands situated at 1454 cm^{-1} (Lewis) and 1545 cm^{-1} (Brønsted), and the following molar extinction coefficients: ε(B) = 1.67 and ε(L) = 2.22 cm·μmol^{-1} [62]. In addition, after the same pretreatment, in situ FTIR of 3-buten-1-ol was performed at room temperature. The unsaturated alcohol was adsorbed at room temperature at an equilibrium pressure of 0.5 Torr for 0.5 h, followed by desorption (10^{-3} Torr) at the same temperature to remove physiosorbed 3B1OL, whereafter the spectra were collected.

3.4. Catalytic Dehydration Experiments

The catalytic experiments were performed on a high-throughput kinetics set-up consisting of tubular reactors with a length of 0.85 m and an inner diameter of 22 mm at 5 bar. All catalysts were pelletized, sieved to 125–150 μm, and dried overnight at 120 °C to remove adsorbed water before loading them in the middle of the reactor between layers of inert α-alumina (140 μm). The reactor was then heated to the reaction temperature, i.e., 300 °C, and kept for at least 4 h under a continuous N_2 (Air Liquide) flow of 10 NLh^{-1}. The catalyst mass was varied between 50 and 60 mg and diluted with the same inert α-alumina until 20 wt.% to avoid hot spots in the catalyst bed. A liquid reactant feed of 20 wt.% 1,3-BDO in 1,4-dioxane (mass flow rate varied between 0.8 and 1.5 g/h) was mixed with N_2 (flow rate varied between 9 and 16 nL/h) and fed over the catalyst bed. All experiments were conducted at an identical site time. The reactor effluent was analyzed on-line by GC-FID (Thermo Fisher Scientific Trace 1310) equipped with a 100 m PONA column using methane as an internal standard. To ensure intrinsic kinetics were measured, engineering correlations were used [63,64]. A carbon balance exceeding 80% is obtained for all experiments, which is in accordance with reported values in the literature [26–28].

The reproducibility of the catalytic test was verified by conducting the dehydration of 1,3-BDO in threefold for c ZSM 22, as shown in Figure S1. Based on the consistent results, this reproducibility level was considered representative of the other zeolite catalysts. Post-reaction characterization could not be applied due to the dilution of the catalyst with inert α-alumina, which prevents physical separation and meaningful analysis. Nevertheless, a visual inspection of the catalyst bed after reaction (as illustrated for c-ZSM-22 in Figure S2) reveals a distinct black coloration, indicative of coke deposition on the zeolite, which is consistent with catalyst deactivation.

Definitions

The difference in acid densities between the zeolites was compensated for by comparing the materials based on site time:

$$\text{Site Time } [\text{molH}^{+}\cdot\text{s}\cdot\text{mol}^{-1}_{1,3\text{-BDO}}] = \frac{W}{F} c_a \tag{3}$$

With W the mass of the zeolite loaded into the reactor, F the molar flow rate of 1,3-BDO, and C_a the concentration of acid sites as obtained from Py-FTIR. The site times of c-ZSM-22, ZSM-22 (45), ZSM-22 (70), and ZSM-22 (100) amounted to 6.6, 6.6, 7.0, and 8.3 $\text{mol}_{H+}\cdot\text{s}\cdot\text{mol}^{-1}{}_{1,3\text{-BDO}}$, respectively.

The conversion (X) of 1,3-BDO and the carbon selectivities (S) towards the products (i) were expressed as

$$X_{1,3\text{-BDO}}[\%] = \frac{F^0_{1,3\text{-BDO}} - F_{1,3\text{-BDO}}}{F^0_{1,3\text{-BDO}}} \times 100\% \tag{4}$$

$$S_i[\%] = \frac{c_i * F_i}{4\left(F^0_{1,3\text{-BDO}} - F_{1,3\text{-BDO}}\right)} \times 100\% \tag{5}$$

where $F^0{}_{1,3\text{-BDO}}$ and $F_{1,3\text{-BDO}}$ are the molar flow rates at the inlet and the outlet of the reactor, respectively. F_i and c_i represent the outlet flow of product i and the carbon numbers per molecule of product i, respectively.

BD productivity (P_{BD}) was calculated using the following equation

$$P_{BD}[g_{BD}\cdot g^{-1}_{catalyst}\cdot h^{-1}] = \frac{54.09 \times X_{1,3\text{-BDO}} \times S_{BD} \times F^0_{1,3\text{-BDO}}}{90.12 \times W \times 10000} \tag{6}$$

where 54.09 and 90.12 are the molecular weights [$g\cdot mol^{-1}$] of BD and 1,3-BDO, respectively, $X_{1,3\text{-BDO}}$ is the conversion of 1,3-BDO, S_{BD} is the selectivity towards BD, $F_{1,3\text{-BDO}}$ the mass flow of 1,3-BDO [$g\cdot h^{-1}$], and W the mass of the catalyst [g].

4. Conclusions

ZSM-22 zeolites with different Si/Al ratios were prepared via a hydrothermal synthesis method, evaluated for the sustainable production of BD by 1,3-BDO dehydration at 300 °C, and compared to a commercial ZSM-22 sample. All synthesized zeolites were characterized by XRD, SEM, Ar sorption, ICP-MS, ^{27}Al, and ^{29}Si MAS NMR, and in situ FTIR with pyridine or 3B1OL as probe molecules. The zeolites displayed the characteristic ZSM-22 topology without impurities and exhibited distinct morphological and textural properties, including bigger particle sizes and higher specific surface areas compared to c-ZSM-22.

The commercial zeolite and both ZSM-22 (38) and ZSM-22 (80) showed a similar trend in 1,3-BDO conversion and product selectivity, i.e., full conversion at early TOS, followed by a decline to approximately 60% conversion, with BD and propylene selectivities around 60% and 10%, respectively, after 22 h TOS. The absence of silanol nests and strong Lewis acid sites in c-ZSM-22 and ZSM-22 (38) favored the dehydration, achieving initial BD

productivities of 2.5 and 2.7 $g_{BD} \cdot g^{-1}_{cata} \cdot h^{-1}$, respectively. After 22 h TOS, the productivities of c-ZSM-22 and ZSM-22 (38) decreased to 1.3 $g_{BD} \cdot g^{-1}_{cata} \cdot h^{-1}$ and 1.2 $g_{BD} \cdot g^{-1}_{cata} \cdot h^{-1}$, respectively, outperforming previously reported zeolite catalysts in the literature. Both c-ZSM-22 and ZSM-22 (38) can be seen as potential catalysts for the sustainable production of BD.

In contrast, ZSM-22 (50) exhibited a conversion of 31% after 22 h TOS, with a lower BD and higher propylene selectivity of 55% and 14%, respectively. This behavior is attributed to the presence of strong Lewis acid sites in this zeolite, which favor the cracking of 3B1OL into propylene. Additionally, the silanol nests within the pore channels of ZSM-22 (50) interact with 3B1OL, forming hydrogen bonds that result in a liquid-like structure inside the pores. These silanol nests may reduce the activity of 3B1OL during dehydration and act as traps for coke precursors, leading to decreased 1,3-BDO conversion and BD selectivity.

Future work could focus on optimizing ZSM-22 (38) by reducing the particle size to introduce shorter diffusion path lengths, potentially enhancing the catalyst stability and ensuring higher 1,3-BDO conversion and productivity rates.

Supplementary Materials: The following supporting information can be downloaded at https://www.mdpi.com/article/10.3390/catal15070655/s1, Figure S1: Catalytic dehydration of 1,3-BDO over c-ZSM-22 executed in threefold. The 95% confidence interval is represented by error margins. Typically, the error in product selectivity ranges from 0.1% to 3%, while the error in conversion ranges from 2% to 11%. Reaction conditions: T = 300 °C, F1,3-BDO = 0.3 g/h, mc-ZSM-22 = 50 mg. Figure S2: Visual representation of catalyst deactivation after reaction. Visual representation of catalyst deactivation due to coke formation on the catalyst. The black material is the catalyst bed, which includes c-ZSM-22 zeolite and inert α-Al_2O_3. Figure S3.1: SEM images of c-ZSM-22 (a), ZSM-22 (38) (b), ZSM-22 (50) (c), and ZSM-22 (80) (d) demonstrating the spheric clusters consisting of elongated needle-like particles of ZSM-22 zeolites prepared via the in-house recipe compared to the commercial sample. Figure S3.2: SEM images of c-ZSM-22 (left) and ZSM-22 (38) (right) demonstrating a more detailed picture of the smaller cubic/rectangular particles of c ZSM 22 compared to the elongated crystals of ZSM-22 (38) forming needle-like bundles. Figure S4: Deconvoluted ^{29}Si MAS NMR spectra of c-ZSM-22, ZSM-22 (38), ZSM-22 (50), and ZSM-22 (80). Figure S5.1: Deconvoluted FTIR spectrum of c-ZSM-22 at 150 °C. Figure S5.2: Deconvoluted FTIR spectrum of ZSM-22 (38) at 150 °C. Figure S5.3: Deconvoluted FTIR spectrum of ZSM-22 (50) at 150 °C. Figure S5.4: Deconvoluted FTIR spectrum of ZSM-22 (80) at 150 °C. Figure S6: Proposed structure for 3-buten-1-ol adsorbed on a zeolite: (a) coordination of the free hydroxyl group with the negative pi cloud of the internal C=C bond, (b) free hydroxyl group adsorbs on the Brønsted acid site. Adapted from reference [25]. Table S1: Si/Al ratio, crystal size, article size, $A_{B,300}/A_{B,150}$ ratio, $A_{L,300}/A_{L,150}$ ratio, and integrated peak area from the silanol nests.

Author Contributions: Conceptualization, L.E. and A.V.; Methodology, L.E. and D.S.; Validation, L.E., J.P. and A.V.; Formal Analysis, L.E., J.A.A. and V.R.; Investigation, L.E., A.D.L., J.A.A. and V.R.; Resources, V.V. and A.V.; Writing—Original Draft Preparation, L.E.; Writing—Review and Editing, L.E., J.P., V.V., M.K.S., J.W.T. and A.V.; Visualization, L.E.; Supervision, M.K.S., J.W.T., J.P. and A.V.; Project Administration: J.P. and A.V.; Funding Acquisition: J.W.T. and A.V. All authors have read and agreed to the published version of the manuscript.

Funding: This work was funded by the Special Research Fund of Ghent University (BOF DOC 2021002901). L.E. also acknowledges the additional financial support from FWO through Grant Number V402725N. V.V. acknowledges partial financial support from the European Union-NextGenerationEU through the National Recovery and Resilience Plan of the Republic of Bulgaria project No. BG-RRP-2.004-0008.

Data Availability Statement: Dataset available on request from the authors.

Acknowledgments: The authors acknowledge Olivier Janssens (Department of Solid State Sciences, Ghent University) for XRD analyses and SEM measurements, Marie Desmurs (Laboratoire Catalyse et Spectrochimie, Université de Caen) for Ar-sorption experiments, and Romain Nardi (Laboratoire

Catalyse et Spectrochimie, Université de Caen) for the in situ FTIR experiments. During the preparation of this manuscript, L.E. used Microsoft Copilot for the purpose of improving readability. L.E. has reviewed and edited the output and takes full responsibility for the content of this publication.

Conflicts of Interest: The authors declare no conflicts of interest.

References

1. Singh, O.; Khairun, H.S.; Joshi, H.; Sarkar, B.; Gupta, N.K. Advancing light olefin production: Exploring pathways, catalyst development, and future prospects. *Fuel* **2025**, *379*, 132992. [CrossRef]
2. Makshina, E.V.; Dusselier, M.; Janssens, W.; Degrève, J.; Jacobs, P.A.; Sels, B.F. Review of old chemistry and new catalytic advances in the on-purpose synthesis of butadiene. *Chem. Soc. Rev.* **2014**, *43*, 7917–7953. [CrossRef] [PubMed]
3. White, W.C. Butadiene production process overview. *Chem. Biol. Interact.* **2007**, *166*, 10–14. (In English) [CrossRef]
4. Camacho, C.C.; Perales, A.V.; Alonso-Fariñas, B.; Vidal-Barrero, F.; Ollero, P. Assessing the economic and environmental sustainability of bio-olefins: The case of 1,3-butadiene production from bioethanol. *J. Clean. Prod.* **2022**, *374*, 133963. [CrossRef]
5. Ren, T.; Patel, M.; Blok, K. Olefins from conventional and heavy feedstocks: Energy use in steam cracking and alternative processes. *Energy* **2006**, *31*, 425–451. [CrossRef]
6. Sun, D.; Li, Y.; Yang, C.; Su, Y.; Yamada, Y.; Sato, S. Production of 1,3-butadiene from biomass-derived C4 alcohols. *Fuel Process. Technol.* **2020**, *197*, 106193. [CrossRef]
7. Pomalaza, G.; Ponton, P.A.; Capron, M.; Dumeignil, F.Y. Ethanol-to-butadiene: The reaction and its catalysts. *Catal. Sci. Technol.* **2020**, *10*, 4860–4911. [CrossRef]
8. Angelici, C.; Weckhuysen, B.M.; Bruijnincx, P.C.A. Chemocatalytic Conversion of Ethanol into Butadiene and Other Bulk Chemicals. *ChemSusChem* **2013**, *6*, 1595–1614. [CrossRef]
9. Janssens, W.; Makshina, E.V.; Vanelderen, P.; De Clippel, F.; Houthoofd, K.; Kerkhofs, S.; Martens, J.A.; Jacobs, P.A.; Sels, B.F. Ternary Ag/MgO-SiO_2 Catalysts for the Conversion of Ethanol into Butadiene. *ChemSusChem* **2015**, *8*, 994–1008. [CrossRef]
10. Alphy, M.P.; Hazeena, S.H.; Binoop, M.; Madhavan, A.; Arun, K.; Vivek, N.; Sindhu, R.; Awasthi, M.K.; Binod, P. Synthesis of C2-C4 diols from bioresources: Pathways and metabolic intervention strategies. *Bioresour. Technol.* **2022**, *346*, 126410. [CrossRef]
11. Zhou, S.; Zhang, Y.; Wei, Z.; Park, S. Recent advances in metabolic engineering of microorganisms for the production of monomeric C3 and C4 chemical compounds. *Bioresour. Technol.* **2023**, *377*, 128973. [CrossRef] [PubMed]
12. Lee, Y.-G.; Seo, J.-H. Production of 2,3-butanediol from glucose and cassava hydrolysates by metabolically engineered industrial polyploid Saccharomyces cerevisiae. *Biotechnol. Biofuels* **2019**, *12*, 204. [CrossRef] [PubMed]
13. Li, L.; Li, K.; Wang, Y.; Chen, C.; Xu, Y.; Zhang, L.; Han, B.; Gao, C.; Tao, F.; Ma, C.; et al. Metabolic engineering of Enterobacter cloacae for high-yield production of enantiopure (2R,3R)-2,3-butanediol from lignocellulose-derived sugars. *Metab. Eng.* **2015**, *28*, 19–27. [CrossRef]
14. Cho, S.; Kim, T.; Woo, H.M.; Kim, Y.; Lee, J.; Um, Y. High production of 2,3-butanediol from biodiesel-derived crude glycerol by metabolically engineered Klebsiella oxytoca M1. *Biotechnol. Biofuels* **2015**, *8*, 146. [CrossRef]
15. Matsuyama, A.; Yamamoto, H.; Kawada, N.; Kobayashi, Y. Industrial production of (R)-1,3-butanediol by new biocatalysts. *J. Mol. Catal. B Enzym.* **2001**, *11*, 513–521. [CrossRef]
16. Kataoka, N.; Vangnai, A.S.; Tajima, T.; Nakashimada, Y.; Kato, J. Improvement of (R)-1,3-butanediol production by engineered Escherichia coli. *J. Biosci. Bioeng.* **2013**, *115*, 475–480. [CrossRef]
17. Islam, T.; Nguyen-Vo, T.P.; Gaur, V.K.; Lee, J.; Park, S. Metabolic engineering of Escherichia coli for biological production of 1, 3-Butanediol. *Bioresour. Technol.* **2023**, *376*, 128911. [CrossRef] [PubMed]
18. Onodera, K.; Nakaji, Y.; Yabushita, M.; Nakagawa, Y.; Tomishige, K. Selective synthesis of 1,3-butadiene by vapor-phase dehydration of 1,4-butanediol over cerium oxide catalyst. *Appl. Catal. A Gen.* **2023**, *663*, 119321. [CrossRef]
19. Yamamoto, N.; Sato, S.; Takahashi, R.; Inui, K. Synthesis of homoallyl alcohol from 1,4-butanediol over ZrO_2 catalyst. *Catal. Commun.* **2005**, *6*, 480–484. [CrossRef]
20. Duan, H.; Sun, D.; Yamada, Y.; Sato, S. Dehydration of 2,3-butanediol into 3-buten-2-ol catalyzed by ZrO_2. *Catal. Commun.* **2014**, *48*, 1–4. [CrossRef]
21. Sato, S.; Takahashi, R.; Sodesawa, T.; Honda, N. Dehydration of diols catalyzed by CeO_2. *J. Mol. Catal. A Chem.* **2004**, *221*, 177–183. [CrossRef]
22. Bekele, B.A.; Poissonnier, J.; Thybaut, J.W. The potential of ZrO_2 catalysts for the dehydration of 2,3-butanediol into 3-buten-2-ol: Impact of synthesis method and operating conditions. *J. Catal.* **2022**, *411*, 200–211. [CrossRef]
23. Gascoyne, J.L.; Bommareddy, R.R.; Heeb, S.; Malys, N. Engineering Cupriavidus necator H16 for the autotrophic production of (R)-1,3-butanediol. *Metab. Eng.* **2021**, *67*, 262–276. [CrossRef]
24. Rodriguez, A.C.; Sad, M.E.; Cruchade, H.; Pinard, L.; Padró, C.L. Study of catalyst deactivation during 1,3-butanediol dehydration to produce butadiene. *Microporous Mesoporous Mater.* **2021**, *320*, 111066. [CrossRef]

25. Lee, J.H.; Hong, S.B. Dehydration of 1,3-butanediol to butadiene over medium-pore zeolites: Another example of reaction intermediate shape selectivity. *Appl. Catal. B Environ.* **2021**, *280*, 119446. [CrossRef]
26. Fang, L.; Jing, F.; Lu, J.; Hu, B.; Pera-Titus, M. Nano-flowered Ce@MOR hybrids with modulated acid properties for the vapor-phase dehydration of 1,3-butanediol into butadiene. *Green Chem.* **2017**, *19*, 4610–4621. [CrossRef]
27. Jing, F.; Katryniok, B.; Paul, S.; Fang, L.; Liebens, A.; Shen, M.; Hu, B.; Dumeignil, F.; Pera-Titus, M. Al-doped SBA-15 Catalysts for Low-temperature Dehydration of 1,3-Butanediol into Butadiene. *ChemCatChem* **2017**, *9*, 258–262. [CrossRef]
28. Jing, F.; Katryniok, B.; Araque, M.; Wojcieszak, R.; Capron, M.; Paul, S.; Daturi, M.; Clacens, J.-M.; De Campo, F.; Liebens, A.; et al. Direct dehydration of 1,3-butanediol into butadiene over aluminosilicate catalysts. *Catal. Sci. Technol.* **2016**, *6*, 5830–5840. [CrossRef]
29. Ichikawa, N.; Sato, S.; Takahashi, R.; Sodesawa, T. Catalytic reaction of 1,3-butanediol over solid acids. *J. Mol. Catal. A Chem.* **2006**, *256*, 106–112. [CrossRef]
30. Rodriguez, A.C.; Sad, M.E.; Padró, C.L. Acid site requirement and reaction pathway for selective bio-butadiene synthesis by 1,3-butanediol dehydration. *Appl. Catal. A Gen.* **2023**, *664*, 119349. [CrossRef]
31. Kurniawan, E.; Yu, L.; Kobayashi, R.; Hara, T.; Yamada, Y.; Sato, S. Vapor-phase dehydration of 1, 3-butanediol to 1, 3-butadiene over WO_3/SiO_2 catalyst. *Appl. Catal. A Gen.* **2023**, *666*, 119408. [CrossRef]
32. Li, Y.; Kurniawan, E.; Sato, F.; Hara, T.; Yamada, Y.; Sato, S. Amorphous silica-alumina modified with silver as an efficient catalyst for vapor-phase dehydration of 1,3-butanediol to 1,3-butadiene. *Appl. Catal. A Gen.* **2024**, *669*, 119493. [CrossRef]
33. Matsumura, Y.; Matsuda, A.; Yamada, Y.; Sato, S. Selective Production of 1,3-Butadiene from 1,3-Butanediol over $Y_2Zr_2O_7$ Catalyst. *Bull. Chem. Soc. Jpn.* **2021**, *94*, 1651–1658. [CrossRef]
34. Zhai, M.; Wu, W.; Xing, E.; Zhang, Y.; Ding, H.; Zhou, J.; Luo, Y.; Liu, J.; Zhu, K.; Zhu, X. Generating TON zeolites with reduced [001] length through combined mechanochemical bead-milling and porogen-directed recrystallization with enhanced catalytic property in hydroisomerization. *Chem. Eng. J.* **2022**, *440*, 135874. [CrossRef]
35. Wang, Q.; Shan, H.; Sim, L.B.; Xie, J.; Ye, S.; Fu, J.; Wang, J.; Zhang, N.; Zheng, J.; Chen, B. ZSM-22 Synthesized Using Structure-Directing Agents of Different Alkyl Chain Lengths for Controlled n-Hexadecane Hydroisomerizations. *Ind. Eng. Chem. Res.* **2023**, *62*, 11470–11479. [CrossRef]
36. Jamil, A.K.; Muraza, O. Facile control of nanosized ZSM-22 crystals using dynamic crystallization technique. *Microporous Mesoporous Mater.* **2016**, *227*, 16–22. [CrossRef]
37. Hong, Z.; Deng, L.; Wang, F.; Zhu, F.; Fang, Y.; Song, L.; Li, L.; Zhu, Z. Intergrowth MFI Zeolite with Inverse Al Zoning and Predominant Sinusoidal Channels for Highly Selective Production of Styrene. *Inorg. Chem.* **2024**, *63*, 20888–20899. [CrossRef]
38. Xu, J.; Wang, Q.; Li, S.; Deng, F. (Eds.) Solid-State NMR Characterization of Framework Structure of Zeolites and Zeotype Materials. In *Solid-State NMR in Zeolite Catalysis*; Singapore Springer: Singapore, 2019; pp. 93–132.
39. Stepanov, A.G. Chapter 4—Basics of Solid-State NMR for Application in Zeolite Science: Material and Reaction Characterization. In *Zeolites and Zeolite-Like Materials*; Sels, B.F., Kustov, L.M., Eds.; Elsevier: Amsterdam, The Netherlands, 2016; pp. 137–188.
40. Qin, Z.; Lakiss, L.; Tosheva, L.; Gilson, J.; Vicente, A.; Fernandez, C.; Valtchev, V. Comparative Study of Nano-ZSM-5 Catalysts Synthesized in OH^- and F^- Media. *Adv. Funct. Mater.* **2014**, *24*, 257–264. [CrossRef]
41. Li, J.; Gao, M.; Yan, W.; Yu, J. Regulation of the Si/Al ratios and Al distributions of zeolites and their impact on properties. *Chem. Sci.* **2023**, *14*, 1935–1959. [CrossRef]
42. Thommes, M.; Kaneko, K.; Neimark, A.V.; Olivier, J.P.; Rodriguez-Reinoso, F.; Rouquerol, J.; Sing, K.S.W. Physisorption of gases, with special reference to the evaluation of surface area and pore size distribution (IUPAC Technical Report). *Pure Appl. Chem.* **2015**, *87*, 1051–1069. [CrossRef]
43. Dai, Q.; Bai, S.; Wang, X.; Lu, G. Facile synthesis of HZSM-5 with controlled crystal morphology and size as efficient catalysts for chlorinated hydrocarbons oxidation and xylene isomerization. *J. Porous Mater.* **2014**, *21*, 1041–1049. [CrossRef]
44. Chen, Z.; Liu, S.; Wang, H.; Ning, Q.; Zhang, H.; Yun, Y.; Ren, J.; Li, Y.-W. Synthesis and characterization of bundle-shaped ZSM-22 zeolite via the oriented fusion of nanorods and its enhanced isomerization performance. *J. Catal.* **2018**, *361*, 177–185. [CrossRef]
45. Ge, S.; Hu, Z.; Xie, H.; Gao, S.; Zhang, Z.; Wu, Z. Shape selection of alkane hydroisomerization over one-dimensional zeolite supported Pt catalyst: Pt/ZSM-48 versus Pt/ZSM-22. *Microporous Mesoporous Mater.* **2024**, *376*, 113179. [CrossRef]
46. Liu, S.; Ren, J.; Zhang, H.; Lv, E.; Yang, Y.; Li, Y.-W. Synthesis, characterization and isomerization performance of micro/mesoporous materials based on H-ZSM-22 zeolite. *J. Catal.* **2016**, *335*, 11–23. [CrossRef]
47. Dalena, F.; Dib, E.; Onida, B.; Ferrarelli, G.; Daturi, M.; Giordano, G.; Migliori, M.; Mintova, S. Evaluation of Zeolite Composites by IR and NMR Spectroscopy. *Molecules* **2024**, *29*, 4450. [CrossRef] [PubMed]
48. Treps, L.; Demaret, C.; Wisser, D.; Harbuzaru, B.; Méthivier, A.; Guillon, E.; Benedis, D.V.; Gomez, A.; de Bruin, T.; Rivallan, M.; et al. Spectroscopic Expression of the External Surface Sites of H-ZSM-5. *J. Phys. Chem. C* **2021**, *125*, 2163–2181. [CrossRef]

49. Gabrienko, A.A.; Danilova, I.G.; Arzumanov, S.S.; Pirutko, L.V.; Freude, D.; Stepanov, A.G. Direct Measurement of Zeolite Brønsted Acidity by FTIR Spectroscopy: Solid-State 1H MAS NMR Approach for Reliable Determination of the Integrated Molar Absorption Coefficients. *J. Phys. Chem. C* **2018**, *122*, 25386–25395. [CrossRef]
50. Holm, M.S.; Svelle, S.; Joensen, F.; Beato, P.; Christensen, C.H.; Bordiga, S.; Bjørgen, M. Assessing the acid properties of desilicated ZSM-5 by FTIR using CO and 2,4,6-trimethylpyridine (collidine) as molecular probes. *Appl. Catal. A Gen.* **2009**, *356*, 23–30. [CrossRef]
51. Hoffmann, P.; Lobo, J.A. Identification of diverse silanols on protonated ZSM-5 zeolites by means of FTIR spectroscopy. *Microporous Mesoporous Mater.* **2007**, *106*, 122–128. [CrossRef]
52. Bevilacqua, M.; Montanari, T.; Finocchio, E.; Busca, G. Are the active sites of protonic zeolites generated by the cavities? *Catal. Today* **2006**, *116*, 132–142. [CrossRef]
53. Losch, P.; Boltz, M.; Bernardon, C.; Louis, B.; Palčić, A.; Valtchev, V. Impact of external surface passivation of nano-ZSM-5 zeolites in the methanol-to-olefins reaction. *Appl. Catal. A Gen.* **2016**, *509*, 30–37. [CrossRef]
54. Zholobenko, V.; Freitas, C.; Jendrlin, M.; Bazin, P.; Travert, A.; Thibault-Starzyk, F. Probing the acid sites of zeolites with pyridine: Quantitative AGIR measurements of the molar absorption coefficients. *J. Catal.* **2020**, *385*, 52–60. [CrossRef]
55. Trombettaa, M.; Buscaa, G.; Rossinib, S.; Piccolib, V.; Cornarob, U. FT-IR Studies on Light Olefin Skeletal Isomerization Catalysis: II. The Interaction of C4 Olefins and Alcohols with HZSM5 Zeolite. *J. Catal.* **1997**, *168*, 349–363. [CrossRef]
56. Kumar, D.; Sauer, J.; Airi, A.; Bordiga, S.; Galimberti, D.R. Assignment of IR spectra of ethanol at Brønsted sites of H-ZSM-5 to monomer adsorption using a Fermi resonance model. *Phys. Chem. Chem. Phys.* **2025**, *27*, 550–563. [CrossRef]
57. Di Iorio, J.R.; Johnson, B.A.; Román-Leshkov, Y. Ordered Hydrogen-Bonded Alcohol Networks Confined in Lewis Acid Zeolites Accelerate Transfer Hydrogenation Turnover Rates. *J. Am. Chem. Soc.* **2020**, *142*, 19379–19392. [CrossRef] [PubMed]
58. Yu, L.; Kurniawan, E.; Ozawa, T.; Kobayashi, H.; Yamada, Y.; Sato, S. Catalytic dehydration of crotyl alcohol into 1,3-butadiene over silica-supported metal oxides: Mechanistic features. *Mol. Catal.* **2023**, *537*, 112939. [CrossRef]
59. Lakiss, L.; Ngoye, F.; Canaff, C.; Laforge, S.; Pouilloux, Y.; Qin, Z.; Tarighi, M.; Thomas, K.; Valtchev, V.; Vicente, A.; et al. On the remarkable resistance to coke formation of nanometer-sized and hierarchical MFI zeolites during ethanol to hydrocarbons transformation. *J. Catal.* **2015**, *328*, 165–172. [CrossRef]
60. Barbera, K.; Bonino, F.; Bordiga, S.; Janssens, T.V.; Beato, P. Structure–deactivation relationship for ZSM-5 catalysts governed by framework defects. *J. Catal.* **2011**, *280*, 196–205. [CrossRef]
61. Thibault-Starzyk, F.; Vimont, A.; Gilson, J.-P. 2D-COS IR study of coking in xylene isomerisation on H-MFI zeolite. *Catal. Today* **2001**, *70*, 227–241. [CrossRef]
62. Travert, A.; Vimont, A.; Sahibed-Dine, A.; Daturi, M.; Lavalley, J.-C. Use of pyridine CH(D) vibrations for the study of Lewis acidity of metal oxides. *Appl. Catal. A Gen.* **2006**, *307*, 98–107. [CrossRef]
63. Mears, D.E. Tests for Transport Limitations in Experimental Catalytic Reactors. *Ind. Eng. Chem. Process Des. Dev.* **1971**, *10*, 541–547. [CrossRef]
64. Berger, R.J.; Stitt, E.H.; Marin, G.B.; Kapteijn, F.; Moulijn, J.A. Eurokin. Chemical Reaction Kinetics in Practice. *CATTECH* **2001**, *5*, 36–60. [CrossRef]

catalysts

MDPI

Article

Regulation of Ag_1Cu_x/SBA-15 Catalyst for Efficient CO Catalytic Degradation at Room Temperature

Fukun Bi [1,2], Haotian Hu [1], Ye Zheng [1], Yanxuan Wang [1], Yuxin Wang [3], Baolin Liu [2], Han Dong [1] and Xiaodong Zhang [1,4,*]

[1] School of Environment and Architecture, University of Shanghai for Science and Technology, Shanghai 200093, China; bifukun@usst.edu.cn (F.B.); huhaotian0109@126.com (H.H.); yezizheng4949@outlook.com (Y.Z.); wangyanxuan@163.com (Y.W.); donghandh7@163.com (H.D.)
[2] School of Health Science and Engineering, University of Shanghai for Science and Technology, Shanghai 200093, China; blliuk@163.com
[3] Institute of Chemical Pharmaceutical, Taizhou Vocation & Technical College, Taizhou 318000, China; wyx790914@aliyun.com
[4] Shanghai Non-Carbon Energy Conversion and Utilization Institute, Shanghai 200240, China
* Correspondence: fatzhxd@126.com; Tel.: +86-159-2126-7160

Abstract

The regulation of the active sites of a catalyst is important for its application. Herein, a series of Ag_1Cu_x/SBA-15 catalysts with different molar ratios of Ag to Cu were synthesized via the impregnation method, and the active sites of Ag_1Cu_x were regulated via various pretreatment conditions. These as-prepared Ag_1Cu_x/SBA-15 catalysts were characterized by many technologies, and their catalytic performance was estimated through CO catalytic oxidation. Among these catalysts, $Ag_1Cu_{0.025}$/SBA-15, with a Ag/Cu molar ratio of 1:0.025 and pretreated under the condition of 500 °C O_2/Ar for 2 h, followed by 300 °C H_2 for another 2 h, presented optimal CO degradation performance, which could realize the oxidation of 98% CO at 34 °C (T_{98} = 34 °C). Meanwhile, $Ag_1Cu_{0.025}$/SBA-15 also displayed great reusability. Characterization results, such as X-ray diffraction (XRD), ultraviolet–visible diffuse reflectance spectra (UV-vis DRS), temperature-programmed H_2 reduction (H_2-TPR), and physical adsorption, suggested that the optimal catalytic performance of $Ag_1Cu_{0.025}$/SBA-15 was ascribed to its high interspersion of Ag nanoparticles, better low-temperature reduction ability, the interaction between Ag and Cu, and its high surface area and large pore volume. This study provides guidance for the regulation of active sites for low-temperature catalytic degradation.

Keywords: catalytic degradation; CO oxidation; Ag_1Cu_x/SBA-15; room-temperature catalysis

1. Introduction

With the rapid development of modern industry and transportation and the sharp increase in energy consumption, the problems of energy shortage and environmental pollution are becoming increasingly serious [1,2]. The incomplete combustion of fossil fuels results in numerous carbon monoxide (CO) emissions into the environment, which brings serious detriment to the environment and human health. Furthermore, because the affinity of CO for hemoglobin in the human body is 200–300 times higher than that of O_2 for hemoglobin, CO easily binds to hemoglobin to form carboxyhemoglobin, causing hemoglobin to lose its ability to bind with oxygen. This leads to the fact that at a relatively low concentration of CO (<300 ppm), CO can be poisonous to the human body [3,4].

Therefore, the removal of CO is very necessary. Generally, the methods used for the elimination of CO are adsorption [5,6], catalytic reduction [7,8], and catalytic oxidation [9–12]. Among these methods, catalytic oxidation, with the advantage of simple operation and no secondary pollution, has been widely applied in the removal of gaseous pollution, such as volatile organic compounds (VOCs) [13–18], nitrogen oxide (NO_x) [19–22], sulfur dioxide (SO_2) [23,24], CO [11,25,26], etc. The core component of catalytic oxidation is the catalyst. Thus, the development of high-efficiency catalysts is important for CO oxidation at low temperatures.

The catalysts used for catalytic oxidation could be divided into metal oxide and supported noble metal (SNM) catalysts. Therein, SNM catalysts presented excellent catalytic performance due to the high activity of the noble metal nanoparticles [2]. Among the numerous noble metals, Ag has attracted extensive attention and is applied for catalytic oxidation due to its high catalytic performance and relatively low price. For example, our previous work [27] found that the CeO_2-supported Ag catalysts presented great catalytic performance for toluene oxidation. Biabani-Ravandi et al. [28] reported that the introduction of Ag nanoparticles greatly enhanced CO oxidation over Fe_2O_3 catalysts. However, because of their high surface energy, Ag nanoparticles often aggregate during synthesis or catalytic reactions [29]. The aggregation of Ag nanoparticles induces a decrease in catalytic performance, or even deactivation. Therefore, the choice of carrier materials is essential for highly efficient Ag catalyst design.

Because of their large pore volume and surface area, porous solid materials, such as molecular sieves (MCM-41, ZSM-5, and SBA-15), metal–organic frameworks (MOFs), etc., have been widely employed as adsorbents and catalyst supports [30,31]. Among them, a mesoporous molecular sieve, SBA-15, with its advantages of high pore volume and surface area and great thermal stability, has been widely used as a support for noble metals. Meanwhile, its high porosity could provide anchor sites for the noble metal to improve its dispersion. For example, Qin et al. [32] prepared an Ag/SBA-15 catalyst with highly dispersed Ag nanoparticles by using the mesopore structure for the anchor sites, which presented great catalytic performance for toluene oxidation. Additionally, our previous work [33] also found that Ag nanoparticles could enter the pore channel of SBA-15 and form highly dispersed small Ag nanoparticles, enhancing CO oxidation. Recently, it has been reported that the introduction of promoters, such as alkali metals and transition metals, could promote noble metal dispersion and boost the metal–carrier interaction. For instance, Lee et al. [34] recorded that the introduction of Cu in Al_2O_3-supported Pt catalysts heightened Pt dispersion, which boosted propane dehydrogenation to produce propylene. Wang et al. [35] found that the addition of Na in SiO_2-supported Pt catalysts improved the electronic interaction between the Pt and SiO_2 supports, inducing the complete degradation of HCHO at the environmental temperature on the Pt-Na/SiO_2 catalyst. Therefore, the catalytic activity of the SNM catalysts could be improved via the addition of a promoter. Additionally, for Ag catalysts, the pretreatment conditions could also influence the dispersion of Ag nanoparticles and active species, adjusting the catalytic activity.

In this work, the mesopore SBA-15 was selected as the support to prepare a series of supported AgCu catalysts with different Ag/Cu molar ratios via the conventional wet-impregnation method. The catalytic activity of the as-synthesized catalysts was studied by CO oxidation. Meanwhile, the active sites were optimized and regulated via different pretreatment conditions. The results showed that the $Ag_1Cu_{0.025}$/S-O-H with the Ag/Cu molar ratio of 1:0.025, pretreated under O_2 atmosphere at 500 °C, followed by the 300 °C H_2 pretreatment, presented the optimal CO oxidation activity, which realized CO oxidation at room temperature. Characterization results suggested that the high surface area, large

pore volume, high dispersion of Ag nanoparticles, low-temperature reducibility, and the strong interaction between Ag and Cu induced its better catalytic performance. This work revealed the influence of pretreatment conditions on the active sites, which could guide the design of high-efficiency-supported catalysts for gaseous pollution elimination.

2. Results and Discussion

2.1. Influence of Ag/Cu Molar Ratio and Pretreated Condition on Catalytic Activity for CO Oxidation

A mesoporous molecular sieve, SBA-15, supported AgCu catalysts (Ag_1Cu_x/SBA-15, x = 0, 0.0125, 0.025, 0.05, 0.25, 0.5, and 1) with Ag/Cu molar ratios of 1:0, 1:0.0125, 1:0.025, 1:0.05, 1:0.25, 1:0.5, and 1:1, and was prepared by the conventional impregnation method, followed by pretreatment under 30.0 vol.% O_2/Ar at 500 °C for 2 h. The synthesized catalysts were named Ag_1Cu_x/SBA-15-O and were abbreviated as Ag_1Cu_x/S-O. Then, the as-prepared Ag_1Cu_x/S-O catalysts were further activated under H_2 atmosphere at 300 °C for another 2 h to obtain Ag_1Cu_x/S-O-H. The actual Ag and Cu loadings were determined using an inductively coupled plasma optical emission spectrometer (ICP-OES), and the results are summarized in Table 1. In all of the as-prepared catalysts, the actual metal loadings were slightly lower than the theoretical loadings.

Table 1. The actual metal loadings of the as-prepared Ag_1Cu_x/SBA-15 pretreated under different conditions.

Ag_1Cu_x/SBA-15 Catalysts	Metal Loading (wt%)			
	Pretreated Under 30.0 vol.% O_2/Ar Atmosphere at 500 °C for 2 h		Pretreated Under 30.0 vol.% O_2/Ar Atmosphere at 500 °C for 2 h and H_2 Atmosphere at 300 °C for 2 h	
	Ag	Cu	Ag	Cu
Ag_1Cu_0/SBA-15	3.95	/	3.93	/
$Ag_1Cu_{0.0125}$/SBA-15	3.94	0.026	3.94	0.024
$Ag_1Cu_{0.025}$/SBA-15	3.90	0.054	3.92	0.052
$Ag_1Cu_{0.05}$/SBA-15	3.88	0.112	3.87	0.115
$Ag_1Cu_{0.25}$/SBA-15	3.85	0.536	3.85	0.532
$Ag_1Cu_{0.5}$/SBA-15	3.82	1.108	3.83	1.110
Ag_1Cu_1/SBA-15	3.80	2.321	3.81	2.324

2.1.1. Characterizations of Ag_1Cu_x/S-O and Ag_1Cu_x/S-O-H Catalysts

To investigate the phase composition of the catalysts, the crystalline structure of SBA-15 and its supported AgCu catalysts was determined via X-ray diffraction (XRD). Because the characteristic diffraction peaks of SBA-15 are located in the $2\theta < 5°$, the narrow-angle XRD patterns of SBA-15 and the supported AgCu catalysts were determined. As shown in Figure 1a, SBA-15 displayed three diffraction peaks at 2θ = 0.89°, 1.51°, and 1.72°, indexed to the (100), (110), and (200) crystal facets, respectively, which corresponded to the 2D hexagonal symmetry of SBA-15 [36]. The result suggested the successful synthesis of the SBA-15 supports [37]. After the introduction of AgCu in the SBA-15 support ($Ag_1Cu_{0.025}$/S-O and $Ag_1Cu_{0.25}$/S-O), the narrow-angle XRD patterns of $Ag_1Cu_{0.025}$/S-O and $Ag_1Cu_{0.25}$/S-O presented a similar XRD peak shapes to that of the SBA-15 support, which suggested the retention of the long-range ordering of the microchannels in the supported AgCu catalysts after the loading of AgCu [38]. However, compared with SBA-15, the diffraction peaks in $Ag_1Cu_{0.025}$/S-O and $Ag_1Cu_{0.25}$/S-O were weakened, which might be attributed to the incorporation of the AgCu metal in the SBA-15 pore channel [38]. Furthermore, the introduction of AgCu species induced the shift of 2θ towards the lower angle, which suggested the changes in the strain, resulting in the increase in structure parameters in the mesoporous sieves [39].

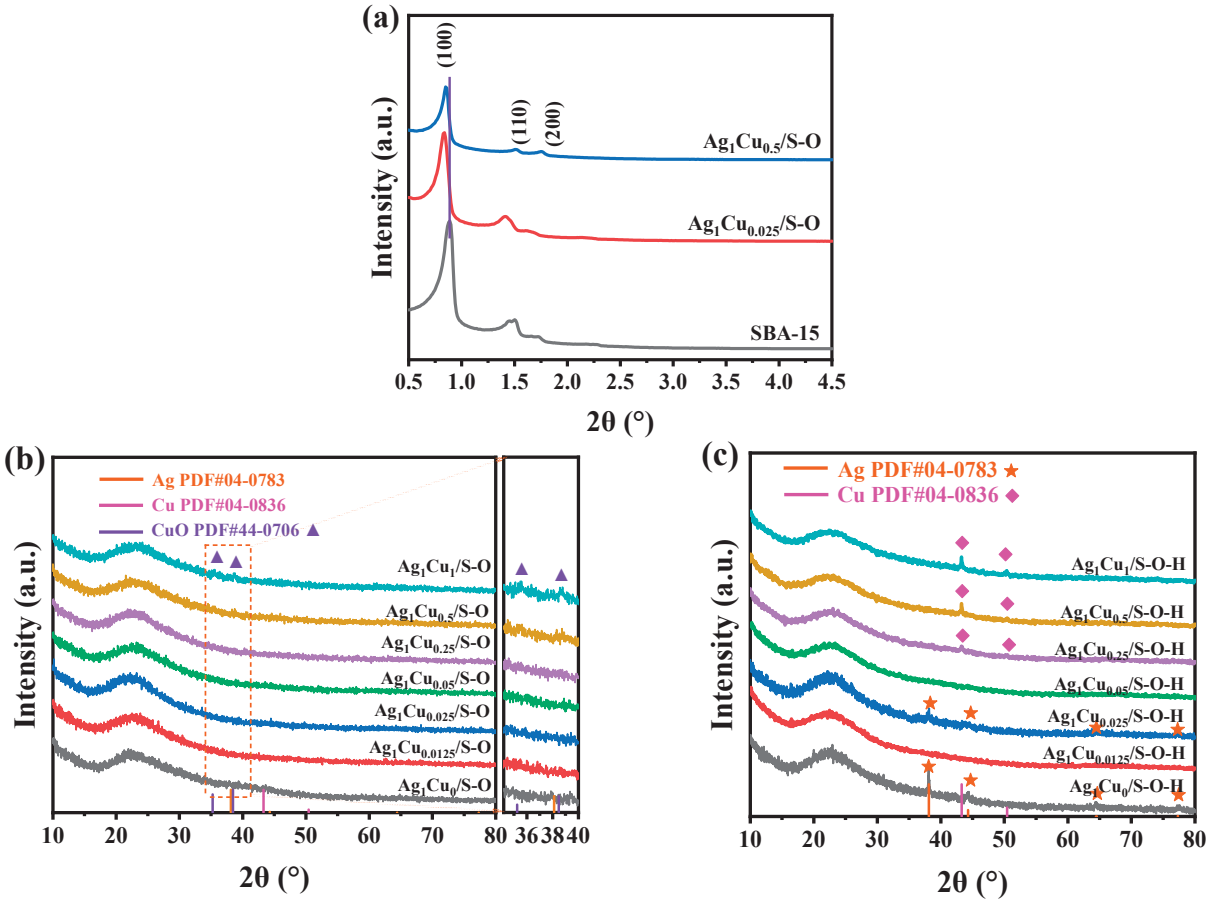

Figure 1. Narrow-angle XRD patterns (**a**) of SBA-15, $Ag_1Cu_{0.025}$/S-O and $Ag_1Cu_{0.5}$/S-O; wide-angle XRD patterns of the Ag_1Cu_x/SBA-15 catalysts with different Ag/Cu molar ratios pretreated under different conditions: (**b**) 30.0 vol.% O_2/Ar atmosphere at 500 °C for 2 h and (**c**) 30.0 vol.% O_2/Ar atmosphere at 500 °C for 2 h followed by H_2 atmosphere at 300 °C for 2 h.

Further, to investigate the dispersion of Ag and Cu species in the catalysts, the wide-angle XRD patterns in the 2θ range of 10–80° were detected on the Ag_1Cu_x/SBA-15 catalysts pretreated under different atmospheres. Figure 1b displays the wide-angle XRD patterns of Ag_1Cu_x/SBA-15 treated under a 30.0 vol.% O_2/Ar atmosphere at 500 °C. As illustrated in Figure 1b, no diffraction peaks about the Ag or Ag_2O were observed in Ag_1Cu_x/S-O, which should be ascribed to the high dispersion of the Ag species or its low loadings [40]. After the introduction of Cu, the XRD peaks of Cu or CuO were also not found in the samples of Ag/Cu molar ratios lower than 1:0.25. With the increase in Cu to the Ag/Cu molar ratio of 1:0.5 and 1:1, two weak small diffraction peaks at 35.2° and 48.5°, corresponding to CuO (PDF#44-0706), were found, which also indicated the high interspersion of the Cu in the SBA-15 support. Figure 1c displays the wide-angle XRD patterns of Ag_1Cu_x/S-O-H, which were the Ag_1Cu_x/S-O catalysts treated under H_2 atmosphere at 300 °C. As shown in Figure 1c, after the treatment of H_2 at 300 °C, the XRD peaks corresponding to the CuO species disappeared. Meanwhile, some new XRD peaks were observed. The XRD peaks at 2θ = 38.1°, 44.3°, 64.4°, and 77.3° were the (111), (200), (220), and (311) crystal phases of Ag nanoparticle (PDF#04-0783), respectively. The peaks at the 2θ of 43.3° and 50.4° were assigned to the (111) and (200) lattice planes of Cu (PDF#04-0836), respectively. The presence of Ag and Cu species suggested that the high valence state of Ag^+ and Cu^{2+} species was reduced via H_2 treatment. Compared with Ag_1Cu_0/S-O-H, the introduction of Cu induced the weakening of Ag diffraction peaks, and the further increase in Cu content resulted in the disappearance of Ag diffraction peaks, which suggested that the

introduction of Cu species could improve the dispersion of Ag species. Meanwhile, with Cu content increased, the intensity of XRD peaks of Cu enhanced gradually, which suggested the enhancement of the Cu particle size.

Due to the limitation of XRD for the detection of low-content species and the sensitivity of solid ultraviolet–visible diffuse reflectance (UV-vis DRS) spectra to Ag and Cu species, UV-vis DRS spectra were measured as a complementary method to recognize the Ag and Cu species in the Ag_1Cu_x/S-O and Ag_1Cu_x/S-O-H catalysts. Figure 2a presents the UV-vis DRS spectra of Ag_1Cu_x/S-O. As depicted in Figure 2a, four adsorption peaks appeared at 220, 275, 414, and 600–800 nm. The ultraviolet adsorption peak at 220 nm was assigned to the $4d^{10}$–$4d^9 5s^1$ electron transfer of hydrated silver ions [41,42]. The peak at 275 nm was attributed to the Ag cluster characteristic absorbance bands [27]. The wide adsorption peak centered at ~414 nm was due to the plasma resonance in the surface of metallic Ag nanoparticles [43]. The absorbance band between 600 nm and 800 nm was assigned to the d-d orbital electron transition of the highly dispersed Cu^{2+} species [44]. All the Ag_1Cu_x/S-O catalysts presented the adsorption peaks at 220 and 275 nm, indicating that the Ag species in Ag_1Cu_x/S-O were hydrated silver ions and a small Ag cluster. With the increase in Cu molar ratio in Ag_1Cu_x/S-O, the peak intensity of surface plasma resonance of metallic Ag nanoparticles decreased and disappeared. Meanwhile, the absorbance band between 600 nm and 800 nm was enhanced. This result suggested that Cu could affect the formation of Ag nanoparticles and improve their dispersion. As presented in Figure 2b, after the treatment of H_2, the adsorption band between 600 and 800 nm, which is ascribed to the d-d orbital electron transition of Cu^{2+} species, disappeared in Ag_1Cu_x/S-O-H. Meanwhile, the $4d^{10}$–$4d^9 5s^1$ electronic transition of Ag^+ also vanished. The results suggested the successful reduction of high-valence-state Cu and Ag species to the metallic state, which was consistent with the XRD results (Figure 1). Additionally, two obvious adsorption bands appeared at ~375 and ~420 nm, which were assigned to the Ag nanoparticles found in all Ag_1Cu_x/S-O-H catalysts. This further confirmed the successful reduction of Ag species. However, the absorbance band at ~230 nm, corresponding to the charge transfer between the ligand O^{2-} and the Cu^{2+} in CuO, was only observed in Ag_1Cu_1/S-O-H, which might be attributed to its high Cu content. Meanwhile, the adsorption peak at ~538 nm was ascribed to the Cu_2O species. Notably, with the increase in Cu molar ratio in Ag_1Cu_x/S-O-H, the intensity of the adsorption peaks centered at ~375 and ~420 nm was gradually reduced, which also suggested the enhancement of Ag nanoparticle dispersion caused by the addition of Cu species. Furthermore, compared with Ag_1Cu_0/S-O-H, the addition of Cu in Ag_1Cu_x/S-O-H catalysts induced the redshift; namely, the band shifted to a higher wavelength, to that of Ag nanoparticles (375 nm and 420 nm), which was ascribed to the interaction between Ag and Cu [45]. Therefore, it could be deduced that the O_2 treatment followed by H_2 treatment induced the formation of Ag-Cu interactions.

The redox properties of the as-prepared Ag_1Cu_x/SBA-15 catalysts pretreated under different conditions were studied by temperature-programmed H_2 reduction (H_2-TPR). For the Ag_1Cu_0/S-O catalyst (Figure 3a), three reduction peaks were found at 115, 333, and 456 °C, which were assigned to the reduction in surface adsorption oxygen species, Ag_2O clusters presented in the outside SBA-15 pores, and small-sized Ag_2O clusters in the SBA-15 channels, respectively [46,47]. However, after the introduction of Cu in the catalysts, the reduction peak of surface adsorption oxygen disappeared. Meanwhile, with the improvement in the Cu molar ratio, reduction peaks for CuO species appeared. The reduction peak centered below 200 °C was attributed to the reduction of Cu^{2+} to Cu^+ [45]. The reduction of Cu^+ to Cu^0 was observed at a higher temperature, at 200–300 °C [48,49]. Notably, as the Cu content increased, some of the Ag_2O species reduction peaks shifted to a higher temperature, which indicated that the recommendation of Cu species might weaken the reduction

of Ag_2O species. Figure 3b depicts the H_2-TPR profiles of Ag_1Cu_x/S-O-H catalysts. As shown in Figure 3b, similar to the Ag_1Cu_0/S-O catalyst, there were also three reduction peaks centered at 119, 334, and 451 °C, corresponding to surface adsorption oxygen species reduction. The Ag_2O in the surface of the SBA-15 support and the small Ag_2O cluster in the pore channel of SBA-15, respectively, were found in Ag_1Cu_0/S-O. After Cu species introduction, new peaks located below 200 °C were observed, which were ascribed to the reduction of Cu_2O or CuO species in the catalysts. Furthermore, as the Cu molar ratio improved, the reduction peaks below 200 °C were enhanced gradually. However, the reduction peaks of Ag^+ species were shifted to higher temperatures. Notably, new weak reduction peaks at 230 and 258 °C, which were assigned to the Ag-Cu interaction, could be found in $Ag_1Cu_{0.0125}$/S-O-H and $Ag_1Cu_{0.025}$/S-O-H, respectively, which suggested the presence of strong Ag-Cu interaction in and $Ag_1Cu_{0.025}$/S-O-H. This was in accord with the result of UV-vis DRS spectra. Additionally, the weakness of these Ag-Cu interaction reduction peaks was ascribed to the ultra-low Cu in $Ag_1Cu_{0.0125}$/S-O-H (0.026 wt%) and $Ag_1Cu_{0.025}$/S-O-H (0.054 wt%). Meanwhile, the low-temperature reducibility could also be found in $Ag_1Cu_{0.025}$/S-O-H. Therefore, the $Ag_1Cu_{0.025}$/S-O-H catalyst with the strong Ag-Cu interaction presented better low-temperature reducibility.

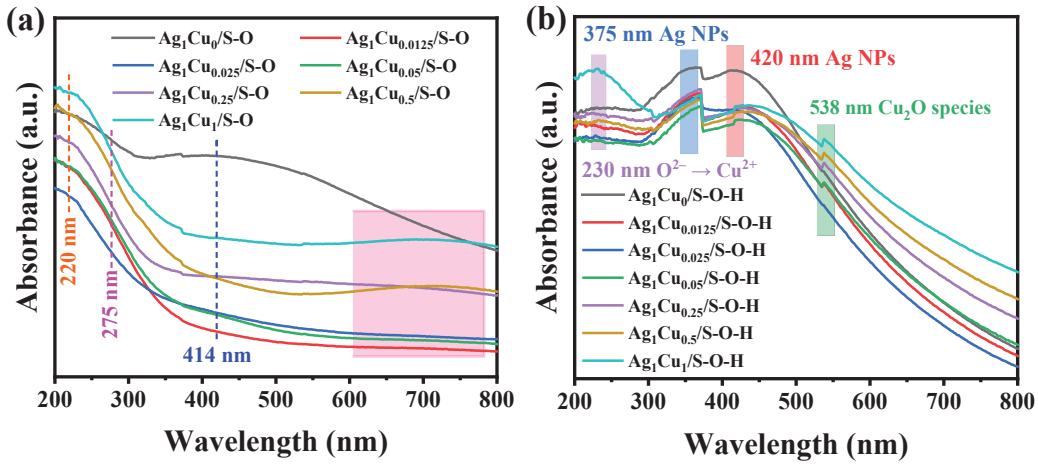

Figure 2. UV-vis DRS spectra of the Ag_1Cu_x/SBA-15 catalysts with different Ag/Cu molar ratios pretreated under different conditions: (**a**) 30.0 vol.% O_2/Ar atmosphere at 500 °C for 2 h and (**b**) 30.0 vol.% O_2/Ar atmosphere at 500 °C for 2 h followed by H_2 atmosphere at 300 °C for 2 h.

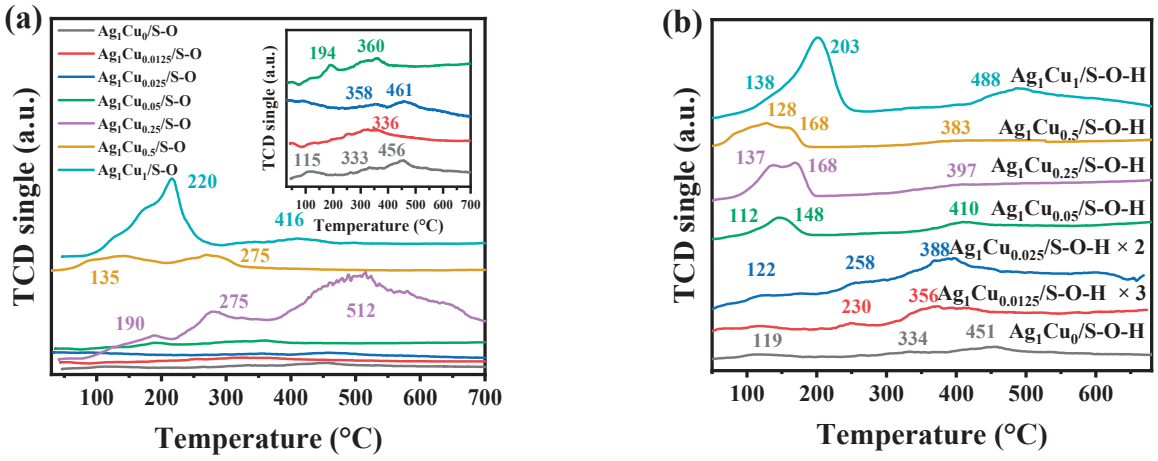

Figure 3. H_2-TPR profiles of the Ag_1Cu_x/SBA-15 catalysts with different Ag/Cu molar ratios pretreated under different conditions: (**a**) 30.0 vol.% O_2/Ar atmosphere at 500 °C for 2 h and (**b**) 30.0 vol.% O_2/Ar atmosphere at 500 °C for 2 h followed by H_2 atmosphere at 300 °C for 2 h.

2.1.2. Catalytic Performance of Ag_1Cu_x/S-O and Ag_1Cu_x/S-O-H for CO Oxidation

The catalytic activity of the as-prepared Ag_1Cu_x/S-O and Ag_1Cu_x/S-O-H catalysts was evaluated by using CO as the probe molecule, and the catalytic performance was depicted in Figure 4. Meanwhile, the temperatures of CO conversion at 50% and 98% (T_{50} and T_{98}) were selected to estimate the catalyst's performance, and the corresponding values are summarized in Table 2. Figure 4a depicts the temperature-dependent CO conversions over the Ag_1Cu_x/S-O catalysts for CO oxidation in the range of 30–160 °C, and the corresponding T_{50} and T_{98} values are itemized in Table 2. As presented in Figure 4a and Table 2, Ag_1Cu_0/S-O could completely oxidize CO at 70 °C with T_{50} and T_{98} values of 37 and 65 °C. After the addition of Cu species, the catalytic performance for CO degradation decreased. Meanwhile, as the increase in Cu molar ratio increased, the catalytic performance decreased gradually. The T_{98} values for $Ag_1Cu_{0.0125}$/S-O, $Ag_1Cu_{0.025}$/S-O, $Ag_1Cu_{0.05}$/S-O, $Ag_1Cu_{0.25}$/S-O, $Ag_1Cu_{0.5}$/S-O, and Ag_1Cu_1/S-O were 79, 80, 90, 110, 128, and 149 °C, respectively. It had been reported that the Ag species mainly contributed to the catalytic oxidation of CO [50]. Jabłońska et al. [51] also found that the introduction of Cu species in the Ag/Al_2O_3 catalysts could cause a decrease in catalytic performance for NH_3 oxidation, which was ascribed to the generation of CuO*x* species on the catalyst surface. Herein, the decrease in catalytic performance for CO oxidation could also be found in the Ag_1Cu_x/S-O catalysts after the addition of Cu species, which could also be ascribed to the formation of CuO*x* species (Figures 1b, 2a and 3a), preventing the accessibility of CO and the Ag species, resulting in the decrease in catalytic activity. Additionally, to further confirm this point, the Ag_0Cu_1/S-O, namely the SBA-15-supported Cu catalyst pretreated under a 30.0 vol.% O_2/Ar atmosphere, was also prepared for CO oxidation. As depicted in Figure 4a, Ag_0Cu_1/S-O presented poor CO catalytic performance with a T_{98} value of 295 °C. This result also demonstrated that the production of CuO*x* species on the catalyst surface would suppress CO oxidation over the Ag_1Cu_x/S-O catalysts.

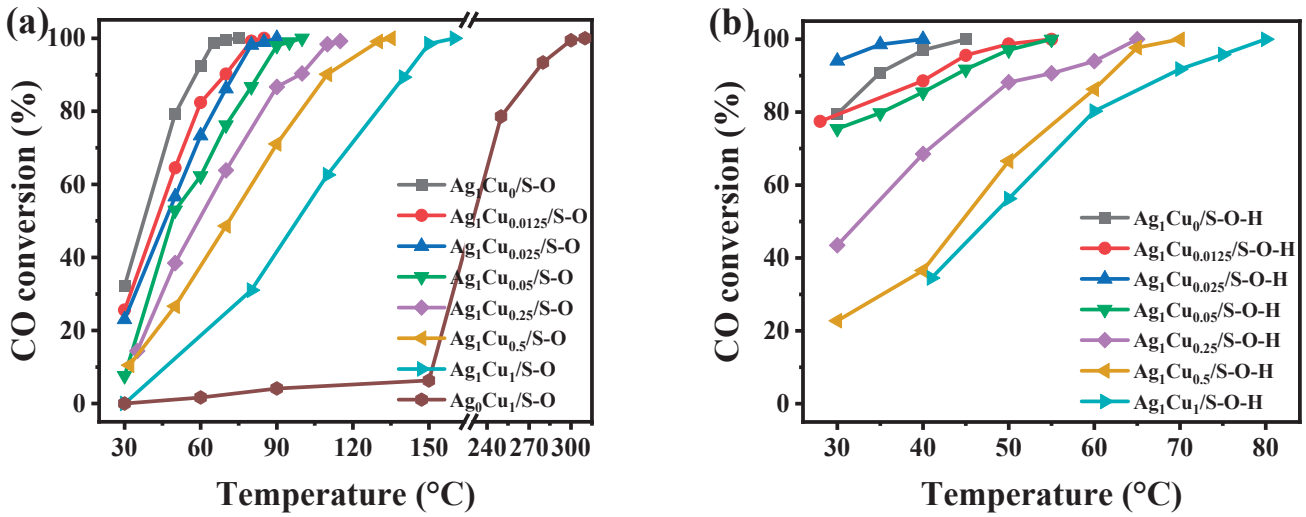

Figure 4. CO conversions of the as-prepared Ag_1Cu_x/SBA-15 catalysts with different Ag/Cu molar ratios pretreated under different conditions for CO oxidation: (**a**) 30.0 vol.% O_2/Ar atmosphere at 500 °C for 2 h and (**b**) 30.0 vol.% O_2/Ar atmosphere at 500 °C for 2 h followed by H_2 atmosphere at 300 °C for 2 h.

Table 2. Catalytic performance of Ag_1Cu_x/SBA-15 catalysts with different Ag/Cu molar ratios, pretreated under different conditions for CO oxidation.

Ag_1Cu_x/SBA-15 Catalysts	Catalytic Performance CO Oxidation (°C)			
	Pretreated Under 30.0 vol.% O_2/Ar Atmosphere at 500 °C for 2 h		Pretreated Under 30.0 vol.% O_2/Ar Atmosphere at 500 °C for 2 h and H_2 Atmosphere at 300 °C for 2 h	
	T_{50}	T_{98}	T_{50}	T_{98}
Ag_1Cu_0/SBA-15	37	65	<30	41
$Ag_1Cu_{0.0125}$/SBA-15	42	79	<30	48
$Ag_1Cu_{0.025}$/SBA-15	45	80	<30	34
$Ag_1Cu_{0.05}$/SBA-15	48	90	<30	51
$Ag_1Cu_{0.25}$/SBA-15	59	110	32	63
$Ag_1Cu_{0.5}$/SBA-15	71	128	44	66
Ag_1Cu_1/SBA-15	98	149	47	77
Ag_0Cu_1/SBA-15	210	295	-	-

To investigate the effect of pretreatment conditions on the catalytic activity of Ag_1Cu_x/SBA-15 for CO oxidation, Ag_1Cu_x/SBA-15 catalysts were further treated under a H_2 atmosphere at 300 °C for 2 h. Because of the inferior catalytic activity of Ag_0Cu_1/S-O, Ag_0Cu_1/S-O was not considered in the following test. Figure 4b illustrates the CO conversion over Ag_1Cu_x/S-O-H catalysts at different temperatures. Compared with these unreduced Ag_1Cu_x/S-O catalysts, the further treatment under H_2 atmosphere at 300 °C led to greatly improved catalytic activity for CO oxidation. As illustrated in Figure 4b and Table 2, with the addition of Cu, the molar ratio increased, and the catalytic activity for CO oxidation was enhanced first and then weakened. Among these Ag_1Cu_x/S-O-H catalysts, $Ag_1Cu_{0.025}$/S-O-H displayed the optimal CO degradation performance with the lowest T_{98} value of 34 °C, followed by Ag_1Cu_0/S-O-H (41 °C), $Ag_1Cu_{0.0125}$/S-O-H (48 °C), $Ag_1Cu_{0.05}$/S-O-H (51 °C), $Ag_1Cu_{0.25}$/S-O-H (63 °C), $Ag_1Cu_{0.5}$/S-O-H (66 °C), and Ag_1Cu_1/S-O-H (77 °C). Combined with the characterization results, it could be deduced that the H_2 reduction could result in the formation of highly active Ag_0 species (Figure 1c), which caused the improvement in the catalytic performance of Ag_1Cu_x/S-O-H in comparison to Ag_1Cu_x/S-O. Additionally, compared with Ag_1Cu_0/S-O-H (T_{98} = 41 °C), the better catalytic performance of $Ag_1Cu_{0.025}$/S-O-H (T_{98} = 34 °C) might be attributed to the strong interaction between Ag and Cu species.

2.2. Influence of H_2 Treatment Temperature on the Catalytic Activity of CO Oxidation

As mentioned above, the H_2 reduction treatment greatly enhanced the catalytic activity of Ag_1Cu_x/S-O for CO degradation. Meanwhile, Ag_1Cu_0/S-O-H (T_{98} = 41 °C) and $Ag_1Cu_{0.025}$/S-O-H (T_{98} = 34 °C) presented better CO degradation activity. Thus, Ag_1Cu_0/S-O and $Ag_1Cu_{0.025}$/S-O were selected to further investigate the influence of H_2 reduction temperatures on CO degradation performance. Ag_1Cu_0/S-O and $Ag_1Cu_{0.025}$/S-O were treated under 100, 200, 300, and 400 °C to obtain Ag_1Cu_0/S-O-yH (y = 100, 200, 300 and 400 °C, represented H_2 reduction temperature) and $Ag_1Cu_{0.025}$/S-O-yH. Among these reduced catalysts, Ag_1Cu_0/S-O-300H and $Ag_1Cu_{0.025}$/S-O-300H were further abbreviated as Ag_1Cu_0/S-O-H and $Ag_1Cu_{0.025}$/S-O-H, respectively.

2.2.1. Characterization of the Ag_1Cu_0/S-O-yH and $Ag_1Cu_{0.025}$/S-O-yH Catalysts

The crystal structure of Ag_1Cu_0/S-O-yH and $Ag_1Cu_{0.025}$/S-O-yH catalysts was studied via XRD. Figure 5a displays the XRD patterns of Ag_1Cu_0/S-O pretreated under an H_2 atmosphere at different temperatures. Compared with Ag_1Cu_0/S-O, as the reduction temperature increased, and the new diffraction peaks, corresponding to Ag species, appeared and were enhanced, which suggested that the H_2 treatment induced the reduction of Ag^+

species to Ag^0 species. Meanwhile, the enhanced diffraction peaks indicated the formation of big Ag nanoparticles, which might be ascribed to the aggregation of Ag species during the high-temperature reduction. Figure 5b presents the XRD patterns of the as-prepared $Ag_1Cu_{0.025}$/S-O-yH catalysts. As illustrated in Figure 5b, compared with $Ag_1Cu_{0.25}$/S-O, H_2 reduction treatment induced the generation of Ag species. Meanwhile, with the reduction temperature improved, the diffraction peak intensity of Ag species gradually increased. However, the diffraction peaks corresponding to Cu or CuO species were not observed in $Ag_1Cu_{0.025}$/S-O-yH, which might be attributed to the lower Cu addition of the high interspersion of Cu or CuO species.

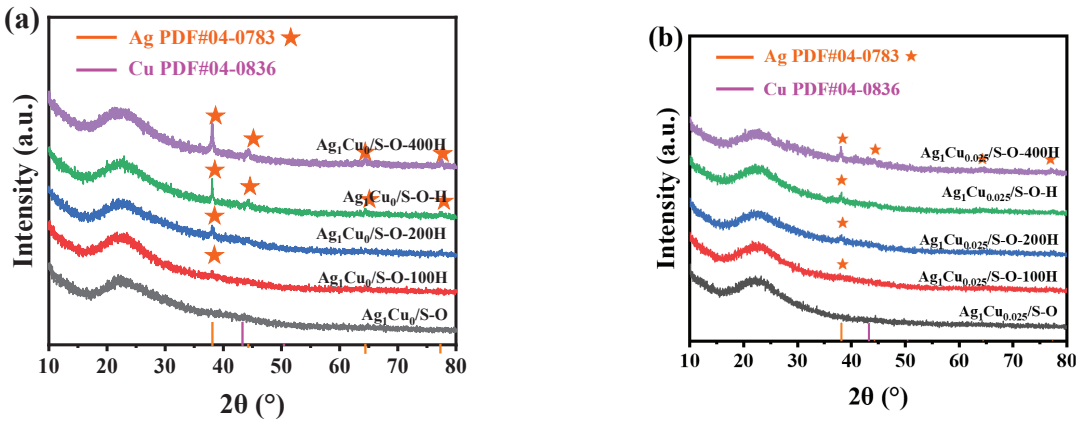

Figure 5. XRD patterns of the Ag_1Cu_0/SBA-15 (**a**) and $Ag_1Cu_{0.025}$/SBA-15 (**b**) catalysts pretreated under 30.0 vol.% O_2/Ar atmosphere at 500 °C for 2 h followed by H_2 atmosphere at different temperatures for 2 h.

Further, the Ag and Cu species in Ag_1Cu_0/S-O-yH and $Ag_1Cu_{0.025}$/S-O-yH were studied by UV-vis DRS spectra. Figure 6 displays the UV-vis DRS spectra of Ag_1Cu_0/S-O-yH and $Ag_1Cu_{0.025}$/S-O-yH. As shown in Figure 6, compared with the oxygen-treated Ag_1Cu_0/S-O and $Ag_1Cu_{0.025}$/S-O, the further H_2 reduction treatment resulted in the formation of Ag nanoparticles, which was in keeping with the XRD results.

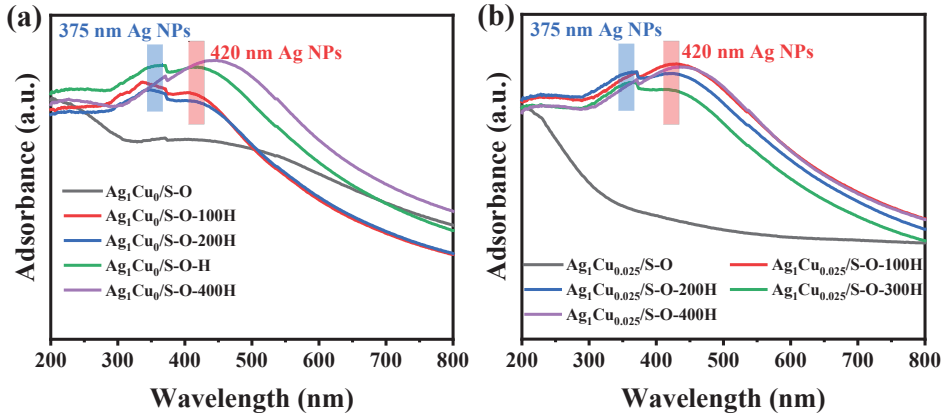

Figure 6. UV-vis DRS spectra of the Ag_1Cu_0/SBA-15 (**a**) and $Ag_1Cu_{0.025}$/SBA-15 (**b**) catalysts pretreated under 30.0 vol.% O_2/Ar atmosphere at 500 °C for 2 h, followed by H_2 atmosphere at different temperatures for 2 h.

Specific surface area, pore size distribution, and the pore volume of Ag_1Cu_0/S-O-yH and $Ag_1Cu_{0.025}$/S-O-yH were determined via N_2 adsorption–desorption curves. Brunauer–Emmett–Teller (BET) and Barrett–Joyner–Halenda (BJH) methods were applied to evaluate the surface area and pore size distribution of the samples, respectively. Figure 7

shows the N_2 adsorption–desorption curves and pore size distribution of Ag_1Cu_0/S-O-yH and $Ag_1Cu_{0.025}$/S-O-yH, and the corresponding physical parameters were summarized in Table 3. As presented in Figure 7a, all the N_2 adsorption–desorption curves of Ag_1Cu_0/S-O-yH presented a typical IV-typed isotherm attendant by an H1-type hysteresis loop, indicating the existence of the mesopore structure in Ag_1Cu_0/S-O-yH [52,53]. Meanwhile, the pore size distribution in Figure 7b illustrates a pore size of 3.0–7.7 nm, which also demonstrates the existence of a mesopore structure in the samples. The result suggested the reduction treatment would not influence the pore size of Ag_1Cu_0/S-O-yH. Notably, the sample treated under an H_2 atmosphere at 300 °C, Ag_1Cu_0/S-O-H, displayed an enhanced peak at 6.5 nm in pore size distribution (Figure 7b), indicating the formation of new pores with a pore size of ~6.5 nm in Ag_1Cu_0/S-O-H after 300 °C H_2 treatment. Meanwhile, the BET surface area and pore volume of Ag_1Cu_0/S-O-H (503 m^2/g and 0.663 cm^3/g) were increased in comparison to Ag_1Cu_0/S-O. Figure 7c,d depict the N_2 adsorption–desorption curves of $Ag_1Cu_{0.025}$/S-O-yH catalysts. As displayed in Figure 7c, similar to Ag_1Cu_0/S-O-yH, all the N_2 adsorption–desorption curves of $Ag_1Cu_{0.025}$/S-O-yH catalysts also presented the typical IV-typed isotherm accompanied by an H1-type hysteresis loop. Meanwhile, similar pore size distributions were also observed in $Ag_1Cu_{0.025}$/S-O-yH. Notably, the introduction of Cu could cause the formation of new pores at a pore diameter of ~6.5 nm (Figure 7d). Additionally, compared with Ag_1Cu_0/S-O-yH, the surface area of $Ag_1Cu_{0.025}$/S-O-yH was decreased, which might be ascribed to the occupation of Cu species in the pore channel, indicating the successful introduction of Cu in $Ag_1Cu_{0.025}$/S-O-yH [54,55]. Furthermore, compared with $Ag_1Cu_{0.025}$/S-O, the BET surface area of $Ag_1Cu_{0.025}$/S-O-yH increased first and then decreased as the reduction temperature increased. Among these, $Ag_1Cu_{0.025}$/S-O-yH presented the largest BET surface area (492 m^2/g), pore volume (0.68 cm^3/g), and pore size, with a higher pore volume. It had been reported that the large surface area and pore volume would be beneficial for the adsorption and diffusion of substrate molecules, which could improve catalytic performance [56,57].

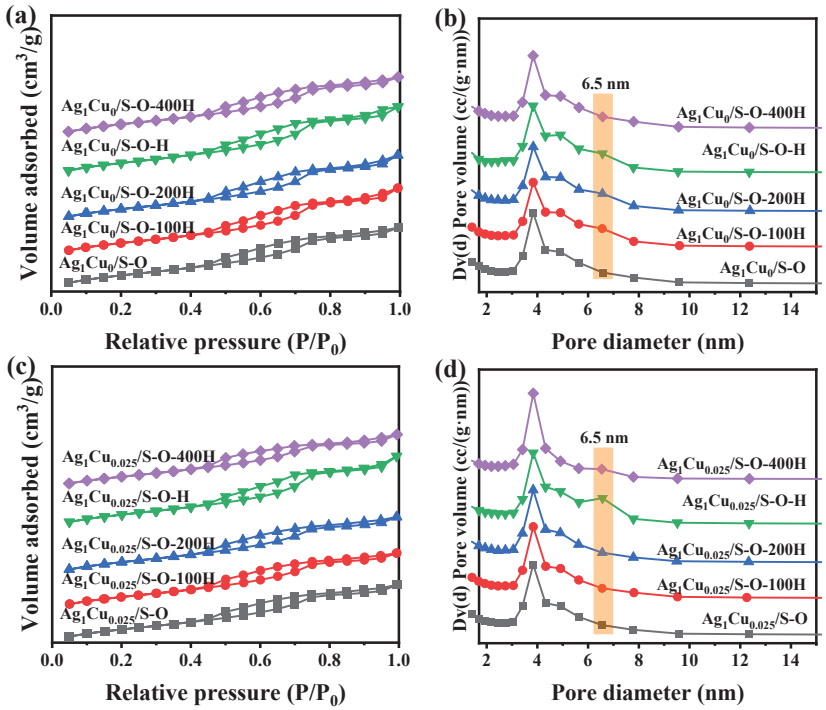

Figure 7. N_2 adsorption–desorption (**a**,**c**) and pore size distribution (**b**,**d**) of the Ag_1Cu_0/SBA-15 (**a**,**b**) and $Ag_1Cu_{0.025}$/SBA-15 (**c**,**d**) catalysts pretreated under 30.0 vol.% O_2/Ar atmosphere at 500 °C for 2 h followed by H_2 atmosphere at different temperature for 2 h.

Table 3. Physical parameter of Ag_1Cu_0/SBA-15 and $Ag_1Cu_{0.025}$/SBA-15 pretreated under different conditions.

Pretreated Conditions	Ag_1Cu_0/SBA-15			$Ag_1Cu_{0.025}$/SBA-15		
	S_{BET} (m^2/g)	V (cm^3/g)	D (nm)	S_{BET} (m^2/g)	V (cm^3/g)	D (nm)
500 °C O_2	494	0.592	3.0–7.7	477	0.560	3.0–7.7
500 °C O_2-100 °C H_2	490	0.650	3.0–7.7	481	0.560	3.0–7.7
500 °C O_2-200 °C H_2	492	0.640	3.0–7.7	485	0.570	3.0–7.7
500 °C O_2-300 °C H_2	503	0.663	3.0–7.7	492	0.680	3.0–7.7
500 °C O_2-400 °C H_2	491	0.590	3.0–7.7	467	0.540	3.0–7.7

2.2.2. Catalytic Performance of the Ag_1Cu_0/S-O-yH and $Ag_1Cu_{0.025}$/S-O-yH Catalysts

The catalytic activity of the Ag_1Cu_0/S-O-yH and $Ag_1Cu_{0.025}$/S-O-yH catalysts was estimated via CO catalytic oxidation. Figure 8 presents the CO conversions of the as-synthesized Ag_1Cu_0/S-O-yH and $Ag_1Cu_{0.025}$/S-O-yH catalysts for CO degradation, and the corresponding T_{98} and T_{50} are listed in Table 4. As displayed in Figure 8a, as the reduction temperature was enhanced, the catalytic performance of these catalysts first increased, and then reached the optimal catalytic activity (T_{98} = 41 °C) at the reduction temperature of 300 °C. With the further improved reduction temperature of 400 °C, the catalytic activity decreased to T_{98} = 41 °C, which might be ascribed to the aggregation of Ag nanoparticles induced by the high-temperature reduction. Figure 8b illustrates the temperature-dependent CO conversions over $Ag_1Cu_{0.025}$/S-O-yH in the range of 25–90 °C. As shown in Figure 8b and Table 4, like Ag_1Cu_0/S-O-yH, the improvement in the reduction temperature resulted in the raising of CO catalytic performance first. With the further increasing reduction in temperature to 400 °C, the CO catalytic performance decreased. The T_{98} values for $Ag_1Cu_{0.025}$/S-O, $Ag_1Cu_{0.025}$/S-O-100H, $Ag_1Cu_{0.025}$/S-O-200H, $Ag_1Cu_{0.025}$/S-O-H, and $Ag_1Cu_{0.025}$/S-O-400H were 81, 61, 55, 34, and 37 °C, respectively. Apparently, $Ag_1Cu_{0.025}$/S-O-H possessed the best catalytic activity for CO oxidation. Meanwhile, compared with the reported supported CuAg, Ag, Pd, and Pt catalysts [26,58–64] listed in Table 5, $Ag_1Cu_{0.025}$/S-O-H with low Ag loadings also presented great catalytic performance for CO oxidation.

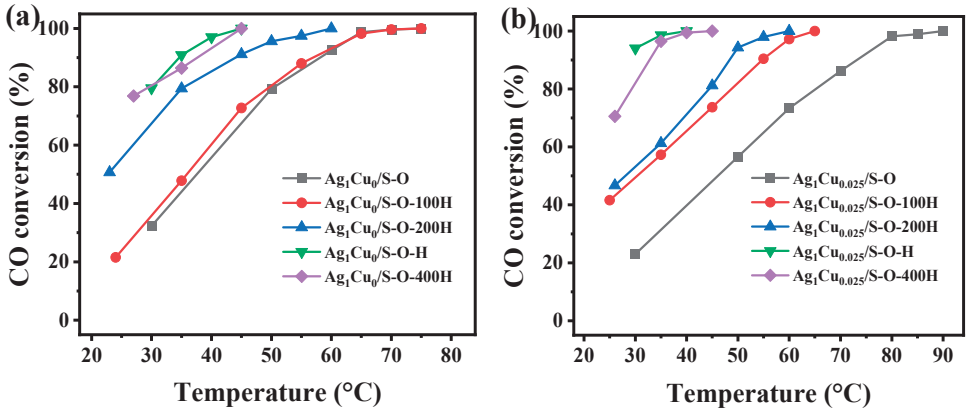

Figure 8. CO conversions of the Ag_1Cu_0/SBA-15 (**a**) and $Ag_1Cu_{0.025}$/SBA-15 (**b**) catalysts pretreated under 30.0 vol.% O_2/Ar atmosphere at 500 °C for 2 h followed by H_2 atmosphere at different temperatures for 2 h for CO oxidation.

Table 4. Catalytic performance of Ag_1Cu_0/SBA-15 and $Ag_1Cu_{0.025}$/SBA-15 pretreated under different conditions for CO oxidation.

Pretreated Conditions	Catalytic Performance CO Oxidation (°C)			
	Ag_1Cu_0/SBA-15		$Ag_1Cu_{0.025}$/SBA-15	
	T_{50}	T_{98}	T_{50}	T_{98}
500 °C O_2	37	65	46	81
500 °C O_2-100 °C H_2	35	65	30	61
500 °C O_2-200 °C H_2	<30	56	<30	55
500 °C O_2-300 °C H_2	<30	41	<30	34
500 °C O_2-400 °C H_2	<30	43	<30	37

Table 5. Comparison of the reported noble metal catalysts for CO oxidation in the literature.

Catalysts	Preparation Method	Noble Metal Loadings (wt%)	Flow Rate (mL/min)	Preparation Conditions	Catalytic Activity (°C)	Ref.
$Ag_2Cu_2O_3$	Co-precipitation	/	1000	/	160 (T_{100})	[58]
$CuAg/CeO_2$	Urea-assisted	5.71	30	550 °C-air-2 h	100 (T_{100})	[59]
$8Ag/SiO_2$-500	Wetness impregnation	8	20	500 °C-air-0.5 h 200 °C-10%H_2/Ar-0.5 h	66 (T_{98})	[60]
Ag/SBA-15	Impregnation	7	30	550 °C-N_2-2 h 550 °C-air-6 h	150 (T_{100})	[61]
Pd/SBA-15	Precipitation	2.8	25	300 °C-air-4 h	115 (T_{100})	[62]
$Pt/Sn_{0.2}Ti_{0.8}O_2$	Impregnation	0.5	100	300 °C-5%H_2-1 h	120 (T_{100})	[26]
PtPdRu/LCO	Sol–gel	/	40	300 °C-H_2	165 (T_{100})	[63]
Pd-Zn/TiO_2/Ti	Plasma electrolytic oxidation	5	50	400 °C-H_2-2 h	180 (T_{100})	[64]
$Ag_1Cu_{0.025}$/S-O-H	Impregnation	4	30	500 °C-30%O_2/Ar-2 h 300 °C-H_2-2 h	35 (T_{98})	This work

2.3. Discussion

According to the characterization and catalytic performance test results of these SBA-15-supported AgCu catalysts, the optimization of the catalyst was discussed as follows. Firstly, for the only oxygen-treated Ag_1Cu_x/S-O catalysts, the introduction of Cu species caused the formation of CuO*x* species, which presented poorer catalytic activity than that of Ag species for CO oxidation, occupying the catalyst surface, resulting in the inferior catalytic performance of Ag_1Cu_x/S-O. Then, further reduced by H_2, the formation of Ag nanoparticles improved the catalytic performance of Ag_1Cu_x/S-O-H. Meanwhile, the addition of appropriate Cu (Ag/Cu molar ratio of 1:0.025) improved the dispersion of Ag nanoparticles and the low-temperature reducibility. Furthermore, the H_2 reduction caused the generation of Ag-Cu interaction and enhanced CO oxidation. Finally, the influence of H_2 reduction temperature was investigated. The suitable H_2 reduction temperature caused the formation of new pores (~6.5 nm) and improved the surface area and pore volume, which promoted the adsorption and diffusion of CO molecules, boosting CO degradation. Therefore, the pretreatment under the 30.0 vol.% O_2/Ar atmosphere at 500 °C, followed by 300 °C H_2 and the introduction of appropriate Cu species, resulted in $Ag_1Cu_{0.025}$/S-O-H realizing complete CO oxidation at room temperature (35 °C).

2.4. Catalytic Stability, Effect of Reaction Velocity, and Reusability

Generally, the stability, effect of weight hourly space velocity (WHSV), and reusability of a catalyst are very important for its practical application. Therefore, $Ag_1Cu_{0.025}$/S-O-H, with an optimal CO degradation performance was selected to investigate the stability, influence of WHSV, and reusability. Figure 9a–c display the stability test, WHSV influence, and reusability test of $Ag_1Cu_{0.025}$/S-O-H for CO oxidation. As shown in Figure 9a, $Ag_1Cu_{0.025}$/S-O-H presented great stability for CO oxidation, which could keep ~98% CO

conversion at 35 °C for 24 h. Figure 9b depicts the influence of WHSV on $Ag_1Cu_{0.025}$/S-O-H for CO oxidation. The result showed that as the WHSV increased, CO catalytic performance decreased slightly, which might be ascribed to the residence time of CO molecules on the catalyst surface decreasing. As illustrated in Figure 9c, after being reused six times, $Ag_1Cu_{0.025}$/S-O-H maintained excellent catalytic performance in CO oxidation, which suggested its better reusability. Therefore, according to the above analysis, $Ag_1Cu_{0.025}$/S-O-H possessed great stability, resistance to WHSV changes, and reusability.

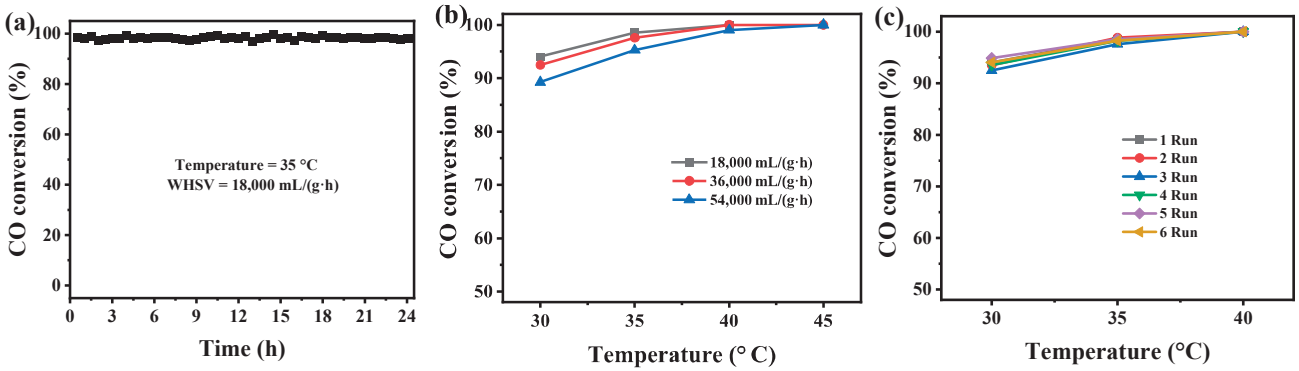

Figure 9. Stability (**a**), the effect of WHSV (**b**), and reusability (**c**) of $Ag_1Cu_{0.025}$/S-O-H for CO oxidation.

3. Materials and Methods

3.1. Chemicals

All the reagents were purchased from commercial sources and used directly. Poly(ethylene oxide)-block-poly(propylene oxide)-block-poly(ethylene oxide) ($EO_{20}PO_{70}EO_{20}$, P123, A.R.) was obtained from Shanghai Adamas Reagent Co., Ltd. (Shanghai, China). Hydrochloric acid (HCl, A.R., 36.0~38.0%), tetrabutyl orthosilicate (TEOS, 98%), anhydrous ethanol (EtOH, A.R., ≥99.7%), silver nitrate ($AgNO_3$, A.R., ≥99.8%), and copper nitrate trihydrate ($Cu(NO_3)_2 \cdot 3H_2O$, A.R., 99.0%) were bought from Sinopharm Chemical Reagent Co., Ltd. (Shanghai, China).

3.2. Catalyst Synthesis

3.2.1. Preparation of the Support

SBA-15 support was synthesized following the reported work [65]. The detailed synthesis process is listed as follows: 4.0 g of P123 was added to 125 mL of hydrochloric acid solution (2 mol/L) and stirred at 40 °C until a clear solution was formed. Then, 8.5 g of TEOS was added to the above-clarified solution and stirred for another 4 h. After that, the mixture solution was transferred into the stainless-steel high-pressure reactor and crystallized in an oven at 100 °C for 48 h. After cooling to the environmental temperature, the initial SBA-15 powder could be obtained via centrifugation, washing with deionized water and anhydrous ethanol several times, and drying at 100 °C for 12 h. Finally, the mesopore SBA-15 support could be acquired after calcinating in air at 540 °C for 10 h. The molar ratio of the precursors used for the synthesis of mesopore SBA-15 support was P123:HCl:H_2O:TEOS = 0.017:5.8:155:1.

3.2.2. Synthesis of Ag_1Cu_x/SBA-15 Catalysts

The Ag_1Cu_x/SBA-15 catalysts were prepared by the conventional wet-impregnation method according to our previous works [54]. Taking the preparation of Ag_1Cu_0/SBA-15 as an example, a certain amount of $AgNO_3$ solution was added to 1.0 g of SBA-15 powder under stirring. After the sample was evenly mixed, it was first dried at the environmental temperature for 12 h and then dried in an oven at 80 °C for another 12 h to acquire the

Ag_1Cu_0/SBA-15 catalyst. The theoretical loading of Ag was 4.0 wt% in the Ag_1Cu_0/SBA-15 catalyst. The Ag_1Cu_x/SBA-15 (x = 0, 0.0125, 0.025, 0.05, 0.25, 0.5 and 1), with Ag/Cu molar ratios of 1:0, 1:0.0125, 1:0.025, 1:0.05, 1:0.25, 1:0.5, and 1:1, could be obtained by tuning the $AgNO_3$ solution to the mixture solution of $AgNO_3$ and $Cu(NO_3)_2$. In the Ag_1Cu_x/SBA-15 catalysts, the loading of Ag was fixed at 4.0 wt%. Additionally, for comparison, the Ag_0Cu_1/SBA-15 was also prepared via the same wet-impregnation method.

To optimize the active sites of the Ag_1Cu_x/SBA-15 catalysts, the Ag_1Cu_x/SBA-15 catalysts were pretreated under different conditions. Firstly, the catalysts were treated under 30.0 vol.% O_2/Ar atmosphere at 500 °C for 2 h to obtain the Ag_1Cu_x/SBA-15-O catalysts, abbreviated as Ag_1Cu_x/S-15-O. Then, the Ag_1Cu_x/S-15-O catalysts were further treated in the H_2 atmosphere at 300 °C for another 2 h to acquire Ag_1Cu_x/S-15-O-H. Finally, to explore the effect of H_2 treatment temperature, the Ag_1Cu_x/S-15-O catalysts were calcinated under an H_2 atmosphere at different temperatures for another 2 h to obtain Ag_1Cu_x/S-15-O-yH (y = 25, 100, 200, 300, and 400 °C, representing the H_2 treatment temperature) catalysts. Among them, the 300 °C H_2 pretreated samples were named Ag_1Cu_x/S-15-O-H.

3.3. Characterizations

The catalysts were characterized by various methods. Detailed information about these characterizations is listed as follows.

(1) XRD patterns were used to measure the crystalline structure of the as-synthesized samples. The XRD patterns were measured in a Bruker D8 Advance X-ray diffractometer (Billerica, MA, USA), equipped with a monochromatic detector and Cu-Kα radiation. During measurement, the working emission current and accelerating voltage were 40 mA and 40 kV, respectively. The narrow-angle XRD patterns were tested in the 2θ range of 0.5–4.5°. The wide-angle XRD patterns were scanned from 10° to 80°.

(2) The UV-vis DRS spectra of the as-prepared catalysts were obtained from a UV-vis spectrometer (UV-2600, Shimadzu, Kyoto, Japan). Before testing, the baseline of the spectrometer was calibrated using $BaSO_4$.

(3) The actual metal loadings of the as-prepared catalysts were determined by ICP-OES (Avio 200, PerkinElmer, Waltham, MA, USA).

(4) An automatic chemical adsorption instrument (ChemBET TPR/TPD, Quantachrome, Boca Raton, FL, USA) equipped with a thermal conductivity detector (TCD) was applied to obtain the H_2-TPR profiles of the samples. Generally, 50 mg of the as-synthesized catalyst was added into a U-type quartz tube reactor and pretreated under N_2 atmosphere at 105 °C for 30 min. After cooling to 30 °C, the gas was switched to a 10.0 vol.% H_2/Ar atmosphere and was left alone for 30 min until the signal was stable. Then, the temperature-programmed process started at 30 and increased to 900 °C at a heating rate of 10 °C/min.

(5) The physical parameters of the catalysts were determined via N_2 adsorption–desorption curves in an automatic physical adsorption instrument (Quantachrome Autosorb iQ2, Quantachrome, Boca Raton, FL, USA). Before testing, 60–80 mg of the sample was degassed at 300 °C for 6 h under vacuum. Then, N_2 adsorption–desorption curves were determined at 77 K. The surface area was computed by the Brunauer–Emmett–Teller (BET) method. The pore diameter distribution was calculated by the Barrett–Joyner–Halenda (BJH) model based on the desorption branch of the N_2 adsorption–desorption curves.

3.4. Catalytic Performance Test

The catalytic activity of the catalysts was evaluated by CO catalytic degradation in a fixed-bed microreactor. Generally, 0.1 g of the catalyst particles (20–40 mesh) were placed

in a U-type quartz tube reactor. The reaction gas consisted of 1.0 vol.% CO and 20.0 vol.% O_2, and the balanced He. The reaction flow rate was 30 mL/min and regulated using a mass flowmeter. The reaction temperature was controlled by an open-type tubular furnace and measured by thermoelectric coupling. CO concentration in the input and outlet was detected using an online gas chromatograph (GC2060, Ruimin, Shanghai, China) equipped with a TCD and a chromatographic column (5A molecular sieve, 3 m × 3 mm). The CO conversion (X_{CO}) was computed using the formula

$$X_{CO} = (C_0 - C_i)/C_i \times 100\%$$

where C_0 and C_i were the CO concentrations in the inlet and outlet, respectively.

4. Conclusions

In summary, the mesopore SBA-15-supported AgCu catalysts with different Ag/Cu molar ratios were successfully synthesized via the wet impregnation method. The active sites were regulated by treatment under different atmospheres. It was found that after being treated under an O_2 atmosphere, the introduction of Cu species could induce the catalytic activity. The characterization results showed that the Cu species was oxidized to form CuO*x* species, which occupied the catalyst surface, suppressing CO oxidation. The further H_2 treatment caused the formation of Ag nanoparticles, promoting the degradation of CO at low temperatures. Meanwhile, the influence of H_2 reduction temperature on CO oxidation was also investigated. Among these SBA-15-supported AgCu catalysts, the $Ag_1Cu_{0.025}$/S-O-H catalyst with a Ag/Cu molar ratio of 1:0.025, and pretreated under 30.0 vol.% O_2/Ar atmosphere at 500 °C for 2 h, followed by H_2 treatment at 300 °C for another 2 h, presented the optimal CO catalytic performance, which could realize the complete degradation of CO at room temperature (35 °C). The results of serial characterizations, including XRD, UV-vis DRS, H_2-TPR, and N_2 adsorption–desorption, revealed that the introduction of Cu species and the treatment of O_2-H_2 could improve the dispersion of Ag nanoparticles, the formation of Ag-Cu interaction, and low-temperature reducibility. Meanwhile, the 300 °C H_2 treatment caused the formation of extra pores (~6.5 nm), which caused the enhancement of surface area and pore volume in $Ag_1Cu_{0.025}$/S-O-H. Based on this, $Ag_1Cu_{0.025}$/S-O-H could possess excellent catalytic performance. This work could provide guidance for the tuning of active sites with excellent catalytic performance for CO oxidation.

Author Contributions: F.B.: writing—original draft, funding acquisition, data curation, and formal analysis. H.H.: data curation, formal analysis, and investigation. Y.Z.: investigation, software, and methodology. Y.W. (Yanxuan Wang): methodology and software. Y.W. (Yuxin Wang): methodology and supervision. B.L.: conceptualization and supervision. H.D.: software and validation. X.Z.: writing—review and editing, funding acquisition, and visualization. All authors have read and agreed to the published version of the manuscript.

Funding: This research was funded by the National Natural Science Foundation of China (No. 12175145) and the Shanghai Rising-Star Program (24YF2729800).

Data Availability Statement: The authors declare that all data supporting the findings of this study are available within the article.

Conflicts of Interest: The authors declare that they have no known competing financial interests or personal relationships that could have appeared to influence the work reported in this paper.

References

1. Daniels, S.T. Products of incomplete combustion (O_x, CO_x, HO_x, NO_x, SO_x RO_x, MO_x and PO_x). *J. Hazard. Mater.* **1989**, *22*, 161–173. [CrossRef]
2. Zhang, J.; Shu, M.; Niu, Y.; Yi, L.; Yi, H.; Zhou, Y.; Zhao, S.; Tang, X.; Gao, F. Advances in CO catalytic oxidation on typical noble metal catalysts: Mechanism, performance and optimization. *Chem. Eng. J.* **2024**, *495*, 153523. [CrossRef]
3. Goldsmith, J.R.; Landaw, S.A. Carbon Monoxide and Human Health. *Science* **1968**, *162*, 1352–1359. [CrossRef] [PubMed]
4. Cao, M.; Shu, Q.; Zhang, R.; Zhang, Q. Structured Mesh-Type Pt/Mn/γ-Al_2O_3/Al Catalyst Enhanced the CO Oxidation at Room Temperature by In Situ Generation of Hydroxyl: Behavior and Mechanism. *Catalysts* **2025**, *15*, 430. [CrossRef]
5. Li, Y.; Li, S.; Xue, D.; Liu, X.; Jin, M.; Sun, L. Incorporation of Cu(II) and its selective reduction to Cu(I) within confined spaces: Efficient active sites for CO adsorption. *J. Mater. Chem. A* **2018**, *6*, 8930–8939. [CrossRef]
6. Ko, K.J.; Kim, H.; Cho, Y.H.; Lee, H.; Kim, K.M.; Lee, C.H. Overview of Carbon Monoxide Adsorption Performance of Pristine and Modified Adsorbents. *J. Chem. Eng. Data* **2022**, *67*, 1599–1616. [CrossRef]
7. Dwyer, D.J.; Hardenbergh, J.H. The catalytic reduction of carbon monoxide over iron surfaces: A surface science investigation. *J. Catal.* **1984**, *87*, 66–76. [CrossRef]
8. Huang, B.; Shi, Z.; Yang, Z.; Dai, M.; Wen, Z.; Li, W.; Zi, G.; Luo, L. Mechanism of CO selective catalytic reduction denitration on Fe-Mn/AC catalysts at medium and low temperatures under oxygen atmosphere. *Chem. Eng. J.* **2022**, *446*, 137412. [CrossRef]
9. Liang, C.; Sun, Y.; Li, P.; Jiang, Y.; Sun, X.; Yang, Z. Effect of Mn/Cu Molar Ratios on CO Oxidation Activity of Mn-Cu Bimetallic Catalysts. *Catalysts* **2025**, *15*, 353. [CrossRef]
10. Lyu, Y.; Xu, J.; Chen, S.; Wang, S.; Liu, X. Simultaneous catalytic oxidation of toluene and CO over Cu-V/Al-Ce catalysts: Physicochemical properties-activity relationship and simultaneous oxidation mechanism. *J. Hazard. Mater.* **2024**, *466*, 133507. [CrossRef]
11. Eid, K.; Gamal, A.; Abdullah, A.M. Graphitic carbon nitride-based nanostructures as emergent catalysts for carbon monoxide (CO) oxidation. *Green Chem.* **2023**, *25*, 1276–1310. [CrossRef]
12. Kovalskii, A.M.; Volkov, I.N.; Evdolimenko, N.D.; Tkachenko, O.P.; Leybo, D.V.; Chepkasov, I.V.; Popov, Z.I.; Matveev, A.T.; Manakhov, A.; Permyakova, E.S.; et al. Hexagonal BN- and BNO-supported Au and Pt nanocatalysts in carbon monoxide oxidation and carbon dioxide hydrogenation reactions. *Appl. Catal. B* **2022**, *303*, 120891. [CrossRef]
13. Zhuo, Z.; Wang, Y.; Hu, H.; Wei, J.; Qiao, R.; Bi, F.; Zhang, X. Recent progress of cerium-based catalysts for the catalytic oxidation of volatile organic compounds: A review. *Fuel* **2025**, *399*, 135603. [CrossRef]
14. Yang, Y.; Bi, F.; Wei, J.; Han, X.; Gao, B.; Qiao, R.; Xu, J.; Liu, N.; Zhang, X. Boosting the Photothermal Oxidation of Multicomponent VOCs in Humid Conditions: Synergistic Mechanism of Mn and K in Different Oxygen Activation Pathways. *Environ. Sci. Technol.* **2025**, *59*, 11341–11352. [CrossRef] [PubMed]
15. Guo, L.; Bi, F.; Liu, N.; Zhang, X. Degradation of volatile organic pollutants over manganese-based catalysts by defect engineering: A review. *Sep. Purif. Technol.* **2025**, *362*, 131934. [CrossRef]
16. Li, L.; Zhang, N. Atomic dispersion of bulk/nano metals to atomic-sites catalysts and their application in thermal catalysis. *Nano Res.* **2023**, *16*, 6380–6401. [CrossRef]
17. Xiao, M.; Han, D.; Yang, X.; Yu, J.; Shi, B.; Guo, Y.; Yu, X.; Ge, M. Active Interfacial Perimeter in Pt/CeO_2 Catalysts with Embedding Structure for Water-Tolerant Toluene Combustion. *Environ. Sci. Technol.* **2024**, *58*, 22808–22817. [CrossRef]
18. Chen, J.; Wang, Y.; Huang, J.; Ma, S.; Zhang, Y.; Bi, F.; Zhang, X. Electron Beam Irradiation Modified UiO-66 Supported Pt Catalysts for Low-Temperature Ethyl Acetate Catalytic Degradation. *Catalysts* **2025**, *15*, 220. [CrossRef]
19. Zhang, N.; He, C.; Jing, Y.; Qian, Y.; Obuchi, M.; Toyoshima, R.; Kondoh, H.; Oka, K.; Wu, B.; Li, L.; et al. Enhanced Nitrous Oxide Decomposition on Zirconium-Supported Rhodium Catalysts by Iridium Augmentation. *Environ. Sci. Technol.* **2025**, *59*, 1598–1607. [CrossRef]
20. Zhang, N.; He, C.; Jing, Y.; Qian, Y.; Toyao, T.; Shimizu, K. Enhanced N_2O decomposition on Rh/ZrO_2 catalysts through the promotional effect of palladium. *Surf. Interf.* **2024**, *46*, 104120. [CrossRef]
21. Huang, J.; Tao, H.; Chen, Z.; Zhou, M.; Na, J.; Chen, X.; Zhang, X. Advances in photocatalytic removal of NO_x and VOCs from flue gas. *Energy Environ. Prot.* **2024**, *38*, 144–154.
22. Ma, M.; Zhang, R.; Shen, Y.; Zhou, X.; Zhai, Y.; Han, Y.; Wang, D.; Zhang, L.; Song, X.; Fang, D.; et al. Mesoporous Ce-Ti Catalysts Modified by Phosphotungstic Acid and Chitosan for the Synergistic Catalysis of CVOCs and NOx. *Catalysts* **2025**, *15*, 119. [CrossRef]
23. Cao, X.; Liu, Y.; Huang, Q.; Chen, Z.; Sun, J.; Sun, J.; Pang, S.; Liu, P.; Wang, W.; Zhang, Y.; et al. Single Droplet Tweezer Revealing the Reaction Mechanism of Mn(II)-Catalyzed SO_2 Oxidation. *Environ. Sci. Technol.* **2024**, *58*, 5068–5078. [CrossRef] [PubMed]
24. Du, Z.; Su, L.; Chen, G.; Deng, Y.; Liu, Y.; Cen, W. Nondissociative activation of O_2 for SO_2 oxidation on metal-free N-doped carbocatalyst. *Surf. Sci.* **2022**, *723*, 122116. [CrossRef]

25. Le, P.H.; Kitamoto, Y.; Yamashita, S.; Cao, K.L.A.; Hirano, T.; Amen, T.W.M.; Tsunoji, N.; Ogi, T. Macropore-Size Engineering toward Enhancing the Catalytic Performance of CO Oxidation over Three-Way Catalyst Particles. *ACS Appl. Mater. Interfaces* **2023**, *15*, 54073–54084. [CrossRef]
26. Chen, J.; Xiong, S.; Liu, H.; Shi, J.; Mi, J.; Liu, H.; Gong, Z.; Oliviero, L.; Mauge, F.; Li, J. Reverse oxygen spillover triggered by CO adsorption on Sn-doped Pt/TiO_2 for low-temperature CO oxidation. *Nat. Commun.* **2023**, *14*, 3477. [CrossRef]
27. Wang, Y.; Bi, F.; Wang, Y.; Jia, M.; Tao, X.; Jin, Y.; Zhang, X. MOF-derived CeO_2 supported Ag catalysts for toluene oxidation: The effect of synthesis method. *Mol. Catal.* **2021**, *515*, 111922. [CrossRef]
28. Biabani-Ravandi, A.; Rezaei, M.; Fattah, Z. Catalytic performance of Ag/Fe_2O_3 for the low temperature oxidation of carbon monoxide. *Chem. Eng. J.* **2013**, *219*, 124–130. [CrossRef]
29. Fu, Y.; Yin, Z.; Qin, L.; Huang, D.; Yi, H.; Liu, X.; Liu, S.; Zhang, M.; Li, B.; Li, L.; et al. Recent progress of noble metals with tailored features in catalytic oxidation for organic pollutants degradation. *J. Hazard. Mater.* **2022**, *422*, 126950. [CrossRef]
30. Xu, W.W.; Dong, M.Y.; Di, L.B.; Zhang, X.L. A Facile Method for Preparing UiO-66 Encapsulated Ru Catalyst and its Application in Plasma-Assisted CO_2 Methanation. *Nanomaterials* **2019**, *9*, 1432. [CrossRef]
31. Shesterkina, A.; Zhdanova, C.; Davshan, N.; Medvedev, A.; Kalmykov, K.; Dunaev, S.; Kustov, L.; Kustov, A. CO_2 hydro-genation to methanol on the incapsulated Cu-Zn catalyst: Effect of the MCM-41 and SBA-15 supports and the method of preparation on catalytic activity. *Green Synth. Catal.* **2025**. [CrossRef]
32. Qin, Y.; Qu, Z.; Dong, C.; Huang, N. Effect of pretreatment conditions on catalytic activity of Ag/SBA-15 catalyst for toluene oxidation. *Chin. J. Catal.* **2017**, *38*, 1603–1612. [CrossRef]
33. Zhang, X.; Qu, Z.; Yu, F.; Wang, Y. High-temperature diffusion induced high activity of SBA-15 supported Ag particles for low temperature CO oxidation at room temperature. *J. Catal.* **2013**, *297*, 264–271. [CrossRef]
34. Lee, H.; Kim, W.I.; Jun, K.D.; Koh, H.L. Effect of Cu promoter and alumina phases on Pt/Al_2O_3 for propane dehydrogenation. *Korean J. Chem. Eng.* **2017**, *345*, 1337–1345. [CrossRef]
35. Wang, J.; He, G.; Wang, C.; Chen, X.; Liu, X.; Li, Y.; Shan, W.; He, H. HCHO oxidation on $Pt\text{-}Na/SiO_2$ catalyst with ultralow Pt loading: New insight into the effect of Si support and Na promoter. *Appl. Catal. B Environ. Energy* **2024**, *347*, 123787. [CrossRef]
36. Zhao, D.; Feng, J.; Huo, Q.; Melosh, N.; Fredrickson, G.H.; Chmelka, B.F.; Stucky, G.D. Triblock Copolymer Syntheses of Mesoporous Silica with Periodic 50 to 300 Angstrom Pores. *Science* **1998**, *279*, 548–552. [CrossRef]
37. Hussien, A.G.S.; Dabbawala, A.A.; Anjum, D.H.; Charisiou, N.D.; Almaksoud, W.; AbouHamad, E.; Kobayashi, Y.; Goula, M.A.; Polychronopoulou, K. Merits of the CeLaCuO ternary oxide as promoter of the Ni/SBA-15 catalyst for the dry reforming of methane reaction. *Chem. Eng. J.* **2024**, *496*, 153948. [CrossRef]
38. Sareen, S.; Mutreja, V.; Singh, S.; Pal, B. Highly dispersed Au, Ag and Cu nanoparticles in mesoporous SBA-15 for highly selective catalytic reduction of nitroaromatics. *RSC Adv.* **2015**, *5*, 184–190. [CrossRef]
39. Gu, J.; Huang, Y.; Elangovan, S.P.; Li, Y.; Zhao, W.; Toshio, I.; Yamazaki, Y.; Shi, J. Highly Dispersed Copper Species within SBA-15 Introduced by the Hydrophobic Core of a Surfactant Micelle as a Carrier and Their Enhanced Catalytic Activity for Cyclohexane Oxidation. *J. Phys. Chem. C* **2011**, *115*, 21211–21217. [CrossRef]
40. Bi, F.; Wei, J.; Gao, B.; Ma, S.; Liu, N.; Xu, J.; Liu, B.; Huang, Y.; Zhang, X. How the Most Neglected Residual Species in MOF-Based Catalysts Involved in Catalytic Reactions to Form Toxic Byproducts. *Environ. Sci. Technol.* **2024**, *58*, 19797–19806. [CrossRef]
41. Bogdanchikova, N.; Meunier, F.C.; Avalos-Borja, M.; Breen, J.P.; Pestryakov, A. On the nature of the silver phases of Ag/Al2O3 catalysts for reactions involving nitric oxide. *Appl. Catal. B* **2002**, *36*, 287–297. [CrossRef]
42. Wang, F.; Ma, J.; He, G.; Chen, M.; Zhang, C.; He, H. Nanosize effect of Al_2O_3 in Ag/Al_2O_3 catalyst for the selective catalytic oxidation of ammonia. *ACS Catal.* **2018**, *8*, 2670–2682. [CrossRef]
43. Wang, Z.; Sun, Q.; Wang, D.; Hong, Z.; Qi, Z.; Li, X. Hollow ZSM-5 zeolite encapsulated Ag nanoparticles for SO_2-resistant selective catalytic oxidation of ammonia to nitrogen. *Sep. Purif. Technol.* **2019**, *209*, 1016–1026. [CrossRef]
44. Choudhury, B.; Dey, M.; Choudhury, A. Defect generation, d-d transition, and band gap reduction in Cu-doped TiO_2 nanoparticles. *Int. Nano Lett.* **2013**, *3*, 25. [CrossRef]
45. Czaplinsks, J.; Sobczak, I.; Ziolek, M. Bimetallic AgCu/SBA-15 System: The Effect of Metal Loading and Treatment of Catalyst on Surface Properties. *J. Phys. Chem. C* **2014**, *118*, 12796–12810. [CrossRef]
46. Bi, F.; Wei, J.; Zhou, Z.; Zhang, Y.; Gao, B.; Liu, N.; Xu, J.; Liu, B.; Huang, Y.; Zhang, X. Insight into the Synergistic Effect of Binary Nonmetallic Codoped Co_3O_4 Catalysts for Efficient Ethyl Acetate Degradation under Humid Conditions. *JACS Au* **2025**, *5*, 363–380. [CrossRef]
47. Zhang, X.; Dong, H.; Wang, Y.; Liu, N.; Zuo, Y.; Cui, L. Study of catalytic activity at the Ag/Al-SBA-15 catalysts for CO oxidation and selective CO oxidation. *Chem. Eng. J.* **2016**, *283*, 1097–1107. [CrossRef]
48. Wen, Z.; Duan, X.; Hu, M.; Cao, Y.; Ye, L.; Jiang, L.; Yuan, Y. Efficient low-temperature soot combustion by bimetallic Ag-Cu/SBA-15 catalysts. *J. Environ. Sci.* **2018**, *64*, 122–129. [CrossRef]
49. Xue, J.; Wu, M.; Song, Y.; Zhao, J.; Wu, J.; Quan, Y.; Run, J. Study on performance of Ag-modified layered copper silicate catalyst for hydrogenation of dimethyl oxalate to methyl glycolate. *J. Fuel Chem. Technol.* **2022**, *50*, 1014–1022. [CrossRef]

50. Mahara, Y.; Ishikawa, H.; Ohyama, J.; Sawabe, K.; Satsuma, A. Ag-M (M: Ni, Co, Cu, Fe) bimetal catalysts prepared by galvanic deposition method for CO oxidation. *Catal. Today* **2016**, *265*, 2–6. [CrossRef]
51. Jabłońska, M.; Beala, A.M.; Nocuń, M.; Palkovits, R. Ag-Cu based catalysts for the selective ammonia oxidation into nitrogen and water vapour. *Appl. Catal. B* **2018**, *232*, 275–287. [CrossRef]
52. Zhang, N.; Tong, J.; Miyazaki, S.; Zhao, S.; Kubota, H.; Jing, Y.; Mine, S.; Toyao, T.; Shimizu, K. Mechanism of NH_3-SCR over P/CeO_2 Catalysts Investigated by Operando Spectroscopies. *Environ. Sci. Technol.* **2023**, *57*, 16289–16295. [CrossRef] [PubMed]
53. Bi, F.; Zhang, Y.; Zhou, Z.; Guo, L.; Zhu, Z.; Liu, B.; Zhang, X. Electron Beam Irradiation-Induced Defects Enhance Pt-TiO_2 Photothermal Catalytic Degradation in PAEs: A Performance and Mechanism Study. *Molecules* **2025**, *30*, 697. [CrossRef] [PubMed]
54. Lu, Z.; Guo, L.; Bi, F.; Ma, S.; Shen, Q.; Qiao, R.; Zhang, X. Insight into the degradation mechanism of mixed VOCs oxidation over Pd/UiO-66(Ce) catalysts: Combination of operando spectroscopy and theoretical calculation. *Sep. Technol. Technol.* **2025**, *354*, 129443. [CrossRef]
55. Wang, X.; Wu, L.; Wang, Z.; Feng, Y.; Liu, Y.; Dai, H.; Wang, Z.; Deng, J. Photothermal synergistic catalytic oxidation of ethyl acetate over MOFs-derived mesoporous N-TiO_2 supported Pd catalysts. *Appl. Catal. B* **2023**, *322*, 122075. [CrossRef]
56. Huang, Z.; Li, H.; Zhang, X.; Mao, Y.; Wu, Y.; Liu, W.; Gao, H.; Zhang, M.; Song, Z. Catalytic oxidation of toluene by manganese oxides: Effect of K^+ doping on oxygen vacancy. *J. Environ. Sci.* **2024**, *142*, 43–56. [CrossRef]
57. Huang, X.; Li, H.; Wang, L.; Tang, M.; Lu, S. Removal of toluene and SO_2 by hierarchical porous carbons: A study on adsorption selectivity and mechanism. *Environ. Sci. Pollut. Res.* **2022**, *29*, 29117–29129. [CrossRef]
58. Svintsitskiy, D.A.; Kardash, T.Y.; Slavinskaya, E.M.; Stonkus, O.A.; Koscheev, S.V.; Boronin, A.I. The decomposition of mixed oxide $Ag_2Cu_2O_3$: Structural features and the catalytic properties in CO and C_2H_4 oxidation. *Appl. Surf. Sci.* **2018**, *427*, 363–374. [CrossRef]
59. Yin, C.; Lei, Y.; Wu, H.; Xu, Y.; Luo, H.; Wang, H. Synergistic effect of Cu and Ag on porous (Cu, Ag) co-doped CeO_2 nanosheets for low-temperature CO oxidation. *Inorg. Chem. Commun.* **2025**, *172*, 113729. [CrossRef]
60. Dutov, V.V.; Mamontov, G.V.; Zaikovskii, V.I.; Liotta, L.F.; Vodyankina, O.V. Low-temperature CO oxidation over Ag/SiO_2 catalysts: Effect of OH/Ag ratio. *Appl. Catal. B* **2018**, *221*, 598–609. [CrossRef]
61. Xu, J.; Zhang, J.; Peng, H.; Xu, X.; Liu, W.; Wang, Z.; Zhang, N.; Wang, X. Ag supported on meso-structured SiO_2 with different morphologies for CO oxidation: On the inherent factors influencing the activity of Ag catalysts. *Microporous Mesoporous Mater.* **2017**, *242*, 90–98. [CrossRef]
62. Soni, Y.; Pradhan, S.; Bamnia, M.K.; Yadav, A.K.; Jha, S.N.; Bhattacharyya, D.; Khan, T.S.; Haider, M.A.; Vinod, C.P. Spectroscopic Evidences for the Size Dependent Generation of Pd Species Responsible for the Low Temperature CO Oxidation Activity on Pd-SBA-15 Nanocatalyst. *Appl. Catal. B* **2020**, *272*, 118934. [CrossRef]
63. Zhang, S.; An, K.; Wang, X.; Wang, H.; Li, S.; Sun, H.; Li, N.; Wu, Y.; Liu, Y. PtPd nanoparticles on $LaCoO_3$ with ruthenium in the interfaces for CO oxidation. *Appl. Surf. Sci.* **2023**, *609*, 155285. [CrossRef]
64. Samadi, P.; Binczarski, M.J.; Maniukiewicz, W.; Pawlaczyk, A.; Rogowski, J.; Szubiakiewicz, E.; Szynkowska-Jozwik, M.I.; Witonska, I.A. Zn Modification of $Pd/TiO_2/Ti$ Catalyst for CO Oxidation. *Materials* **2023**, *16*, 1216. [CrossRef]
65. Qu, Z.; Zhang, X.; Yu, F.; Liu, X.; Fu, Q. Role of the Al chemical environment in the formation of silver species and its CO oxidation activity. *J. Catal.* **2015**, *321*, 113–122. [CrossRef]

MDPI AG
Grosspeteranlage 5
4052 Basel
Switzerland
Tel.: +41 61 683 77 34

Catalysts Editorial Office
E-mail: catalysts@mdpi.com
www.mdpi.com/journal/catalysts

MDPI

Academic Open
Access Publishing

mdpi.com

ISBN 978-3-7258-5592-6